Intermetallics 2023

OTTO VON GUERICKE UNIVERSITÄT MAGDEBURG

Educational Center Kloster Banz • Germany

ABSTRACTS

www.intermetallics-conference.de

ISBN: 978-3-948023-33-1

Table of Contents

Organisation and imprint

Venue
Educational Center Kloster Banz
Hans-Seidel-Stiftung e.V.
96231 Bas Staffelstein, Germany

Date
02-06 October 2023

Scientific organiser
Prof. Dr.-Ing. Manja Krüger
Otto-von-Guericke University
Institute of Materials and joining Technology (IWF)
Universitätsplatz 2
39106 Magdeburg, Germany

Scientific co-organisers and programme committee

Prof.Dr.-Ing. Martin Heilmaier	Karlsruhe Institute of Technology / *Karlsruhe, Germany*
Prof. Dr. Florian Pyczak	Helmholtz-Zentrum Hereon / *Geesthacht, Germany*
Dr. Martin Schloffer	MTU Aero Engines AG / *Munich, Germany*
Dr. Frank Stein	Max-Plank-Institut für Eisenforschung GmbH / *Düsseldorf, Germany*

International advisory board

Bernard Bewlay	GE Global Research / *Niskayuna, NY / US*
Gabriele Caccciamani	University of Genova / *Genova, Italy*
Nathalie Dupin	Thermo Calcul / *Orcet, France*
Martin Friák	Institute of Physics and Materials / *Brno, Czech Rep.*
Easo George	Oak Ridge National Laboratory / *Oak Ridge, TN / US*
Haruyuki Inui	Kyoto University / *Kyoto, Japan*
John Perepezko	University of Wisconsin-Madison / *Madison, WI / US*
Cláudio Schön	University São Paulo / São Paulo, Brazil
Masao Takeyama	Tokyo Institute of Technology / *Tokyo, Japan*
Michel Vilasi	University of Lorraine / *Nancy, France*

Conference organization
Conventus Congressmanagement & Marketing GmbH
Carl-Pulfrich-Strasse 1
07745 Jena, Germany
www.conventus.de

Online programme for your mobile device
You want to know what is going on at the Intermetallics Conference?
You want to have all programme details at a glance?

Just scan the QR-code with your mobile devise and be up to date during your time at Kloster Banz.

ISBN - 978-3-948023-33-1

School on Thermodynamics of Intermetallics – 02 October 2023

As an additional offer for students and young colleagues, there will be the opportunity to participate in a short school about the basics of thermodynamics of intermetallic materials. The school is especially intended for students and young postdocs, the number of participants is limited and will be filled on a first come – first serve basis. The participation is free of costs but a registration beforehand is necessary.

09:00-10:30 **SoT 1 - Phase diagrams and phase transformations**
Frank Stein (Düsseldorf/DE)

Phase diagrams are the basis for any materials development. They contain information not only about phase equilibria and about the occurrence of phase transformations for a material of any chemical composition. By additionally having some knowledge about the kinetics of possibly involved phase transformations, phase diagrams also tell us a lot about the microstructure of a material with a certain chemical composition, which in turn already allows concluding on the mechanical properties to be expected for this material. After a brief introduction to the basics of phase diagrams, the primary objective of the lecture will be to show how phase diagrams can be used and which information can be read from them.

11:00-12:30 **SoT 2 - Key experiments and experimental techniques**
Martin Schloffer (Munich/DE)

Different experimental techniques exist for the determination of phase equilibria and phase transitions. Metallography and quantitative analysis of phases by X-ray diffraction (XRD) are two of them which help to compare microstructure and phase contents. Analysis both in parallel will allow to interpret if phase contents from high temperature were able to freeze during quenching or if in-situ experiments have to be chosen to evaluate the high temperature phase contents. As result, a proper heat treatment and experimental setup can be defined to attain and preserve thermodynamic equilibrium data. The different results of these techniques and the right interpretation will be briefly introduced with some real examples from the intermetallic Ti-Al system. Discussion will focus on practical aspects, e.g. how to decide whether a sample is in thermodynamic equilibrium, how the quality of individual data can be judged, and which additional methods like SEM-EDS, EPMA, and DSC have to be used to quantify the results.

School on Thermodynamics of Intermetallics – 02 October 2023

14:00-15:30 **SoT 3 - The CALPHAD method – advanced approach to thermodynamic modelling of phase diagrams and thermodynamic properties of complex materials**
Aleš Kroupa (Brno/CZ)

Phase diagrams are a key tool in the search for new or further development of existing materials, especially in terms of understanding the relationships between phase structure and their material properties. The current rapid advances in theoretical methods for studying materials, covering the full range of dimensions from the quantum to the continuum world, offer new opportunities for such developments that were previously unavailable. Advanced theoretical approaches and models make it possible to predict processes in advanced materials and anticipate their key properties.
A fundamental theoretical method that is directly applicable to both basic research and practical application development is the semi-empirical CALPHAD method, which allows modelling of phase diagrams and thermodynamic properties of complex systems. This method can be applied to very complex real materials and allows to significantly reduce the experimental work and speed up their development. Currently, the combination of CALPHAD-type calculations with highly theoretical methods (ab-initio calculations, phase field methods, etc.) allows not only to predict phase equilibria and structures in real materials, but also trends in their behaviour and material properties. In the search for materials with favourable properties, we can theoretically test a large number of compositions.
This talk will describe the basic principles of CALPHAD methods, including the latest models for describing the Gibbs energies of arbitrary existing phases, along with examples of their use, their strengths and weaknesses, prediction capabilities, etc. Attention will be paid to the modelling of intermetallic phases, which usually significantly affect the properties of the materials studied. Basic information on existing software packages, methods of creating basic thermodynamic datasets and large-scale thermodynamic databases will also be mentioned in the lecture.

16:00-17:30 **SoT 4 - Theory-guided materials design of intermetallic compounds**
Martin Friák (Brno/CZ)

Quantum-mechanical (so-called ab initio) methods have recently achieved considerable reliability when predicting materials properties. Ab initio calculations provide a deeper insight and understanding of matter at the atomic scale with an unprecedented level of detail and accuracy. Owing to their universality and reliability, they are becoming increasingly useful not only when studying existing materials but also when designing new ones. Importantly, whenever experimental data are missing, quantum-mechanical calculations represent a unique source of information for other modeling approaches, e.g., semi-empirical thermodynamic calculations of phase diagrams (CALPHAD), atomistic and continuum methods, or multiscale materials simulations. The quality of the ab initio description is not limited to ground-state parameters – material responses to rather extreme external conditions can reliably be determined as well. The lecture will (i) exemplify the use of ab initio calculations in current computational materials science, (ii) overview available software tools, (iii) identify major challenges, and (iv) outline a few foreseen future trends.

SCP2.1R

Oxidation-related degradation of the mechanical properties in TiAl: How does it occur or mitigated?

Mathias Galetz[1], Lukas Mengis[1], Ceyhun Oskay[1], Nadine Laska[2], Maciej Bik[3], Maciej Sitarz[3] P. Watermayer[4] and C. Liebscher[4]

[1]DECHEMA Forschungsinstitut, Theodor-Heuss-Allee 25, 60435, Frankfurt, Germany, galetz@dechema.de
[2]Deutsches Zentrum für Luft-und Raumfahrt e.V., Linder Höhe 4, 51147 Cologne, Germany
[3]AGH University of Science and Technology, Faculty of Materials Science and Ceramics, al. Mickiewicza 30, 30-059 Kraków, Poland
[4]Max-Planck-Institut für Eisenforschung GmbH, Max-Planck-Straße 1, 40237, Düsseldorf, Germany

Introduction

Intermetallic titanium aluminides (TiAl) offer a unique combination of well-balanced oxidation resistance and mechanical properties up to 700-750°C with an excellent specific high temperature strength. Since more than 10 years they have been used now as a high temperature material for turbine blades in the low-pressure section of airplane engines. Nevertheless, use at even higher temperature is hindered by the formation of a mixed TiO_2/Al_2O_3-scale at high temperatures along with oxygen uptake into the subsurface zone. Especially the formation of detrimental phases below the oxide scale dissolving higher amounts of oxygen compared to γ–TiAl strongly embrittle the alloys during exposure. To enhance resistance against oxidation, surface treatment is necessary. Many approaches of modifications of the metal surface through diffusion treatments and phenomena like the halogen effect were investigated in the past to alter the oxidation mechanism at elevated temperatures. This article shows recent advancements in the understanding the mechanisms of embrittlement during oxidation, recent coating approaches and outlines the requirements for future research.

Materials and Methods

The data shown was collected using the GE 4822 and TNM-B1 substrates, which are both alloys of industrial relevance. Samples were cut and exposed at different temperatures up to 1000h. Afterwards a brought analysis including SEM, EPMA, Raman and TEM was conducted, as described elsewhere [1,2]. Additionally recent coating approaches to slow down oxidation and suppress the oxygen embrittlement are shown and discussed with regards to their potential to mitigate the embrittlement at temperature.

Embrittlement during oxidation

Even after undergoing oxidation at 600°C for only 100 hours, the mechanical properties of TiAl alloys can be adversely affected at room temperature, despite the absence of β_0-phase transformation in the subsurface region and minimal mass gains. It has been found, that the progressive embrittlement is linked to an enrichment of oxygen in the subsurface zone, a phenomenon previously documented at elevated temperatures, e.g. [3]. As the β_0-Ti(Al) phase transforms into α_2-Ti_3Al, the overall solubility of oxygen in the subsurface region increases, augmenting its potential to induce brittleness. This process is well-known in Ti-alloys, where the formation of an oxygen-enriched α-case layer can enhance the alloy's strength, resulting in increased hardness, but also substantially reducing its ductility [4]. The presence of interstitially dissolved oxygen can lead to significant internal stresses and alter the movement of dislocations in titanium [5]. Although the results for TiAl reveal similar tendencies in β_0-Ti(Al)-containing TiAl alloys, the consequences for the investigated alloys are somewhat different. The embrittlement impact on the TNM-B1 alloy is less pronounced compared to the GE 4822 alloy, as TNM-B1 demonstrates linear-elastic fracture behavior in the HIPed condition, despite having a higher overall α_2- and β_0-phase content. Conversely, for the GE 4822 alloy after exposure, the existence of a brittle Laves phase, uniformly distributed in the subsurface region alongside the α_2-Ti_3Al phase, was confirmed. The specific contribution of this Laves phase to the embrittlement of the GE 4822 alloy should be explored in more detail in the future.

Coatings to mitigate embrittlement during exposure.

Researchers were investigating many coatings for TiAl [6]. Nevertheless, today still a maximum working temperature of 700-750°C still exists for TiAl alloys, the need for alternatives still exists. This is mostly caused by the negative influence of the coatings on the mechanical properties, as it is for example the case for Al-rich, intermetallic coatings based on the $TiAl_2$- or $TiAl_3$-phase.

A novel approach is followed by the application of polymer derived ceramics (PDCs), which attract attention due to their high thermomechanical stability, oxidation and chemical resistance. Being mainly silicon-based, PDCs

also offer the possibility to modify the chemical composition in order to tailor the structure and desired properties. Recently more and more work on PDCs for high temperatures has been published. Among these, silicon oxycarbide (SiOC) glasses, sometimes called “black” glasses due to their color, are very interesting. Considerable improvement in oxidation resistance was observed for SiOC-coated TiAl [7]. This was further improved In Figure 1 a PDC coating is shown that additionally contains Al within the SiOC layer on TiAl. This coating can reduce the partial pressure below the coating significantly, but cannot the suppress the detrimental microstructural changes in the subsurface zone, as obvious in form of the Cr-rich zone after 300h at 750°C.
Another most recent approach is the combination of characteristics of metallic and ceramic materials by applying MAX-phases, which are looked at in detail win the last couple of years. Max phases offer attractive chemical, physical, and mechanical properties and show high oxidation resistance due to the formation of a protective Al_2O_3 scale for the Al-containing MAX-phase [8,9]. Ti_2AlC, Ti_2AlN as well as Cr_2AlC are considered the most promising candidates.
The synthesis, oxidation resistance, and mechanical properties of a Cr_2AlC-based MAX-Phase coating on Ti4822 were investigated. After high temperature oxidation, an intermixed TiO_2/Al_2O_3-scale was found on top of the uncoated Ti4822 alloy while for the Cr_2AlC-phase coated samples an extremely thin, well-protective Al_2O_3+Cr_2O_3-scale formed, leading to much lower overall mass gains especially at 800°C. During exposure Al-inward diffusion from the Cr_2AlC-coating into the substrate occurred and led to the stabilization of Cr_7C_3, $Cr_{23}C_6$ as well as Cr_2Al. While the mechanical properties of the coated samples are very promising in the initial condition, they are negatively affected by the successive thermal decomposition of the coating.

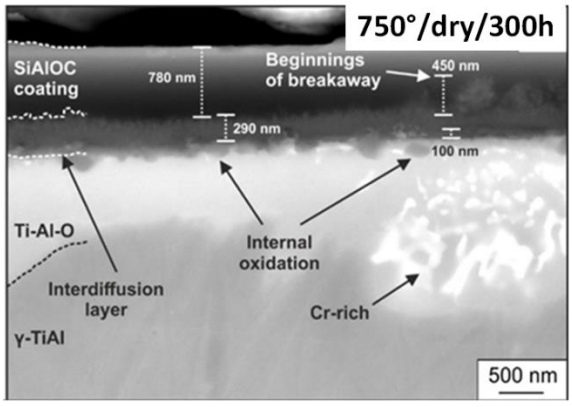

Fig. 1: Cross-sectional microstructure and EPMA analysis of SiAlOC-coated 4822 TiAl alloy oxidized for 300 h in dry air conditions

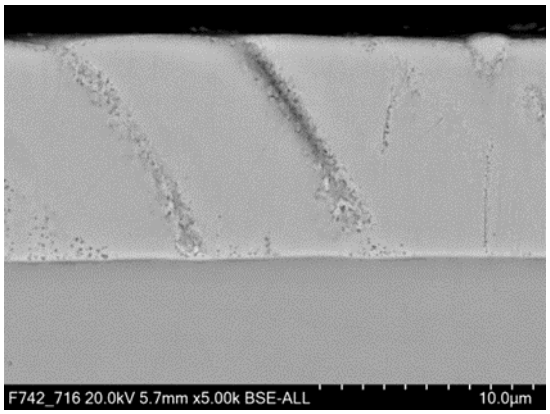

Fig. 2: SEM BSE image of the Cr2AlC-based coating on the Ti4822 alloy after heat treatment at 700°C for 1 h in Ar

References

[1] L. Mengis, A.S. Ulrich, P. Watermeyer, C.H. Liebscher, M.C. Galetz, Corrosion Science. 2021, 178, 109085
[2] M. Bik, M. Galetz, L. Mengis, E. White, W. Wieczorek, K. Łyszczarz, K. Mroczka, J. Marchewka, M. Sitarz, Appl Sur Sci, 2023, 157601
[3] S.L. Draper, D. Isheim, Intermetallics, 2012, 22, 77-83,
[4] R. Gaddam, B. Sefer, R. Pederson, M-L Antti., IOP Conf. Ser.: Mater. Sci. Eng., 2013, 48
[5] N. Chaari, D. Rodney, E. Clouet, Mat., 2019, 162, 200-203
[6] R. Pflumm, S. Friedle, M. Schütze, Intermetallics, 2015, 56, 1-14
[7] M. Bik, A. Gil, M. Stygar, J. Dąbrowa, P. Jeleń, E. Długoń, M. Leśniak, M. Sitarz. 2019, 105, 29–38
[8] D. B. Lee, T. D. Nguyen, S. W. Park, Oxid. Met., 2012 , 77, 275–287
[9] J. L. Smialek, Metall. Mater. Trans. A Phys. Metall. Mater. Sci., 2018, 49, 782–792

SCP2.2

Microstructure related electrochemical corrosion behavior of intermetallic Fe-25Al-5Cr-0.5Zr and Fe-25Al-5Cr-0.5Zr+TiC iron aluminides

René Daniel Pütz and Daniela Zander

Chair of Corrosion and Corrosion Protection, Foundry Institute, RWTH Aachen University, 52072 Aachen, Germany, r.puetz@gi.rwth-aachen.de, d.zander@gi.rwth-aachen.de

Introduction

It is well known that iron aluminides are a potential material group for high temperature applications based on the easily accessible elements like Al and Fe, good wear resistance, high strength-to-weight ratio, and promising high temperature oxidation resistance [1-3]. Additionally, their usage in aqueous conditions might also be promising due to their wide passivity range in acidic environments [4]. Under aqueous conditions, Al facilitates the formation and stability of a passive layer at the surface of iron aluminides [5]. While several studies [6-8] agree on an enrichment of Al^{3+} within the passive layer, the formation of divergent layer sequences in H_2SO_4 containing solutions were proposed. These include the formation of only one layer with a mixed oxide/hydroxide containing Fe- and Al-cations [6], the formation of a sandwich like layer model with an accumulation of Al^{3+} in the center [7], or the formation of a two-layered film composed of an outer mixed Fe-Al oxide/hydroxide and an inner layer containing primarily Al cations [8]. While most aqueous corrosion investigations focus on the passive film formation and the resistance against Cl^- induced pitting corrosion, the influence of phases regarding micro-galvanic coupling has barely been investigated. Negache et al. [9] indicated that among others, Zr-rich phases might lead to selective corrosion phenomena. However, a more in-depth analysis is necessary to understand the impact of phase manifestation on the electrochemical corrosion behavior in more detail. Therefore, the microstructure related electrochemical corrosion behavior of Fe-25Al-5Cr-0.5Zr and the same alloy modified with TiC additions were analyzed using electrochemical methods to identify the role of Zr-rich phases like the $(Fe,Al)_2Zr$ Laves phase and Zr-rich carbides on the occurring aqueous corrosion mechanisms. A previous study [12] could already identify the role of the adjusted microstructure on the high temperature oxidation behavior at 700 °C by reducing the inner oxidation depth of Zr-rich phases using TiC as an additive for Fe-25Al-5Cr-0.5Zr iron aluminide.

Materials and Methods

The iron aluminides (in at.%) Fe-25Al-5Cr-0.5Zr and Fe-25Al-5Cr-0.5Zr+TiC were produced using an investment casting procedure that was performed by Access e.V. (Aachen, Germany). Approximately 0.7 wt.% TiC were added before the melting process to the second alloy system to adjust the microstructure.

To analyze the as-cast microstructure of the materials, scanning electron microscopy (SEM), energy dispersive X-ray spectrometry (EDS), and X-ray diffraction (XRD) were performed. The electrochemical testing of the iron alumindes was utilized in a regular three-electrode set-up in which the sample is the working electrode (WE), a platinum sheet is the counter electrode (CE), and a saturated calomel electrode (SCE) that is connected via a bridge-tube capillary, serves as the reference electrode (RE). The samples were stepwise ground and polished until 0.02 µm grit and cleaned with ethanol prior to the corrosion testing. A thermostat provided a constant solution (acidified with H_2SO_4) temperature of 25 °C by heating water in a double walled beaker. The open circuit potential (OCP) was measured for 3600 s after the sample was immersed into the solution. Electrochemical impedance spectroscopy (EIS) was performed at OCP with 10 points per decade and an AC amplitude of 10 mV_{rms}. Additionally, potentiodynamic polarization (PDP) measurements were utilized with a scan rate of 0.167 mV/s.

Results and Discussion

The materials characterization of Fe-25Al-5Cr-0.5Zr revealed the formation of an interdendritic $(Fe,Al)_2Zr$ Laves phase network within the ordered Fe-Al matrix. The addition of TiC hampered the manifestation of a $(Fe,Al)_2Zr$ Laves phase network that was then rather discontinuously found at the grain boundaries and within the grains. Additionally, Zr-rich carbides were formed at the grain boundaries and in the grain interior due to the high affinity of Zr to C. In Fig. 1 a), the Nyquist plots (data and fitting) at OCP in 0.25 M H_2SO_4 solution after 3600 s of immersion for both iron aluminides are depicted showing the imaginary (-Z'') and real (Z') part of the impedance. For both alloys, one capacitive arc in the high frequency region and one inductive arc in the low frequency region can be identified. These two arcs suggest the presence of two time constants, which can also be identified in the Bode plot of the phase angle in Fig. 1 b). The appearance of the inductive arc for both alloys indicates the impact of adsorption processes at the reaction front. These can also be observed for various Fe-based materials in H_2SO_4 solutions [10,11]. The diameters of the capacitive semi-circles in the Nyquist plot (Fig. 1 a)) as well as the absolute impedance |Z| values in Fig. 1 b) already indicate a decreased corrosion susceptibility of the microstructural

modified Fe-25Al-5Cr-0.5Zr+TiC compared to Fe-25Al-5Cr-0.5Zr under the stated conditions. The reduced corrosion susceptibility is suggested to be reasoned by the changed behavior of micro-galvanic coupling between the Fe-Al matrix and the present phases.

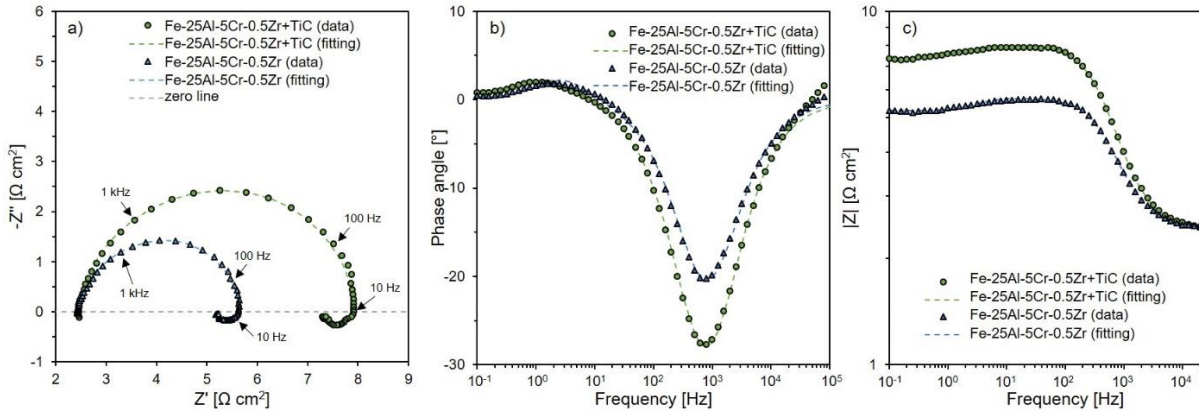

Fig. 1: EIS data and fitting for both iron aluminides at OCP in 0.25 M H_2SO_4 solution after 3600 s of immersion in the a) Nyquist plot, b) Bode plot of the phase angle, and c) Bode plot of the absolute impedance |Z|.

Acknowledgement
The authors thank Access e.V. (Aachen, Germany) for providing the material. The partial financial support from the Federal Ministry for Economic Affairs and Climate Action (BMWK) under grant no. [03ET7077B] is highly acknowledged.

References

[1] M. Zamanzade, A. Barnoush, C. Motz, Crystals. 2016, 6, 1-29.
[2] D.G. Morris, M.A. Muños-Morris, Advanced Engineering Materials. 2011, 13, 43-47.
[3] D.G. Morris, M.A. Muños-Morris, Materials Science and Engineering A. 2007, 462, 45-52.
[4] T.N. Kutz, D. Zander, Corrosion. 2017, 73, 648–654.
[5] N. De Cristofaro, S. Frangini, A. Mignone, Corrosion Science. 1996, 38, 307-315.
[6] V.S. Rao, Electrochimica Acta. 2004, 49 ,4533-4542.
[7] D. Schaepers, H.H. Strehblow, Corrosion Science. 1997, 39, 2193-2213.
[8] S. Frangini, N.B. De Cristofaro, A. Mignone, J. Lascovich, R. Giorgi, Corrosion Science. 1997, 39, 1431-1442.
[9] M. Negache, K. Taibi, N. Souami, H. Bouchemel, R. Belkada, Intermetallics. 2013, 36, 73-80.
[10] M. Keddam, O.R. Mattos, H. Takenouti, Journal of Electrochemical Society. 1981, 128 ,257–266.
[11] R.D. Pütz, T. Allam, J. Wang, J. Nowak, C. Haase, S. Sandlöbes-Haut, U. Krupp, D. Zander, Corrosion Science. 2022, 208, 110633.
[12] D. Zander, R.D. Pütz, Intermetallics. 2020, 126, 106924.

SCP2.3

Effect of Alloy Composition on Oxidation Resistance and Microstructure of Refractory Metals-Based Complex Concentrated Alloys (RCCAs)

Florian Häslich[1], Uwe Gaitzsch[1] and Thomas Weißgärber[1,2]

[1]Fraunhofer IFAM Dresden, Winterbergstraße 28, 01277 Dresden, Germany,
florian.haeslich@ifam-dd.fraunhofer.de, uwe.gaitzsch@ifam-dd.fraunhofer.de
[2]Technische Universität Dresden, Chair of Powder Metallurgy, 01062 Dresden, Germany,
thomas.weissgaerber@ifam-dd.fraunhofer.de

Introduction

High-entropy alloys (HEAs) and complex concentrated alloys (CCAs) based on refractory metals (RHEAs, RCCAs) alloyed with light metals have shown promising combinations of low density and high strength at high temperatures resulting in extensive research efforts to exploit their full potential for high-temperature applications.

In this work, the three RCCAs $AlMo_{0.5}NbTa_{0.5}TiZr$ [1], AlCrMoNbTi [2] and AlCrMoTaTi [2] were chosen as (near-) equimolar starting compositions for a comparative study. By systematically varying elemental concentrations of Al, Cr/Zr and Ti (stoichiometric factors: Al 1…3, Cr 1…0.5, Zr 1…0.25, Ti 1…3), the three base RCCAs are experimentally screened in terms of microstructure and isothermal oxidation resistance at 1000 °C for 48 h in ambient air. Additionally, the effect of minor additions of Si (1…5 atomic per cent) is investigated.

Screened RCCAs with highest oxidation resistance, beneficial phase composition and microstructure and promising mechanical properties will be further improved by microalloying in terms of high-temperature strength in future work.

Materials and Methods

Elemental bulk materials with purities >99.9 % were melted in an AM 500 vacuum arc melting furnace in 0.6 bar Ar atmosphere. Each slug was flipped over at least five times to ensure macroscopic homogeneity. After solidification, almost all alloys under investigation showed cracks as well as macroscopically inhomogeneous microstructures with grain sizes from µm-range to several mm. Thus, powder metallurgy processes were chosen to produce dense, crack-free samples with macroscopic homogeneous microstructure. Vacuum arc-melted alloy slugs were crushed and milled to powder using a vibrating disc mill with 1500 rpm for 10 s in ambient air. Powders were compacted by spark plasma sintering (SPS) to discs with 20 mm diameter and 2 mm height using graphite tools at 1300 °C and 50 MPa with a dwell time of 5 min in <0.1 mbar vacuum. After sandblasting and flat grinding all disc samples, homogenisation heat treatment at 1300 °C for 48 h in Ar atmosphere followed. Samples for oxidation testing were ground and polished using SiC abrasive papers down to grit 1200. For screening purposes, oxidation samples were cleaned in ethanol and weighed before as well as after isothermal oxidation testing at 1000 °C for 48 h in ambient air. The measured mass gain is an indicator for each alloy's oxidation resistance.

Selected promising alloys with highest oxidation resistance were investigated in more detail regarding phase composition, microstructure, mechanical properties and oxidation behaviour by thermal gravimetric analysis (TGA), scanning electron microscopy (SEM), energy dispersive X-ray spectroscopy (EDS), X-ray diffraction (XRD), differential scanning calorimetry (DSC), Vickers hardness testing, compression testing and Archimedes method.

Experimental investigations are supplemented by CALPHAD simulations using Thermo-Calc software with TCHEA5 database which is specifically designed for HEAs and CCAs.

Results and Discussion

For $AlMo_{0.5}NbTa_{0.5}TiZr$, isothermal oxidation results showed mass gain of 164 mg/cm² which decreased to 152 mg/cm² for $AlMo_{0.5}NbTa_{0.5}TiZr$-5Si, 142 mg/cm² for $AlMo_{0.5}NbTa_{0.5}TiZr_{0.25}$ and 113 mg/cm² for $Al_{2.5}Mo_{0.5}NbTa_{0.5}TiZr$, respectively. Varying Ti concentration did not change oxidation mass gain significantly. Both the base RCCA and all its chemical derivatives showed apparent dense oxide scales with considerable increase in volume, resulting in extensive cracking of the oxide scales. This was presumably caused by high Pilling-Bedworth ratios of Nb_2O_5 (2.68), Ta_2O_5 (2.50), TiO_2 (1.73) and ZrO_2 (1.56). [3] Thus, no protective oxide scales were formed. Investigations of Lu et al. [4] regarding varying Al concentrations showed the same trend, although mass gains were lower with 101 mg/cm² for $AlMo_{0.5}NbTa_{0.5}TiZr$ down to 70 mg/cm² for $Al_{1.5}Mo_{0.5}NbTa_{0.5}TiZr$, all in as-cast condition. Oxidation results for AlCrMoNbTi, AlCrMoTaTi and their chemical derivatives will be addressed in the talk.

Phase composition and microstructure of $AlMo_{0.5}NbTa_{0.5}TiZr$ and AlCrMoTaTi are strongly affected by varying element concentrations, respectively (Fig. 1). Phase composition ranges from two (Fig. 1c, g, h, i) to five apparent phases (Fig. 1b, j) judging by BSE contrast. CALPHAD simulations confirm these findings, suggesting a high

potential for tailoring beneficial phase composition and microstructure for high-temperature applications in future work. Microstructure results for AlCrMoNbTi and its chemical derivatives will be addressed in the talk.
Hardness testing resulted in high hardness values of 614 ± 12 HV10 for $AlMo_{0.5}NbTa_{0.5}TiZr$, 841 ± 30 HV10 for $\underline{Al_{2.5}}Mo_{0.5}NbTa_{0.5}TiZr$, 438 ± 4 HV10 for $AlMo_{0.5}NbTa_{0.5}\underline{Ti_{2.5}}Zr$, 682 ± 10 HV10 for $AlMo_{0.5}NbTa_{0.5}TiZr_{0.25}$ and 673 ± 21 HV10 for $AlMo_{0.5}NbTa_{0.5}TiZr$-5Si. In comparison, cast and heat-treated IN713C (355 ± 55 HV10 [5]) and powder metallurgical processed and heat-treated MoSiB (630 ± 15 HV10) show considerably lower hardness values at room temperature. Hardness results for AlCrMoNbTi, AlCrMoTaTi and their chemical derivatives as well as results of more detailed investigations will be addressed in the talk.

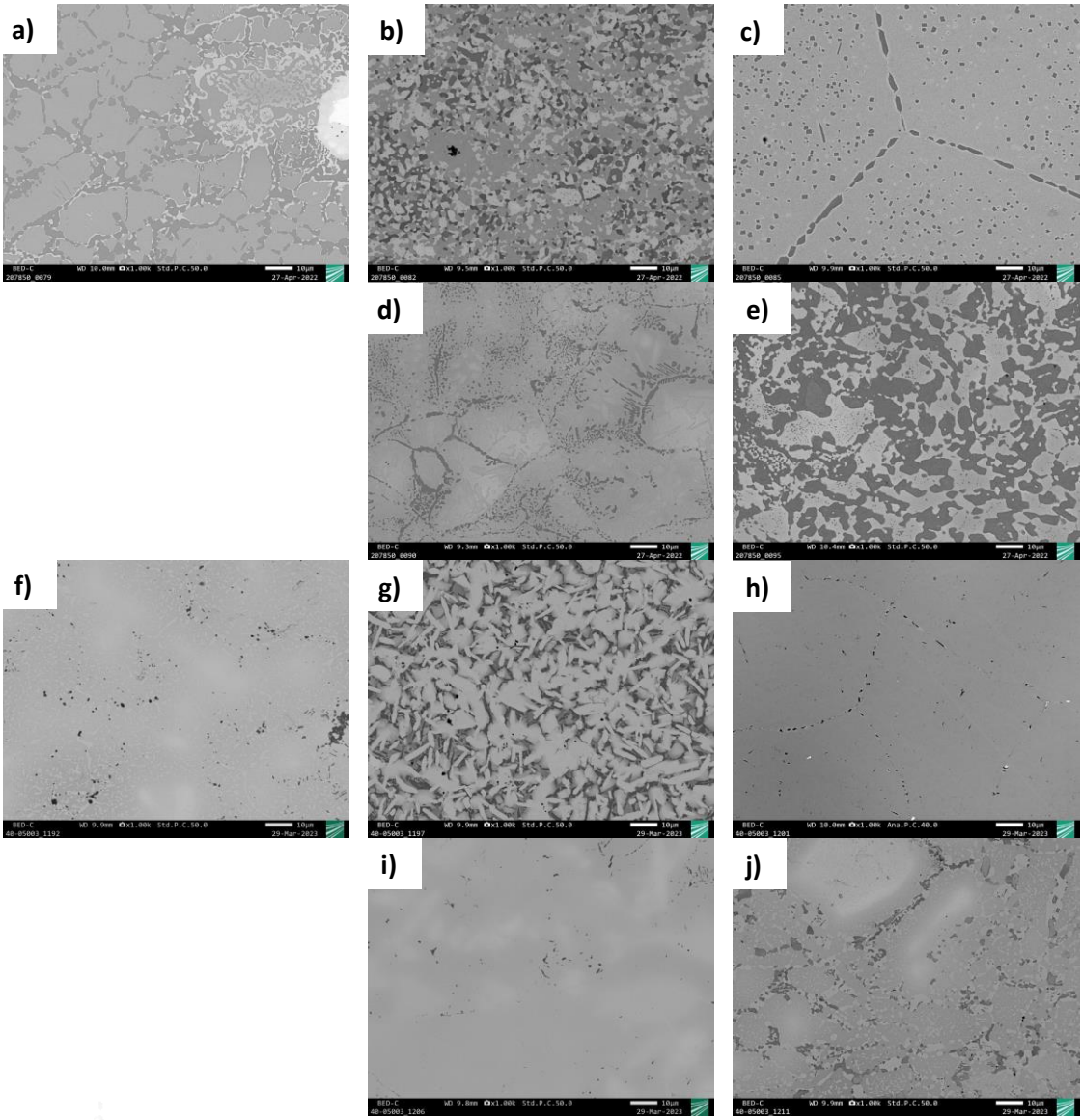

Fig. 1: SEM-BSE micrographs at identical magnifications of $AlMo_{0.5}NbTa_{0.5}TiZr$ and AlCrMoTaTi with varying compositions in homogenised condition: a) $AlMo_{0.5}NbTa_{0.5}TiZr$, b) $\underline{Al_{2.5}}Mo_{0.5}NbTa_{0.5}TiZr$, c) $AlMo_{0.5}NbTa_{0.5}\underline{Ti_{2.5}}Zr$, d) $AlMo_{0.5}NbTa_{0.5}TiZr_{0.25}$, e) $AlMo_{0.5}NbTa_{0.5}TiZr$-5Si, f) AlCrMoTaTi, g) $\underline{Al_3}CrMoTaTi$, h) $AlCrMoTa\underline{Ti_3}$, i) $AlCr_{0.5}MoTaTi$ and j) AlCrMoTaTi-5Si.

References

[1] O.N. Senkov, S.V. Senkova, C. Woodward, Acta Materialia. **2014**, *68*, 214–228.
[2] B. Gorr, F. Müller, M. Azim, H.-J. Christ, T. Müller, H. Chen, A. Kauffmann, M. Heilmaier, Oxidation of Metals. **2017**, *88*, 339–349.
[3] R. Bürgel, H.J. Maier, Th. Niendorf: Handbuch Hochtemperatur-Werkstofftechnik. Vieweg + Teubner, Wiesbaden, **2011**.
[4] S. Lu, X. Li, X. Liang, W. Shao, W. Yang, J. Chen, International Journal of Refractory Metals and Hard Materials. **2022**, *105*, 105812–105824.
[5] Nickel Institute: Engineering Properties of Alloy 713C.

SCP2.4

A novel pesting resistant Cr-Si-Mo alloy

Frauke Hinrichs[1], Alexander Kauffmann[1], Daniel Schliephake[1], Katharina Beck[3], Mathias Galetz[3], Zhongmin Long[2], Hemanth Thota[2], Yolita Eggeler[2], Astrid Pundt[1] and Martin Heilmaier[1]

[1]Institute for Applied Materials (IAM-WK), Karlsruhe Institute of Technology (KIT), Engelbert Arnold Str.4, 76131 Karlsruhe, Germany, frauke.hinrichs@kit.edu, alexander.kauffmann@kit.edu, daniel.schliephake@kit.edu, bonita.beichert@student.kit.edu, astrid.pundt@kit.edu, martin.heilmaier@kit.edu

[2]Microscopy of Nanoscale Structures & Mechanisms, Laboratory for Electron Microscopy (LEM), Karlsruhe Institute of Technology (KIT), Wolfgang-Gaede Str.1a, 76131 Karlsruhe, Germany, hemanth.thota@kit.edu zhongmin.long@kit.edu, yolita.eggeler@kit.edu

[3]DECHEMA-Forschungsinstitut, High Temperature Materials, Theodor-Heuss-Allee 25, 60486 Frankfurt am Main, Germany, katharina.beck@dechema.de, mathias.galetz@dechema.de

Introduction

Refractory metals and alloys have come into the focus of research of novel high temperature alloys due to their high melting points and solidus temperatures. However, refractory metal alloys often suffer from poor oxidation resistance at intermediate or elevated temperatures [1]. Significant progress was recently made in the development of oxidation-resistant Mo-Si-Ti alloys [2–4]. It was found that substantial Ti addition leads to a surprisingly protective TiO2/SiO2 scale in these alloys, preventing them from catastrophic oxidation ("pesting") at intermediate temperatures (~ 800 °C). Similar or even superior results might be achieved in other Mo-Si-X systems through alloying with elements that are considered passivating, like Cr. To investigate the potential pesting resistance of Cr-Si-Mo alloys, an alloy design approach was applied that aimed for a fine lamellar, two phase microstructure consisting of a solid solution and an intermetallic compound. Cr-13.5Si-32.2Mo (at.%) was identified as promising candidate in the Cr-Si-Mo system, as described below. Cr-13.5Si-32.2Mo (at.%) was subjected to cyclic oxidation at 800, 1100 and 1200 °C for up to 100 h to address the following fundamental questions:

- How do fine-lamellar Cr-Si-Mo alloys compare to similar Mo-Si-Ti alloys with respect to oxidation resistance, especially in the pesting regime (around 800 °C) with potential MoO_3 evaporation and beyond 1100 °C where CrO_3 starts to evaporate?
- How does solute partitioning of Cr in Cr-Si-Mo compare to Ti in Mo-Si-Ti in view of the continuous phase fields of $(Cr,Mo)_{ss}$ and $(Cr,Mo)_3Si$?

Materials and Methods

Microstructure analysis: Cr-13.5Si-32.2Mo ingots were cast from pure Mo foils (EVOCHEM, 99.95 %) Si pieces (ChemPur, 99.99 %) and Cr granules (ChemPur 99.99%) by arc melting (AM/0,5 Arc Melter, Edmund Bühler GmbH). The chamber was evacuated and flooded with Ar (> 99.998 %) at least three times. For arc melting an Ar base pressure of 600 mbar was used. The ingots were flipped and remelted five times in a water cooled Cu crucible to ensure homogeneity. Prior to all oxidation experiments, the ingots were heat treated at 1200 °C for 100 h in a protective Ar atmosphere (> 99,998 % purity) using a HTRH 70-600/18 resistance tube furnace (Carbolite GeroGmbH & Co. KG). To protect the ingots from impurities in the Ar atmosphere, Ti sponge was used as getter material in the tube furnace. No O uptake was detected. For microstructural analysis of the as-cast (AC), heat-treated (HT) and oxidized conditions, cross sections were prepared for scanning electron microscope (SEM) analysis. Backscattered electron contrast imaging (BSE) micrographs of AC and HT conditions as well as the oxide scales were taken at 20 kV on a LEO Gemini 1530 (Carl Zeiss AG) SEM. The phases present in the bulk material, as well as the phases formed during cyclic oxidation were investigated through X-ray diffraction (XRD) using a D2 Phaser (Bruker). Energy dispersive X-ray spectroscopy (EDS) was used to determine the local chemical composition of the individual phases in the non-oxidized HT condition and to analyze the oxide scale after cyclic oxidation at 800 °C for 100 h. SEM based EDS was performed on an Auriga 60 (Carl Zeiss AG) using 14 kV acceleration voltage. Scanning transmission electron microscopy (STEM) based EDS was performed on a FEI using an acceleration voltage of 200 kV. For STEM-EDS a lamella was prepared using a FEI Strata 400S Focused Ion Beam with a Ga Ion source.

Cyclic oxidation: Cuboidal samples of (5 × 5 × 5) mm^3 in dimensions were cut from HT material by electrical discharge machining and ground to grit P2500. The initial sample surface area was obtained using a Wild-Heerbrugg M420 optical macroscope and the software Olympus Stream Enterprise 1.7 (Olympus). Cyclic oxidation was performed in laboratory air using muffle furnaces (Gero and Nabertherm) at 800, 1100 and 1200 °C. Oxidation cycles were performed following the scheme described in Ref.[5] up to an exposure time of 100 h.

Mass changes of the oxidation samples were tracked after each oxidation cycle using a Sartorius precision balance with an accuracy of 1 µg. Oxide scale thicknesses were determined by processing BSE micrographs of sample cross sections using ImageJ

Results and Discussion

Cr-13.5Si-32.2Mo (at.%) solidifies as metastable single phase σ-phase (Cr_6Fe_7 prototype) with a dendritic microstructure during arc melting. Heat treatment leads to the decomposition into a fine-lamellar microstructure of $(Cr,Mo)_{ss}$ (W prototype) and $(Cr,Mo)_3Si$ (Cr_3Si prototype) through a solid state reaction as previously reported by Rudy and Nowotny [7] for similar alloy compositions. The Cr concentration varies only marginally between the two phases. A protective Cr_2O_3 layer with low growth rates was formed upon cyclic oxidation at 800, 1100 and 1200 °C for up to 100 h. Scale thicknesses after 100 h were below 1, 5 and 18 µm, at 800, 1100 and 1200°C, respectively. In addition to the Cr_2O_3 layer, the formation of an internal silicon oxide layer is found for 1200 °C. Chromia formation leads to Mo and Si enrichment in the subsurface region and the formation of a Mo-rich $(Cr,Mo)_3Si$ region that prevents the material from nitridation. The oxidation occurred not only remarkably free of nitridation, but neither spallation nor pesting were observed. Oxidation scales show a quartic growth rate at 800 °C and parabolic growth rates at 1100 and 1200 °C. At 1100°C, also mass changes showed a parabolic growth rate. The obtained oxidation rate constants associated with quartic and parabolic rate laws are very low compared to other Cr_2O_3 formers. The results of this study were published in Ref. [6].

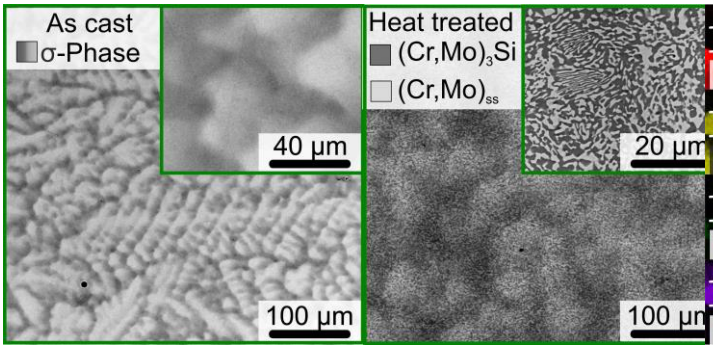

Fig. 1: BSE micrographs, overview and magnifications of the AC and HT microstructures

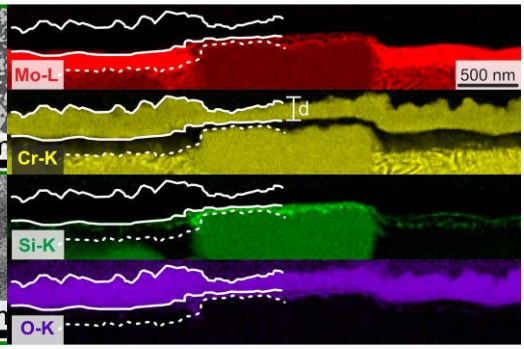

Fig. 2: STEM-EDS mapping of the oxide scale after 100 h cyclic oxidation at 800 °C [6]

References

[1] J.H. Perepezko, M. Krüger, M. Heilmaier, Materials Performance and Characterization, 2021, 10, 20200183.

[2] S. Obert, A. Kauffmann, M. Heilmaier, Acta Materialia, 2020, 184, 132–142.

[3] S. Obert, A. Kauffmann, S. Seils, S. Schellert, M. Weber, B. Gorr, H.-J. Christ, M. Heilmaier, Journal of Materials Research and Technology, 2020, 9, 8556–8567.

[4] D. Schliephake, A. Kauffmann, X. Cong, C. Gombola, M. Azim, B. Gorr, H.-J. Christ, M. Heilmaier, Intermetallics, 2019, 104, 133–142.

[5] S. Obert, A. Kauffmann, R. Pretzler, D. Schliephake, F. Hinrichs, M. Heilmaier, Metals, 2021, 11, 169.

[6] F. Hinrichs, A. Kauffmann, A.S. Tirunilai, D. Schliephake, B. Beichert, G. Winkens, K. Beck, A.S. Ulrich, M.C. Galetz, Z. Long, H. Thota, Y. Eggeler, A. Pundt, M. Heilmaier, Corrosion Science, 2022, 207, 110566.

[7] E. Rudy, H. Nowotny, Monatshefte für Chemie, 1974, 156–168.

SCP3.1R

Fatigue thresholds in EBM additively manufactured TiAl intermetallic alloys

Mauro Filippini

Politecnico di Milano, Department of Mechanical Engineering, Via La Masa 1, 20156 Milano, Italy,
mauro.filippini@polimi.it

Introduction

Gamma titanium aluminide-based alloys are considered more and more as a potential substitute of the currently employed nickel superalloys for structural applications in the aeroengines industry, as the material of choice for low-pressure turbine blades [1-2]. Development and advancement of gamma titanium aluminides technologies is regarded as a key factor for achieving the targets of engine efficiency and reduction of carbon dioxide emissions in new generation gas turbine engines [3]. Additive manufacturing by Electron Beam Melting (EBM) can be used to effectively produce gamma titanium aluminide (TiAl) intermetallic alloys with mechanical properties suitable for structural components, [4]. TiAl alloys are now considered as a substitute of some traditionally employed alloys in some specific applications in the energy, aerospace, and automotive industry (e.g., turbochargers wheels and engine valves), [5]. Even if TiAl alloys provide favorable specific strength at the relevant temperatures compared to competing nickel superalloys, they're regarded as more complex to design components with, due to their specific mechanical properties compared with conventional alloys. Moreover, depending on their final microstructure, fatigue strength is one of the most important design requirements, in the view of designing structural parts.

In this work, the fatigue crack growth properties of a high-Nb containing TiAl alloy (Ti-45Al-8Nb-2Cr, at. %) produced by additive manufacturing by Electron Beam Melting (EBM) technology is experimentally analyzed. Fatigue crack growth experiments with sub-size SENT specimens have been conducted with the aim of highlighting the interaction with the microstructure of fatigue cracks in the threshold region of this TiAl alloy, with special focus to the contribution of shielding mechanisms and crack closure in the near threshold regime.

Materials and Methods

The gamma titanium aluminide (γ-TiAl) Ti-45Al-8Nb-2Cr (at. %) intermetallic alloy studied in this work was produced by powder bed fusion additive manufacturing technique by electron beam melting (EBM), by means of the EBM A2 machine manufactured and distributed by ARCAM AB (Sweden). After EBM, the as-built material undergoes hot isostatic pressing (HIP, as described also in [4]) and subsequent heat treatment. Depending on the heat treatment parameters, fully lamellar or duplex microstructures may be obtained, [6]. In the case of the material studied in the present work, final microstructure is predominantly made by lamellar grains with grain size ranging from 200 to 500 µm, with an average grain size of about 300 µm.

Small squared-section blocks (12x12 mm cross section, 28 mm height) were cut by EDM from samples of heat-treated material. For each block, at mid-height, a deep notch with a small tip radius of about 150 µm was manufactured by thin wire EDM, so that fatigue cracks could be generated at the notch root by employing a specific compression pre-cracking procedure, [7-8]. Finally, sub-size SENT specimens were cut by EDM out of the pre-cracked blocks (Fig. 1), and a set of custom clevis grips was designed and manufactured, so that fatigue tests could be performed at loading ratio R=0.05. The evolution of the fatigue cracks was observed by optical microscope observations, allowing to reconstruct the progressive interaction of the growing cracks with the microstructure.

Results and Discussion

In the 2D view of the crack propagation as observable on the lateral surfaces of the specimens, it can be observed that fatigue accumulation damage is governed by the local microstructure, [9]. Fatigue crack paths are heavily controlled by the orientation of lamellar grains respect to the main loading direction and the crack propagation direction, resulting in a complex zig-zag pattern. By the observation made on propagating cracks, it became evident that a certain amount of crack deflection is always present, as the propagation direction usually changes when the fatigue cracks cross lamellar grains with different orientations, (Fig. 2). This phenomenon results in relatively rough fracture surfaces, with the premature contact between the fracture surface asperities during the unloading phase of the fatigue cycle, suggesting that roughness induced closure may play an important role in the fatigue damage process. For this reason, crack closure levels have been experimentally measured by applying the compliance offset method, with measured ratios of K_{cl}/K_{max} in the range of 32-38%.

In order to model the roughness induced closure phenomenon, the micro-geometric model of Suresh-Ritchie [10] was applied, allowing to assess that a key component of the closure effect on the fatigue crack threshold (between 70% and 85%) can be attributed to the roughness of the fracture surfaces.

The crack propagation rates measured within the miniaturized SENT specimens are in line with the data previously collected with standard C(T) specimens, giving confidence that the present test technique could be applied extensively for assessing the fatigue properties of TiAl alloys, at least in the early material development phase, when limited amounts of material are available. The lamellar microstructure is responsible for different "apparent" strengthening mechanisms, such as bridging, crack deflection, crack branching and microcrack shielding. The intensity of the closure phenomenon is remarkable, as can be observed from the experimentally determined crack opening forces. According to the Suresh-Ritchie model a significant part of the closure phenomenon can be attributed to roughness-induced closure. Further activities will require to acquire more data on crack propagation and especially on the contact between fracture surface asperities, which is responsible for roughness-induced closure.
More refined crack closure model(s) will provide more reliable closure levels assessment and allow to identify the effective stress intensity threshold $\Delta K_{th,eff}$ for the fatigue design of mechanical structural components.

Fig. 1: Sub-size SENT specimen employed for the fatigue crack growth tests

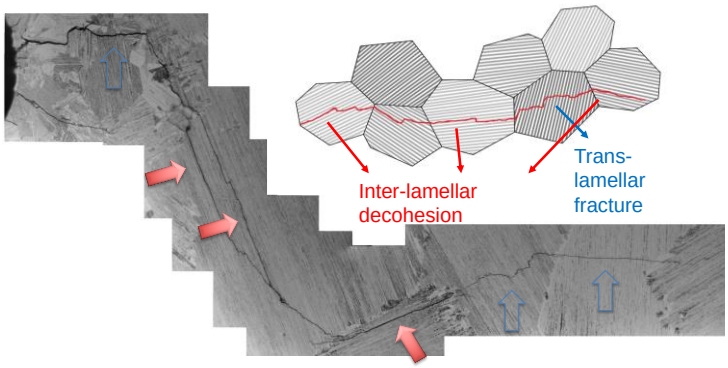

Fig. 2: Observation of evolution of fatigue cracks and interaction with microstructure

References

[1] F. Appel, J. D. H. Paul, M. Oehring, Gamma titanium aluminide alloys: science and technology. John Wiley & Sons **2011**.
[2] C. Leyens, M. Peters (Eds), Titanium and Titanium Alloys, WILEY-VCH, **2003**.
[3] B.P. Bewlay, S. Nag, A. Suzuki, M. J. Weimer, Mater. High Temp., 33(4-5), 549–559, **2016**.
[4] S. Biamino, A. Penna, U. Ackelid, et al., Intermetallics, 19(6), 776-81, **2011**.
[5] H. Clemens, S. Mayer, Advanced Engineering Materials, 15(4), 191–215, **2013**.
[6] M. Terner, S. Biamino, A. Penna, et al., EuroPM 2012 Conference, Vol. 1: PM Applications and new processes, **2012**.
[7] R. Pippan, P. Hageneder, W. Knabl, H. Clemens, T. Hebesberger, B. Tabernig, Intermetallics, 9(1), 89–96, **2001**.
[8] S. Eck, J. Maierhofer, C. Tritremmel, et al., Intermetallics, 121, 1067–70, **2020**.
[9] L. Patriarca, M. Filippini, S. Beretta, Intermetallics, 75, 42–50, **2016**.
[10] S. Suresh, R.O. Ritchie, Metall. Trans. A, 13(9), 1627–1631, **1982**.

SCP3.2

Optimized process parameters of advanced PBF-EB technology enabling the dual microstructure concept of γ-TiAl for industrial application

Marcel Reith[1], Martin Franke[1] and Carolin Körner[2]

[1]Neue Materialien Fürth, Dr.-Mack-Str. 81, 90762 Fürth, Germany, marcel.reith@nmfgmbh.de, martin.franke@nmfgmbh.de

[2]Chair of Material Science and Engineering for Metals, Friedrich-Alexander-Universität Erlangen-Nürnberg, Martensstraße 5, 91058 Erlangen, carolin.koerner@fau.de

Introduction

The dual microstructure concept of gamma titanium aluminides (γ-TiAl) is based on the idea of adjusting the local aluminum content by applying different melting parameters during electron beam powder bed fusion (PBF-EB) [1]. During subsequent heat treatment, regions with a low aluminum content are in the α phase field, leading to a fully lamellar (FL) microstructure, while regions with a higher aluminum content are in the α+γ phase field, resulting in a nearly lamellar (NL) microstructure [1]. While the FL microstructure provides increased creep strength [2], the NL microstructure shows a higher ductility [3]. In this way, complex geometries, for example, turbine blades, can be tailored to the local working loads during application [4]. *Knörlein et al.* demonstrated first, that this concept is feasible using conventional PBF-EB systems for the TNM γ-TiAl alloy [1]. However, the heat treatment window is too small for industrial applications.

Materials and Methods

The γ-TiAl powder Ti-44.5Al-4Nb-1Mo-0.1B (at%), called TNM, is processed on a prototype PBF-EB machine named HELIOS. The freely programmable prototype is developed by *pro-beam GmbH & Co. KGaA (Gilching, Germany)* and runs on a script programmed by the *Chair of Material Science and Technology for Metals at the Friedrich-Alexander-Universität (Erlangen, Germany)*. The machine is capable of 150 kV acceleration voltage and up to 45 kW power. Furthermore, in-situ process observation via electron optics (ELO) is available [5]. Subsequent heat treatments are conducted in a vacuum furnace *LHTM 250/300 (CarboliteGero GmbH und Co. KG, Neuhausen, Germany)*. The microstructure is analyzed in the scanning electron microscope *Helios NanoLab 600i (FEI Company, Hillsboro, Oregon, USA)* by a circular backscatter electron detector (CBS). Finally, the aluminum content is determined by electron probe microanalysis (EPMA) with the *Jeol JXA 8100 (JEOL, Akishima, Japan)*.

Results and Discussion

The high acceleration voltage enables the processing of γ-TiAl in a vacuum atmosphere ($2*10^{-5}$ mbar) without processing gas. Further, 150 kV widens the processing window to lower area energies and higher lateral velocities (see Fig. 1). The larger processing window enables the production of dense samples over a larger range of area energies, which is beneficial for the dual microstructure concept. Further, the EPMA measurements reveal a more homogeneous microstructure of 150 kV samples compared to conventionally manufactured (60 kV) samples. Both aspects, homogeneous microstructure, and enlarged processing windows facilitate a heat treatment window of 25°C, which should be suitable for industrial application.

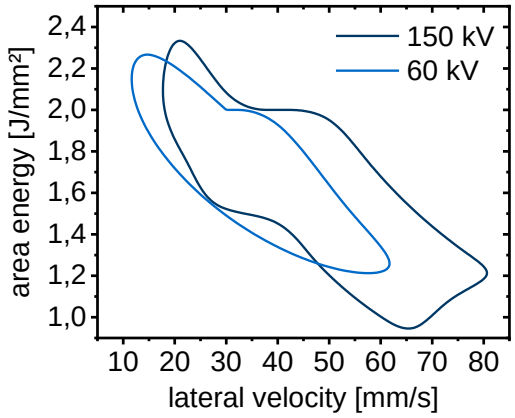

Fig. 1: Processing window of electron beam powder bed fusion for the γ-TiAl TNM alloy. The increased acceleration voltage widens the processing window to lower area energies and higher lateral velocities.

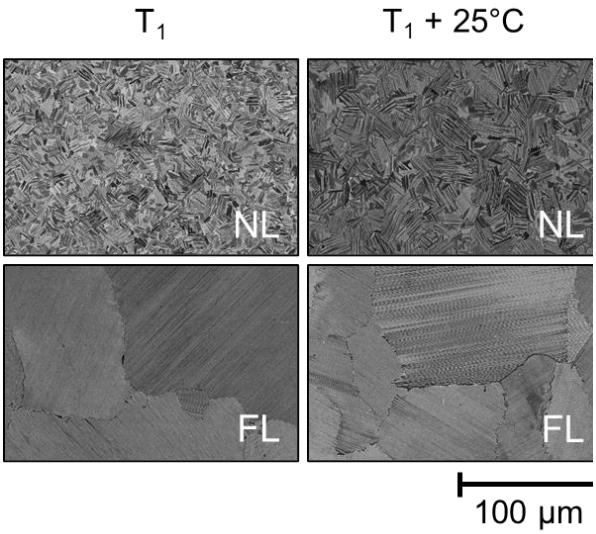

Fig. 2: Scanning microscope images after heat treatment. Two separate heat treatments with a temperature difference of 25°C are conducted. Both samples, left and right, show dual microstructures consisting of fully lamellar (FL) and nearly lamellar (NL).

References

[1] J. Knörlein, M. Franke, M. Schloffer, C. Körner, Additive Manufacturing 2022, 59, 103132
[2] S. Mayer, M. Kastenhuber, H. Clemens, Materials Science Forum 2018, 941, 1484-1489
[3] Y.-W. Kim, Materials Science and Engineering: A 1995, 192-193, 519-533
[4] M. Schloffer, M. Franke, C. Körner, Proceedings Intermetallics 2021, 179
[5] M. Franke, C. Arnold, C. Körner, Progress in Additive Manufacturing 2023, 8, 55–60

SCP3.3

Influence of tungsten addition on the deformation mechanisms of TiAl alloys

Benjamin Galy[1], Muriel Hantcherli[1], Alain Couret[1], Guy Molénat[1], Michael Musi[2], Petra Spoerk-Erdely[2], Helmut Clemens[2] and Jean-Philippe Monchoux[1]

[1]CEMES, Université de Toulouse, CNRS, 29 rue Jeanne Marvig, BP 94347, 31055 Toulouse, France
benjamin.galy@cemes.fr, muriel.hantcherli@cemes.fr, alain.couret@cemes.fr, guy.molenat@cemes.fr, jean-philippe.monchoux@cemes.fr
[2]Department of Materials Science, Montanuniversität Leoben, Franz-Josef-Straße 18, 8700 Leoben, Austria
michael.musi@unileoben.ac.at, petra.spoerk-erdely@unileoben.ac.at, helmut.clemens@unileoben.ac.at

Introduction

Tungsten has been found to increase the mechanical strength of γ-TiAl based intermetallics up to 800 °C [1], an effect which lead to the IRIS alloy of composition of Ti-48Al-2W-0.08B [at.%] [2]. This alloy exhibits high strength at elevated temperature and reasonably good ductility at room temperature, thanks to an optimized microstructure consisting of resistant fine lamellar colonies ≈ 40 µm in size, surrounded by ductile equiaxed γ grains. Here, we examine in detail the role of tungsten addition on the deformation mechanisms, which effect is suspected to result from its low diffusivity [3]. In particular, we will examine whether the presence of tungsten in solid solution induces changes in the controlling mechanisms (climb vs. glide of ordinary dislocations), and if modifications on the kinetics of these phenomena can be observed, by means notably of *in-situ* TEM heating and straining investigations. For these purposes, two model alloys have been processed, one of binary composition and the other containing tungsten (referred to as TiAl and TiAl-W, respectively). Thus, a powder metallurgy route, i.e. ingot casting, gas atomization and subsequent powder densification by spark plasma sintering (SPS), has been employed. On these materials, creep tests have been conducted at 800°C.

Materials and Methods

Specimens of Ti-48.4Al-0.1B (TiAl) and Ti-46.3Al-2.2W-0.2B (TiAl-W) compositions have been processed by SPS, using prealloyed powders provided by GFE Metalle und Materialien GmbH (Nuremberg, Germany). For the determination of the mechanical properties, sintering conditions have been employed to adjust lamellar microstructures, that is, by selecting elaboration temperatures of 1350°C-1375°C. For the investigations of the microscopic deformation mechanisms of the γ phase by TEM, specimens of near-γ microstructures have been elaborated at 1260°C-1300°C. To determine the creep strength of the materials of lamellar microstructure, tests have been conducted at 800°C under 200 MPa. For TEM *post-mortem* analysis, the tests were carried out with the specimens of near-γ microstructure at 800°C under 36 MPa, and interrupted after 3-5 % of plastic strain. The TEM *in-situ* investigations have been carried out at ≈ 800 °C, using commercial (Gatan) and home-made sample holders.

Results and Discussion

The creep tests (800°C-200 MPa) on the lamellar materials gave lifetimes of 19 h and 146 h, and secondary deformation rates of 2.6×10^{-7} s^{-1} and 1.4×10^{-7} s^{-1} for the TiAl and TiAl-W alloys, respectively. Therefore, tungsten addition leads to significant increase of the creep strength, as already reported. TEM *post-mortem* and *in-situ* investigations in the TiAl and TiAl-W alloy showed that the deformation mechanisms were glide and mixed climb of $a/2\langle 110]$ dislocations, as classically reported [4]. However, uncommon $a[001]$ dislocations have also been detected, which studies of our group have identified in the case of planar loops developing in (001) habit planes [5]. However, in contrast with this previous study, the a[001] dislocations identified here exhibited complex, helical non-planar morphologies (Fig. 1). This is therefore a new deformation mechanism, which requires now to be described in more details. Nevertheless, the helical morphology, which implies that the Burgers vector b=a[001] is not contained in the habit plane of the dislocation, is another direct evidence that climb is involved, and probably controls the deformation kinetics. However, the TEM *in situ* experiments at ≈800 °C in the binary TiAl alloy, coupled with determination of the habit planes of the dislocations, have unambiguously demonstrated that pure glide of ordinary $a/2\langle 110]$ dislocations is also activated (Fig. 2), and that the velocities of the dislocations for the glide and climb mechanisms are of close orders of magnitude (in the 0.5 – 5 nm/s range) [4]. This observation is surprising, pure glide being frequently supposed to involve much higher kinetics than glide. Finally, measurements in TiAl-W alloy gave rise to dislocation velocities of 3-9 nm/s, that is, close to that observed in the binary TiAl alloy, considering the scattering of the data.

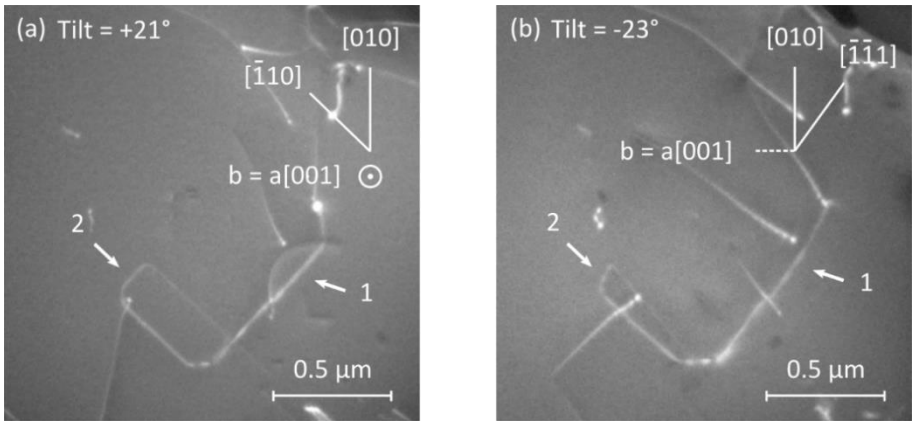

Fig. 1. C-type a[001] dislocation of complex morphology formed during creep at 800°C in a binary TiAl alloy. Micrographs (a) and (b) show this dislocation for tilt angles of the sample holder of +21° and -23°, respectively, allowing to show that the segment labelled 1 is not contained in the loop plane labelled 2, which demonstrates a helical morpho

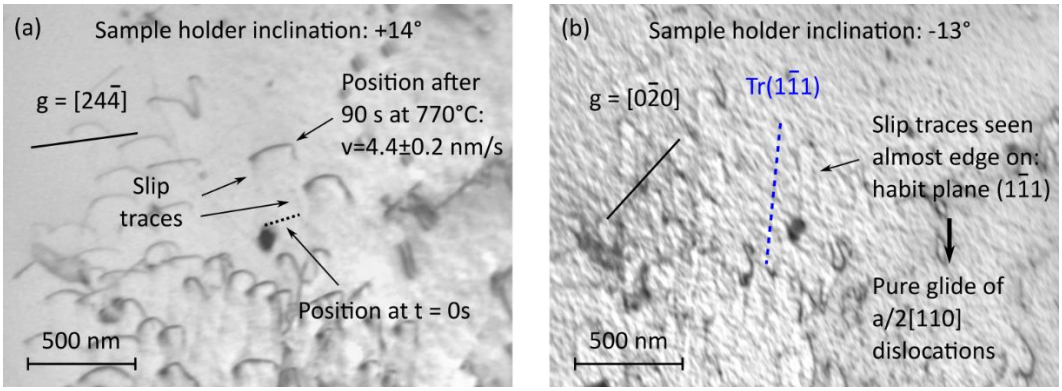

Fig. 2. Dislocation moving by glide at 770°C. (a) Image extracted from an *in-situ* TEM experiment, showing that a dislocation has moved at a velocity of 4.4 ± 0.2 nm/s. (b) Image of the same region after inclination of the sample holder, showing that the slip traces left by the dislocation during its motion at 770°C are contained in a pure glide $(1\bar{1}1)$ plane.

Conclusions

The TEM observations showed similar deformation mechanisms (glide and climb) at ≈800°C for both the TiAl and TiAl-W alloys. Therefore, no clear mechanism transition seems to be induced by the addition of tungsten. The dislocation velocity measurements (0.5 – 5 nm/s for TiAl and 3 - 9 nm/s for TiAl-W), gave also close orders of magnitude in the two alloys. However, potential effects of the addition of W on the dislocation kinetics can also be hidden by the scattering of the experimental data.

Acknowledgements

This study has been has been funded by the Austrian-French project “Hi-TiAl - 18-CE91-0008-01” co-supported by the French Agence Nationale de la Recherche (ANR) and the Fonds zur Förderung der wissenschaftlichen Forschung (FWF).

References

[1] T. Voisin, J.P. Monchoux, M. Thomas, C. Deshayes and A. Couret, Metall. Mater. Trans. A. **2016**, *47*, 6097.
[2] A. Couret, T. Voisin, M. Thomas and J.P. Monchoux, JOM. **2017**, *69*, 2576.
[3] A. Couret, J.P. Monchoux, D. Caillard, Acta Materialia. **2019**, *181*, 331.
[4] B. Galy, M. Musi, M. Hantcherli, G. Molénat, A. Couret, P. Spoerk-Erdely, H. Clemens, J.P. Monchoux, Scripta Materialia. **2023**, *228*, 115333.
[5] S. Naanani, J.P. Monchoux, C. Mabru, A. Couret, Scripta Materialia. 2018, *149*, 53.

SCP3.4

Recent progress on the Spark Plasma Sintering of TiAl alloys

Jean-Philippe Monchoux[1], Pierre Sallot[2], Agathe Deborde[3], Marc Thomas[4], Arnaud Bolsonella[5], Foad Naimi[5] and Alain Couret[1]

[1]CEMES, Université de Toulouse, CNRS, 29 rue Jeanne Marvig, BP 94347, 31055 Toulouse, France, alain.couret@cemes.fr, jean-philippe.monchoux@cemes.fr
[2]Safran Tech, Materials and Processes, Rue des Jeunes Bois, Châteaufort, 78114 Magny-Les-Hameaux, France, pierre.sallot@safrangroup.com
[3]IRT M2P (MetaFensch), 109 rue de Thionville, 57270 Uckange, France, agathe.deborde@irt-m2p.fr
[4]DMAS, ONERA, Université Paris Saclay, F-92322 Châtillon – France marc.thomas@onera.fr
[5]SINTERMAT, 9 rue de l'Oze, 21150 Venarey-Les-Laumes, France, arnaud.bolsonella@sinter-mat.com, foad.naimi@sinter-mat.com

Spark plasma sintering (SPS) has been used for developing TiAl alloys over the past fifteen years [1]. SPS is a consolidated powder metallurgy (PM) technique in which a graphite assembly containing the powder is simultaneously exposed to uniaxial pressure and a direct high intensity pulsed electric current [2]. Due to its short processing cycle, this method produces original microstructures with enhanced properties coupled with non-textured and homogenous structures, which are common to all PM techniques. As a result, the IRIS alloy ($Ti_{49.9}Al_{48}W_2B_{0.1}$) was developed for structural applications in gas turbine and automotive engines operating at temperatures up to 800°C [3]. The IRIS alloy has a microstructure which consists of small lamellar colonies surrounded by γ single-phase borders.

Under the leadership of Safran-Tech, french companies and research institutions have been working together for the past three years to enhance the entire SPS value chain used to produce TiAl alloys, more specifically the IRIS alloy.

The present talk is aiming at presenting four of these improvements:

- It has been demonstrated in the past that a crucial factor in producing high-quality alloys is related to the powder's homogeneity, particularly its chemical homogeneity when heavy elements like tungsten are used [4]. [Ref]. In particular, it has been found that the EIGA atomisation process generates inhomogeneities linked to the production of the electrode. It will be shown that processing the initial ingot for atomization via the PAM-CHR approach enables the production of powders free of tungsten inhomogeneities;
- In order to reduce the temperature gradient, a hybrid SPS system was used to sinter large billets of material. An external induction/resistance heating system is employed to help the original heating system driven by the current flowing in the graphite assembly. As a result, billets with good structural homogeneity were produced, measuring up to 10 mm in height and 300 mm in diameter;
- The high-temperature service properties of these PAM-EIGA powder-sintered IRIS alloys, including creep, fatigue, and oxidation resistance, were assessed and compared with those of the most recent TiAl alloys. The ability of the SPS-IRIS alloy to operate effectively at high temperatures has been confirmed;
- An improved chemical composition, called as IRIS+, was proposed after the effects of the incorporation of additional elements on the alloy characteristics were assessed. It is primarily based on the addition of carbon, which improves alloy resistance without significantly lowering low temperature ductility.

Acknowledgements

This study has been has been funded by the French project "Essential" supported by BPI France and FEDER Grand-Est.

References

[1] A. Couret, T. Voisin, M. Thomas, J.P. Monchoux, Journal of Metallurgy, 2549-6, 69(12), 2576-2582, 2017, DOI: 10.1007/s11837-017-

[2] T. Voisin, J.P. Monchoux, L. Durand, N. Karnatak, M. Thomas, A. Couret, Advanced Engineering materials, 17, 10, 1414, 2015, DOI: 10.1002/adem.201500019

[3] T. Voisin, J.P. Monchoux, M. Thomas, C. Deshayes, A. Couret, A, Metall. Mater. Trans. A 2016, 47, 6097–6108. DOI.org/10.1007/s11661-016-3801-3.

[4] A. Couret, M. Allen, M.W. Rackel, B. Galy, J.P. Monchoux, V. Guether, F. Pyczak, Materialia, 18, 1-10, 2021, DOI.org/10.1016/j.mtla.2021.101147

Figure. Illustrations of the successive steps of this work. A) PAM-CHR ingot, b) powder particles, c) large SPS billet, d) microstructure of the IRIS alloy and e) comparison of the creep properties at 800°C-200 MPa of the IRIS and IRIS+ alloy

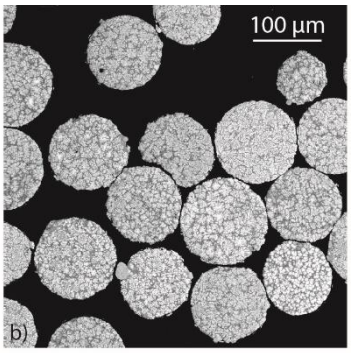

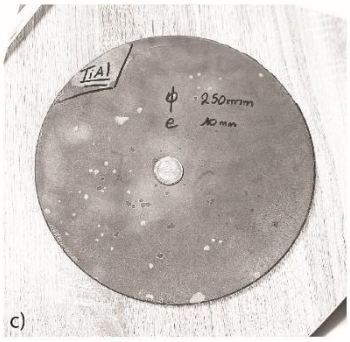

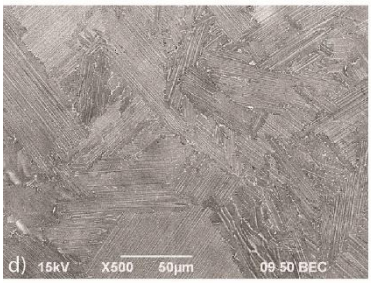

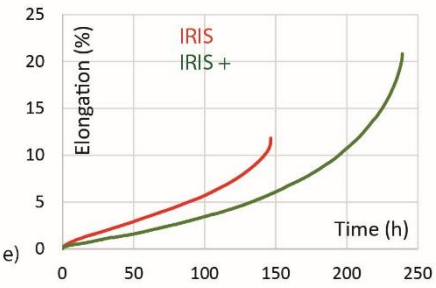

SCP4.1R

In situ synchrotron experiments addressing thermodynamic disequilibrium and the additive manufacturing of intermetallic γ-TiAl based alloys

Petra Spoerk-Erdely[1,2], Gloria Graf[1], Michael Musi[1], Peter Staron[3], Andreas Stark[3] and Helmut Clemens[1]

[1]Department of Materials Science, Montanuniversität Leoben, Franz Josef-Straße 18, 8700 Leoben, Austria, gloria.graf@unileoben.ac.at, michael.musi@unileoben.ac.at, helmut.clemens@unileoben.ac.at
[2]Institute of Materials Science, Joining and Forming, Graz University of Technology, Kopernikusgasse 24/I, 8010 Graz, Austria, petra.spoerk-erdely@tugraz.at
[3]Institute of Materials Research, Helmholtz-Zentrum Hereon, Max-Planck-Straße 1, 21502 Geesthacht, Germany, peter.staron@hereon.de, andreas.stark@hereon.de

Introduction

Intermetallic titanium aluminide alloys based on the ordered γ-TiAl phase are promising materials for lightweight high-temperature applications. In addition to their low density of roughly 4 $g \cdot cm^{-3}$, their high specific Young's modulus and strength even at elevated temperatures as well as their good oxidation and burn resistance, especially their excellent creep properties make these alloys a material of choice for challenging structural applications [1]. Following intensive research and development activities, γ-TiAl based alloys have recently entered service in the automotive and aircraft engine industries, e.g. as low-pressure turbine blades in environment-friendly jet engines, as engine valves in sports and racing cars, or as turbocharger turbine wheels [2]. In the course of the past decades, the development of these complex multi-phase alloys has benefited greatly from the application of *in situ* synchrotron X-ray techniques [3]. Diffraction and scattering techniques, in particular, have offered access to the atomic structure of the material and provided information on a variety of microstructural parameters. Advanced experimental setups, which are steadily refined, have even allowed the exploration of elaborate manufacturing processes and yielded insights that have so far been inaccessible by means of conventional methods. In this contribution, we will present several examples of *in situ* high-energy X-ray diffraction (HEXRD) experiments that were designed to understand specific aspects of engineering alloys connected with thermodynamic disequilibrium, such as critical *e.g.* to the additive manufacturing (AM) of γ-TiAl based alloys.

Materials and Methods

The first part of this contribution will attempt to provide a brief overview on different experimental setups and specimen environments that can be used at a synchrotron radiation source to study AM-related aspects. The topics addressed include the rapid solidification behaviour of γ-TiAl based alloys [4], the microstructural evolution during AM [5], as well as the characterisation of γ-TiAl based powder [6], which can serve as feedstock material. Most of the examples presented rely, at least in some form, on the dilatometer setup currently available at the Hereon-run High-Energy Materials Science beamline P07 at PETRA III at the Deutsches Elektronen-Synchrotron (DESY) in Hamburg, Germany [7]. Since the dilatometer permits an accurate control over temperature and atmosphere, isolated features of AM processes can be simulated and studied in great detail. For example, specimens can be subjected to temperature profiles measured previously on specific sample locations during AM, in order to investigate the phase transformations and microstructural evolution during an intrinsic heat treatment with good grain statistics.

When it comes to studying the rapid solidification behaviour of γ-TiAl based alloys, though, a dilatometer might not be the device of choice. The reason for this is not only that it is difficult to melt dilatometer samples in a controlled manner, but also that the cooling rates of real AM processes simply cannot be reached. For such experiments, a dedicated setup, thus, had to be developed, which will be presented in detail in the second part of this contribution. The following paragraphs of this abstract refer to this very case study, parts of which have been published in Ref. [4].

The setup employed for the *in situ* solidification experiments was based on a laser powder bed fusion (LPBF) chamber adapted for use at a synchrotron radiation source [8]. The laser, which was moved by a scanner unit, was used to melt the upper edge of a sample mounted on a sample holder. During the process, both the laser and the sample unit were contained in a chamber flooded with inert Ar gas. Due to the adaptation of the LPBF chamber, the synchrotron X-ray beam could be positioned perpendicular to the sample as well as the laser beam, pointing on a stationary point just below the upper edge of the sample. Consequently, the phase transformations upon melting and re-solidification could be probed in the gauge volume in transmission geometry. As the laser was set to move along the upper edge of the sample, an entire melting cycle including heating, melting, and

subsequent cooling could be traced. The use of the LPBF setup and the connected small melt pool size ensured that conditions, and especially cooling rates, close to those encountered during actual AM were met.
For this experiment to work, however, it is imperative that at a certain point in time the entire gauge volume is made up of melt. In a powder-bed based setup, this requirement is not easily met, since a sufficient sample thickness is necessary for a suitable diffraction signal. In this case, it is unlikely that all powder particles in the gauge volume will be simultaneously melted by the laser, independent of the hatch pattern, and the remaining solid particles will obstruct any analysis of, *e.g.*, primary solidifying phases. To circumvent this problem, thin platelet-shaped specimens were inserted into the sample holder, and, while being single-track fused along the upper edge, the laser parameters were carefully selected to ensure a suitable melt pool size with respect to the X-ray beam.
The *in situ* solidification experiments shown in the following were conducted on an intermetallic γ-TiAl based alloy with a nominal chemical composition of Ti-48Al-2Cr-2Nb (at.%). Platelets with cross-sections of 5 × 5 mm^2 and thicknesses ranging from 200 to 500 µm were cut from as-cast material. Following an extensive laser parameter study, which was performed in close collaboration with the Laser- and Plasma-Technologies of the Joanneum Research Forschungs-gesellschaft mbH, Niklasdorf, Austria, the *in situ* HEXRD experiments were conducted at beamline P07 at DESY using a mean photon energy of 100 keV and a PILATUS3 X CdTe 2M area detector.

Results and Discussion
Figure 1 shows an example of the evolution of the azimuthally integrated intensities of various reflections pertaining to the different phases in the investigated Ti-48Al-2Cr-2Nb (at.%) alloy during one melting cycle. Based on the amorphous region that occurs roughly between 35 and 45 ms and is labelled as “L” (for liquid), it can be concluded that the experiment was successful in the sense that the entire gauge volume was melted at one given moment. In contrast to thermodynamic calculations based on the T_0 concept [9], which predicted for the alloy Ti-48Al-2Cr-2Nb (at.%) a change in the primarily solidifying phase from β to α for high cooling rates, the *in situ* HEXRD experiments permitted the identification of the primary phase forming even at cooling rates of 10^3-10^4 K/s as β (see the following region “L+β” in Fig. 1). After solidification, the microstructure mainly consisted of α_2 phase. Experiments with detector frame rates varying from 50 Hz [4] to 250 Hz (Fig. 1) highlighted the importance of fast area detectors for the investigation of such rapid phase transformations, since only at the highest rates the unambiguous identification of β forming from the melt was possible. While no change in the solidification pathway was confirmed experimentally, the tests with varying sample thicknesses showed that in fact the interplay between temperature gradient and solidification rate plays a decisive role in the microstructural evolution. Further experiments, coupled with a dedicated simulation by means of finite element modelling, are planned to extricate these exact influences.

Acknowledgements
We acknowledge DESY (Hamburg, Germany), a member of the Helmholtz Association HGF, for the provision of experimental facilities at PETRA III. Parts of this research were carried out at beamline P07 at PETRA III and we would like to thank Dr. Norbert Schell for assistance in using the beamline and Jan Rosigkeit for the fruitful collaboration on the experiments. Beamtime was allocated for proposal I-20191411. The authors thank Erwin Krohmer, Institute for Machine Tools and Factory Management, Technische Universität Berlin, Germany, for access to the LPBF setup.

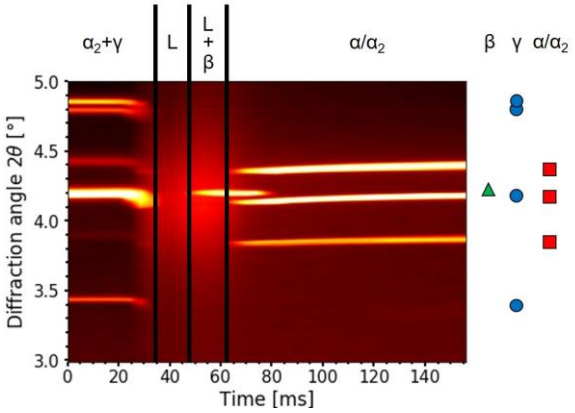

Fig. 1: Azimuthally integrated diffraction patterns stacked as a function of time during an *in situ* rapid solidification experiment on a Ti-48Al-2Cr-2Nb (at.%) alloy.

References

[1] F. Appel, J.D.H. Paul, M. Oehring: Gamma Titanium Aluminide Alloys. Weinheim: Wiley-VCH, **2011**.

[2] B.P. Bewlay, S. Nag, A. Suzuki, M. J. Weimer, Materials at High Temperatures. **2016**, *33*, 549.

[3] P. Spoerk-Erdely, P. Staron, J. Liu, N. Kashaev, A. Stark, K. Hauschildt, E. Maawad, S. Mayer, H. Clemens, Advanced Engineering Materials. **2021**, *23*, 2000947.

[4] G. Graf, J. Rosigkeit, E. Krohmer, P. Staron, R. Krenn, H. Clemens, P. Spoerk-Erdely, Advanced Engineering Materials. **2021**, *19*, 2100557.

[5] T. Klein, G. Graf, P. Staron, A. Stark, H. Clemens, P. Spoerk-Erdely, Materials Letters. **2021**, *303*, 130500.

[6] M. Musi, H. Clemens, A. Stark, P. Spoerk-Erdely, Advanced Engineering Materials. **2023**, *25*, 2201242.

[7] N. Schell, A. King, F. Beckmann, T. Fischer, M. Müller, A. Schreyer, in: Materials Science Forum. **2014**, *772*, 57.

[8] E. Krohmer, F. Schmeiser, B. Wahlmann, J. Rosigkeit, G. Graf, P. Spoerk-Erdely, H. Clemens, P. Staron, C. Körner, W. Reimers, E. Uhlmann, Review of Scientific Instruments. **2022**, *93*, 065104.

[9] R. Wartbichler, H. Clemens, S. Mayer, C. Ghibaudo, G. Rizza, M. Galati, L. Iuliano, S. Biamino, D. Ugues, Advanced Engineering Materials. **2021**, *23*, 2101199.

SCP4.2

Study of microstructural effects on diffraction elastic constants in γ-TiAl based alloys

David Obersteiner[1], Benjamin Seligmann[1], Emad Maawad[2] and Petra Spoerk-Erdely[1]

[1]Department of Materials Science, Montanuniversität Leoben, Franz-Josef-Straße 18, 8700 Leoben, Austria, david.obersteiner@unileoben.ac.at, benjamin.seligmann@unileoben.ac.at, petra.spoerk-erdely@unileoben.ac.at

[2]Institute of Materials Physics, Helmholtz-Zentrum Hereon, Max-Planck Straße 1, 21502 Geesthacht, Germany, emad.maawad@hereon.de.

Introduction

Lightweight intermetallic γ-TiAl based alloys are advanced engineering materials and have gained significant interest in recent years. Their mechanical properties, such as high-temperature strength, low density, and high resistance against creep and oxidation, make them ideal candidates for high-temperature applications up to 750 °C. Consequently, this alloy class has already been successfully implemented in internal combustion engines for the aerospace and automotive industry [1,2]. One particular group of γ-TiAl based alloys are the so-called β-stabilized TNM alloys with a nominal chemical composition of Ti-43.5Al-4Nb-1Mo-0.1B (at.%). The microstructure of these TNM alloys is mainly made up of the γ-phase ($L1_0$ structure) and the α_2-phase ($D0_{19}$ structure). In addition, depending on the thermomechanical processing including hot working and heat treatments, a certain amount of β_o-phase (B2 structure) is also present. In general, this particular class of γ-TiAl based alloys with increased β-stabilizing elements such as Nb and Mo is characterized by improved hot workability. In addition to workability with conventional forging tools, this has led to the development of new heat treatments resulting in novel microstructures with balanced properties [2-4]. For the development and optimization of modern manufacturing and joining technologies, it is important to determine residual stresses with high precision. A commonly used method for determining residual stresses is based on X-ray diffraction as well as the application of the diffraction elastic constants (DECs) S_1 and $\frac{1}{2}S_2$ [5,6]. These constants link the experimentally determined lattice strains with the macroscopic stresses prevailing in the material and can be obtained either by measurement or calculation. However, studies have indicated that DECs can be affected by various factors, such as texture, microstructure and alloying elements [7-10]. Therefore, this work investigates the impact of various microstructures of TNM alloys on the DECs. The experimental evaluation was performed using tensile tests and in-situ high-energy X-ray diffraction (HEXRD) at a synchrotron radiation source. In addition, the experimental results were corroborated by theoretical calculations based on a finite element model (FEM). Finally, DECs were determined for the γ-phase and the α_2-phase in the TNM alloy.

Materials and Methods

The material investigated in this study was a nominal TNM alloy. In order to explore the influence of the morphology and fractions of the individual phases, cylindrical tensile samples with different microstructures were prepared by heat-treating the initial cast material. In particular, samples with a nearly lamellar γ (NL-γ) as well as with a nearly lamellar β (NL-β) microstructure, were produced. In the NL-γ microstructure, which offers balanced mechanical properties for technological purposes [1], the γ-phase is present in two morphologies. The microstructure consists of lamellar α_2/γ colonies surrounded by globular γ-grains and a β_o-seam. In contrast, the NL-β microstructure does not contain globular γ-grains. The α_2-phase is present as fine lamellae in both conditions. Furthermore, microstructures were adjusted in which the constituents are predominantly present in globular form. Finally, an α_2-β_o duplex microstructure was adjusted. For more detailed information about the microstructures, the reader is referred to Refs. [2,3].

In-situ HEXRD experiments during tensile loading using a uniaxial testing machine were conducted at the side station of the High Energy Materials Science beamline P07B run by Helmholtz Zentrum Hereon at PETRA III at DESY in Hamburg, Germany. By continuously recording 2D diffraction patterns in transmission geometry during loading, it was possible to observe the elastic behavior of individual sets of lattice planes based on the shifts in the reflection positions. These shifts correspond to lattice strains, which permit to determine the *hkl*-determine DECs for each phase if coupled with the information on the increasing macroscopic stress. Finally, the expressions

$$S_1 = -\nu_{hkl}/E_{hkl}. \quad (1)$$

and

$$\tfrac{1}{2}S_2 = (1+\nu_{hkl})/E_{hkl}. \quad (2)$$

were used to calculate the DECs S_1 and $\frac{1}{2}S_2$ based on the diffraction elastic moduli E_{hkl} and Poisson's ratios ν_{hkl} as determined from the slopes of the lattice strain vs. macroscopic stress curves evaluated parallel and perpendicular to the loading axis. A detailed description of the evaluation methodology can be found in Ref. [9]. The theoretical approach using FEM started with the modeling of the aforementioned microstructures. Firstly, a sufficient number of grains was generated, approximating the morphology corresponding to the desired structure. After assigning the phase fractions, a random orientation was applied to the grains in accordance with the negligible texture of the TNM samples that solidified entirely via the β phase during casting [11]. By subjecting the model to a load, lattice strains could be determined from the displacement in a particular direction of nodal points within specific grains. By averaging these strains, the DECs of the individual phases could also be calculated using Eq. 1 and Eq. 2 as laid out in Ref. [6].

Results and Discussion

This section discusses the influence of the different phase morphologies in the microstructures by comparing the experimental results of the α_2-phase. Figure 1 shows two investigated conditions of the TNM alloy. In the first microstructure, indicated as TNM-A, the α_2-phase predominantly occurs in fine-lamellar α_2/γ colonies that are surrounded by a continuous fringe of β_o-phase containing coarse γ-platelets and some globular α_2-grains. In contrast, all phases in TNM-B predominantly exhibit a globular form. Occasionally, some coarse-lamellar α_2/γ colonies are also present. In both states, the α_2-phase has a volume fraction of about 14 m.%. Regarding the determination of the DECs, it should be noted that only those diffraction peaks can be analyzed that did not overlap with those of other phases. Therefore, only three peaks of the α_2-phase could be unambiguously evaluated. The results for S_1 and $\frac{1}{2}S_2$ of the α_2-phase in both microstructures are presented in Fig. 2. It can be clearly seen that, despite an identical chemical composition, there is a certain offset between the values determined on TNM-A and TNM-B.

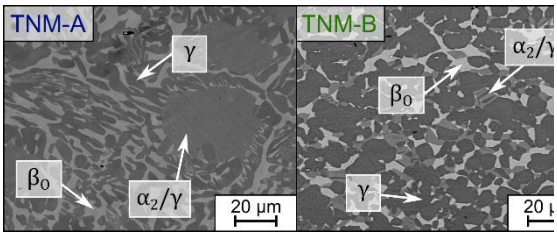

Fig. 1: Scanning electron microscopy images, taken in backscattered electron mode, depicting two different microstructures of the TNM alloy. The morphology of the α_2-phase differs in the two conditions.

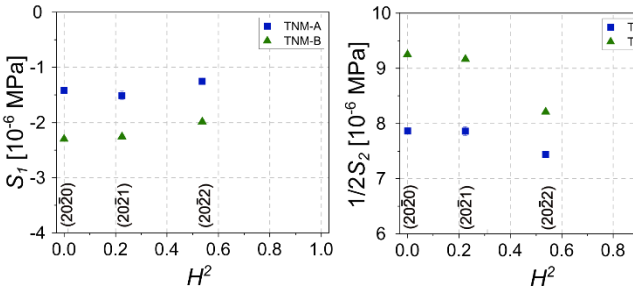

Fig. 2: Comparison between the experimentally determined DECs S_1 and $\frac{1}{2}S_2$ of the α_2-phase in TNM-A and TNM-B condition. The results are plotted as a function of the orientation parameter H^2 specific to the hexagonal crystal symmetry [6].

In conclusion, the findings suggest that the individual phases' morphology and interaction with the surrounding matrix can significantly influence the DECs. The current approach using FEM modeling is able to predict this behavior and provided insights into possible explanations for this material behavior. To ensure an accurate calculation of residual stresses, either experimental measurements or advanced modeling techniques are necessary. The data obtained in this study will be used to further improve the FEM approach for the simulation of multiphase microstructures and the prediction of their elastic and plastic properties.

Acknowledgments

The cast TNM sample material used in this study was generously provided by Dr. V. Güther and M. Allen from GfE Metalle und Materialien GmbH, Germany. We acknowledge DESY (Hamburg, Germany), a member of the Helmholtz Association HGF, for the provision of experimental facilities. Part of this research were carried out at the Hereon-run beamline P07B at PETRA III and we would like to thank Dr. N. Schell, Dr. P. Staron and B. Schwebke for assistance in using the tensile testing setup.

References

[1] F. Appel, J.D.H Paul, M. Oehring: Gamma Titanium Aluminide Alloys. John Wiley & Sons, **2011.**

[2] H. Clemens, S. Mayer: Advanced Engineering Materials. **2013**, *15*, 191-215.

[3] E. Schwaighofer, H. Clemens, S. Mayer, J. Lindemann, J. Klose, W. Smarsly, V. Güther, Intermetallics. **2014**, *44*, 128-140.

[4] L. Cha, H. Clemens, G. Dehm, International Journal of Materials Research. **2011**, *102*, 703-708.

[5] W. Reimers, A.R. Pyzalla, A. Schreyer, H. Clemens: Neutrons and Synchrotron Radiation in Engineering Materials Science. John Wiley & Sons, **2008.**

[6] V. Hauk: Structural and Residual Stress Analysis by Nondestructive Methods. Elsevier, **1997.**

[7] D. Faurie, P.O. Renault, E. Le Bourhis, Ph. Goudeau: Acta Materialia. **2006**, *54*, 4503-4513.

[8] S. Ganeshan, L. Shang, Y. Wang, Z.-K. Liu: Acta Materialia. **2009**, *57*, 3876-3884.

[9] E. Maawad, H.-G. Brokmeier, Z.Y.Zhong, N. Al-Hamdany, M. Salih, L. Wagner, N. Schell: Materials Science and Engineering A. **2014**, *594*, 62-67.

[10] H. Gabrisch, M. Janovská, M. W. Rackel, F. Pyczak, A. Stark, Journal of Alloys and Compounds. **2023**, *932*, 167578.

[11] V. Küstner: Küstner, V. (2006). Untersuchungen zur Gefügebildung bei der Erstarrung von γ-Titanaluminid-Legierungen unterschiedlicher Konstitution. Christian-Albrechts-Universität zu Kiel, **2003.**

SCP4.3

Investigation of the phase-specific plastic properties of γ-TiAl based alloys: experiments and simulations

Benjamin Seligmann[1], David Obersteiner[1], Thomas Antretter[2] and Petra Spoerk-Erdely[1]

[1]Department of Materials Science, Montanuniversität Leoben, Franz-Josef-Straße 18, 8700 Leoben, Austria, benjamin.seligmann@unileoben.ac.at, david.obersteiner@unileoben.ac.at, petra.spoerk-erdely@unileoben.ac.at

[2]Chair of Mechanics, Montanuniversität Leoben, Franz-Josef-Straße 18, 8700 Leoben, Austria, thomas.antretter@unileoben.ac.at

Introduction

Intermetallic γ-titanium aluminide (TiAl) based alloys are structural multi-phase materials applied at temperatures up to 750°C. During service, they often have to withstand high tensile stresses and resist creep, for example when used in aircraft engines [1]. Due to their diverse crystal structures, the mechanical responses of the individual phases (*i.e.* γ ($L1_0$ structure), α_2 ($D0_{19}$ structure), and in β-stabilized variants also β_o (B2 structure)) are quite different from each other and in part also temperature-dependent [1, 2]. At the onset of plastic deformation, load redistribution from plastically deforming phases (*e.g.* γ) to phases with higher yield limits (*e.g.* α_2 and β_o) can be observed [2]. This information is crucial for understanding the interplay of multiple phases in a material. Especially the β_o phase is known to be very brittle at room temperature. However, it is still not fully understood why, and depending on the chemical composition and condition of the investigated alloy the influence of the ω_o phase ($B8_2$ structure) has to be considered [3]. Findings from *in situ* high-energy X-ray diffraction (HEXRD) can be used to observe the elastic/plastic behavior in detail [2]. *In situ* tensile tests at synchrotron radiation sources allow to pinpoint the conditions, *e.g.* regarding the applied load, for the onset of specific deformation mechanisms and stages in the specimens. These pieces of information can be used as a support for microstructural design in the future, especially when assisted and quantified by finite element modelling (FEM).

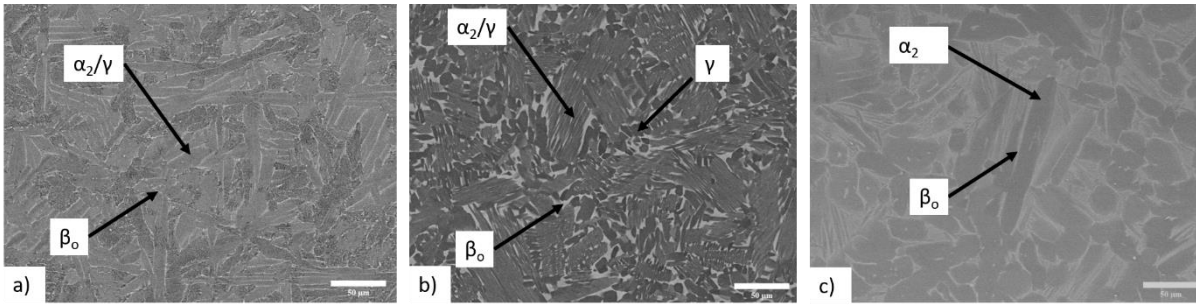

Fig. 1: Examples for microstructures used in the experiments. Nearly lamellar β without a globular γ content (a), nearly lamellar γ (b) and a dual-phase microstructure consisting of α_2 and β_o only (c).

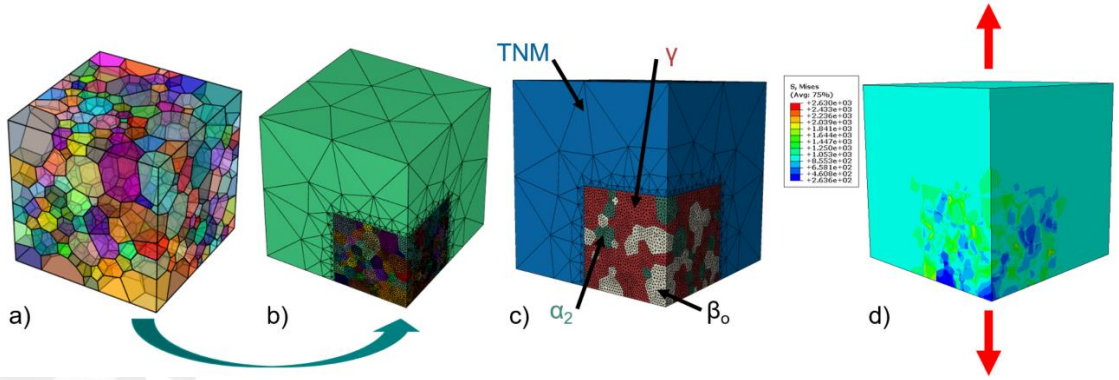

Fig. 2: Process of building up the FEM simulation: (a) sample microstructure of 500 globular grains constructed using NEPER (edge length of 500 µm), (b) manipulation of the tessellation to embed the microstructure inside a bulk TNM cube (edge length of 1 mm), (c) assignment of phases according to experimentally determined phase volume fractions and (d) a sample tensile test, which shows the von Mises stress distribution under an elastic load of 1000 MPa.

Materials and Methods

The investigated material is the so-called TNM alloy with a nominal chemical composition of Ti-43.5Al-4Nb-1Mo-0.1B (in at.%). Using established heat treatments, it is possible to set different microstructures [4]. Examples of these microstructure can be seen in Fig. 1. Starting with technological microstructures like NL β (Fig. 1a) and NL γ (Fig. 1b) which consist of lamellar α_2/γ colonies and a β_o seam at the grain boundaries, NL γ also contains globular γ grains. A dual-phase microstructure is shown in Fig. 1c, consisting of α_2 grains and a β_o seam. For the present work, cylindrical

tensile test samples of different microstructures were manufactured and tested *in situ* using HEXRD and a universal testing machine for tensile loading. The experiments were conducted at the Hereon-run high-energy materials science beamline P07B at PETRA III at the Deutsches Elektronen-Synchrotron in Hamburg, Germany, in a setup as described in Ref. [2]. The diffraction data were analyzed using in-house Python scripts, which yielded, for example, experimental load *vs.* lattice strain curves for various sets of lattice planes of all intermetallic phases present.

To complement the qualitative interpretation of these data and quantify certain aspects pertaining to the deformation behavior of the TNM alloy, a FEM routine was established. Using NEPER, a software designed for microstructure modelling [5], a realistic globular microstructure was derived and implemented via automated Python routines into the commercial FE-package ABAQUS (R2019, Dassault Systemes Simulia Corp., Providence, RI, USA). This process can be followed in Fig. 2, which shows a sample microstructure consisting of 500 grains as modelled by NEPER (Fig. 2a). For reference, the edge length of the cube was taken to be 500 µm. In this program it is possible to alter grain sizes and distributions, add lamellae or elongated grains, all depending on actual microstructures. Altering the tessellation of this microstructure (*i.e.* the position of vertices, edges and faces), a bulk TNM cube can be implemented (edge length of 1 mm in total), which houses the actual microstructure (Fig. 2b). After meshing in NEPER, some Python routines were implemented to assign material parameters and orientations of the grains, depending on the orientation relationships between the phases (Fig. 2c). Utilizing elastic constants for the individual phases calculated earlier by means of density functional theory, it is possible to generate a FEM model, which depends only on calculated elastic material parameters extended by material models for the plastic response. Figure 2d shows the sample under an elastic load case, to visualize that orientations and phase material parameters affect the stresses experienced by individual grains.

Furthermore, using sophisticated user subroutines and multiscale modelling, it is possible to simulate the fine lamellae found in this type of intermetallic alloys. The generated model will be used to compare the experiment with simulation.

Results and Discussion

The diffraction patterns gained by means of HEXRD during tensile loading were evaluated and provided information about the lattice strain evolution of the individual intermetallic phases. These results were correlated with the macroscopic stress to show the yield points of the individual phases. The developed FEM simulation routine was used.

to reproduce the experimental findings in a computational way. This allowed a quantitative interpretation of the experimental results, for the first time taking into account the actual microstructure of the specimens.

The interplay of the individual phases is significant to the macroscopic mechanical response of the material. Therefore, several different microstructures have been used to provoke as different mechanical responses as possible. During tensile testing, peak positions measured with HEXRD will shift in their respective position, allowing the measurement of the change in lattice spacing regarding the individual phases. This change can be interpreted as a lattice strain, which can be correlated with the macroscopic stress. Using many different microstructures with different volume fractions of the different phases, it is possible to collect parameters for the elastic and plastic regime to set up a FEM model. The FEM model in return delivers the same information (lattice strain and macroscopic stress) and it is therefore possible to gain insights into the prevailing deformation mechanisms.

During the simulation part of this work, novel approaches were taken by simulating realistic 3D-microstructures consisting of a great number of grains by means of FEM in comparison to previous work conducted in the field of γ-TiAl based alloys [6], which relied on simplifications like periodic grains [7], dimensionality [8] or single phase simulations [9] Additionally, the conducted simulations in this work are self-consistent, implying that *e.g.* elastic parameters of the phases are derived from density functional theory.

Acknowledgments
The authors thank Dr. V. Güther and M. Allen, GfE Metalle und Materialien GmbH, for providing the cast TNM sample material. We acknowledge DESY (Hamburg, Germany), a member of the Helmholtz Association HGF, for the provision of experimental facilities. Parts of this research were carried out at the Hereon-run beamline P07B at PETRA III and we would like to thank Dr. N. Schell, Dr. P. Staron, Dr. E. Maawad and B. Schwebke for assistance in using the tensile testing setup.

References
[1] H. Clemens, S. Mayer, Advanced Engineering Materials. 2013, 15, (4), 191-215.
[2] P. Erdely, P. Staron, E. Maawad, H. Clemens, S. Mayer, Acta Materialia. 2018, 158, 193-205.
[3] G. Molénat, B. Galy, M. Musi, M. Thomas, H. Clemens, J.-P. Monchoux, A. Couret, Intermetallics. 2022, 151, 107653.
[4] E. Schwaighofer, H. Clemens, S. Mayer, J. Lindemann, J. Klose, W. Smarsly, V. Güther, Intermetallics. 2014, 44, 128-140.
[5] R. Quey, P. Dawson, F. Barbe, Computer Methods in Applied Mechanics & Engineering. 2011, 200, (17-20), 1729-1745.
[6] F. Appel, H. Clemens, F.-D. Fischer, Progress in Materials Science. 2016, 81, 55-124.
[7] M. Grujicic, Y. Zhang, Materials Science & Engineering A. 1999, 265, 285-300.
[8] H. Ganesan, I. Scheider, C. J. Cyron, Materials & Design. 2021, 212, 110282.
[9] B. Yin, X. Xue, B. Tang, W. Y. Wang, H. Kou, J. Li, Materials Science & Engineering A. 2022, 831, 142283.

SCP4.4

Ti Diffusion Coefficients in γ-TiAl Intermetallics measured by Mechanical Spectroscopy

Jose M. San Juan[1], Michael Oehring[2], Helmut Clemens[3] and Maria L. Nó[1]

[1]Dpt. of Physics, Faculty of Science and Technology, University of the Basque Country (UPV/EHU), Apdo 644, 48080-Bilbao, Spain jose.sanjuan@ehu.es, maria.no@ehu.es
[2]Helmholtz-Zentrum Geesthacht, Institute for Materials Research, Max-Planck-Str. 1, 21502 Geesthacht, Germany, michael.oehring@hzg.de
[3]Dpt. of Physical Metallurgy and Materials Testing, Montanuniversität Leoben, Roseggerstr. 12, 8700 Leoben, Austria, helmut.clemens@unileoben.ac.at

Introduction

In the last decades there has been a growing interest in developing new intermetallic families, which would we able to improve the specific performances of superalloys at high temperature. The TNB (Ti-Al-Nb) and the TNM (Ti-Al-Nb-Mo) families were developed to fulfil the required performances. In particular, the creep resistance should be improved and consequently the study of the diffusion mechanisms and the associated relaxation processes become very useful to get a deep understanding of the physics involved during creep. Mechanical spectroscopy, including the measurement of the internal friction spectra and the dynamic modulus curves as a function of temperature between 600 K and 1400 K allowed approaching the study of such processes.

Previous works on several γ-TiAl alloys show several relaxation processes associated with the Ti diffusion in the □2 phase [1-3] and with the Al diffusion in the γ phase [4], as well as an internal friction background at high temperature, which is associated with the creep behaviour [2]. At present, a new generation of γ-TiAl, called TNM+, is being developed to improve the creep resistance by microalloying with C and Si [5]. However, to extend the creep resistance on temperature and on time, the stability of the microstructure should be guaranteed or, as in the case of superalloys, well mastered in what concerns to its evolution.

The aim of the present work is to overview the relaxation processes associated with Ti diffusion in □2 phase and, from the analysis of the relaxation processes, obtain the diffusion coefficient of Ti in each particular alloy. However, Nb and C atoms in solid solution could have a secondary effect on creep resistance by slowing down the diffusion of Ti in the constitutive phases.

Materials and Methods

The experimental part of this work is based on the internal friction measurements made by mechanical spectroscopy at different frequencies and in different alloys, TNB, TNM, TNM+ and Nb-free TiAl, [1-5]. Then, the theory of mechanical spectroscopy [6] is developed to establish the relationship between the relaxation time and the diffusion coefficient. The local atomic configuration and the models for internal friction are taken into account to obtain the corresponding equations.

The experimental validation of this approach has been carried out by the comparison of the diffusion coefficients obtained through internal friction with those from the literature [7].

Results and Discussion

An experimental work was approached in previous publication in which the relaxation processes associated with Ti diffusion were observed in several alloys with different amounts of Nb and C in solid solution, such as the TNB, TNM. TNM+ and Nb-free TiAl alloys. In the present work, the relaxation processes observed by internal friction are related, through the activation parameters, to the diffusion coefficients of the different atomic species and compared, when possible, with those from the literature. To do it, the theory of relaxation during the internal friction measurements is theoretically and experimentally compared and related with the classical atomic diffusion theory, establishing the corresponding equations. As an example, Fig. 1 shows the diffusion coefficient of Ti in □2 phase obtained by both methods; the blue squares are the data measured in a binary TiAl alloy, from the ref. [7], and the red dots are the points obtained through the analysis of the internal friction data, measured on a Nb-free TiAl alloy in ref. [2]. The diffusion parameters are in an exceptional agreement for both kind of measurements; the mean activation energy is $E(Ti)= 2.99 \pm 0.02$ eV and $D0=2.5 \pm 0.1 \times 10\text{-}5$ s.

Conclusions

It can be concluded that internal friction measurements allow to obtain a plot of the diffusion coefficients of Ti in several families of γ-TiAl alloys with different amounts of Nb, and, in addition, in an expanded temperature range closer to the temperatures used in service conditions.

Acknowledgements
The present work was supported by the University of the Basque Country, UPV/EHU, through the financial support of the Excellence Research Group GIU-21/024.

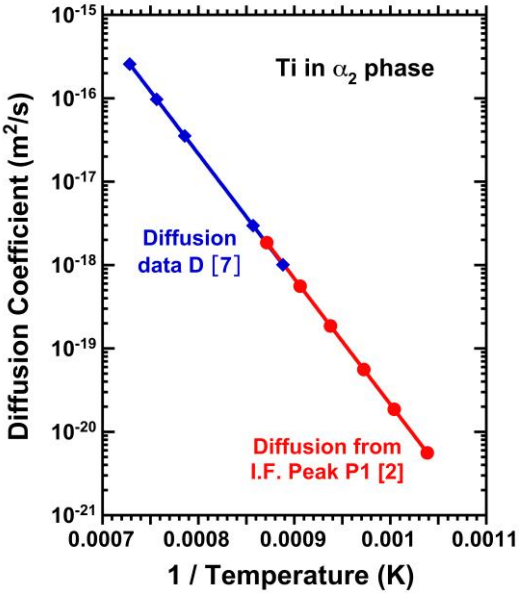

Fig. 1: Diffusion coefficient of Ti in the lattice of the ?2 phase. Diffusion data taken from Ref. [7] (in blue). Diffusion coefficient measured from internal friction in a Nb-free Ti-Al alloy, from the data of Ref. [2] (in red).

References

[1] J. San Juan, P. Simas, T. Schmoelzer, H. Clemens, S. Mayer, M.L. Nó, Acta Mater. 65, 2014, 338.
[2] M. Castillo-Rodriguez, M.L. Nó, J.A. Jimenez, O. Ruano, J. San Juan, Acta Mater. 103, 2016, 46.
[3] J. Ibáñez-Pérez, M.L. Nó, M. Oehring, H. Clemens, J. San Juan, J. Alloys & Comp. 867, 2021, 158880.
[4] L. Usategui, T. Klein, M.L. Nó, S. Mayer, H. Clemens, J. San Juan, Acta Mater. 200, 2020, 442.
[5] T. Klein, L. Usategui, B. Rashkova, M.L. Nó, J. San Juan, H. Clemens, S. Mayer, Acta Mater. 128, 2017, 440.
[6] J. San Juan, Mechanical Spectroscopy, Mater. Sci. Forum 366-368, 2001, 32-73.
[7] Y. Mishin, Chr. Herzig, Diffusion in the Ti-Al system, Acta Mater. 48, 2000, 589-623.

SCP4.5

Directional solidification of TiAl alloys studied by in-situ X-ray diffraction

Michael Oehring[1], Dirk Matthiessen[1], Malte Blankenburg[2], Norbert Schell[1] and Florian Pyczak[1,3]

[1]Helmholtz-Zentrum Hereon, Max-Planck-Straße 1, 21502 Geesthacht, Germany,
[2]Deutsches Elektronen-Synchrotron DESY, Notkestraße 85, 22607 Hamburg,
[3]Brandenburgische Technische Universität Cottbus-Senftenberg, Konrad-Wachsmann-Allee 17, 03046 Cottbus, Germany, florian.pyczak@hereon.de

Introduction

γ-TiAl alloys are competitive alternatives to Ni-base superalloys as material for turbine blades in aero engines in the low pressure turbine section due to their lower density and at least comparable specific creep strength. However, being composed of ordered intermetallic phases, which are responsible for the high strength, but are also inherently brittle, it is necessary to impose a good microstructure control during processing to ensure sufficient damage tolerance of the parts [1]. Already small deviations from the desired target microstructure can otherwise reduce the already low ductility and damage tolerance to unacceptable levels. Casting is an important processing method for TiAl, either to directly produce parts or as processing step prior to e.g. forging. Also in the upcoming additive manufacturing processes melting and solidification steps are frequently involved. To understand the microstructure formation and phase constitution of TiAl alloys during solidification is hampered by the complexity of the Ti-Al phase diagram in the Al range in question between ca. 42 to 48 at.%. Not only is the high temperature situation masked by lower temperature phase transformations, but also the solidification path itself changes depending on the Al content. For lower Al contents a solidification via the primary β-phase takes place, while for Al contents starting from slightly below 45 at.% and above the material solidifies peritectically [2]. Nevertheless, the textures found in such alloys rule out that α phase formed during the solidification grew from the β phase with the expected Burgers orientation relationship. Accordingly, while a complete understanding and reliable prediction of the solidification behavior of TiAl alloys is desirable, it is still necessary to unveil its details by sophisticated experiments and validate models by their results. Two binary TiAl alloys with different Al content were directionally solidified varying the withdrawal rate to change the solidification conditions. The device used for this allows to observe the situation at different distances from the solidification front by in situ X-ray diffraction [3]. Accordingly, it was possible to determine the types of solidifying phases and their orientation and compare these results with the predictions of the nucleation and constitutional undercooling (NCU) model [4].

Experimental

Two binary alloys with the nominal chemical compositions Ti-45Al and Ti-48Al (all in at.%) were produced by arc melting, and in a final arc melting step cast to bars of 12 mm diameter and 150 to 160 mm length. The rods were mounted in a zone melting device, which is specially constructed to allow directional solidification under in situ observation with high energy X-rays produced at a synchrotron storage ring. For this, the device is equipped with windows to allow the illuminating X-ray beam to hit the specimen and the diffracted beam to leave the device to be recorded with an area detector. In addition, the induction coil to heat the specimen is constructed so that the entry and exit of the beam is not blocked, even in the molten zone located inside the induction coil. The X-ray diffraction experiments were done in transmission at the high-energy material science beamline (HEMS) operated by Helmholtz-Zentrum Hereon at the PETRA III storage ring of the DESY synchrotron in Hamburg, Germany. Due to the high X-ray energy of nearly 98.189 keV the investigation could be conducted in transmission. During the solidification the temperature is measured at two locations by pyrometers allowing to calculate the temperature gradient. The withdrawal rate was changed between 6 mm/h and 360 mm/h, and by lowering or lifting the device relative to the X-ray beam height diffraction signals at different distances from the solidification front can be recorded. During the experiments the bars were rotated with 10 rotations per minute to allow for a more homogeneous temperature distribution in the specimen. The X-ray diffraction data was afterwards processed with the software Fit2D and the software package MAUD for Rietveld analysis.

Results and Discussion

Figure 1 shows the diffraction patterns recorded during an experiment with the Ti-48Al alloy. The specimen was positioned at a height, where the X-ray beam transmitted a volume of the specimen, where melt and solid material co-exist to get an insight to the initial situation of solidification. In the quarter section of the area detector image shown at the bottom of Figure 1 a), when using a withdrawal rate of 6 mm/h, a diffuse ring is visible which belongs to the melt combined with weaker sharp diffraction rings of the already solidified material.

This solidified material can be identified as α phase. This can be seen easier in the diffraction pattern at the top of Figure 1 a), which was generated by azimuthally integrating the X-ray intensity of the area detector. Due to the fact that the intensity is homogeneously distributed around the diffraction rings belonging to the α phase on the area detector, it can also be concluded that the α phase has formed with no preferential orientation. This can be interpreted that the withdrawal rate was slow enough to allow for planar solidification of the α phase. The situation for a faster withdrawal rate of 360 mm/h resulting in a lower ratio between thermal gradient G and withdrawal rate V – G/V – is shown in Figure 1b. Again, a diffuse ring belonging to the melt is present. But the solid phases show a different behavior. Phases α and β are present in about equal fractions, and from increased intensities on some sections of the corresponding diffraction rings it is also evident that both now exhibit preferential crystallographic orientation (see yellow arrows in Figure 1 b)). Obviously, the G/V ratio is decreased to such an extent that now a parallel dendritic growth of α and β phase takes place.
In addition to the results shown similar experiments were conducted with Ti-45Al. Here, solidification always took place via the β phase, but again depending from G/V different preferred crystallographic orientations resulted, which could also be explained by a transition from planar to dendritic solidification mode. The results can qualitatively be explained by the NCU model. Quantitative discrepancies may occur due to not well-known input parameters for the NCU model, as for example the diffusion rate in the liquid.

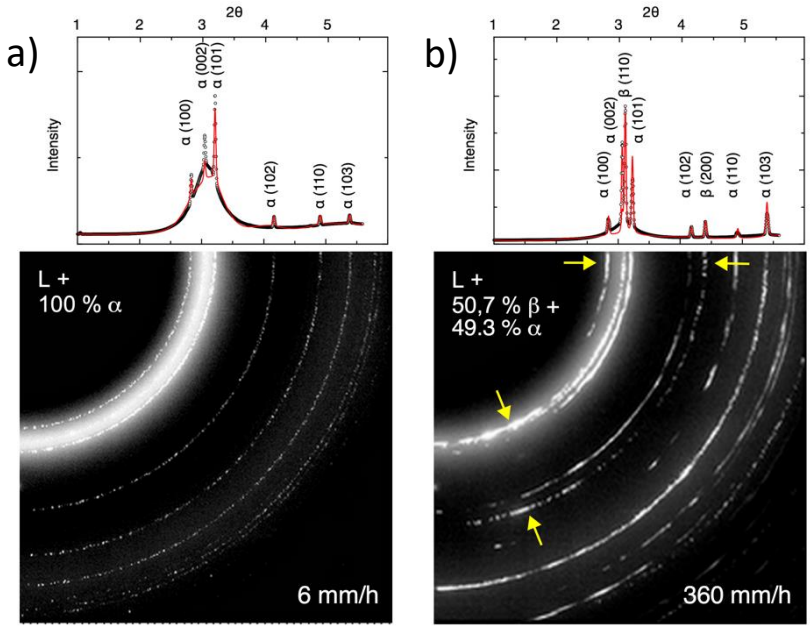

Fig.1. Diffraction patterns of Ti-48Al recorded during a directional solidification experiment in the solid-liquid region: a) withdrawal rate of 6 mm/h; b) withdrawal rate of 360 mm/h;

Conclusions

Using a specially designed specimen environment it was possible to investigate directional solidification of two TiAl alloys. While the primary phase depended on G/V for an alloy with an Al content of 48 at.%, being α phase for high G/V and α and β phase for low G/V, in an alloy with 45 at.% Al solidification always took place via the β phase. In both alloys a transition from planar growth for high to dendritic growth for low G/V is observed. These observations are in qualitative agreement with predictions of the NCU model.

References

[1] B. P. Bewlay, S. Nag, A. Suzuki, M. J. Weimer, TiAl alloys in commercial aircraft engines, Mater. High Temp. 2016, 33, 549-559.

[2] V. Küstner, M. Oehring, A. Chatterjee, V. Güther, H.-G. Brokmeier, H. Clemens, F. Appel, An investigation of microstructure formation during solidification of gamma titanium aluminides alloys, in Gamma Titanium Aluminides 2003 (Eds.: Y-W. Kim, H. Clemens, A.H. Rosenberger), TMS, Warrendale, PA, 2003, 89 - 96.

[3] C. Gombola, G. Hasemann, A. Kauffmann, I. Sprenger, S. Laube, A. Schmitt, F. Gang, V. Bolbut, M. Oehring, M. Blankenburg, N. Schell, P. Staron, F. Pyczak, M. Krüger, M. Heilmaier, A zone melting device for the in-situ observation of directional solidification using high-energy synchrotron X-rays, Rev. Sci. Instr. 2020, 91,093901.

[4] O. Hunziker, M. Vandyoussefi, W. Kurz, Phase and microstructure selection in peritectic alloys close to the limit of constitutional undercooling, Acta Mater. 1998, 46, 6325-6336.

SCP5.1

Balanced properties of Mo-V-Si-B alloys modified with small amounts of titanium

Dennis Zang, Georg Hasemann and Manja Krüger

Institute of Materials and Joining Technology, Otto-von-Guericke University Magdeburg, Magdeburg, Germany, dennis.zang@ovgu.de, georg1.hasemann@ovgu.de, manja.krueger@ovgu.de

Multiphase Mo-Si-B alloys have a great potential for replacing nickel-based superalloys in the aerospace and energy sector because they show excellent mechanical properties and the potential for good oxidation characteristics, due to the Mo silicide phases. However, the oxidation behavior of such alloys is still a critical issue, since catastrophic oxidation failure occurs locally at the Mo solid solution phase at intermediate temperatures [1]. It was shown that the addition of vanadium to Mo-Si-B alloys leads to a significant density reduction, which is even lower than the density of a state-of-the-art nickel-base superalloy CMSX-4. This phenomenon is directly related to the high solubility of vanadium in molybdenum and the respective Mo silicides, while vanadium has no effect on the phase fractions of the Moss-Mo3Si-Mo5SiB2 triangle. In this context it was found that alloys with the composition Mo-40V-9Si-8B exhibit the best set of properties with respect to normalized mechanical strength and ductility. On the other side, alloying with vanadium leads to a reduction in creep resistance. In addition, such alloys have a significantly higher oxygen content [2]. For this reason, titanium is will be added to the Mo-V-Si-B alloy in order to somewhat mitigate disadvantages of the vanadium addition. Furthermore, titanium has a high affinity for oxygen and therefore it is believed that titanium may act as a getter for dissolved oxygen and thus contribute to improve the ductility as well as to minimize internal oxidation in these alloys.

Elemental powders of Mo, V, Si, B and TiH2 of 99.95%, 99,5%, 99,5%, 98% and 99,5 % purity, respectively, were used to produce different alloys with chemical composition of Mo-40V-9Si-8B-xTiH2 (in at. %, x=0, 2, 5) by a multi-step powder metallurgical process. Mechanical alloying of the powders was carried out in a planetary ball mill with powder to ball weight ratio of 1:13 and a rotational speed of 300 rpm. Weighing, mixing and powder removal was done under protective argon atmosphere in order to keep the oxygen content as low as possible. In the first step of this work, a milling study of mechanically alloyed Mo-40V-9Si-8B was carried out in order to optimize the powder metallurgical processing route. Then, 2 at. **%** and 5 at. % titanium were added to this alloy, substituting both the molybdenum and the vanadium in all constituents, which improves the stress-strain properties even further. The analytical methods used to determine the milling progress of the respective powder alloys include SEM analysis, XRD analysis, oxygen content analysis, microhardness measurements and laser diffraction. In the next step, the Ti-modified alloy powders and the reference material (Mo-40V-9Si-8B) were subjected to heat treatment. In this way, a multi-phase microstructure was formed in which the intermetallic phases Mo3Si and Mo5SiB2 are embedded in a continuous Mo matrix [3]. After compaction via field assisted sintering the compacted material was analyzed with respect to microstructure, mechanical properties and oxidation resistance to verify whether the addition of titanium contributes to an improvement in this respect.

In the following, initial results from the milling studies will be presented. The milling progress for the first two alloys can be seen from the SEM images in Fig. 1. At the beginning of ball milling (2 h), larger light (light grey, molybdenum-rich phase) and darker areas (vanadium-rich phase) occur within the individual powder particles. As the milling time increases (10 h), a lamellar structure then gradually forms, indicating that vanadium is increasingly dissolving in the molybdenum and, as a result, the microstructure is becoming more homogeneous.

However, after 20 h of ball milling, a completely homogeneous microstructure is not yet evident, because lamellar structures can still be detected in some particles for both alloys, which in turn suggests that the mechanical alloying of the powders is not yet fully completed at this point.

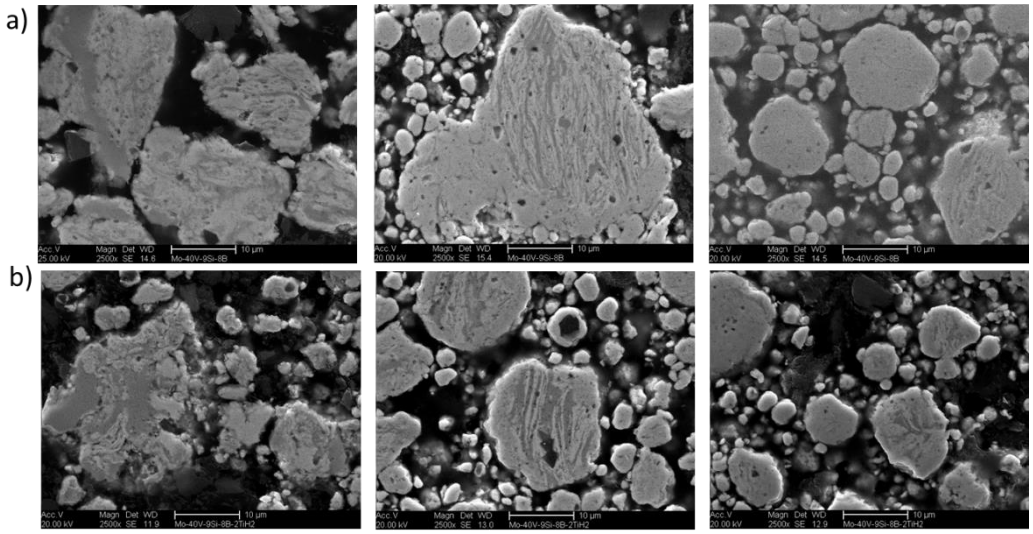

Fig. 1: Microstructure of the mechanically alloyed powders after 2, 10 and 20 h. a) Mo-40V-9Si-8B b) Mo-40V-9Si-8B-2TiH$_2$

Furthermore, microhardness measurements were carried out as a function of milling time (see Figure 2), in order to obtain a first tendency regarding the mechanical properties. In the first five hours of milling, the microhardness in both alloys initially increases, which, in addition to solid solution strengthening, is also due to grain refinement and work hardening at this early stage of mechanical alloying. In the further course, the microhardness does not change significantly. However, the microhardness of the reference alloy Mo-40V-9Si-8B is at a slightly higher level throughout the milling time than that of the alloy with 2 at. % TiH2, which means that titanium dihydride, at least in small amounts, does not lead to any improvement in this respect in the powder state. This will probably change after a heat treatment.

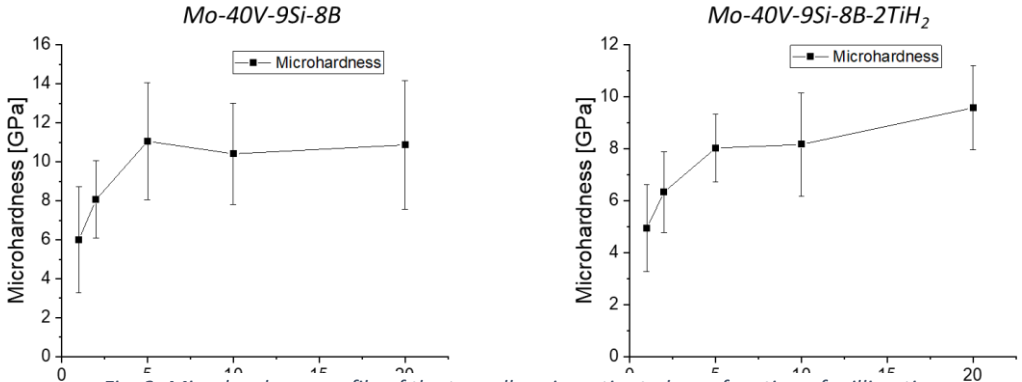

Fig. 2: Microhardness profile of the two alloys investigated as a function of milling time

References:

[1] Berczik DM. METHOD FOR ENHANCING THE OXIDATION RESISTANCE OF A MOLYBDENUM ALLOY, AND A METHOD OF MAKING A MOLYBDENUM ALLOY. United States Pat. 1997;

[2] Becker J, Betke U, Hoffmeister M, et al. Density Reduction of Mo-Si-B Alloys by Vanadium Alloying. Jom. 2018;70:2574–2581.

[3] Krüger M, Franz S, Saage H, et al. Mechanically alloyed Mo-Si-B alloys with a continuous α-Mo matrix and improved mechanical properties. Intermetallics. 2008;16:933–941.

SCP5.2

MoSiB(Ti) next generation superalloys

Uwe Gaitzsch[1], Alexander Kirchner[1], Anders Magnusson[2] and Thomas Weißgärber[1,3]

[1]Fraunhofer IFAM Dresden, Winterbergstraße 28. 01277 Dresden, uwe.gaitzsch@ifam-dd.fraunhofer.de
[2]Quintus Technologies AB, Quintusvägen 2, 72166 Västeras, Sweden,
[3]Technische Universität Dresden, Powder Metallurgy, 01062 Dresden, Germany

Introduction

MoSiB alloys have been introduced explicitly to replace Nickel-based superalloys in gas turbine applications. High strength at high temperatures is provided by refractory metal intermetallic phases [1,2]. A critical feature is the phase distribution of the metallic Molybdenum solid solution phase. Only if this phase is present as a coherent metallic matrix, ductility can be achieved in the alloy, which is critical for damage tolerance or toughness. Solidification from the melt usually leads to an intermetallic matrix, as Molybdenum solidifies first forming islands through the solidification process Therefore, powder metallurgical manufacturing routes have been under investigation for years [3,4]. The second critical property is the silicon content in the solid solution phase. This needs to be as low as possible. Silicon tends to segregate to the grain boundaries and, therefore, causes embrittlement [5]. This problem can be tackled in several ways. First, the maximum consolidation or processing temperature can be selected as low as possible, just enough to ensure densification, for example using hot isostatic pressing (HIP) or spark plasma sintering (SPS) compaction. Second, the material can be heat treated to allow for silicon diffusion to the nearby existing silicide phases. For this method to work, the silicon diffusion paths need to be small and molybdenum grain boundaries should be avoided, as well. Third, Titanium (or another appropriate reactive element) can be introduced in the alloy to form silicides within the metallic matrix upon heat treatment or cooling [6,7]. The addition of Titanium also destabilizes the A 15 phase causing a different phase field equilibrium consisting of Molybdenum solid solution, the ternary Mo5SiB2 T2 phase and the Mo5Si3 T1 phase.

Materials and Methods

Starting point of the investigations was the composition Mo-9Si-8B (at.-%), which corresponds to Mo-3Si-1B (wt.-%), and has been the starting point for several compositional modifications or basic research done within the Berczik triangle, also in the latest years. As Titanium occupies the lattice sites of Molybdenum, the atomic percentages of Silicon and Boron were kept constant. The investigated composition is Mo-25Ti-9Si-8B (at.-%). Powders of Molybdenum, MoSi2, TiH2 and Boron were used as starting materials for the experiments. The oxygen content of the powder mixture was about 5000 ppm.

The powders were milled using a Netzsch planetary ball mill under Argon with a vial volume of 2000 ml containing 250 g powder and 2 kg steel balls (diameter 10 mm). The abrasion of iron has been determined to be less than 500 weight ppm. The resulting powder mixture was compacted using an FCT Spark Plasma Sinter furnace equipped with graphite tools (diameter 20 mm or 60 mm). At 600 °C a dehydrogenation treatment was performed for 10 min to decompose the TiH2. The max. temperature was 1600 °C for a dwell time of 20 min at uniaxial pressure of 30 MPa. The whole process was performed in vacuum ($p < 1$ mbar).

Following the compaction phase formation annealing was performed in vacuum to decompose the A 15 phase (if existent) and to allow for Ti5Si3 precipitation in Molybdenum solid solution phase. Temperatures between 1350 °C and 1500 °C were tested and dwell times were between 3 h and 48 h.

Discs for mechanical testing were SPS compacted. After compaction, the whole disc was annealed at 1400 °C for 24 h in vacuum followed by hot isostatic pressing, using a Quintus QIH 15L URQ, at 1400 °C and 200 Mpa with a dwell time of two hours. After the dwell time the samples were rapidly quenched to 400 °C with a cooling rate between 30 K/s and 100 K/s (gas temperature). As the samples became brittle after quenching, they were then annealed at 1200 °C for 2 h in vacuum to allow for spark cutting mechanical test samples. Bars were eroded and ground to 3x4x50 mm³ and tested in high temperature 4-point bending at temperatures of 900 °C and 1000 °C, respectively. In comparison, non HIPed samples were mechanically tested at 900 °C, as well.

Additionally atomized powder of the composition Mo-9Si-8B was provided by Taniobis with a particle size distribution of 63-150 µm and an oxygen content of 400 ppm.

Additive manufacturing was performed by electron beam powder bed fusion (PBF-EB) on an Arcam 2X machine.

Results and Discussion

The probably most important parameter for the toughness of the alloy is a continous Mo matrix. This is confirmed by the micro images as present in the samples (not shown here). Annealing caused a partly decomposition of the A 15 phase. Said decomposition leaves an eutectoid stripe-like mixture of Molybdenum solid solution and Mo5Si3

phase (i.e., (Mo,Ti)5Si3 or (Ti,Mo)5Si3 depending on the Titanium content and the crystal structure). The attempt to distinguish those has not been performed in this study and the phase will be called Mo5Si3 hereafter. It cannot be stated if the Molybdenum emerging from the eutectoid composition is thoroughly connected or not. However, this fine microstructure is supposed to help strengthen the material (Hall-Petch relationship). The phase composition, with and without full decomposition of the A 15, could be calculated using the overall composition. However, this was not the case for phase densities due to unknown local titanium content. As a guideline, the phase compositions of the titanium-free alloy, with and without full decomposition of the A 15 phase, have been calculated using the densities of the Titanium-free phases. Considering a minimum amount of 50 % for a continuous Molybdenum solid solution phase, the content of 53 % or 60 % should be enough to form a connected phase. Grey scale analysis was used to determine the volume phase fraction in the 1400 °C 24 annealed sample. However, variations are introduced depending on where grey scale thresholds are set. The mechanical testing showed a bending strength of roughly 500 MPa at 900 °C in the non HIPed condition. No plasticity could be reached at this temperature. This is in agreement with data from MoSiB-literature, where the DBTT was between 1000 °C and 1200 °C for metallic matrix materials [8]. After HIP the strength increased significantly to over 700 MPa at 900 °C and 1000 °C, as well (s. fig. 1). Surprisingly the bending strength does not vary significantly between those two temperatures. However, no plasticity was reached up to 1000 °C. The reasons for that can be either the diffusion of the remaining silicon to the grain boundaries or the large oxide particles which can act as crack initiation sites. Silicon is known to cause embrittlement due to the following mechanism. At the highest processing or service temperature silicon is partly dissolved in the Molybdenum solid solution phase. Upon cooling the solubility decreases causing the silicon to diffuse to the grain boundaries where silicide precipitation occurs, which can cause crack initiation. This crack initiation at precipitates on the grain boundaries is the common embrittlement mechanism in MoSiB alloys as it was found by Jain et al. and Lemberg et al. among others [5,9]. The strength of both the HIPed and non-HIPed alloys exceeds the tensile strength of the commercial superalloy IN 713C (275 MPa at 930 °C [10]). The HIPed alloys are close to the tensile strength of the high temperature superalloy CMSX 4 (811 MPa at 980 °C [11]). The strength of the PBF EB samples will be addressed in the talk.

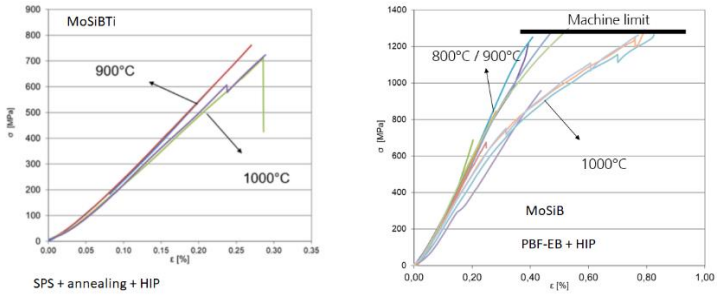

Fig. 1: 4 point bending strength of MoSiBTi alloy (left [12]) by powder metallurgy and MoSiB alloy by PBF-EB. Both alloys were HIPed.

References

[1] P. Jéhanno, M. Heilmaier, H. Saage, H. Heyse, M. Böning, H. Kestler, J.H. Schneibel, Scripta Materialia 55 (2006) 525–528.

[2] D.M. Dimiduk, J.H. Perepezko, MRS Bull. 28 (2003) 639–645.

[3] A. Wiltner, B. Klöden, I. Hilger, T. Weißgärber, B. Kieback, J. Am. Ceram. Soc. 98 (2015) 3569–3575.

[4] M. Krüger, S. Franz, H. Saage, M. Heilmaier, J.H. Schneibel, P. Jéhanno, M. Böning et al., Intermetallics 16 (2008) 933–941.

[5] P. Jain, K.S. Kumar, Scripta Materialia 62 (2010) 1–4.

[6] D. Schliephake, M. Azim, K. von Klinski-Wetzel, B. Gorr, H.-J. Christ, H. Bei, E.P. George et al., Metall and Mat Trans A 45 (2014) 1102–1111.

[7] M. Azimovna Azim, S. Burk, B. Gorr, H.-J. Christ, D. Schliephake, M. Heilmaier, R. Bornemann et al., Oxid Met 80 (2013) 231–242.

[8] J.A. Lemberg, R.O. Ritchie, Advanced materials (Deerfield Beach, Fla.) 24 (2012) 3445–3480.

[9] J.A. Lemberg, M.R. Middlemas, T. Weingärtner, B. Gludovatz, J.K. Cochran, R.O. Ritchie, Intermetallics 20 (2012) 141–154.

[10] B. Fasteners, Inconel Alloy 713 C - Boltport Fasteners. www.boltport.com/materials/inconel/alloy-713c/.

[11] A. Sengupta, S.K. Putatunda, L. Bartosiewicz, J. Hangas, P.J. Nailos, M. Peputapeck, F.E. Alberts, JMEP 3 (1994) 664–672.

[12] U. Gaitzsch, A. Magnusson, T. Weißgärber, International Journal of Refractory Metals and Hard Materials special Issue "Plansee Seminar" (2023).

SCP5.3

Microstructure and mechanical properties of V-Si-B alloys with chromium additions

G. Hasemann[1], S. Ida[2], K. Yoshimi[2] and M. Krüger[1]

[1]Otto-von-Guericke University Magdeburg, Institute of Materials and Joining Technology, Universitätsplatz 2, 39106 Magdeburg, Germany, georg1.hasemann@ovgu.de, manja.krueger@ovgu.de
[2]Tohoku University Sendai, Department of Materials Science, Graduate School of Engineering, Sendai, Miyagi, 980-8579, Japan, shuntaro.ida.e1@tohoku.ac.jp, yoshimi@material.tohoku.ac.jp

Introduction

The V-Si-B system has gained scientific interest as a new low-density, refractory metal-based structural intermetallic alloy system. The alloy design is strongly influenced and driven by the developments in the field of Mo-Si-B alloys and shares some interesting structural and microstructural features. Very recently, the formation of ternary eutectic V_{SS}-V_3Si-V_5SiB_2 microstructure has been reported which contains the same isomorphous phases as the ternary eutectic in the well-studied Mo-Si-B system: a refractory metal-based solid-solution phase (Mo_{SS} or V_{SS}) and the two intermetallic phases with either an A15 (Mo_3Si and V_3Si) or a $D8_l$ (Mo_5SiB_2 and V_5SiB_2) structure. However, while the Mo-Si-B-based ternary eutectic shows some oxidation resistance due to its intermetallic character, oxidation of the V-based eutectic is an even more serious issue. To address this problem, different amounts of Cr were added to a eutectic V-Si-B alloy to study the microstructural influence on the ternary eutectic reaction, the phase stability as well as the mechanical and oxidation properties as a function of Cr concentration. Alloys with Cr additions between 5 – 30 at.% were fabricated by conventional arc-melting and were analyzed in the as-cast state or heat-treated at 1400 °C for 100 hrs.

Materials and Methods

The present study is focused on the compressive stress-strain behavior of ternary eutectic V-Si-B alloys with 10, 20 and 30 at.% Cr additions. Compression tests were performed using an electro-mechanical universal testing machine and a constant crosshead speed corresponding to an initial (engineering) strain rate of 10^{-3} s^{-1}. The yield stresses were determined by the 0.2% offset method. The temperature dependence of its compressive yield stress between room temperature and 1000 °C was investigated in the as-cast and annealed state (1400 °C for 100 hrs) and compared to the Cr-free ternary eutectic alloys V-9Si-6.5B as well as V-Si-B alloys taken from the literature.

Results and Discussion

Prior to the mechanical compression tests the microstructures of the Cr-added ternary eutectic alloys V-9Si-6.5B were investigated. Even at high Cr-additions of 30 at.% the eutectic V_{SS}-V_3Si-V_5SiB_2 microstructure could be maintained. Thus, Cr has almost no influence on the solidification behavior in this part of the V-Si-B system, which seems to be plausible since Cr stabilizes all three eutectic phases [1]. As an example, the microstructures of the base alloys and an alloy with 30 at.% Cr additions is shown in Fig. 1, including a heat treatment at 1400 °C for 100 hrs. According to XRD analysis, the newly discovered phase V_8SiB_4 could also be detected in all eutectic alloys with Cr additions after the heat treatment.

The ternary eutectic alloy V-9Si-6.5B features the ductile V_{SS} phase as the major phase. Thus, first compression test revealed a deformability even at room temperature. However, the yield strength decreases quickly with increasing test temperatures and is even more pronounced in the heat-treated state. In order to develop a comparably low-density materiel for high temperature structural applications, the high-temperature strength (and later on, the creep resistance) should be further improved by Cr-additions. Cr dissolves in all the ternary eutectic phases and, as mentioned before, does not influence the eutectic formation. This fact makes Cr an ideal candidate to study the strengthening behavior of the alloys by subsequently increasing its Cr content. With increasing Cr-additions the compressive yield strength increased, too. Accompanied with the hardening effect, Cr leads to a drastic increase of brittle-to-ductile transition temperature (BDTT) of the alloys investigated. The strengthening effect is mainly attributed to solid-solution strengthening of the V_{SS} phase, which forms the major phase (about 50-60% phase fraction) in the Cr-free and Cr-added alloys. Since Cr is also dissolved in the intermetallic phase, a strengthening effect may also occur in these phases. However, the intermetallic phases already act as second phase strengthener and have an even higher BDTT as compared to the solid-solution phase.

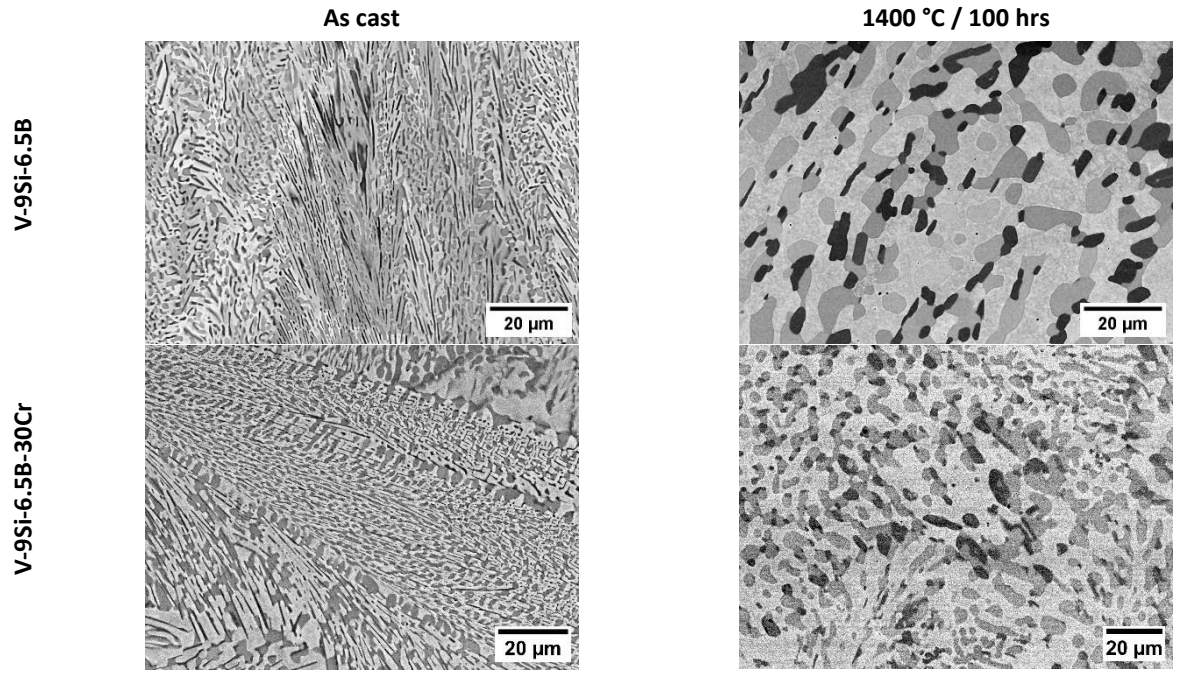

Fig 1: Exemplary microstructures auf the ternary eutectic base alloy V-9Si-6.5B (top) and theV-9Si-6.5B-30Cr alloys (bottom) in the as-cast or heat-treated state.

References

[1] R. Sakidja, J.H. Perepezko, S. Kim, N. Sekido, Acta Mater. 56 (2008) 5223–5244.

SCP5.4

Effects of Mo, V and Zr Additions on the Microstructure and Properties of Multi-elemental Nb-Si Based Ultrahigh Temperature Alloys

Xiping Guo[1], Rui Ma[1], Ping Guan[2] and Yanqiang Qiao[1]

[1]State Key Laboratory of Solidification Processing, Northwestern Polytechnical University, Xian 710072, China, xpguo@nwpu.edu.cn, ruima@nwpu.edu.cn, qyq@nwpu.edu.cn

[2]School of Chemistry and Chemical Engineering, Northwestern Polytechnical University, Xian 710129, China, guanping1113@nwpu.edu.cn

Introduction

Nb-Si based ultrahigh temperature alloys are the potential alternative for Ni based superalloys to operate at higher temperature (1200~1400 ℃) due to their lower densities and excellent high temperature strength. However, their insufficient room temperature fracture toughness and poor high temperature oxidation resistance are the bottlenecks for the practical applications of Nb-Si based ultrahigh temperature alloys [1]. Alloying is an effective way to improve the comprehensive properties of the alloys. It has been reported that alloying with V or Zr in the binary Nb-Si alloy improves the room temperature fracture toughness and high temperature oxidation resistance, while lowers high temperature strength [2]. Considering that Mo element has higher melting point and thus is beneficial for high temperature strength, the present work aims to add Mo, V and Zr simultaneously to improve the comprehensive properties of Nb-Si based ultrahigh temperature alloys. Additionally, Nb-Si based ultrahigh temperature alloys have been developed to multi-elemental systems with six or more elements [3]. In multi-elemental Nb-Si based ultrahigh temperature alloy systems, the composite alloying effects become more and more complex and is worthy of exploring. Recently, the reports on Mo, V and Zr alloying primarily focus on the ternary or quaternary Nb-Si based ultrahigh temperature alloys, and hardly involve their composite effects in multi-elemental Nb-Si based ultrahigh temperature alloys [4]. Therefore, it is essential to systematically investigate the effects, especially the composite effects of Mo, V and Zr on the comprehensive properties of multi-elemental Nb-Si based ultrahigh temperature alloys for further compositional optimization.

Materials and Methods

Fifteen multi-elemental Nb-Si based ultrahigh temperature alloys with nominal compositions of Nb-22Ti-15Si-5Cr-3Al-2Hf-*x*Mo-*y*V-*z*Zr (at.%) (referred as *x*Mo-*y*V-*z*Zr alloy hereafter) were prepared by vacuum non-consumable arc melting. The alloying effects of Mo, V and Zr on the arc-melted (referred as AC) and heat-treated (referred as HT) microstructures have been investigated. The heat treatment was conducted at 1450 ℃ for 50 h. The oxidation performances of fifteen arc-melted multi-elemental Nb-Si based ultrahigh temperature alloys were evaluated at 1250 °C for 1 and 20 h, respectively. The microhardness, three point bending and compression at 1250°C measurements were conducted for revealing the effects of Mo, V and Zr additions on the room and high temperature mechanical properties of the multi-elemental Nb-Si based ultrahigh temperature alloys.

Results and Discussion

The phase constituents of the multi-elemental Nb-Si based ultrahigh temperature alloys are Nbss (Niobium solid solution), α/γ$(Nb,X)_5Si_3$ and Laves Cr_2Nb phases. As shown in Fig. 1, alloying with V or Zr promotes the formation of hypereutectic structure, and cooperatively alloying with V and Zr further increases the content of primary silicides. While, in the presence of V or Zr, further adding Mo decreases the content of primary silicides. The additions of Mo, V and Zr can suppress the formation of α$(Nb,X)_5Si_3$, whilst promote the formation of γ$(Nb,X)_5Si_3$. During heat treatment at 1450 ℃ for 50 h, some γ$(Nb,X)_5Si_3$ phases in 0Mo-0V-0Zr and 0Mo-3V-0Zr alloys have transformed to α$(Nb,X)_5Si_3$ phases, but this phase transformation is not observed in Mo- or Zr-containing alloys. In addition, the heat treatment at 1450 ℃ for 50 h eliminates segregation microstructures and promotes the formation of $(Nb,X)_3Si$ phase in the alloys. Adding V causes serious element segregation in the solidified microstructure of Nb-Si based ultrahigh temperature alloys, and thus increases the content of Cr_2Nb/Nbss eutectic, Cr_2Nb/Nbss/$(Nb,X)_5Si_3$ three phase eutectic, Nbss dendrites and H-shaped primary silicides. Adding Mo promotes to form lamellar Nbss/γ$(Nb,X)_5Si_3$ eutectic structure. Adding Zr decreases the content of silicides during eutectic solidification, and thus promotes the formation of fine Nbss/γ$(Nb,X)_5Si_3$ eutectic structure. Additionally, V and Mo elements primarily dissolve in Nbss, while Zr almost wholly dissolves in silicides.

After oxidation at 1250 °C for 1 and 20 h, respectively, all scales formed on the alloy have double layered structure, namely outer layer and inner layer. Both of them consist of Nb_2O_5, $(Ti,X)O_2$ and $TiNb_2O_7$ oxides. Besides, some V_2O_5, $CrVNbO_6$ and Nb_9VO_{25} oxides form in the scales of V-containing alloys. Solely adding Mo or V ameliorates the adhesion of the scales and thus improves the oxidation resistance of the alloys. Solely adding Zr

does not affect the adhesion of the scales, but can improve the oxidation resistance of the alloys by increasing the oxidation resistance of silicide phases. Cooperative additions of Mo and Zr further improves the high temperature oxidation resistance, and the mass gain per unit area of 5Mo-0V-4Zr-AC alloy oxidized at 1250 ℃ for 20 h is only 30.3 mg/cm^2. The cooperative additions of V with Mo/Zr do not improve, but degrade the oxidation resistance of alloys, since more liquid V_2O_5 flow out of the scales. In the presence of V and Zr, the limited addition of Mo (2 at.%) marginally improves the oxidation resistance of the alloys, while further increasing the Mo content decreases the oxidation resistance of the alloys.

The microhardness of γ(Nb,X)$_5$Si$_3$ is improved by solely adding Mo, V or Zr, and is further improved by cooperative additions of them. The microhardness of γ(Nb,X)$_5$Si$_3$ phase in 5Mo-3V-8Zr-HT alloy shows the highest value, and is 1593 MPa. Solely adding Zr hardly affects the microhardness of Nbss due to the lower content of Zr in Nbss (not exceed 0.2 at.%). Solely adding Mo significantly increases the microhardness of Nbss, while sole addition of V reduces the microhardness of Nbss by its solid solution softening effect, and the microhardness of Nbss in 5Mo-0V-4Zr-AC alloy reaches 682 MPa. The composite effects of Mo and V on the microhardness of Nbss is related to their relative contents. When Mo content exceeds the V content, the cooperative additions of Mo and V show positive effects on the microhardness of Nbss. After heat treatment at 1450 ℃ for 50 h, the redistribution of alloying elements causes the increase in the microhardness of γ(Nb,X)$_5$Si$_3$ and the decrease in the microhardness of Nbss. The room temperature fracture toughness of the alloys has been improved by sole addition of V or Zr, and is further improved by cooperative additions of them. The 0Mo-3V-4Zr-AC alloy has the highest K_Q values of room temperature fracture toughness among the fifteen alloys (15.3 MPa·m$^{1/2}$). These positively composite alloying effects are strengthened by increase in Zr content. In the presence of V and Zr, the room temperature fracture toughness of the alloys is ameliorated by lower content addition (2 at.%) of Mo and is degraded by the addition of higher content of Mo (5 or 10 at.%). The effects of Mo and Zr additions, especially their composite additions significantly improve the high temperature compressive strength of the alloys, and the compressive strength at 1250 ℃/0.005 s^{-1} of 5Mo-0V-4Zr-AC alloy reaches 393 MPa. When simultaneously adding Mo, V and Zr, the compressive strength at 1250°C of the alloys is improved with increase in Mo content, but is hardly influenced by the addition of more than 4 at.% Zr.

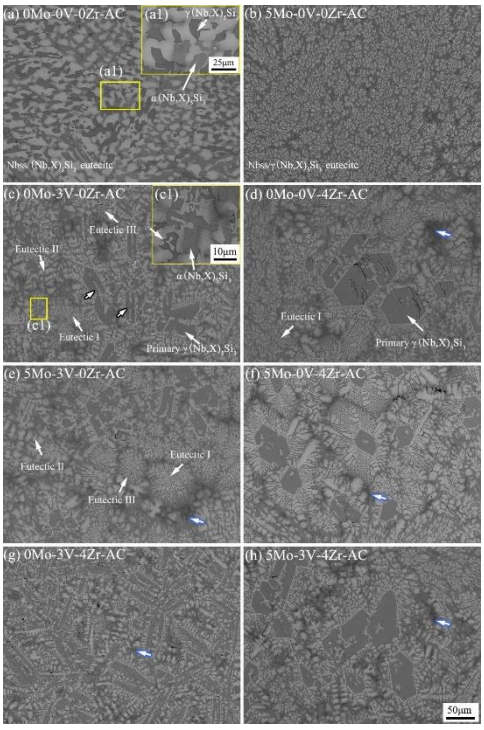

Fig. 1: BSE images of arc-melted multi-elemental Nb-Si based ultrahigh temperature alloys: (a) 0Mo-0V-0Zr-AC, (b) 5Mo-0V-0Zr-AC, (c) 0Mo-3V-0Zr-AC, (d) 0Mo-0V-4Zr-AC, (e) 5Mo-3V-0Zr-AC, (f) 5Mo-0V-4Zr-AC, (g) 0Mo-3V-4Zr-AC and (h) 5Mo-3V-4Zr-AC; (a1) and (c1) are enlarged BSE images of local areas labelled in (a) and (c), respectively

References

[1] P. Tsakiropoulos: Progress in Materials Science, **2022**, 123, 100714.

[2] N. Sekido, K. Hildal, R. Sakidja, J.H. Perepezko: Intermetallics, **2013**, 41, 104-112.

[3] J.H. Kim, T. Tabaru, M. Sakamoto, S. Hanada: Materials Science and Engineering A, **2004**, 372, 137-144.

[4] R. Ma, X.P. Guo: Journal of Materials Science & Technology, **2023**, 132, 27-41.

SCP5.5

Microstructure-based modeling of the temperature-dependent yield strength of γ/γ' Ni-base superalloys

Moritz Müller, Felix Schleifer, Michael Fleck and Uwe Glatzel

University of Bayreuth, Chair for Metals and Alloys, Bayreuth, Germany, moritz.mueller@uni-bayreuth.de, felix.schleifer@uni-bayreuth.de, michael.fleck@uni-bayreuth.de, uwe.glatzel@uni-bayreuth.de

Introduction

Ni-base superalloys show great mechanical strength at high operating temperatures and thus are a widely used material for high-temperature load-bearing applications, like turbine blades. The strength of Ni-base superalloys strongly depends on their precipitation microstructure. The most common type of Ni-base superalloys features an fcc γ matrix in which intermetallic Ni_3Al $L1_2$ ordered γ' precipitates are distributed. The interactions between these precipitates and dislocations are the cause for major strengthening effects, which are still relevant at elevated temperatures near the alloy's melting temperature. These interactions depend strongly on the morphology of the precipitates, their size, shape, and distance from each other. A model to predict tensile properties based on the observed precipitate microstructure is of high interest to further accelerate the development of alloys and new processes.

Grain structures and textures resulting from different processing methods, influencing the elastic and plastic deformation behavior of the materials, are additional influences that need to be considered. This work describes the development of a model predicting the temperature-dependent yield strength of medium to high γ' volume fraction Ni-base superalloys based on a statistical description of grain and precipitation microstructure.

Materials and Methods

The materials discussed in this work are different Ni-base superalloys with a medium to high γ' volume fraction $0.35 < V_{\gamma'} < 0.7$. The materials γ/γ' microstructure was characterized from scanning electron images. The technique used for evaluating accurate distributions of the parameters of interest, the precipitate size d as well as the channel width L, is described in [1].

Fig. 1 describes the process schematically. A neural net is used to segment the images and identify precipitates, which are then characterized for their size d. The minimal distance between neighboring precipitates is evaluated as a measure for the channel width L. The described procedure can also be applied to 3D data sets, like such resulting from phase-field simulations, while delivering consistent performance.

From EBSD maps the grain microstructure is analyzed for the direction-dependent grain size and the crystal orientation using the MTEX toolbox. Both parameters are considered in the model, influencing the yield strength.

The model for the yield strength is based on the previous work of Galindo-Nava et. al. [2] and Goodfellow et. al. [3]. It considers the contributions of different chemistry- and microstructure-based effects on the overall yield strength of the material. These effects include grain boundary strengthening, solid solution strengthening, precipitate dislocation interactions through anti-phase boundary shearing and the Orowan mechanism, the effect of the lattice parameter misfit between matrix and precipitate phases, as well as the temperature-dependent effect through Kear-Wilsdorf locks. The contributions are combined in a nonlinear way, trying to mimic their physical relationship as close as possible. Temperature dependence of the yield strength is described through the consideration of many temperature-dependent material parameters, as well as microstructure, which also changes with temperature.

Results and Discussion

Different combination strategies of the contributions are compared for their fit to the analyzed alloys. It was found that linear summation of all contributions leads to worse results than using a parallel combination of the anti-phase boundary shearing and Orowan contributions in conjunction with linear summation of the remaining contributions. Different ways of defining this parallel combination were explored, including a minimum switch and setup similar to an electronic parallel circuit of resistors.

Fig 2 shows an example of these combination schemes including the prediction of the yield strength of a single crystalline material at room temperature. These changes improve the room temperature model as described in the literature. The performance is also validated against several datasets published in the literature.

In terms of the temperature dependence of the yield strength, different implementations of temperature dependence are compared. Considering the change of different material parameters, like elastic or shear moduli and anti-phase boundary energy does not have a sufficient influence on the prediction, leading to overestimation at higher temperatures. Further, including the change in microstructure that is present due to a reduction in γ' volume fraction at higher temperatures and thus resulting in a change in precipitate size d and channel width L, improves the performance only slightly. Including the influence of Kear-Wilsdorf locks through experimental data as an additional contribution, leads to further improvement. In another enhancement, the measured distributions for the precipitate size d and channel widths L are used to consider the higher mobility of dislocations at higher temperatures and thus their ability to select weaker obstacles, e.g. through climbing, improving the prediction of the model.

In conclusion, the literature model was improved in terms of its performance at room temperature, and high-temperature prediction capabilities were added, coming closer to the real word use case of Ni-base superalloys.

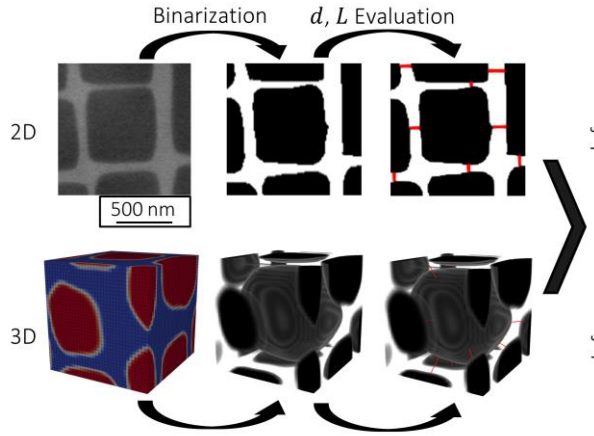

Fig. 1: Schematic showing the statistical characterization of the key microstructure parameters precipitate size d and channel width L from 2D and 3D data sets, resulting in distributions for each parameter. A detailed description of the channel width evaluation method can be found in [1].

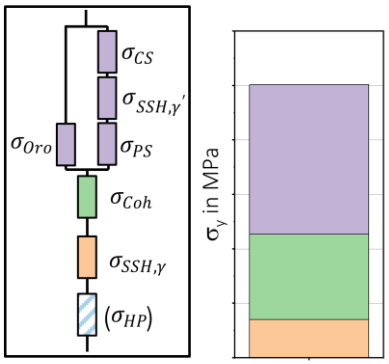

Fig. 2: Left: example of a combination scheme of different contributions to the overall yield strength; Right: example of resulting prediction.

References

[1] M. Müller, B. Böttger, F. Schleifer, M. Fleck, U. Glatzel, Integrating Materials Manufacturing Innovation. **2023**, *12*, 27-40.

[2] E.I. Galindo-Nava, L.D. Connor, C.M.F. Rae, Acta Materialia. **2015**, 98, 377-390.

[3] A.J. Goodfellow, E.I. Galindo-Nava, C.W.M. Schwalbe, H.J. Stone, Materials & Design. **2019**, 173, 107760.

SCP5.6

Development of a NiAl-based eutectic alloy processed via electron beam powder bed fusion

Katharina Titz[1], Jan Vollhüter[2], Benjamin Wahlmann[1], Steffen Neumeier[2], Mathias Göken[2] and Carolin Körner[1]

[1]Friedrich-Alexander-Universität Erlangen, Materials Science and Engineering for Metals, Erlangen, Germany, katharina.titz@fau.de, benjamin.wahlmann@fau.de, carolin.koerner@fau.de

[2] Friedrich-Alexander-Universität Erlangen, Materials and Engineering Institute I, Erlangen, Germany, jan.vollhueter@fau.de, steffen.neumeier@ww.uni-erlangen.de, mathias.goeken@fau.de

Introduction

The demand for alloys with excellent physical and mechanical properties in the aircraft industry requires the development of new high-temperature structural materials. The intermetallic NiAl B2-phase is a prime candidate for such applications as it possesses a higher melting point, lower density, and thus lower specific weight in comparison to other Ni-based-superalloys and exceptional oxidation behavior [1]. Nevertheless, the application as a structural material is limited due to low room temperature ductility and fracture toughness, as well as low creep resistance [2]. By embedding a second phase of (Cr,Mo) with lamellar morphology into the NiAl matrix these drawbacks can be mitigated [3–5].

One promising alloy in this material class is the so-believed eutectic 33Ni-33Al-28Cr-6Mo (all following concentrations are given in at.%). Typically, this material has been processed in a conventional Bridgman process. The microstructure exhibits NiAl and (Cr,Mo) lamellae that are ordered in a circular manner inside the eutectic cells [6]. By refining the lamellae spacing with adjusted withdrawal rates, it was possible to enhance the high-temperature properties. Contrary to the literature, Förner et al. [7] found in the as-cast microstructure primary NiAl-dendrites, which is a result of non-fully eutectic solidification. This is in good agreement with the updated thermodynamic modeling of the Ni-Al-Cr-Mo system done by Peng [8]. In addition, Förner et al. [7] present a feasibility study towards additive manufacturing of NiAl-(Cr,Mo). Because of the higher solidification rate, the non-eutectic alloy solidifies in a eutectic manner with phase distances of less than 10 nm.

To exploit the full potential of the material class, a eutectic composition with a lamellar microstructure and fine phase distances is necessary. The aim of this research is to establish and characterize a novel eutectic NiAl-(Cr,Mo) in-situ composite processed via electron beam powder bed fusion (PBF-EB/M).

Materials and Methods

The alloy development is realized with the in-house developed alloy design tool PyMultOpt. The tool is based on the CALPHAD (Calculation of Phase Diagrams) method and uses the updated thermodynamical calculations of the quaternary Ni-Al-Cr-Mo alloy system by Peng [8]. The software determines for various chemical compositions the difference between solidus temperature and liquidus temperature, which is described as the solidification interval. In this case, a small solidification interval is desired to obtain an optimal microstructure of the strengthening (Cr,Mo)-phase. Therefore, the composition is optimized towards a minimal solidification interval.

Gas atomized powder by Praxair Surface Technologies GmbH was used and characterized with a Zeiss Axio Imager M1m light microscope (Carl Zeiss AG, Germany) and a Mastersizer 3000 particle size analyzer (Malvern Panalytical, United Kingdom). The optimized eutectic powder is processed via electron beam powder bed fusion on an Arcam A2 (GE Additive – former: Arcam AB, Mölndal, Sweden). In total, 400 cuboids with a geometry of 15x15x20 mm^3 are produced to characterize the processability of the alloy. Therefore, a porosity and microstructural analysis is carried out. The area within 1 mm to the edge is neglected in order to analyze the bulk material properties. Each sample is divided into three sections: bottom, middle and top. The grain size is measured by the linear intercept method, and the phase distances is determined via scanning electron microscopy images.

For a first classification of the mechanical properties creep tests are conducted. The creep tests are done on a pneumatic in-house-built creep testing machine at temperatures between 750 °C and 900 °C. The applied stresses are between 250 and 500 MPa. Cylindrical compression creep specimens with a height of 6 mm and a diameter of 4 mm are produced by wire electrical discharge machining.

Results and Discussion

Fig.1 summarizes the presented approach and characterization of the novel NiAl-(Cr,Mo) alloy. The optimization with the design tool PyMultOpt yielded a chemical composition of Ni-36Al-31.4Cr-2Mo and a solidification interval of around 0.3 °C. This is significantly lower than the so-believed eutectic 33Ni-33Al-28Cr-6Mo alloy, which exhibits a calculated solidification interval of 17 °C. Arc-melted samples as well as directional solidified

samples of the optimized alloy have shown a significantly refined microstructure consisting of lamellar (Cr,Mo)-phase in the NiAl-matrix. With the processability study a process map, in which samples are categorized in porous, dense and bulged, is presented. The microstructural investigation exhibits a fine cellular microstructure with a dark NiAl-matrix and a bright discontinuous (Cr,Mo) network. The PBF-EB samples show an average grain size below 10 µm. In comparison, the grain size for directionally solidified samples of Ni-33Al-33Cr-1Mo with solidification rates ≥ 25.4 mm/h measures around 200 µm [9]. This means, by processing via electron beam powder bed fusion an approximately 20-times finer grain can be achieved. The lamellae spacing follows the same trend. To examine the influence of the grain refinement, creep tests were conducted. In general, a pronounced improvement compared to the intermetallic NiAl was observed. As expected, the directionally solidified 33Ni-33Al-28Cr-6Mo alloy exhibits good creep properties in build direction, whereas perpendicular to the build direction the properties decrease. The optimized NiAl-(Cr,Mo) alloy performs at 900 °C comparable to TiAl-based alloys, which are already used in industry for high temperature applications as an alternative for Ni-based superalloys. At 750 °C the optimized alloy performs slightly better than the TiAl-based alloy. In addition, the drawback of a strong anisotropy behavior as seen in the conventionally casted material could be reduced by processing the material via PBF-EB/M.

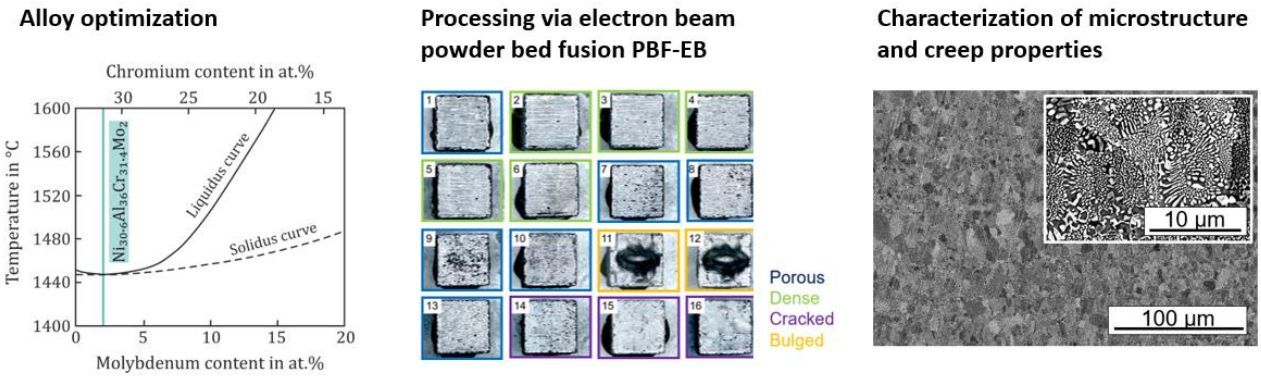

Fig. 1: The alloy optimization result displayed by the calculated liquidus and solidus curve on the left. A processability study for the PBF-EB process is presented in form of a process map, presented in the center. The as-built microstructure is shown on the right.

Fundings

The authors thank the German Research Foundation (Deutsche Forschungsgemeinschaft, DFG) for its financial support within the research project “Additive manufacturing of nanostructured eutectic NiAl-(Cr,Mo) in-situ composite” (Project number: 491441582).

References

[1] W.S. Walston, R. Darolia, MRS Proc., 1992, 288.
[2] R.D. Noebe, R.R. Bowman, M.V. Nathal, International Materials Reviews, 1993, 38, 193.
[3] J.L. Walter, H.E. Cline, Metall and Materi Trans, 1970, 1, 1221.
[4] H.E. Cline, J.L. Walter, E. Lifshin, R.R. Russell, Metall and Materi Trans, 1971, 2, 189.
[5] H.E. Cline, J.L. Walter, Metall and Materi Trans, 1970, 1, 2907.
[6] Demitras H. PhD, Prof. Gungor A., ed., Effect of alloying elements on the microstructure and mechanical properties of NiAl-Cr(Mo) eutectic alloy 2015.
[7] A. Förner, S. Giese, C. Arnold, P. Felfer, C. Körner, S. Neumeier, M. Göken, Scientific reports, 2020, 10, 15153.
[8] J. Peng, Experimental investigation and thermodynamic modeling of the Al-Cr-Mo-Ni system and its sub-systems, Karlsruhe 2016.
[9] J.D. Whittenberger, S.V. Raj, I.E. Locci, J.A. Salem, Metall and Mat Trans A, 2002, 33, 1385.

SCP6.1R

B2 precipitation-strengthened refractory compositionally complex alloys

Martin Heilmaier, Alexander Kauffmann, Stephan Laube and Bronislava Gorr

Institute for Applied Materials (IAM), Karlsruhe Institute of Technology (KIT), Engelbert Arnold Str.4, 76131 Karlsruhe, Germany, martin.heilmaier@kit.edu, alexander.kauffmann@kit.edu, Stephan.laube@kit.edu, Bronislava.gorr@kit.edu

Introduction

Refractory compositionally complex alloys (RCCA) are promising candidates for high-temperature structural applications. Recently, Senkov and co-workers [1] reported a microstructure with coherent cuboidal (disordered A2) precipitates in an ordered B2 matrix yielding promising high-temperature strength in the Al-Mo-Nb-Ta-Ti-Zr system. However, the alloy lacks ductility at room temperature.

Results and Discussion

Following along above conceptual path we review here the current status of our investigations within the Ta-Mo-Ti-Cr-Al system, which exhibits a promising combination of strength and oxidation resistance at elevated temperatures [2]. Thermodynamic calculations were employed with an in-house database to predict specific transformation sequences of ordering and diffusion-controlled phase separation within this system. As observed in the Ta-free subsystem MoTiCrAl, Al has a significant effect on the ordering transition from A2 towards B2 [3]. However, in the case of MoTiCrAl, no multi-phase field was found after the homogenization. The situation changes by the addition of Ta, as a multi-phase field is thermodynamically predicted [4]. The microstructure of two compositions (high and low in Al) were investigated experimentally by scanning and transmission electron microscopy, while the phase transitions were determined by means of differential scanning calorimetry. The microstructure of the alloy with high Al concentration exhibited a B2 matrix with A2 precipitates; in contrast, an A2 matrix with B2 precipitates was found in the Al-lean alloy. The necessary reaction sequences are discussed in detail and provide information about the phase diagram necessary to reproducibly obtain the desired two-phase microstructures. Microstructural peculiarities, such as segregation at planar defects as well as their implications on the mechanical properties will be also discussed.

References

[1] O. N. Senkov, C. Woodward and D. B. Miracle, "Microstructure and Properties of Aluminum-Containing Refractory High-Entropy Alloys," *JOM,* vol. 66, pp. 2030-2042, 2014.

[2] B. Gorr, F. Müller, S. Schellert, H.-J. Christ, H. Chen, A. Kauffmann and M. Heilmaier, "A new strategy to intrinsically protect refractory metal based alloys at ultra high temperatures," *Corrosion Science,* vol. 166, p. 108475, 2020.

[3] S. Laube, H. Chen, A. Kauffmann, F. Müller, B. Gorr, J. Müller, B. Butz, H.-J. Christ and M. Heilmaier, "Controlling crystallographic ordering in Mo–Cr–Ti–Al high entropy alloys to enhance ductility," *Journal of Alloys and Compounds,* vol. 823, p. 153805, 2020.

[4] S. Laube, S. Schellert, A. Tirunilai, D. Schliephake, B. Gorr, H.-J. Christ, A. Kauffmann and M. Heilmaier, "Microstructure tailoring of Al-containing compositionally complex alloys by controlling the sequence of precipitation and ordering," *Acta Materialia,* vol. 218, p. 117217, 2021.

SCP6.2

Microstructure analysis and tensile behavior of hexagonal rare earth based low, medium, and high entropy alloys made from Ho-Dy-Y-Gd-Tb

Laura Rosenkranz[1], Qianqian Lan[2], Michael Feuerbacher[2] and Uwe Glatzel[1]

[1]University of Bayreuth, Chair for Metals and Alloys, Bayreuth, Germany, Laura.Rosenkranz@uni-bayreuth.de, uwe.glatzel@uni-bayreuth.de

[2]Forschungszentrum Jülich GmbH, Ernst Ruska-Centre (ER-C) for Microscopy and Spectroscopy with Electrons, Jülich, Germany, Lan, q.lan@fz-juelich.de, m.feuerbacher@fz-juelich.de

Introduction

High entropy alloys (HEA) consist of at least five elements (5-35 at.%) without a main alloy element [1-3]. Unlike conventional alloys, HEA are located in the middle of multi-dimensional phase diagrams. HEA are single solid solution phases, preferably with simple crystal structures, which means a combination of chemical complexity with topological order. This circumstance offers a whole new bunch of possible combinations of alloying elements with the potential to meet the increasing demands for high-performance materials. HEA are reported to possess promising properties, e.g., high strength and ductility [4]. While conventional alloys have been studied for decades, the relations between microstructure and the resulting properties of HEA remain mostly unknown [4]. Recent research focuses on a few known HEA, with a large amount of research on the face-centered cubic (fcc) Cantor alloy Cr-Mn-Fe-Co-Ni and the body-centered cubic (bcc) Senkov alloy Ti-Zr-Hf-Nb-Ta [1,2]. Only a few hcp HEA are known so far, with Ho-Dy-Y-Gd-Tb (HEA-Fb, Feuerbacher alloy) being one of the very few single-phase hcp HEA reported today [5,6]. The equiatomic HEA Ho-Dy-Y-Gd-Tb with extraordinarily similar constituent elements is ideal for assessing the widely discussed high entropy effect of HEA. To assess this possible high entropy effect, the microstructures and tensile behavior of equiatomic alloys made from one to five rare earth elements were evaluated (see Fig. 1, [6]).

Materials and Methods

Single element alloys, equiatomic low, and medium entropy alloys were derived from the high entropy alloy HEA consisting of the elements Ho, Dy, Y, Gd, and Tb to vary the configurational entropy, see Fig. 1. Details on the compositions of the alloys, the alloy production via arc melting, specimen preparation, and tensile testing at room temperature (RT) as well as microstructure analysis via scanning electron microscopy (SEM), energy dispersive X-Ray spectroscopy (EDS) and X-Ray diffractometer (XRD) can be found in [6].

Furthermore, a detailed microanalysis of HEA-Fb as well as the medium entropy alloy Ho-Dy-Gd-Tb (4-Y) via (scanning) transmission electron microscopy ((S)TEM) was carried out with different microscopes. The TEM specimens were prepared via focused ion beam (FIB) Helios NanoLab 600. The microstructures of both alloys in the as-cast state and after their stress-strain curves were compared. Changes in their microstructures were assessed to understand their tensile behavior better. Bright-field (BF) and dark field (DF), high-angle annular dark field (HAADF) imaging in (S)TEM, STEM EDS elemental mappings and line scans, as well as diffraction patterns (DF) in (S)TEM, were conducted.

Results and Discussion

The results of this study enable the determination of the often-discussed high entropy effect of HEA using HEA-Fb and other medium and low entropy alloys from the same elements with minimized solid solution strengthening (SSS). This alloy system is highly susceptible to oxidation, making sample preparation and testing challenging. In Fig. 1, all stress-strain curves are compared, with pure elements in Fig. 1 a), ductile alloys in Fig. 1 b), and brittle alloys in Fig. 1 c). As the strength of all tested samples is comparable, minimized SSS is confirmed. At the same time, a direct correlation of the configurational entropy and the tensile behavior at RT is excluded for HEA-Fb. Interestingly, the alloys 2+Y, 3+Y, and HEA-Fb behave very brittle, while all other tested pure elements and alloys show a higher ductility during tensile tests. While HEA-Fb appears single phase in XRD and SEM EDS analysis, 2+Y, and 3+Y possess a Y-rich second phase at the grain boundaries, which explains their embrittlement. More details, e.g., on the tensile behavior and EDS elemental mappings, may be found in [6].

For HEA-Fb and 4-Y, a detailed study via (S)TEM provides the first explanation for the differences in their tensile behavior. All specimens have a Mg-type hcp structure, and twinning is observed in the as-cast state. The twin grain boundary formation in HEA-Fb is slightly increased during tensile testing. However, while the brittle HEA-Fb contains only occasional dislocations after the tensile test, more dislocations were generated in the ductile 4-Y. Most dislocations were formed within the twins and along the interfaces of twins and parent material, creating outlines of the twin grain boundaries. Additional glide planes were observed in the alloys after tensile tests. By

this TEM analysis of the microstructures and formation of dislocations, the different tensile behavior of HEA-Fb and 4-Y can be reasoned.

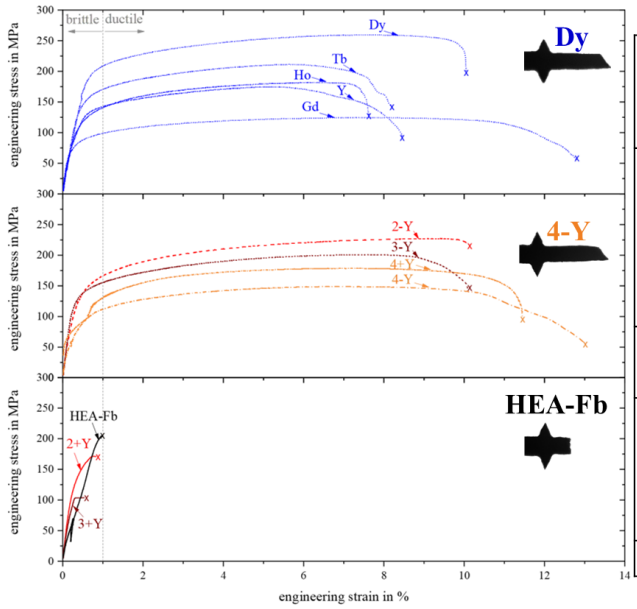

	number of elements	composition (equiatomic)	denom.
pure elements	1	Gadolinium (Gd)	Gd
		Terbium (Tb)	Tb
		Dysprosium (Dy)	Dy
		Holmium (Ho)	Ho
		Yttrium (Y)	Y
LEA	2	Ho-Y	2+Y
		Ho-Dy	2-Y
MEA	3	Ho-Y-Gd	3+Y
		Ho-Dy-Tb	3-Y
	4	Ho-Y-Gd-Tb	4+Y
		Ho-Dy-Gd-Tb	4-Y
HEA	5	Ho-Dy-Y-Gd-Tb	HEA-Fb

Fig. 1: Left: Stress-Strain curves from tensile testing of all alloys. Pure elements on top, ductile alloys in middle and brittle alloys in lower diagram [6]. Right: Compositions used in this work. The number elements, the and the denominations of these compositions are given.

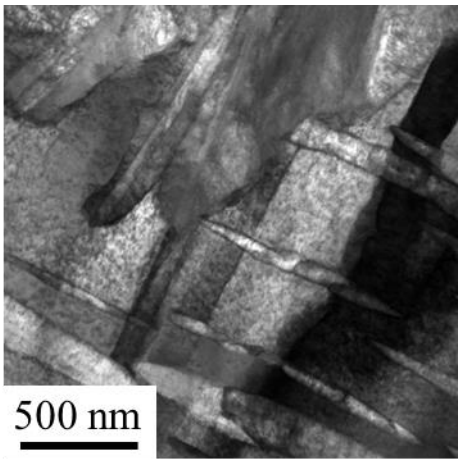

Fig. 2: 4-HAADF STEM image of 4-Y. The outlines of the twins (diagonal structures from upper left to lower right) indicate the formation of dislocations preferably at the interfaces.

Acknowledgments

The authors thank the German Research Foundation (DFG) for the financial support by GL181/56–2 and FE 571/4-2, and through the Priority Program SPP 2006 “Compositionally Complex Alloys – High Entropy Alloys (CCA-HEA)”.

References

[1] B. Cantor, I. Chang, P. Knight, A. Vincent, 375-377, Mater. Sci. Eng., A, **2004**, 213–218.
[2] J.-W. Yeh, S.-K. Chen, S.-J. Lin, J.-Y. Gan, T.-S. Chin, T.-T. Shun, C.-H. Tsau, S.-Y. Chang, Adv. Eng. Mater. 6, **2004**, 299–303.
[3] E.P. George, D. Raabe, R.O. Ritchie, Nat. Rev. Mater. 4, **2019**, 515–534.
[4] R.K. Nutor, Q. Cao, X. Wang, D. Zhang, Y. Fang, Y. Zhang, J.-Z. Jiang, Adv. Eng. Mater. 22, **2020**, 2000466.
[5] M. Feuerbacher, M. Heidelmann, C. Thomas, Hexagonal high-entropy alloys, Materials Research Letters 3, **2015**, 1–6.
[6] Rosenkranz, L., Feuerbacher, M., Gadelmeier, C., Schleifer, F., & Glatzel, U., Intermetallics, 155, **2023**, 107835.

SCP7.1

Defect-stabilized off-stoichiometric Al_2Ge_2Mg □-phase intermetallics: a combined theoretical and experimental study

Martin Friák, Ondřej Zobač and Aleš Kroupa

Institute of Physics of Materials, Czech Academy of Sciences, Žižkova 22, Brno, 616 00, Czech Republic,
friak@ipm.cz, zobac@ipm.cz, kroupa@ipm.cz

Introduction

The Al-Ge-Mg system has been studied in the past for its potential applications in the aerospace and automotive industries. The phase equilibria in the Al-Ge-Mg system were experimentally described already in 1958 by Badaeva [1] using methods of thermal analysis. Various vertical sections of the phase diagram were investigated. No ternary phase was mentioned in the paper [1] but several candidate phases have been later discussed in literature and stoichiometric ternary τ-phase Al_2Ge_2Mg was identified in the work of Pukas et al. [2]. This phase was confirmed in our recent study [3], but the composition of the ternary phase was found to be off-stoichiometric with the measured composition close to $Al_9Ge_9Mg_7$, see Figure 1(a) and Ref. [3]. Considering this partly conflicting literature data, we have decided to use theoretical tools, in particular quantum-mechanical calculations, in order to shed some light on the experimental results.

Methods

Our *ab initio* calculations were performed using the Vienna Ab initio Simulation Package (VASP) [4,5]. We have employed projector augmented wave (PAW) pseudopotentials [6,7]. The exchange and correlation energy was treated within the generalized gradient approximation (GGA), in particular the Perdew-Burke-Ernzerhof (PBE) parametrization [8]. When calculating properties of off-stoichiometric states of the τ-phase, we have used multiples of the 5-atomic unit cell of Al_2Ge_2Mg, see Figure 1(b), for example a 20-atom supercell shown in Fig. 1(c) as a 2x2x1 multiple of the 5-atom cell. The plane-wave energy cut-off was equal to 520 eV. The product of the number of k-points in the reciprocal space and the number of atoms was equal to 10 240, i.e. a 16x16x8 k-point mesh was used in the case of 5-atom cell of the stoichiometric Al_2Ge_2Mg, see Fig. 1(b) and a 8x8x8 mesh in the case of the 20-atom supercell as, e.g., that in Figure 1(c). The thermodynamic stability of both stoichiometric Al_2Ge_2Mg and its defects-containing off-stoichiometric variants $Al_xGe_yMg_z$ were assessed by calculating the formation energy E_f. In general, for a $Al_xGe_yMg_z$ the E_f is defined as:

$$E_f(Al_xGe_yMg_z) = \{ E_f(Al_xGe_yMg_z) - x\cdot\mu^{Al} - y\cdot\mu^{Ge} - z\cdot\mu^{Mg} \}/(x+y+z) \quad (1)$$

using the chemical potentials μ, i.e. energies (per atom) of elements in their ground states, here face-centered Al, diamond-structure Ge and hexagonal close-packed Mg. The formation energy was evaluated for a series of Al_2Ge_2Mg defect-containing states in which atoms of one chemical species are replacing atoms of another element at its sublattice within the structure. Figure 1(c) shows a substitution of one Al atom at the Al sublattice by an Mg atom in an Mg-rich $Al_7Ge_8Mg_5$ as an example. A chemical formula reflecting the composition of individual sublattices is $(Al_7,Mg_1)Ge_8Mg_4$.

Next to the thermodynamic stability, we have also tested the mechanical stability by determining and analyzing a complete tensor of second-order elastic constants using the stress-strain method [9]. Further, the dynamic stability of a few selected compositions was examined by computing phonon modes employing the PHONOPY software [10].

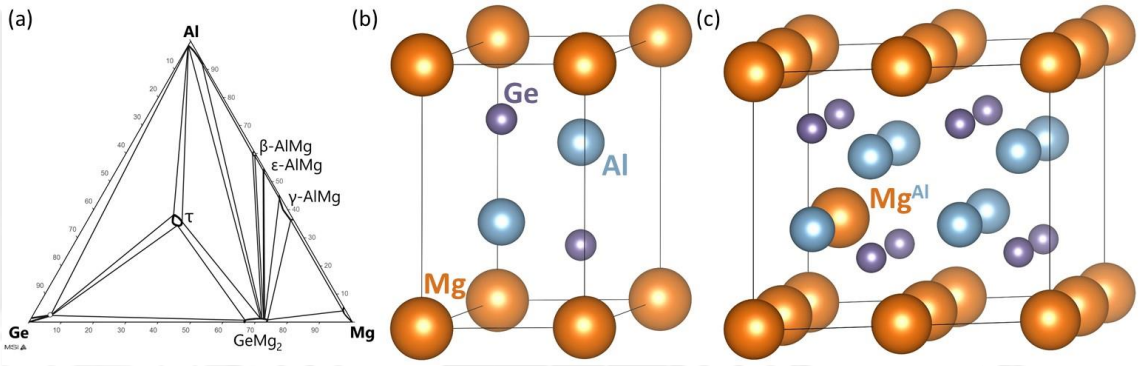

Fig. 1: The Al-Ge-Mg phase diagram for the temperature 250 °C (adapted from our paper [3]) including a region with the off-stoichiometric Al_2Ge_2Mg τ-phase (a). A 5-atom computational unit cell of the stoichiometric

Al_2Ge_2Mg intermetallics together with its 20-atom 2x2x1 multiple, which we used for our calculations of off-stoichiometric states, are shown in parts (b) and (c), respectively. Part (c) visualizes a particular case when Mg replaces Al atoms at the Al sublattice (see the atom marked as Mg^{Al}). Please mind that some atoms are visualized with their periodic images.

Results and Discussion

Our calculations show that an off-stoichiometric Mg-rich $Al_7Ge_8Mg_5$ as visualized in Fig. 1(c) has a formation energy lower than the stoichiometric Al_2Ge_2Mg (or, equivalently, its 2x2x1 multiple $Al_8Ge_8Mg_4$) by 7 meV/atom. It means that the defect-containing state is thermodynamically more stable. Both Al_2Ge_2Mg and $Al_7Ge_8Mg_5$ also exhibit elastic constants corresponding to mechanically stable systems, i.e. they fulfill all the conditions of mechanical stability [11]. Further, phonon frequencies of both intermetallics are all real, without any imaginary ones (so-called soft phonon modes), as an indication that both compounds are also dynamically stable.

Importantly, the Al-Ge-Mg system is quite sensitive to the type of defects. Another type of substitution leading to the composition $Al_8Ge_7Mg_5$, when an Mg atom replaces a Ge atom at the Ge sublattice, $Al_8(Ge_7Mg_1)Mg_4$, illustrates this sensitivity. This substitution results in (i) a significant increase of the formation energy by 71 meV/atom with respect to the formation energy of the stoichiometric Al_2Ge_2Mg ($Al_8Ge_7Mg_5$ is therefore much less thermodynamically stable) and also (ii) soft phonon modes which render the system dynamically unstable (it cannot exist unless externally stabilized).

Funding

The authors acknowledge the Czech Science Foundation for the financial support within the Project No. 22-22187S.

Acknowledgement

Computational resources were provided by the Ministry of Education, Youth and Sports of the Czech Republic under the Projects e-INFRA CZ (ID:90140) at the IT4Innovations National Supercomputing Center and e-Infrastruktura CZ (e-INFRA LM2018140) at the MetaCentrum as well as CERIT Scientific Cloud, all provided within the program Projects of Large Research, Development and Innovations Infrastructures. The Figure 1 was visualized using the VESTA software [12] (version 3, National Museum of Nature and Science, 4-1-1, Amakubo, Tsukuba-shi, Ibaraki 305-0005, Japan).

References

[1] T. Badaeva, and R. Kuznetsova, Liquidus Surface and Aluminum Solid Solutions in the Al–Mg–Ge System, Metalloved. Term. Obrab. Met., **1958**, *3*, 216–230.

[2] S. Pukas, L. Pylypchak, O. Matselko, P. Demchenko, R. Gladyshevskii, "$MgAl_2Ge_2$"- a new representative of the structure type $CaAl_2Ge_2$, Chem. Met. Alloys, **2012** 5.1/2, 59

[3] O. Zobač, L. Karpíšková, A. Kroupa, Experimental Study of the Ternary Phase Diagram Al–Ge–Mg. J. Phase Equilib. Diffus. **2023,** *44*, 127–136. https://doi.org/10.1007/s11669-023-01025-3.

[4] G. Kresse, J. Hafner, Ab initio molecular dynamics for liquid metals, Phys. Rev. B. **1993**, *47*, 558-561.

[5] G. Kresse, J. Furthmüller, Efficient iterative schemes for ab initio total-energy calculations using a plane-wave basis set. Phys. Rev. B. **1996**, *54*, 11169-11186.

[6] P. E. Blöchl, Projector augmented-wave method. Phys. Rev. B. **1994**, *50*, 17953-17979.

[7] G. Kresse, D. Joubert, From ultrasoft pseudopotentials to the projector augmented-wave method. Phys. Rev. B. **1999**, *59*, 1758-1775.

[8] J. P. Perdew, K. Burke, M. Ernzerhof, Generalized gradient approximation made simple. Phys. Rev. Lett. **1996**, *77*, 3865-3868.

[9] L. Zhou, D. Holec, P.H. Mayrhofer, First-principles study of elastic properties of cubic $Cr_{1-x}Al_xN$ alloys. J. Appl. Phys. **2013**, *113*, 043511.

[10] A. Togo, I. Tanaka, First principles phonon calculations in materials science, Scripta Mater. **2015**, *108,* 1–5.

[11] F. Mouhat, F.X. Coudert, Necessary and sufficient elastic stability conditions in various crystal systems. Phys. Rev. B **2014**, *90*, 224104.

[12] K. Momma, F. Izumi, VESTA 3 for three-dimensional visualization of crystal, volumetric and morphology data. J. Appl. Crystallogr. **2011**, *44*, 1272-1276.

SCP7.2

Applications of CALPHAD-based computational tools to Ti- and TiAl-alloys

Yang Yang, Reza Naraghi and Anders Engström

Thermo-Calc Software AB, Råsundavägen 18, 169 67 Solna, Sweden
yang@thermocalc.se

Titanium alloys have been widely applied in biomedical, aerospace and chemical industries due to the exceptional strength-to-weight ratio, excellent corrosion resistance and good biological compatibility [1]. The microstructure, phase constituents of Ti alloys and their properties strongly depend on the composition and manufacturing procedure. Now, for an improved energy efficiency and reduced environmental effects, the development of novel Ti alloys with higher temperature resistance for gas turbine engines attracts considerable attentions. In a general manner, the conventional processing routes like casting for low-pressure turbine blades made from γ titanium aluminides might restrict the use of these materials to simple shapes and moderate dimensions due to relatively poor room temperature mechanical properties caused by processing defects. Therefore, alternative manufacturing routes including additive manufacturing are being investigated with the aim of producing complex-shaped titanium components achieving the geometrical, technical and functional properties.

Regarding the development of advanced materials, we need to be able to analyze material properties during processing to ensure the ability to make performance predictions of components and the optimizations of material-specific requirements. A challenge is that properties data from handbooks and data repositories tend to be limited in the scope of materials (compositions) and/or the temperature ranges (processing conditions). The CALPHAD approach captures the composition and temperature dependence of properties as well as their temporal evolution for multi component alloys, which offers a unique and remarkable advantage to simulate for envisaged compositions or conditions.

In this talk, we will present the successful extension of a CALPHAD database by incorporating thermophysical properties and exemplify how CALPHAD based tools can be used to aid alloy design and process optimization of titanium alloys.

The γ-solvus temperature is one important reference temperature to develop heat treatment procedures of TiAl-based alloys. Fig. 1 shows a comparison between experimental and calculated γ-solvus temperatures for typical alloys using TCTI5 [2]. In most cases, the deviation is within ±20 °C which is represented by the two dashed lines. Thermal conductivity is usually an essential input for processing simulations. This transport property has been modeled in accordance with the principles of CALPHAD in TCTI5 database. Fig. 2 shows a comparison between measured and calculated thermal conductivity for a wide variety of commercial titanium alloys. The respective calculation is made by freezing-in the state at the typical heat treatment temperature of manufacture for each alloy. Deviations are expected because the thermal conductivity of alloys varies depending on the thermal-mechanical processing and actual composition. The black solid line in the plot shows where calculated values are equal to experimental data. The blue dashed lines mark for 10% deviations while the red dashed lines are for 20% deviations.

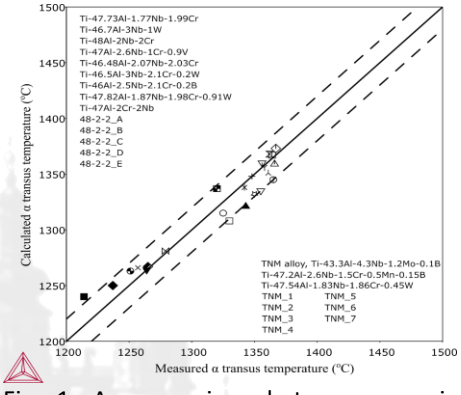

Fig. 1: A comparison between experimental and calculated γ-solvus temperatures.

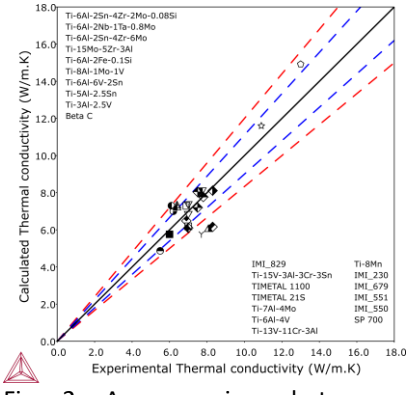

Fig. 2: A comparison between measured and calculated thermal conductivity of various Ti alloys at room temperature.

References

[1] G. Lütjering, J. C. Williams, Titanium, Springer, Berlin, **2007**.

[2] Thermo-Calc Software, TCTI Titanium and TiAl-based Alloys Database, version 5
< https://thermocalc.com/products/databases/titanium-and-titanium-aluminide-based-alloys/ >

SCP7.3

Thermodynamic Analysis of Al–Ni Intermetallics within the Framework of 3rd Generation CalPhaD Descriptions

Alexander Walnsch, Andreas Leineweber and Mario J. Kriegel

TU Bergakademie Freiberg, Institute of Materials Science, Freiberg, 09599, Germany,
alexander.walnsch@iww.tu-freiberg.de, andreas.leineweber@iww.tu-freiberg.de,
mario.kriegel@iww.tu-freiberg.de

Introduction

The demand for materials with superior structural and functional properties is constantly increasing, which leads to the development of new material systems that can meet these requirements. In this regard, alloy design is becoming increasingly reliant on physically meaningful simulation methods, such as phase field, density-functional theory, and molecular dynamics simulations, as well as Calculation of Phase Diagrams (CalPhaD) calculations.

Currently, a paradigm shift is underway in the CalPhaD approach to achieve an increase in physicality through the introduction of new thermodynamic models. These models are connected to physically reasonable descriptions, such as Einstein functions for heat capacity, instead of simple phenomenological polynomials [1]. This enables the development of a consistent thermodynamic description of solid and liquid phases in a multicomponent system over a wide temperature range.

The purpose of this work is to contribute to this development by introducing a modelling approach that overcomes the drawbacks of the currently adopted models [2]. Specifically, the proposed approach reconsiders the thermodynamic description of crystalline solids in the range of instability and incorporates a physically meaningful description of thermal vacancies, which contribute significantly to the heat capacity at elevated temperatures [3].

To verify the applicability of the proposed models, the Al–Ni system was chosen as a model system due to its combination of two unaries with vastly different melting temperatures and the presence of the high-melting *B*2-ordered intermetallic phase AlNi (see Fig. 1) [4]. This study utilizes additional heat-capacity measurements of the intermediate intermetallic compounds at cryogenic and elevated temperatures, as well as *ab initio* calculations for the metastable and martensitic phases from literature, to generate a holistic and physically meaningful description of the thermodynamics of the Al–Ni system.

Materials and Methods

The heat capacities of *B*2-AlNi and $L1_2$-$AlNi_3$ were experimentally determined to provide a more comprehensive thermodynamic description of the Al–Ni system. The corresponding alloys were prepared by arc-melting in Ar atmosphere using high-purity metal mixtures. The microstructures of the prepared alloys were investigated using complementary methods like electron-backscattered diffraction (EBSD), X-ray diffraction (XRD) and electron-probe microanalysis (EPMA). To measure the heat capacity of the different intermetallics, the three-step continuous method was applied in a power compensated differential-scanning calorimeter in the temperature range of 100 K to 900 K.

Results and Discussion

The stoichiometric intermetallics *B*2-AlNi and $L1_2$-$AlNi_3$ could be successfully produced by arc-melting, and their heat capacity was determined to aid in the development of a comprehensive thermodynamic modelling. Exemplarily, the heat capacity of the $L1_2$ phase is illustrated in Fig. 2 in comparison to the tentatively modeled heat capacity using the presently adopted models.

These models include the hybrid Neumann-Kopp approach, which is based on the thermodynamic data of the individual unary descriptions and combines these with a phase-specific description of the Einstein-contribution to the heat capacity [5]. For that, in order to prevent artifacts, e.g., due to the melting of Al on the heat capacity of the intermediate compounds, the unary descriptions were updated using two-state models and physically based descriptions of thermal vacancies.

Together with the available data in literature, where recently the thermodynamic properties of the peritectically forming phases Al_3Ni and Al_3Ni_2 were investigated [6], a physically meaningful thermodynamic description of the whole system was developed. In addition, special aspects, such as site occupancies for varying chemical compositions and temperatures, were considered in the present thermodynamic description. Hereby, the interplay between constitutional vacancies, anti-site atoms, and thermal vacancies, and their effect on the thermodynamic properties of the phases was a crucial part of the present work. Based on the presently adopted

models, a holistic thermodynamic description of the Al–Ni system was achieved, allowing the prediction of the phase stabilities and thermodynamic properties of stable and metastable phases in this system.
The application of the four-sublattice models for the fcc-based ($L1_0$, $L1_2$) and bcc-based ($B2$, $D0_3$) phases, together with the incorporation of *ab initio* calculations from literature, enabled the consideration of aspects such as the martensitic transformation of AlNi-based $B2$ towards $L1_0$-like states on a physically profound basis, also in compositional regions where these transformations are highly unstable (e.g., for $x_{Al} \geq 50$ at.%). Since these considerations are of immense importance for the description of the transformation behavior of novel Fe–Mn–Al–Ni shape memory alloys, the present thermodynamic description not only further improves the applicability of thermodynamic calculations on prominent applications like superalloys but also opens up new possibilities for novel application fields for the Al–Ni system.

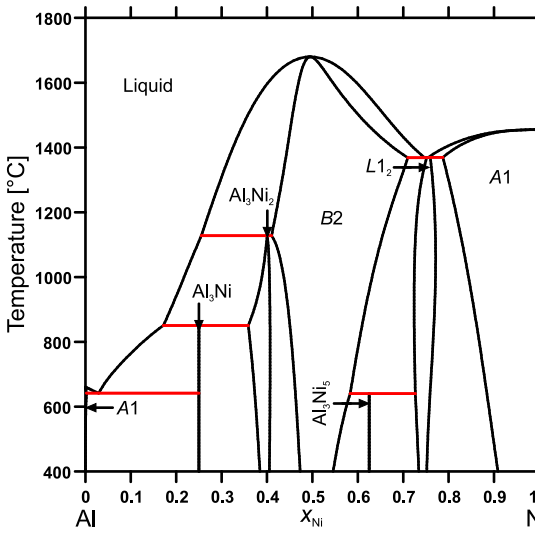

Fig. 1: Exemplary phase diagram of the Al–Ni system, calculated using the thermodynamic description of Ref. [4].

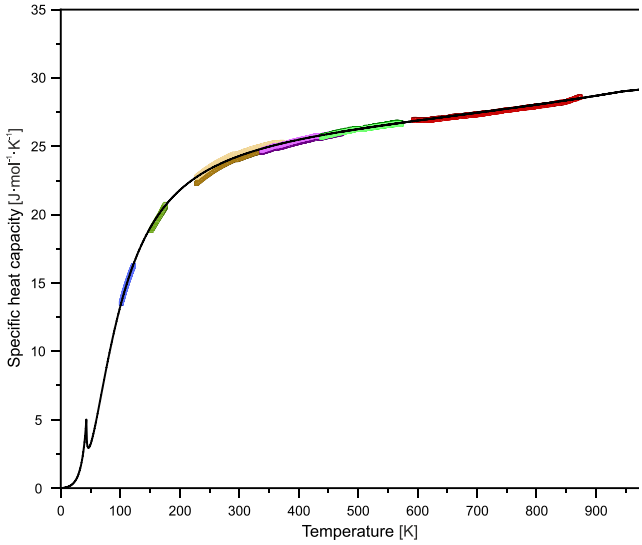

Fig. 2: Calculated heat capacity of $L1_2$-$AlNi_3$ in the indicated temperature range using the present thermodynamic models, illustrated as a black line. The colored points indicate the experimental heat capacity data, determined in the present work.

References

[1] Q. Chen, B. Sundman, Journal of Phase Equilibria. **2001**, *22*, 631-644.
[2] R. Schmid-Fetzer, Journal of Phase Equilibria and Diffusion. **2022**, *43*, 304-316.
[3] A. Obaied, I. Roslyakova, M. To Baben. Scientific Reports, **2022**, *12*, 13385.
[4] I. Ansara, N. Dupin, H. L. Lukas, B. Sundman. Journal of Alloys and Compounds, **1997**, *247*, 20-30.
[5] Z. He, B. Kaplan, H. Mao, M. Selleby. Calphad, **2021**, *72*, 102250.
[6] I. Saenko, H. Engelhardt, P. Hornig, O. Fabrichnaya, S. Lippmann. Calphad, **2021**, *74*, 102294.

SCP7.4

Thermodynamic Modeling of G-phase in Steel using Sparse Modeling

Satoshi Minamoto[1], Toshiaki Horiuchi[2], Takamichi Miyazaki[3] and Hiroshi Abe[3]

[1]National Institute for Materials Science (NIMS), Tsukuba, Ibaraki, 304-0044, Japan,
MINAMOTO.Satoshi@nims.go.jp
[2]Hokkaido University of Science, Sapporo, Hokkaido, 006-8585, Japan
[3]Tohoku University, Sendai, Miyagi, 980-8579, Japan

Introduction

The CALPHAD (Computer Coupling of Phase Diagrams and Thermochemistry) method, a thermodynamic method for calculating phase equilibria, requires hypothetical compound energies and interaction parameters between compounds. In designing the interaction parameters between compounds, only the relationship between the major and minor elements in the sublattice has generally been described. While this simplifies the description of thermodynamic functions, it is problematic because it increases the number of interaction combinations when equal amounts of elements are present in a given sublattice. On the other hand, the full model, a sublattice model that includes all end members using crystallographic information, has been proposed [1]. An advantage of the full model is that the importance of the interaction parameters is reduced, however, the problem is that the design of the parameters becomes difficult due to the extremely large number of combinations. When the amount of experimental data is small, setting a large number of interaction terms can result in an evaluation that overfits the experimental data, leading to an overlearning situation.
The precipitation of the G-phase ($Ni_{16}Mn_6Si_7$) plays an important role in the long-term microstructural stability of steel [2]. Although several thermodynamic models have been reported for the G-phase in steel [3], the distribution of elements in the sublattice remains controversial due to a lack of experimental data.

Methods

In this study, a thermodynamic model with three sublattices reflecting the crystallographic information (*cF*116) of the G-phase was established, and a full model was developed assuming solid solution of six elements (Fe, Cr, Mn, Mo, Ni, Si) in each sublattice. First-principles calculations were performed to obtain data for the end-members, and the description based on the assumption of the Neumann-Kopp rule was added. Several promising interaction parameters were then selected and fitted the experimental data. The fitting was carried out by variable reduction using Ridge and Lasso regression to avoid overfitting the experimental data while selecting important interaction parameters. Figure 1 shows a schematic of the optimization of Ridge regression and higher-order polynomial function. Ridge regression can ensure prediction accuracy outside of the sample points without overfitting the sample points.

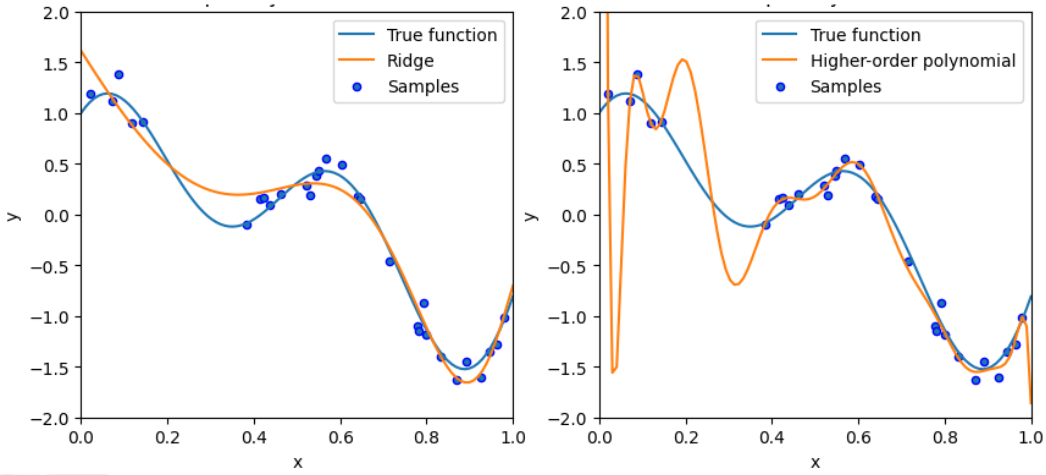

Fig. 1: Schematic of optimizations with Ridge regression (left) and higher-order polynomial (right).

Results and Discussion

As a result, we were able to describe the experimental data without overfitting. This means an ability to describe the thermodynamic function of the G-phase without major parameter changes in specific experimental data or in the future when reference data can be obtained.

The developed thermodynamic database reproduces different solid solution states of the G-phase. First, the difficulty of Fe entering the G-phase was clarified. This result does not support the previous experimental data, however, since the experimental data were obtained using APT and TEM, it is possible that some information of the matrix phase is mixed in. Second, we believe that the Si site is robustly realized with Si as the main element and other elements are difficult to enter the Si site.

Acknowledgement

Part of this work was supported by JSPS KAKENHI Grant Numbers JP19H02472 and MEXT Innovative Nuclear Research and Development Program Grant Number JPMXD0222682225.

References

[1] K. Yaqoob, J.-M. Joubert, J. Solid State Chemistry. **2012**, *196*, 320–325.

[2] X.-F.Guo, Y.-Y. Ni, J.-M. Gong, L.-Y. Geng, J.-Q. Tang, Y. Jiang, X.-K. Jia, X.-Y. Yang, Acta Metall. Sin. (Engl. Lett.). **2017,** *30*, 829–839.

[3] A. Jacob, C. Domain, G. Adjanor, P. Todeschini, E. Povoden-Karadeniz, J. Nucl. Mater. **2020**, *533*, 152091.

SCP8.1R

Predicting stability of TiAl-based BCC high entropy alloys

David Holec, Lukas Hatzenbichler, Stefan Zeisl and Helmut Clemens

Department of Materials Science, Montanuniversität Leoben, Franz-Josef-Straße 18, 8700 Leoben, Austria
david.holec@unileoben.ac.at, lukas.hatzenbichler@unileoben.ac.at, stefan.zeisl@unileoben.ac.atl

Introduction

High Entropy Alloys (HEAs) attracted massive interest in recent years as they are expected to withstand high temperatures and exhibit outstanding properties, such as high hardness, fracture toughness, fatigue, wear, and oxidation, as well as corrosion resistance [1]. HEAs consist of at least five different, often metallic, elements in equiatomic composition [2]. Due to the combination of various elements, one would expect a high affinity for forming intermetallic phases. However, the dominant feature of this material group, namely the high entropy or rather the high configurational entropy contribution, works against the decomposition of the alloy. In the present work, we focus on two sample systems, namely equimolar TiAlNbVMo and TiAlNbVMn alloys, and discuss their phase stability based on first principles calculations and experimental observations.

Materials and Methods

The calculations are based on Density Functional Theory implemented in the VASP package. All chemically disordered systems were modeled using Special Quasi-random Structures (SQS) obtained by the sqsgenerator tool [3]. The energetics were corroborated with coherent potential approximation (CPA) calculations implemented in the EMTO package.

The thermodynamic stability evaluations were based on Gibss energy difference between the high entropy five-component HEA and all possible decompositions into combinations of respective unary, binary, ternary, and quaternary alloys (all with equiatomic compositions), leading to overall 51 routes (see Fig. 1). We have considered all systems as disordered (SQS) structures and having a BCC structure. For the Mn-containing variant, we have additionally considered the hexagonal C14 phase for systems containing Mn.

In addition to the change of mixing enthalpy ΔH_{mix}, various entropy contributions to the Gibbs energy were considered. Most importantly, the change of the vibrational entropy, ΔS_{conf}. Also, strain stabilization due to differences in specific volume, and time effects in the Debye harmonic approximation, were considered.

Further computational details can be found in Ref. [4].

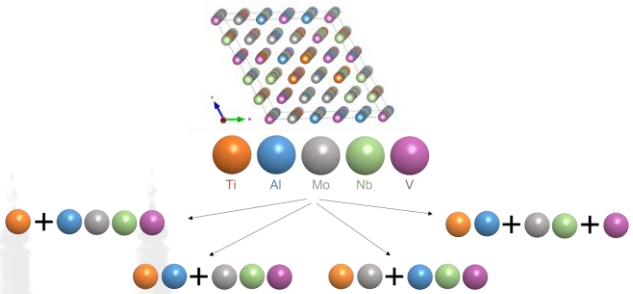

Fig. 1: Schematic figure showing a 125-atomic SQS representing BCC HEA, and 4 possible decomposition routes.

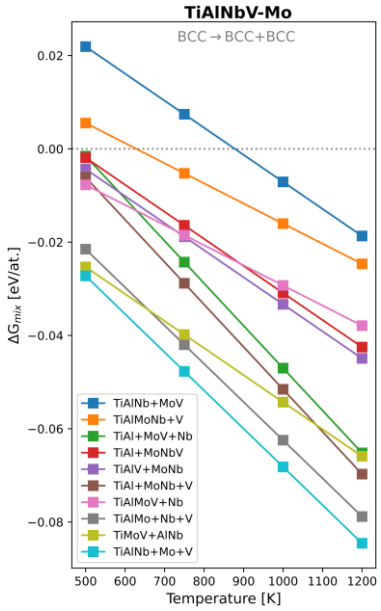

Fig. 2: Change of the Gibbs free energy for various decomposition routes of the TiAlNbVMo BCC HEA. Positive values highlight thermodynamic force for decomposition.

Results and Discussion

As a starting point, the mixing enthalpies of the systems were evaluated at zero temperature. Several elemental combinations yielding stable solid solutions have been identified. The VASP-SQS results are qualitatively confirmed by the EMTO-CPA method.

In the next step, the entropy term has been included in the form of its configurational entropy contribution. This allowed calculating the Gibbs free energy of mixing by implicitly introducing temperature. Hence, an insight into the phase stability could be gained at different temperatures, and the stabilization effect of the configurational entropy was estimated. Our calculations predicted that the BCC TiAlNbVMo HEA was not fully stable down to room temperature (Fig. 2). The TiAlNbVMn HEA exhibited a driving force for decomposition up to more than 1200 K. For this system also the HCP-C14 Laves phase has been considered as a decomposition product, which led to the same conclusion.

Including contributions of vibrational entropy, using the harmonic Debye approximation shifts the transition temperature to lower values. Nonetheless, the effect is not significant enough, and neither TiAlNbVMo nor TiAlNbVMn represented stable BCC HEAs down to room temperature, even with this further stabilization. Moreover, it has been shown that the consideration of vibrational entropy could also lead to a destabilization of the HEAs for specific decomposition routes.

The comparison with experimental methods gave insight into the microstructural evolution of the BCC HEAs. The TiAlNbVMo HEA has been observed to be stable at room temperature after heat treatment. While we could not observe any decomposition effects, a result disagreeing with the theoretical predictions, TiAlNbVMo is proposed to be a kinetically stabilized HEA. Therefore, it has good prerequisites for further alloy development. The experimental outcome for BCC TiAlNbVMn proves the existence of a two-phase BCC+HCP microstructure in accordance with the theoretical results.

References

[1] F. Liu, P. K. Liaw, Y. Zhang, Metals. **2022**, *12*, 501.

[2] M.-H. Tsai, J.-W. Yeh, Materials Research Letters. **2014**, *2*, 107–123.

[3] D. Gehringer, M. Friák, D. Holec, Computer Physics Communications. **2023**, *286*, 108664.

[4] L. Hatzenbichler, S. Zeisl, H. Clemens, D. Holec, Intermetallics. **2023**, *158,* 107893.

SCP8.2

Growth, structural characterization, DFT study, and magnetic properties of {Sc,Nd,Sm}AuIn intermetallics

V.V. Romaka[1], M.L. Amigó[1], C.G.F. Blum[1], D. Franco[2,3], L.T. Corredor[1], S. Wurmehl[1], B. Büchner[1] and S. Seiro[1]

[1]Leibniz Institute for Solid State and Materials Research (IFW) Dresden, Helmholtzstr. 20, 01069 Dresden, Germany, v.romaka@ifw-dresden.de

[2] Max Planck Institute for Chemical Physics of Solids, Nöthnitzer Str. 40, 01187 Dresden, Germany

[3]Centro Atómico Bariloche and Instituto Balseiro, Comisión Nacional de Energía Atómica (CNEA), Universidad Nacional de Cuyo, Consejo Nacional de Investigaciones Científicas y Técnicas (CONICET), Av. E. Bustillo 9500, R8402AGP San Carlos de Bariloche, Río Negro, Argentina

Introduction

Series of equiatomic RTX compounds, where R – rare-earth element, T – transition d-metal, and X – p-block element were attracting attention for decades caused by their intriguing magnetic properties [1]. Quite recently, the interest was revoked to the RAuIn intermetallics [2,3] with non-centrosymmetric hexagonal ZrNiAl-type structure (an ordered ternary variant of the Fe_2P-type), where in the case of antiferromagnetic coupling between nearest neighbors, the frustration of the magnetic interactions is induced by this topology leading to potential magnetic texture formation. Magnetic ordering was observed for almost all RAuIn compounds with magnetic rare-earths, except Sm, Pr, and Nd, despite the negative Weiss parameter for Pr and Nd [4] suggesting the presence of strong magnetic frustration. In the present work, we report growth, DFT study, and magnetic properties of NdAuIn and SmAuIn, accompanied by the detailed characterization of the new representative of the RAuIn series - ScAuIn compound.

Materials and Methods

Pure elements in form of Sc, Nd, and Sm pieces (99.9%), Au bars (99.999%), and In pieces (99.999%) were used for the preparation of alloys by conventional arc-melting technique followed by annealing in a vacuum at 500 (2 weeks), 600 (2 weeks), and 800°C (1 week) and water quenching. All samples were characterized by the standard powder XRD, SEM/EDX, and DTA methods described in [5]. For the crystal growth of NdAuIn, a feed rod cast using a Hukin-type copper water-cooled crucible was used. The FZ crystal growth process with radiation heating was performed in a vacuum chamber under a flowing Ar atmosphere resulting in the NdAuIn single crystals of about 5 mm in diameter and 30 to 40 mm in length. The orientation of single crystals was determined by the X-ray Laue back-scattered method. Single-crystal XRD data were collected using the complete sphere mode at 100, 200, and 300 K.

The DFT calculations were carried out with the Vienna Ab initio Simulation Package VASP v.5.4.4 (PAW-type potentials w/ and w/o spin-orbit coupling) and Elk v4.3.06 – all-electron FP-LAPW code. The Perdew-Burke-Enzerhoff exchange-correlation functional in the generalized gradient approximation (GGA) was used. Full geometry relaxation (atomic positions as well as lattice parameters) was achieved to calculate the enthalpy of formation. For machine learning, the support vector machines method (both classification and regression) was used. Magnetization measurements down to 1.8 K on a crystal were carried out in a SQUID-VSM from Quantum Design. All field-dependent measurements were done after a zero-field cooling procedure (ZFC). Further magnetic measurements in the temperature range of 0.43–2.5 K were performed using SQUID equipped with an IHELIUM3 option. Specific heat was measured from 1.8 K to room temperature.

Results and Discussion

A crystal of NdAuIn was successfully grown using the optical floating zone technique. Single-crystal, powder XRD and SEM/EDX analysis confirmed that NdAuIn adopts a hexagonal ZrNiAl-type structure (space group *P*-62*m*) with almost equiatomic composition. The crystals extracted from as-cast alloys have a prismatic shape with a hexagonal cross-section and their morphology is in good agreement with the modeled using the Bravais-Friedel, Donnay-Harker (BFDH), which indicated the presence of {10-10} prism and {0001} basal pinacoid open forms. DTA analysis revealed that the NdAuIn phase melts congruently at 1136°C. The unit cell volume of NdAuIn linearly increases with temperature in the 100-300 K temperature range giving a thermal expansion coefficient (α) of $4.1(3)\times10^{-5}$ K^{-1}. Several crystals of a cubic/rectangular shape were cut from the main crystal after orientation using the Laue method (Fig. 1). The experimentally derived density of the NdAuIn crystals of 10.53(4) g/cm^3 appeared to reach 98.9% from the theoretical (d_x = 10.652 g/cm^3).

A new representative of the RAuIn series was discovered in the Sc-Au-In system with a crystal structure that differs from other RAuIn compounds. The new ScAuIn compound was predicted to crystallize in the HfRhSn-type

structure (space group *P*-62*c*) by using the support vector machines classification method. The predicted lattice parameters appeared to be close to experimentally obtained after crystal structure determination from powder XRD data using a replica exchange MCMC sampling. The HfRhSn-type structure of ScAuIn could be derived from the ZrNiAl-type through group-subgroup relations (*P*-62*m* → k2 → *P*-62*c*).
DFT modeling of the NdAuIn compound was performed w/ and w/o spin-orbit coupling (soc) with semi-core f-electrons treated as core states. The calculated values of the enthalpy of formation (−742.846 meV/atom w/o soc, −774.192 meV/atom w/ soc) are rather close but both are less negative in comparison to the ScAuIn phase (-910.315 meV/atom) [5]. To shed more light on the bonding of NdAuIn and ScAuIn and check our assumption about their polarity nature, the calculations of the charge density, its difference, and electron localization function (*elf*) were performed. A strong deficit of the charge density on the Nd atoms, and an excess of the charge density on the Au1 and Au2 atoms, which form strong bonding with the nearest In atoms are observed. Bader charge analysis revealed the following net atomic charges: Nd (+1.426), Au1 (−1.316), Au2 (−1.479), In (−0.001). The obtained charge redistribution among the elements in the NdAuIn compound is in good agreement with the difference in electronegativity (Pauling scale) of the constituents: χ(Nd) = 1.14, χ(Au) = 2.54, χ(In) = 1.78, where the Au atoms as the most electronegative attract electron density, while the Nd atoms as the least electronegative - lose it. Analysis of the density of electronic states distribution of ScAuIn, NdAuIn, and SmAuIn reveals the absence of the band gap near the Fermi level (E_F) predicting its metallic type of conductivity. The theoretically derived Sommerfeld constant for the ScAuIn compound is = 2.85 mJ/K^{2}mol.

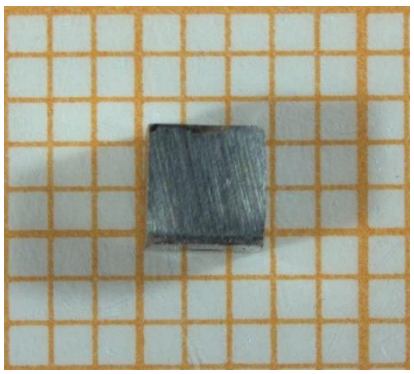

Fig. 1: The oriented and cut along the 6-fold hexagonal axis crystal of NdAuIn.

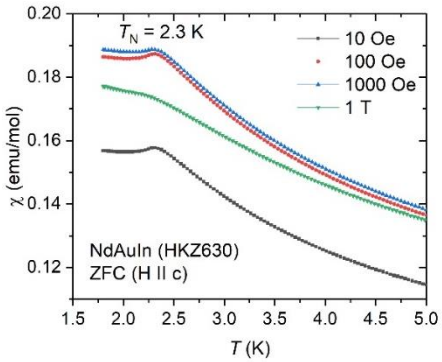

Fig. 2: Molar magnetic susceptibility of the NdAuIn crystal with the field parallel to the six-fold axis (H || c)

Magnetization measurements of the NdAuIn crystal (Fig. 2) with the field parallel and perpendicular to the six-fold axis of the crystal revealed that NdAuIn is a Curie-Weiss paramagnet down to 25 K. The calculated effective magnetic moment is 3.61(1) and 3.64(1) μ_B/Nd for the magnetic field parallel and perpendicular to the six-fold axis of the crystal, with Weiss parameters of -0.562 and -17.044 K, respectively. The compound exhibits antiferromagnetic ordering at 2.3 K (H || c) and 2.5 K (H ⊥ c), which agrees with the specific heat results. Crystals of the SmAuIn intermetallic also reveal Curie-Weiss behavior with antiferromagnetic ordering at T_N = 7.1 K. ScAuIn is a Pauli paramagnet with magnetic susceptibility of ~6×10^{-5} emu/mol (300 K). The Sommerfeld coefficient γ of 2.8 mJ/K^{2}mol derived from the specific heat measurements is comparable with that obtained from the DFT calculations. The distortion of the triangular rare-earth sublattice introduced in the HfRhSn-type structure can be expected to strongly influence the magnetic behavior, in particular considering the tendency to magnetic frustration effects in RTX compounds.

The authors thank U. Nitzsche for technical assistance in running the DFT calculations on the ITF/IFW compute cluster. This work was supported by the BMBF UKRATOP project (01DK18002), DFG Collaborative Research Center SFB1143 (project B01, project-id 247310070), M.L.A. acknowledges support from the Alexander von Humboldt Foundation through the Georg Forster program. L.T.C. is funded by the DFG (project-id 456950766).

References

[1] A. Szytula, Handbook of Magnetic Materials, North-Holland, Amsterdam. **1991,** 85.
[2] D. Rossi, R. Ferro, V. Contardi, R. Marazza, Zeitschrift für Metallkunde. **1977**, *68*, 493-494.
[3] A.E. Dwight, Proc. of the Rare Earth Research Conference, 12th, Colorado. **1976**, *1*, 480-489.
[4] Ł. Gondek, A. Szytuła, D. Kaczorowski, Ya. Kalychak, B. Penc, J. Hernandez-Velasco, Yu. Tyvanchuk, Chemistry of Metals and Alloys. **2008**, *1*, 92-96.
[5] V.V. Romaka, M.L. Amigó, D. Franco, L.T. Corredor, S. Wurmehl, B. Büchner, S. Seiro, Journal of Solid State Chemistry. **2022,** *314*, 123416.

SCP8.3

Twinning in tetragonal intermetallics – *ab initio* study

Martin Heczko[1], Martin Zelený[1], Petr Šesták[2], Andriy Ostapovets[3] and Tomáš Kruml[3]

[1]Institute of Material Sciences and Engineering, Faculty of Mechanical Engineering, Brno University of Technology, Technická 2896/2, Brno, CZ-61669, Czech Republic, martin.heczko1@vutbr.cz, zeleny@fme.vutbr.cz

[2]Institute of Physical Engineering, Faculty of Mechanical Engineering, Brno University of Technology, Technická 2896/2, Brno, CZ-61669, Czech Republic, sestak@fme.vutbr.cz

[3]Institute of Physics of Materials, Czech Academy of Sciences, Žižkova 513/22, Brno, CZ-61600, Czech Republic, ostapov@ipm.cz, kruml@ipm.cz

Introduction

Mechanical twinning is one of the most common deformation mechanisms, which plays significant role in perspective functional materials e.g., shape memory alloys. This kind of deformation occurs, when local shear stress, i.e., twinning stress, is large enough for a twin to nucleate and propagate [1]. For theoretical estimation of twinning stress, general planar fault energy curves (GPFE) minima and maxima can be used [2]. These curves represent energies during twin nucleation in the form of intrinsic stacking fault (ISF) and its consequent growth. The theory of mechanical twinning is very well developed for cubic and hexagonal materials [3], in which this type of deformation occurs often due to high strain rate or limited dislocation slip at low homologous temperatures or when the number of slip systems is limited. Mechanical twins can be observed also in fcc materials with low stacking fault energy [4]. Here, Shockley partial dislocations on $(\bar{1}11)$ planes with Burgers vector $\vec{b}$ equal to $a/6 \cdot [\bar{1}12]$ are responsible for shearing crystal planes into mirrored positions. In face-centred materials, where *c*/*a* ratio differs from 1, such as Ni_2MnGa or Ni_2FeGa shape memory alloy martensites, the situation is complicated due to geometrical reasons, as $\vec{b} = a/6 \cdot [\bar{1}12]$ does not lead to perfect mirror positions. Hence, the scaling factor different than 1/6 have been developed recently and is equal to previously reported shear deformation [4]. The final shearing vector is given by formula [5]:

$$\vec{s} = \frac{1}{2}\left(\frac{2(c/a)^2 - 1}{2(c/a)^2 + 1}\right) \cdot [\bar{1}12]. \qquad (1)$$

Here we present GPFE curves of three intermetallic materials: γ-TiAl, Ni_2MnGa and Ni_2FeGa with different *c*/*a* ratios to show the effect of tetragonality. The effect of structural optimization during shear deformation was studied as well.

Materials and Methods

We performed calculations using the spin-polarized DFT method implemented in the Vienna Ab Initio Simulation Package (VASP) [6]. The electron-ion interaction was described by the potential based on projector augmented-waves [7, 8]. The electron exchange and correlation energy were treated within the generalized gradient approximation in the Pedrew-Burke-Ernzerhof formalism [9].

In this study, we considered three different intermetallic materials – γ-TiAl, a material widely used in aerospace due to its low density and high corrosion and heat resistance, which exhibits *c*/*a* = 1.016. Thus, using the Eq. 1, $|\vec{s}|/|\vec{b}|$ ratio is equal to 1.06. As the counterpart with c/a < 1, Ni_2FeGa ferromagnetic shape memory alloy was used. *c*/*a* ratio of this material is 0.953 and $|\vec{s}|/|\vec{b}|$ is equal to 0.87. As a representative of even lower c/a ratio, namely 0.801, the non-modulated martensite of Ni_2MnGa ferromagnetic shape memory alloy represented by tetragonally deformed $L1_0$ structure was chosen. $|\vec{s}|/|\vec{b}|$ of this alloy is 0.663

All three compounds were modelled by monoclinic supercell with 32 atoms in 8 $(\bar{1}11)$ layers. After structural optimization of the lattices the GPFE curves were calculated by shearing *n* successive $(\bar{1}11)$ layers in a supercell along the $[\bar{1}12]$ direction in similar way as explained for example in Ref. [2]. The minimum corresponding to ISF was found by continuous translating (sliding) layers 5–8 relative to layers 1–4 about $1/14\vec{b}$. The two-layer and three-layer twins were obtained by further translating (sliding) of layers 6–8 and 7–8, respectively, starting from the minimum estimated in the previous step.

Results and Discussion

In γ-TiAl alloy, the theoretical values of shearing vector are in perfect agreement with our calculations, when the structure is not optimized. The $|\vec{s}|/|\vec{b}|$ ratio is equal to 1.06 independently on twin thickness, which is very close to the predicted value. The optimization changes the situation on ISF, where the $|1\vec{s}|/|\vec{b}|$ shortens to 1.00 which is slightly lower value than expected. The shortening does not appear for wider twins, where average $|\vec{s}|/|\vec{b}|$ is

still equal to 1.06. In the case of γ-TiAl, tetragonality of the lattice has very limited impact, because the deviation of $\vec{s}$ from $\vec{b} = 1/6[\bar{1}12]$ is negligible.

The non-optimized GPFE curve of Ni_2FeGa displayed on Fig. 1(a) exhibits minimum for ISF at $|\vec{s}|/|\vec{b}|$ equal to 0.87 which corresponds very well to the predicted value. The magnitude of $\vec{s}$ decreases even more for wider twins, as the values of $|2\vec{s}|/|\vec{b}|$ and $|3\vec{s}|/|\vec{b}|$ are smaller than predicted values of 1.74 and 2.61, respectively. Structural optimization results in the increased magnitude of $\vec{s}$. However, the optimized twins magnitudes of $\vec{s}$ never reach the integer numbers, the energies of optimized and non-optimized twins are very different too. This may be caused by disadvantageous geometry of ideal twin boundary. Although the energy of thicker twins should converge to a constant value which is further independent on the twin thickness as can be seen in the case of γ-TiAl, the energy of three-layer twin in Ni_2FeGa is about 25% bigger, then energies of ISF and two-layer twin. It indicates a strong mutual interaction of twin boundaries for twins with small thickness.

The situation becomes even more complicated in similar ferromagnetic shape memory alloy – non-modulated martensitic phase of Ni_2MnGa alloy, depicted on Fig. 1(b). Here, the non-optimized ISF occurs at $|1\vec{s}|/|\vec{b}|$ = 0.79, which is much more than expected value of 0.663. Then, the values of $|2\vec{s}|/|\vec{b}|$ and $|3\vec{s}|/|\vec{b}|$ are 1.28 and 1.90 respectively, slightly lower than predicted. Optimization of internal parameters leads to even higher $|1\vec{s}|/|\vec{b}|$ of ISF = 0.91. This effect is much less significant for wider twins. In this material the interaction of adjacent twin boundaries results in even higher stability of two-layer twin than detwinned structure [10].

To summarize our work, here the completely new approach is applied on Burgers vector calculations. Rescaled Burgers vectors are very precise in the case of γ-TiAl alloy and are acceptable for wider twins of investigated shape memory alloys. However, their intrinsic stacking faults need to be examined carefully, as the ideal twin geometry is not energetically advantageous. Structural relaxation also has non-trivial effect on GPFE minima position.

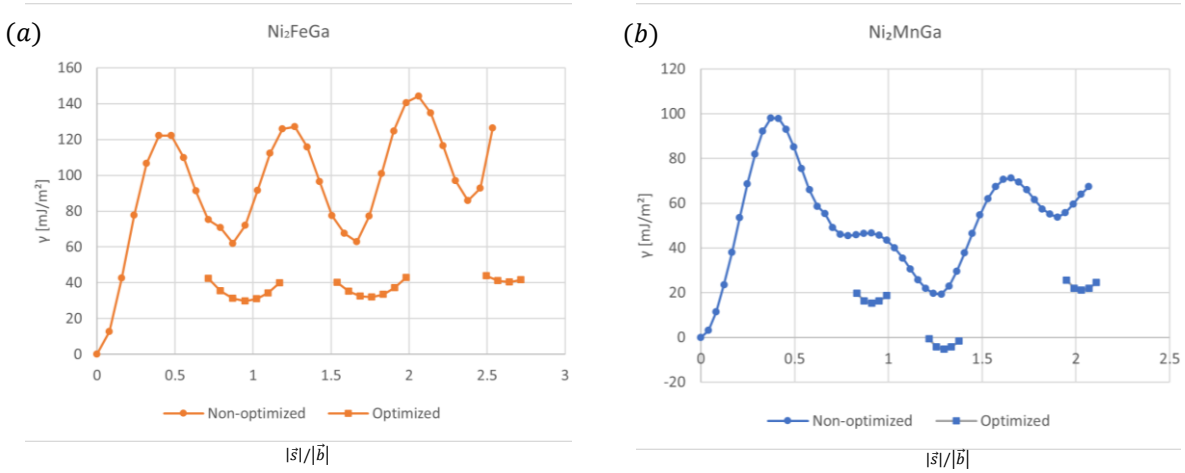

Fig. 1: Comparison of Ni_2FeGa (a) and Ni_2MnGa (b) GPFE curves

Acknowledgement

The authors acknowledge the Czech Science Foundation for the financial support within the Project No. 21-06613S. The theoretical calculations were performed at the IT4I facilities, which are supported through the project e-INFRA CZ [ID:90140].

References

[1] P.M. Anderson, J.P. Hirth, J. Lothe, Theory of Dislocations, 3rd ed., Cambridge, University Press, Cambridge, England, **2017**.
[2] J. Wang, H. Sehitoglu, Acta Materialia, **2013**, *61*, 6790–6801.
[3] J. Wang, J.P. Hirth, C.N. Tomé, Acta Materialia, **2009**, *57*, 5521–5530.
[4] J.W. Christian, S. Mahajan, Progress in Materials Science, **1995**, *39*, 1–157.
[5] M. Zelený, A. Ostapovets, L. Fridrich, P. Šesták, M. Heczko, T. Kruml, Philosofical Magazine, **2023**, *103*, 119–136.
[6] G. Kresse, J. Furthmüller, Physical Review B, **1996**, *54*, 11169.
[7] G. Kresse, J. Furthmüller, Computational Material Science, **1996**, *6*, 15.
[8] P. E. Blöchl, Physical Review B, **1994**, *50*, 17953.
[9] J. P. Perdew, K. Burke, M. Ernzerhof, Physical Review Letters, **1996**, *77*, 3865.
[10] M. Zelený, L. Straka, A. Sozinov, O. Heczko, Physical Review B, **2016**, *94*, 224108.

SCP8.4

Ab initio Investigation of Intermetallic Phases in the Ge-Mg-Sn Ternary System

Ondřej Fikar[1], Martin Zelený[1, 2]

[1]Faculty of Mechanical Engineering, Brno University of Technology, Brno, Czech Republic,
Ondrej.Fikar@vutbr.cz, Zeleny@fme.vutbr.cz
[2]Institute of Physics of Materials, Czech Academy of Sciences, Žižkova 22, Brno 616 00, Czech Republic

Introduction

Ge-Mg-Sn is a perspective system that has been recently given attention for its potential thermoelectric, photovoltaic or even medical application [1-3]. In the binary subsystems there are two intermetallic compounds present, namely Mg_2Ge and Mg_2Sn, which have the same anti-fluorite crystal lattice [4]. Also, a hexagonal ternary intermetallic compound $Mg_6Ge_1Sn_2$ has been reported to be very close above the Mg_2Ge-Mg_2Sn convex hull [5]. The stability of this ternary intermetallic with temperature has not been studied yet, which is the main objective of this work to investigate. Also, the composition of this metastable ternary compound lies directly in the quasi-binary diagram Mg_2Ge-Mg_2Sn, which has been investigated as well to assess the solubility in the binary intermetallics.

Methods

This work was carried out using *ab initio* methods based on Density Functional Theory (DFT) [6] and phonon calculations. DFT calculations were performed using Vienna Ab Initio Simulation Package [7, 8] to investigate the energy of all phases at 0 K. The exchange-correlation energy was approximated using Generalized Gradient Approximation (GGA) with the parametrization of Perdew, Ernzerhof and Burke (PBE) [9]. Projector Augmented Waves (PAW) [10, 11] were used to describe the set of basis functions. The temperature dependent energy contributions were calculated using Phonopy [12]. Vibrational Helmholtz energy was determined using finite-displacement method and the energy contribution of thermal expansion was calculated from quasi-harmonic approximation.

The plane-wave energy cut-off for Mg_2Ge and Mg_2Sn was set to 600 eV and a 10x10x10 k-point mesh was used. To calculate the forces acting on atoms within the finite-displacement method supercells containing 96 atoms with a mesh of 15x15x15 points for subsequent phonon calculations were used for both binary intermetallics. In case of the ternary intermetallic compound the energy cut-off of 600 eV and the k-point mesh of 8x8x18 points were used. Supercell for this compound contains 108 atoms and the mesh for phonon calculations comprise of 11x11x26 points. The supercell approach was employed as well to create a model for solid solubility calculation. In both 96-atom supercells of Mg_2Ge and Mg_2Sn one atom (or two atoms) of Ge was substituted with an Sn atom and vice versa. The inclination to form a substitutional solid solution can be approximately assessed from these supercells.

In order to assess the phase stability, the energy of formation E_f was calculated for all investigated phases, including the solid solution supercells, as:

$$E_f^{ABC} = E_{tot}^{ABC} - (x(A)E_{tot}^{A} + x(B)E_{tot}^{B} + x(C)E_{tot}^{C}), \quad (1)$$

where the *ABC* denotes a general intermetallic phase, E_{tot} denotes total energies of the intermetallic phase and pure elements it consists of, and *x(A)*, *x(B)* and *x(C)* are molar fractions of respective elements contained in the intermetallic phase.

Results and Discussion

All three intermetallic phases (Mg_2Ge, Mg_2Sn, $Mg_6Ge_1Sn_2$) as well as solid solution supercells and all pure elements for reference were investigated using the methods mentioned in the previous section. From calculations at 0 K using Eq. 1, it has been confirmed that both binary intermetallic phases are significantly more stable than the respective pure elements as well as the metastable nature of the ternary $Mg_6Ge_1Sn_2$ [5, 13]. To illustrate this confirmation, the energies of formation E_f of these intermetallics related to the pure elements are shown in Fig. 1. The dashed line in the Fig. 1 represents the Mg_2Ge-Mg_2Sn convex hull. Additionally, the formation energies of solid solutions are included in the Fig. 1.

The energy of solid solution supercell on the side of Mg_2Ge lies 1,3 meV/atom above the convex hull. This indicates that at 0 K this solid solution is not stable, but it is close enough to the convex hull it should easily

stabilize with increasing temperature. On the other hand, the energies of formation of solid solution supercells containing one or two substitutional Ge atoms in Mg_2Sn lie 0,06 and 1,2 meV/atom above the convex hull respectively. A difference this small suggests a limited solubility starts to appear at very low temperatures on this side of the quasi-binary diagram. These results are in good agreement with current, admittedly quite limited, understanding of this quasi-binary system [14, 15]. A further investigation of this system is planned in order to predict the solvus lines.

Temperature dependent thermodynamical quantities were calculated using the finite displacement method and quasi-harmonic approximation. As an example, heat capacities at constant volume for selected intermetallic phases are shown in the Fig. 2. The heat capacities of the solid solutions follow the respective binary intermetallics very closely, which should be expected, because of very similar chemical composition. Overall, the results for binary intermetallics agree very well with previously published experimental and theoretical works [13, 16, 17].

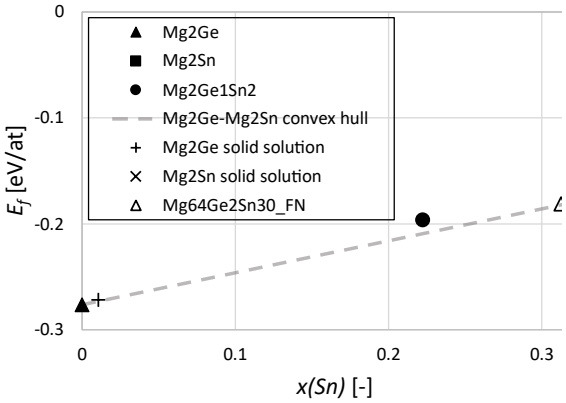

Fig. 1: Energies of formation E_f of investigated phases.

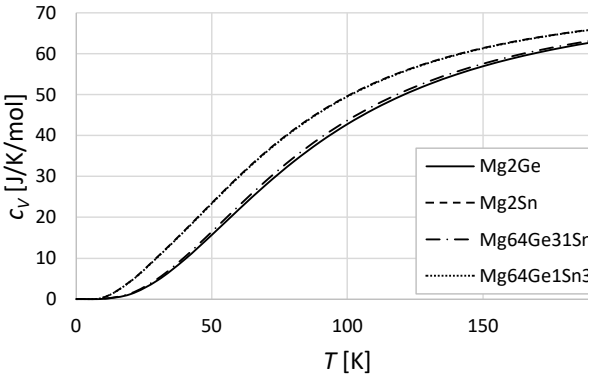

Fig. 2: Calculated heat capacities at constant volume of selected phases.

Acknowledgement
The authors acknowledge the Czech Science Foundation for the financial support within the Project No. 22-22187S. The theoretical calculations were performed at the IT4I facilities, which are supported through the project e-INFRA [ID:90140].

References

[1] J. de Boor et al., Acta Materialia. **2016**, *120*, 273-280.
[2] Y.-Q. Zhou et al., J. of Materials Chemistry A. **2021**, *9*, 6955-6961.
[3] X. Wei et al., J. of Alloys and Compd. **2023**, 169813.
[4] G. Grosch and K.-J. Range, J. of Alloys and Compd. **1996**, *235*, 250-255.
[5] A. Jain et al., APL Materials. **2013**, *1*, 011002. Data retrieved from Materials Project for Mg6Sn2Ge (mp-1222093) from database version v2022.10.28.
[6] P. Hohenberg and W. Kohn, Phys. Rev. **1964**, *136*, B864-B871.
[7] G. Kresse and J. Hafner, Phys. Rev. B. **1993**, *47*, 558-561.
[8] G. Kresse and J. Furthmüller, Phys. Rev. B. **1996**, *54*, 11169-11186.
[9] J. Perdew, K. Burke, M. Ernzerhof, Phys. Rev. Lett. **1996**, *77*, 3865-3868.
[10] P. E. Blöchl, Phys. Rev. B. **1994**, *50*, 17953-17978.
[11] G. Kresse and D. Joubert, Phys. Rev. B. **1999**, *59*, 1758-1775.
[12] Atsushi Togo and Isao Tanaka, Scr. Mater. **2015**, *108*, 1-5.
[13] S. Ganeshan et al., Journal of Alloys and Compd. **2010**, *498*, 191-198.
[14] E. S. Makarov et al., Izv. Akad. Nauk SSSR. **1966**, *2*, 2116-2119.
[15] I. H. Jung and J. Kim, Journal of Alloys and Compd. **2010**, *494*, 137-147.
[16] B. C. Gerstein et al., J. Phys. Chem. Solids. **1966**, *27*, 1161-1165.
[17] F. J. Jelinek et al., J. Phys. Chem. Solids. **1967**, *28*, 267-270.

SCP9.1R

Microstructure design of Nb_2Co_7-Co dual-phase alloys utilizing metastable $L1_2$ Co_3Nb

Toshiaki Horiuchi[1], Konatsu Yamada[1], Takamichi Miyazaki[2], Yuheng Liu[3], Masanori Enoki[4], Hiroshi Ohtani[5], Seiji Miura[6] and Frank Stein[7]

[1]Hokkaido University of Science, 006-8585 Sapporo, Japan, horiuchi@hus.ac.jp, 9222003@hus.ac.jp
[2]Tohoku University, 980-8579 Sendai, Japan, takamichi.miyazaki.a5@tohoku.ac.jp
[3]Osaka University, 565-0871 Suita, Japan, yuheng.liu@mat.eng.osaka-u.ac.jp
[4]Shimane University, 690-8504 Matsue, Japan, masanori.enoki@mat.shimane-u.ac.jp
[5]Toyota PCRI, 480-1192 Nagakute, Japan, otani@toyotariken.jp
[6]Hokkaido University, 060-8628 Sapporo, Japan, miura@eng.hokudai.ac.jp
[7]Max-Planck-Institut für Eisenforschung GmbH, 40237 Düsseldorf, Germany, f.stein@mpie.de

Introduction

The binary intermetallic compound Nb_2Co_7 has a complex monoclinic layered crystal structure with a space group of C2/*m*, *m*C18 [1]. Authors have recently elucidated that Nb_2Co_7 is classified into a novel crystalline type named "mille-feuille structure" (MFS) material that exhibits excellent mechanical properties due to kink formation during compressive deformation [2]. Authors have also clarified that Nb_2Co_7-Co solid solution dual-phase microstructure can be obtained in the Co-Nb binary system by appropriate heat treatment, and it is expected to be applied as a hybrid-type MFS material. On the other hand, a metastable $L1_2$ Co_3Nb phase has been found to form in the Co-Nb binary system [3]. However, the phase stability of $L1_2$ Co_3Nb and its influence on the subsequent microstructure evolution have been poorly understood. In the present study, various Co-Nb binary alloys are investigated both experimentally and theoretically to evaluate the phase stability of $L1_2$ Co_3Nb and the potential for microstructure design by utilizing it.

Materials and Methods

A Co-3.9 at% Nb alloy was cast into a *f*20mm cylindrical ingot, and *f*3×3mm cylindrical samples were cut out. The samples were solution heat-treated (SHT) at 1240°C for up to 10h in a differential thermal analyzer (DTA) to attain a single-phase fcc-Co solid solution. Subsequently, the samples were subjected to isothermal heat treatments at 700/900/1000°C for up to 3000h to promote various phase transformations and precipitation processes. Microstructure and crystal structure were investigated by scanning electron microscopy (SEM), transmission electron microscopy (TEM), X-ray diffraction (XRD), and electron backscatter diffraction (EBSD).
For the computational study, 264 fcc-based ordered structures were prepared, and their structure energies were evaluated by first-principles calculations. Effective cluster interaction (ECI) energies of many-body clusters were then estimated by the cluster expansion method. The metastable phase diagram of the fcc phase in the Co-Nb binary system was constructed by introducing these ECI energies directly into the Monte Carlo method. A grand canonical ensemble that fixes chemical potentials was applied to calculate phase boundaries. On the other hand, thermodynamic quantities such as internal energy were evaluated by the canonical ensemble.

Results and Discussion

During cooling from SHT at 1240°C to room temperature, a prominent DTA exothermic peak is observed in the Co-3.9 at% Nb alloy at 791°C, although there is no phase boundary in the equilibrium phase diagram. The microstructure after the SHT appears as a single-phase fcc-Co solid solution without any visible precipitates observed by SEM. However, a detailed high-resolution TEM analysis reveals that it contains finely dispersed $L1_2$-ordered regions with a significantly increased Nb content, while Nb-depleted regions only show a basic fcc structure, as shown in Fig. 1 [3]. Although the boundaries of the $L1_2$-ordered regions are indistinct, the $L1_2$ ordering is also confirmed by XRD. These results indicate that the $L1_2$ ordering from Nb supersaturated fcc-Co solid solution occurs at 791°C.
$L1_2$ Co_3Nb is estimated as the most stable structure at the composition of Co-25 at% Nb by the first-principles calculations at the ground state. A clustering of the $L1_2$-ordered Co_3Nb regions is also confirmed at the initial stage of aging in Co-4 at% Nb alloy by the Monte Carlo simulation. Figure 2 shows the calculated metastable phase diagram of the fcc phase in the Co-Nb binary system determined by the Monte Carlo method. Red circles are the phase boundaries calculated by the grand canonical ensemble, while blue triangles represent the order-disorder transition points calculated from peaks of differential values of the internal energies, which are determined by the canonical ensemble. In the Co-3.9 at% Nb alloy, the experimentally observed clusters shown in Fig. 1 should be related to the $L1_2$ Co_3Nb in the fcc-Co matrix because the experimentally observed order-disorder transition temperature of 791°C (1064K) is located in the fcc-$L1_2$ Co_3Nb dual-phase region in the calculated metastable phase diagram. Therefore, the calculated results are consistent with the experimental

ones. However, the calculated order-disorder transition point for the Co-4 at% Nb alloy is 1205K. The discrepancy between the experimental and calculated results is probably due to the undercooling effect of DTA and the inappropriate evaluation of ECIs, which will be modified in future works.
During isothermal heat treatment, the equilibrium Nb_2Co_7 phase forms with a plate-like morphology, having a specific crystallographic orientation relationship with the hcp-Co matrix. The microstructure of the samples in which $L1_2$ Co_3Nb is formed before isothermal heat treatment is much finer than that of the samples without forming $L1_2$ Co_3Nb, indicating that Co_3Nb acts as a nucleation site for Nb_2Co_7. Therefore, the Nb_2Co_7-Co solid solution dual-phase microstructure is expected to be extensively controlled by utilizing metastable $L1_2$ Co_3Nb.

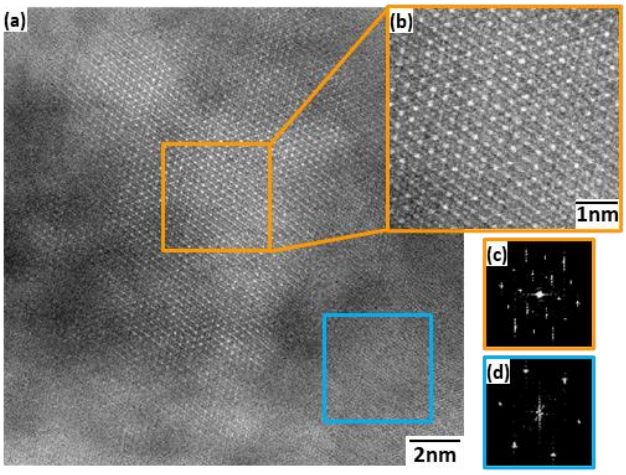

Fig. 1: (a) HAADF-STEM image of Co-3.9 at% Nb alloy after SHT at 1240°C, (b) magnified image of the area marked with the orange square, (c) respective FFT image, (d) FFT image from the area marked with the blue square in (a) [3].

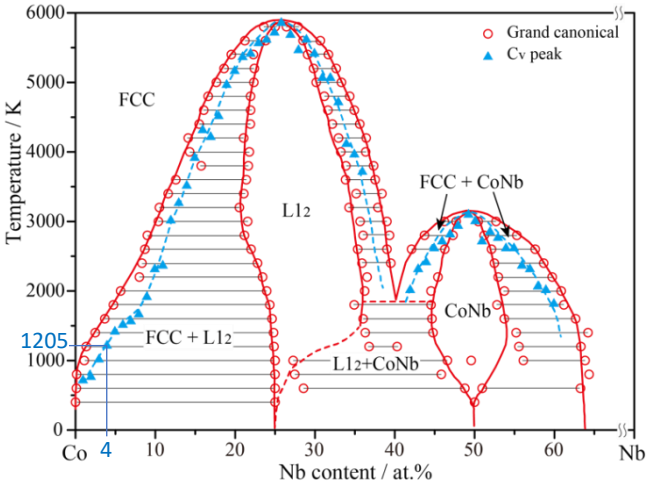

Fig. 2: Metastable phase diagram of the fcc phase in the Co-Nb binary system determined by the Monte Carlo method.

Acknowledgments
The authors thank Mr. Shunsuke Taniguchi, Dr. Christian Liebscher at MPIE, and Mr. Kenji Ohkubo at Hokkaido University for their works and valuable comments. A part of this work was supported by a grant from JSPS KAKENHI for Scientific Research on Innovative Areas “MFS Materials Science” (Grant Numbers JP18H05482) and “Advanced Research Infrastructure for Materials and Nanotechnology in Japan (ARIM)” (Proposal Number JPMXP1222HK0068) of the Ministry of Education, Culture, Sports, Science and Technology (MEXT).

References
[1] A. Leineweber, G. Kreiner, D. Grüner, R. Dinnebier, F. Stein: Intermetallics, **2012**, 25, 34-41.
[2] T. Horiuchi, K. Yamada, S. Saito, K. Ikeda, S. Miura, F. Stein: Materials Transactions, **2023**, 64, 1622-1630.
[3] T. Horiuchi, F. Stein, K. Abe, K. Yamada: Proc. Intermetallics 2017, Bad Staffelstein, Germany, **2017**, 142-143.

SCP9.2

Compressive deformation behavior of Nb_2Co_7-Co solid solution dual-phase alloys

Konatsu Yamada[1], Toshiaki Horiuchi[2], Shigeru Saito[2], Ken-ichi Ikeda[3], Seiji Miura[3] and Frank Stein[4]

[1]Division of Engineering, Hokkaido University of Science, 006-8585 Sapporo, Japan, 9222003@hus.ac.jp
[2]Laboratory of Advanced Materials for Cold Region, Hokkaido University of Science, 006-8585 Sapporo, Japan, horiuchi@hus.ac.jp, saito-sg@hus.ac.jp
[3]Division of Materials Science and Engineering, Faculty of Engineering, Hokkaido University, 060-8628 Sapporo, Japan, ikeda.ken-ichi@eng.hokudai.ac.jp, miura@eng.hokudai.ac.jp
[4]Max-Planck-Institut für Eisenforschung GmbH, 40237 Düsseldorf, Germany, f.stein@mpie.de

Introduction

Materials with “mille-feuille structure” (MFS) have attracted attention in recent years because of their excellent mechanical properties due to the unique deformation mechanism caused by kink formation [1]. MFS materials can be categorized into (1) crystalline type, (2) microstructure type, and (3) hybrid type. A crystalline MFS material is expected to be applied to a hybrid MFS material. However, a novel crystalline MFS material has not been easily found. Authors have reported that an intermetallic compound Nb_2Co_7, which has a complex layered structure (mC18) [2], is a novel crystalline MFS material with good compressive deformation properties [3,4] and that Nb_2Co_7-Co solid solution dual-phase microstructure can be obtained in a heat-treated Co-3.9Nb alloys. However, the mechanical properties and deformation behavior of a Nb_2Co_7-Co solid solution dual-phase alloys have been poorly understood. In the present study, compressive deformation behavior and microstructural evolution of a Nb_2Co_7-Co solid solution dual-phase alloys are investigated mainly focusing on kink formation.

Materials and Methods

The Co-1.0, 2.0, 3.9 at% Nb alloys were vacuum induction melted and were cast as φ20×200mm cylindrical ingots. The samples were cut into 1.5×1.5×3mm^3 or 2×2×4mm^3 rectangular parallelepiped samples. The samples were solution heat-treated (SHT) at 1240°C for 1h in the differential thermal analyzer (DTA) to attain a single-phase fcc-Co solid solution. Some samples were subsequently cooled to 900°C and heat-treated for 1h to precipitate Nb_2Co_7. Others were subsequently cooled to room temperature resulting in a fine dispersion of metastable $L1_2$ Co_3Nb phase, followed by a heat treatment at 900°C for 1h. Uniaxial compression tests were carried out with a strain rate of 3.75×10^{-4}/s or 1.0×10^{-4}/s. Microstructure and crystal structure were investigated by scanning electron microscopy (SEM) and electron backscatter diffraction (EBSD) before and after the tests.

Results and Discussion

After the heat treatment, Nb_2Co_7 precipitates at grain boundaries and within grains in all the samples. The amount of the precipitated Nb_2Co_7 increases with increasing Nb content. The Nb_2Co_7 precipitated within grains shows plate-like morphology, having a specific crystallographic orientation relationship with the hcp-Co matrix. In the samples with metastable $L1_2$ Co_3Nb, Nb_2Co_7 is more finely dispersed than in those without $L1_2$ Co_3Nb because Co_3Nb acts as a nucleation site for Nb_2Co_7. The resultant compressive stress-nominal strain curves are shown in Fig.1. The compressive stress-nominal strain curve for single-phase Nb_2Co_7 is also shown in the figure for comparison. The 0.2% flow stresses for the Nb_2Co_7-Co solid solution dual-phase alloys increase with increasing Nb content. In addition, the strength and ductility of the alloys are relatively higher than those of a single-phase Nb_2Co_7.

The results of detailed EBSD analyses for the Co-3.9 at% Nb alloy without metastable $L1_2$ Co_3Nb before and after the compression test are shown in Fig.2. The Co matrix around Nb_2Co_7 has an hcp structure. Although Nb_2Co_7 is considered to precipitate along the lower IQ regions, it is not identified as Nb_2Co_7 but as an hcp-Co matrix because of the extremely thin thickness of the precipitated Nb_2Co_7. Strain accumulation is also observed around Nb_2Co_7 after the compression test, suggesting that Nb_2Co_7 acts as a barrier to dislocation glide, and hence higher strength is attained in the manner of precipitation strengthening by Nb_2Co_7. As shown in the figure, a kink-like structure has formed on some sample surfaces without any cracks or delamination. It is one of the essential features of MFS materials. The results of the crystallographic orientation relationship across the interface of the kink-like structure show that all the interfaces are small-angle boundaries with a rotation axis of almost [hkl0], which is an in-plane direction in the basal (0001) plane. In addition, streaks are observed in the pole figure after the compression test, implying that a specific crystallographic orientation relationship does not exist at the interface of kink-like structures, but a continuous change in crystallographic orientation occurs. Therefore, these kink-like structures are not due to twinning but a result of deformation kinking. The excellent mechanical properties of the Nb_2Co_7-Co solid solution dual-phase alloys can be achieved by the solid solution strengthening

of Nb, precipitation strengthening of Nb_2Co_7, and kink formation. Among them, kink formation should play an indispensable role in the excellent ductility of the alloys. It is thus concluded that Nb_2Co_7-Co solid solution dual-phase alloys are promising candidates for hybrid-type MFS materials.

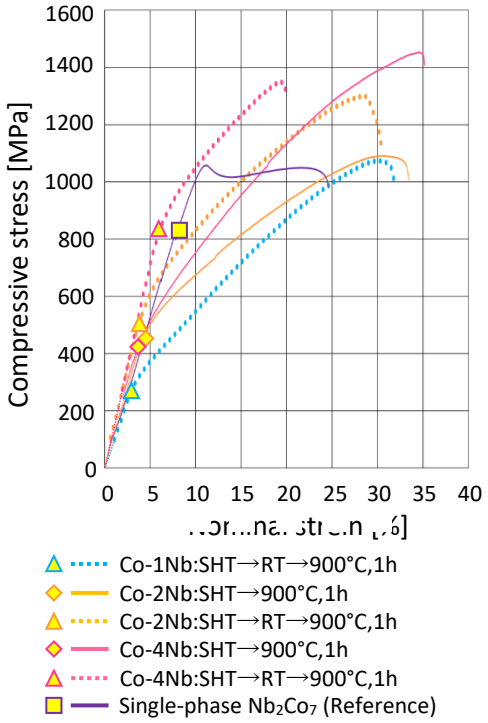

Fig. 1: Compressive stress-nominal strain curve for Co-1.0, 2.0, 3.9 at% Nb alloys. The symbol indicates 0.2% flow stress.

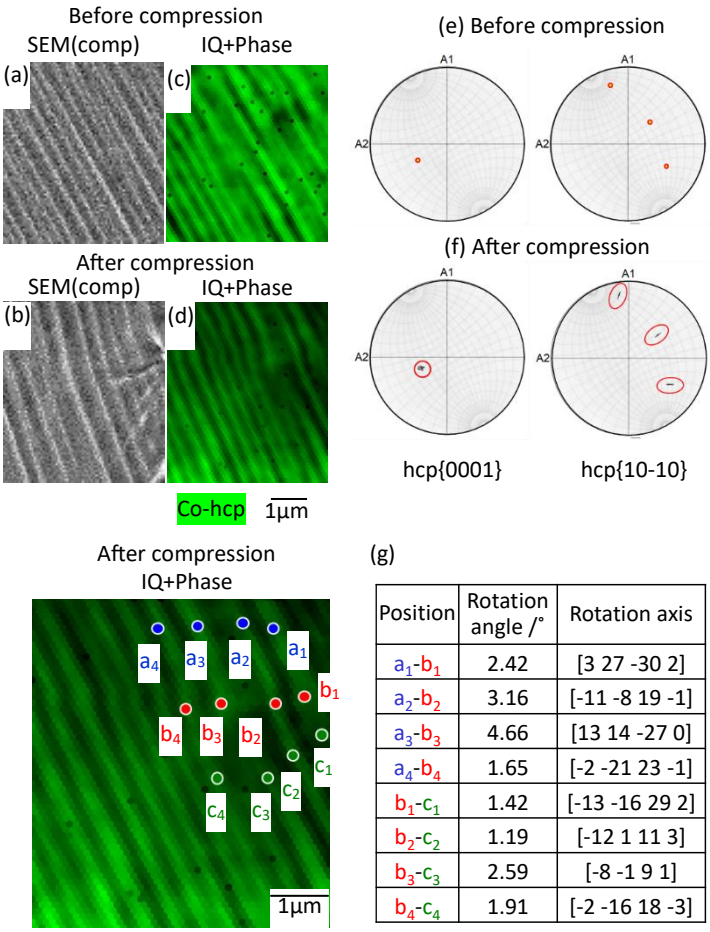

(g)

Position	Rotation angle /°	Rotation axis
a_1-b_1	2.42	[3 27 -30 2]
a_2-b_2	3.16	[-11 -8 19 -1]
a_3-b_3	4.66	[13 14 -27 0]
a_4-b_4	1.65	[-2 -21 23 -1]
b_1-c_1	1.42	[-13 -16 29 2]
b_2-c_2	1.19	[-12 1 11 3]
b_3-c_3	2.59	[-8 -1 9 1]
b_4-c_4	1.91	[-2 -16 18 -3]

Fig. 2: Results of detailed EBSD analyses for the Co-3.9 at% Nb alloy without metastable $L1_2$ Co_3Nb before and after the compression test. (a),(b) SEM images, (c),(d) EBSD IQ and phase maps, (e),(f) EBSD PFs, (g) rotation angles and axes across the interface of the kink-like structure.

Acknowledgements

The authors thank Mr. Kenji Ohkubo at Hokkaido University. A part of this work was supported by a grant from JSPS KAKENHI for Scientific Research on Innovative Areas “MFS Materials Science” (Grant Numbers JP18H05482) and “Advanced Research Infrastructure for Materials and Nanotechnology in Japan (ARIM)” (Proposal Number JPMXP1222HK0068) of the Ministry of Education, Culture, Sports, Science and Technology (MEXT).

References

[1] K. Hagihara, R. Ueyama, M. Yamasaki, Y. Kawamura, T. Nakano: Acta Materialia, **2021**, 209, 116797.
[2] A. Leineweber, G. Kreiner, D. Grüner, R. Dinnebier, F. Stein: Intermetallics, **2012**, 25, 34-41.
[3] L. Siggelkow, U. Burkhardt, G. Kreiner, M. Palm, F. Stein: Materials Science and Engineering A. **2008**, 497, 174-180.
[4] T. Horiuchi, K. Yamada, S. Saito, K. Ikeda, S. Miura, F. Stein: Materials Transactions, **2023**, 64, 1622-1630.

SCP9.3

Phase Formation, Crystallography, and Eutectoid Decomposition in CuZn30||CuZn80 Diffusion Couples

Martin Seyring[1], Johann Möbius[2] and Stephanie Lippmann[2]

[1]Microscopy and Materials Diagnostics Laboratory, Schmalkalden University of Applied Science, Blechhammer 9, 98574 Schmalkalden, Germany, m.seyring@hs-sm.de

[2]Otto Schott Institute of Materials Research, Friedrich Schiller University, Löbdergraben 32, 07743 Jena, Germany, johann.moebius@uni-jena.de, and stephanie.lippmann@uni-jena.de

Introduction

The phase formation in binary CuZn30||CuZn80 diffusion couples is investigated. The crystallographic relationships between the forming phases are characterized in detail regarding the occurrence of special orientation relationships. The frequency of orientation relationships allows estimating the impact of interfacial energies on the heterogeneous nucleation during solid-state phase transformation and subsequent coarsening [1]. Two orientation relationships are reported in the literature [2]: During nucleation of the α (fcc) in β (bcc) and vice versa, Kurdjumov-Sachs (K-S) orientation relationships are formed between the two phases (Eq. 1). Moreover, the β (bcc) phase precipitating from the ordered cubic γ (Cu_5Zn_8) phase exhibits a cube-on cube orientation relationship (Eq. 2).

The utilization of Zn-rich diffusion partners also allows a detailed characterization of the phase formation in the less studied Zn-rich part of the phase diagram, such as the eutectoid decomposition of the δ-phase.

Materials and Methods

Cylinders of two binary alloys, with the nominal composition (wt.%) of CuZn30 (α) and CuZn80 (ε), have been diffusion welded at 565°C under a joining pressure of 6 MPa. Details of the alloy preparation and the mechanical polishing of the joining interfaces can be found elsewhere [3]. The diffusion annealing was performed in a specially designed air-tight thin wall stainless steel capsule to allow fast inductive heating under protective Ar-atmosphere [4]. After diffusion annealing and subsequent quenching to room temperature, longitudinal sections of the diffusion couples were prepared by metallographic preparation utilizing vibration polishing for 2h as finish [3]. The resulting microstructure has been analyzed by optical microscopy and scanning electron microscopy (SEM) in combination with energy dispersive x-ray spectroscopy (EDX) and electron backscatter diffraction (EBSD) according to [5].

Results and Discussion

After annealing of the CuZn30//CuZn80 diffusion couple at 565°C, a multilayered microstructure is already present even after 5 s, consisting in total of four phases (Fig. 1). Between the initial phases of the diffusion partners α and ε completely closed layers of the intermetallic phases β, γ and δ (γ + ε) are grown according to the Cu-Zn phase diagram. The δ-phase, which is only stable above 558°C, is decomposing eutectoidically during quenching of the diffusion couple, the resulting two-phase region consists of the γ- and ε-phase (Fig. 1). The black areas in the microstructure are pores existing in ε prior to heat treatment of the diffusion couple. In the γ-phase, a vertical crack has been formed during metallographic preparation running along the former joining surface of the two initial diffusion partners.

The occurrence of numerous orientation relationships between adjacent phases has been revealed by detailed EBSD analyses:

More than 60% of the analyzed α/β interface was found to display Kurdjumov-Sachs (K-S) orientation relationships, that are described as follows

$$\{111\}_\beta \,||\, \{110\}_\alpha \text{ und } \langle 110\rangle_\beta \,||\, \langle 111\rangle_\alpha. \quad (1)$$

Additionally, almost 60% of the investigated β/γ phase boundary exhibits a cube-on-cube orientation relationship according to the equation

$$\{100\}_\beta \,||\, \{100\}_\gamma \text{ und } \langle 010\rangle_\beta \,||\, \langle 010\rangle_\gamma. \quad (2)$$

The formation of such orientation relationships in diffusion couples and even with high probability is not referred so far in the literature and reveals an impact of interfacial energies during solid-state phase transformations in diffusion couples.

After eutectic decomposition of δ into a lamellar structure of γ (Cu_5Zn_8) and ε (hcp), almost all grains of the eutectoid ε-phase show the same orientation as adjacent grains of the initial ε-phase. Furthermore, a considerable fraction of the eutectoid γ-phase is also oriented to the eutectoid ε-phase according to the newly discovered orientation relationship

$$\{10\bar{1}0\}_\varepsilon \,||\, \{110\}_\gamma \text{ und } \langle 0001\rangle_\varepsilon \,||\, \langle 110\rangle_\gamma \quad (3)$$

indicating a coupled growth of both phases during eutectoid decomposition.
The eutectic decomposition during quenching is accompanied by the formation of Widmanstätten plates (Fig. 2) of ε in the Zn-rich γ-Phase due to its retrograde solubility. The alignment of the ε plates inside the γ-grains implies the presence of a specific orientation relationship that will be investigated. Furthermore, kinetic and thermodynamic aspects of the Widmanstätten structure formation and the eutectoid decomposition will be evaluated.

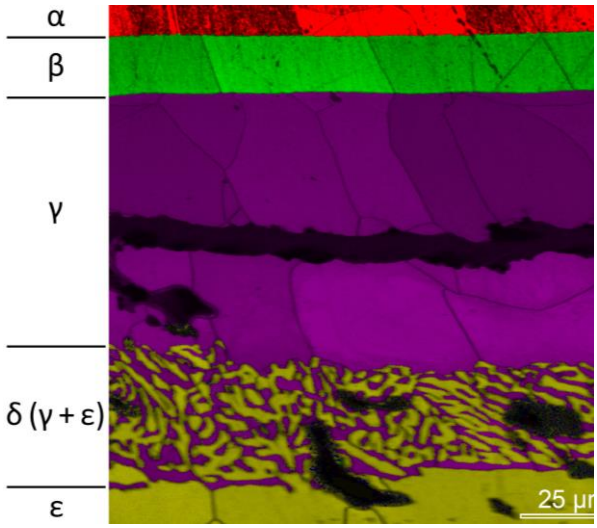

Fig. 1: EBSD phase map superimposed with image-quality map (grey scale) of a CuZn30||CuZn80 diffusion couple annealed at 565°C for 5s

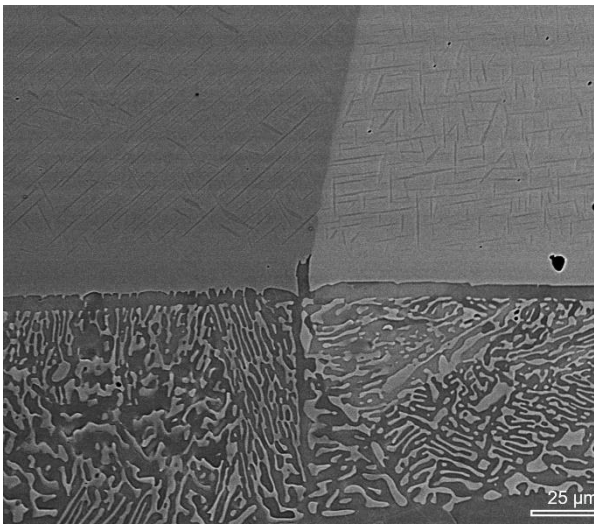

Fig. 2: BSE image of the eutectoidically decomposed δ (γ+ε) region (bottom) together with the Zn-rich γ phase displaying numerous Widmanstätten plates (top) after annealing at 565°C for 15min followed by quenching

References

[1] D.A. Porter, K.E. Easterling: Phase Transformation in Metals and Alloys. Chapmann & Hall, London, **1992.**
[2] G.F. Vaander Voort (Ed): ASM Handbook Metallography and Microstructures, Vol. 9. ASM International, Materials Park **2004**.
[3] J. Möbius, S. Lippmann, M. Seyring, Praktische Metallographie-Practical Metallography, *accepted,* **2023.**
[4] M. Seyring, F. Wanierke, T. Kaaden, S. Lippmann, M. Rettenmayr, Materials Characterization **2021**, *174 (7)*, 111032.
[5] M. Seyring, M. Rettenmayr, Acta Materialia **2021**, *208 (8)*, 116713.

SCP10.1

Navigating in systems with complex intermetallic phases: the case of Fe-Al-Si

Andreas Leineweber, Hanka Becker and Stefan Martin

Institute of Materials Science, TU Bergakademie Freiberg, Gustav-Zeuner-Straße 5, 09599 Freiberg, Germany,
andreas.leineweber@iww.tu-freiberg.de, hanka.becker@iww.tu-freiberg.de,
stefan.martin@iww.tu-freiberg.de

Introduction

According to the current knowledge, the Fe-Al-Si system is one of the most complicated ternary systems with 11 truly ternary equilibrium phases occurring as a function of composition and temperature; see e.g. [1,2]. It is emphasized here that the crystal structures of these phases are more than simply "labels". Instead, the atomic structure of a particular phase (i) is the basis for the actual thermodynamics of the phases (via chemical bonding and vibrational and point-defect properties), (ii) the basis to understand important transport properties like atomic mobility, and, last but not least, (iii) basis for the correct phase and orientational identification in the course of microstructural analysis.

In our research group we have conducted research in the Al-rich part of the Fe-Al-Si system (sometimes under influence of further elements) in view of Fe removal from Al melts and in the course of different types of joining processes of Fe- with Al-base alloys. We put emphasis on reliable phase identification based on diffraction evidence as crucial step to understand the actual microstructure evolution. Such an analysis, however, revealed intriguing phenomena related with the crystal structures of the Fe-Al-Si phases.

Materials and Methods

Materials were, in particular, Al-Fe-Si(-*M*) alloys with *M* being further transition metals of the 3d series which were solidified under various conditions. Analysis happened after cross-sectional metallographic preparation. Furthermore, intermetallic reaction layers having formed under different types of interactions of Al-base alloy melts and solid steel were produced and prepared in cross-sectional geometry. Special geometries were used to make specimens available for X-ray diffraction(XRD) in reflection geometry.

Microstructure analysis was, in particular, performed by field-emission scanning electron microscopy (SEM; JEOL JSM 7800F) including energy dispersive X-ray spectroscopy (EDX) and electron backscatter diffraction (EBSD). Transmission electron microscopy (TEM) was performed after applying focused ion beam techniques on alloy pieces preselected by SEM techniques. Occasionally also transmission Kikuchi diffraction was performed on TEM specimens using the mentioned SEM. XRD was conducted on a Bruker D8 diffractometer working with $CoK_{\alpha 1}$ radiation, which is especially suitable for Fe-containing alloys, which are strongly absorbing for Cu radiation.

Results and Discussion

The following main insights beyond the individual works were obtained:

(a) The homogeneity ranges of most of the Al-rich phases can be understood in terms of formulas of the type $Fe(Al, Si)_n$ with constant *n* for a given phase. Accordingly, Al substitutes Si, but the Fe atoms reside on one or several separate "sublattices". The iron atoms, however, may be substituted, to some extent, by other transition metals *M* of the 3d series $((Fe,M)(Al,Si)_n)$.

(b) Al and Si differ only very slightly in scattering power so that Al vs Si ordering is difficult to detect by, e.g., XRD methods. Likely, due to lack of further knowledge Al vs Si ordering is assumed to be absent in phases of the type $Fe(Al, Si)_n$. However, our TEM evidence on the β phase (agreeing with previous isolated evidence on the δ phase) suggests pronounced order of Al vs Si, which might indicate that Al vs. Si ordering is more the rule than the exception. This insight is supported by first principles calculations of cooperation partners [3]. It might be speculated that Al vs. Si ordering might be more the rule than an exception in Al/Si containing phases.

(c) While $Fe(Al, Si)_n$ phases occur in a specific $y_{Si} = x_{Si}/(x_{Al}+x_{Si})$ range (with x_i being the molar fraction of the element *i* in the phase), in particular in the case of the β and δ phases, the characteristic ranges for y_{Si} shift to higher values if Fe is substituted by Mn, Cr, V..., being elements with fewer electrons than Fe. In contrast, the ranges for y_{Si} appear to shift to lower values if Fe is substituted by Co, Ni, ..., being elements with more electrons than Fe. This implies a role of the total electron content per atom (e/a ratio) on the homogeneity range of the phase in quaternary systems, where substitution of Fe by electron-poor (rich) *M* is compensated by a higher (lower) Si content on the (Al,Si) sublattice(s).

(d) An exception to the principles (a) and (c) seems to be the cubic α phase, which is only metastable in the Fe-Al-Si system but can be formed under certain circumstances, and which is stabilized by very minor amounts of electron-poor elements. While crystallographic analyses available in the literature imply a formula $(Fe,M)(Al,Si)_{4.75}$ (see, e.g., [4]), the analyzed molar fraction of Fe (or Fe+Mn or Fe+Cr) for this phase seems to

scatter appreciably as compared to other phases, in contrast to point (a). Also, the correlation of the *M* and Si contents is not as clear as for the β and δ phases mentioned in (c). While the basic crystal structure type of the α phase has received attention as 1/1 approximant to icosahedral quasicrystals, the details how the molar fraction of the transition metal is varied is unknown on the atomic level.

(e) The β phase can grow with a heavily faulted structure as well as in two apparently distinct periodic polytypes (monoclinic and tetragonal). Likely, once the intermetallic has formed, e.g., upon solidification of the alloy, its internal structural degrees of freedom are frozen. This might be related with a low homologous temperature present in the intermetallic also at its formation temperature and small driving forces, e.g. to improve the stacking order. It is also noted that intergrowth of β and δ phases occurs as demonstrated by TEM investigations, which also allowed developing SEM/EBSD protocols for robust phase and orientation identification [3,5]. Such a protocol includes development of dedicated structure models suitable for robust indexing of EBSD patterns [5].

(f) Comparison of our results with the literature reveals a couple of forgotten works on crystal structures not listed in the prominent review by Ghosh [1], which can contain crucial information to complete the picture for a couple of rarely investigated phases. Some of the forgotten crystal structure information was confirmed in the course of results from our microstructural analyses and could be reconciled with presently available phase equilibria data [2]. This in particular concerns the relatively simple hexagonal Na_3As-type crystal structure of the τ_{10} phase [6], which was encountered in transmission Kikuchi diffraction and XRD from interdiffusion layers [2]

The authors propose that the phenomena observed for the various phases of the Fe-Al-Si system may be hidden in also many other intermetallic systems, which may not be evident when results of constitutional, structural and microstructural analysis are not carefully and critically reconciled.

References

[1] G. Ghosh, MSI Eureka, Ed. by G. Effenberg, Stuttgart (Germany), 2013.

[2] S. Martin, D. Sulik, X.F. Fang, H. Becker, A. Leineweber, Intermetallics **2022**, *151*, 107712.

[3] H. Becker, N. Bulut, J. Kortus, A. Leineweber, Journal of Alloys and Compounds **2022**, *911*, 165015.

[4] M. Cooper, K. Robinson, Acta Crystallogr. **1966**, 20, 614-617.

[5] H. Becker, T. Bergh, P. E. Vullum, A. Leineweber, Y. Li, Journal of Alloys and Compounds **2019**, *780*, 917-929.

[6] N.V. German, O.S. Zarechnyuk, O.V. Ventskobskyy, T.I. Yanson, V.O. Lysogub, M. B. Manyako, Visn. L'viv, Derzh. Univ. Set. Khim. **1991**, *31,* 8-10.

SCP10.2

Intermetallic powder alloys of the Fe – Al system as promising materials for high-temperature applications

Oleksandr Tolochyn[1], Oleksandra Tolochyna[1,2] and Gennadii Bagliuk[1]

[1]Frantsevich Institute for Problems of Materials Science of National Academy of Sciences of Ukraine, Kyiv 03142, Ukraine, tolochyn@gmail.com, gbag@ukr.net
[2]Department of Materials Science, Montanuniversität Leoben, Leoben, 8700, Austria, oleksandra.tolochyna@unileoben.ac.at, tolochyna@gmail.com

Introduction

Recently, the issue of increasing the power, energy efficiency and safety of power machines and energy modules has gained considerable scope in the world. The increase in efficiency in such systems is associated with an increase in the temperature in the working area and the replacement of existing materials with more higher – temperature ones. The creation of power plants with ultra-supercritical steam parameters requires materials that operate at temperatures of 650-750 °C, and the development of new types of reactors requires materials that reliably operate at 1000 °C [1]. Therefore, iron aluminides are of technical interest because of their attractive mechanical and corrosion -resistant properties, as well as relatively low cost. They are relatively light, with a density of about 75-85% of iron density, and have very high specific modules of elasticity. They are characterized by high heat resistance and high-temperature strength, and the high yield strength compared to steels and alloys based on nickel and cobalt allows them to be used at high temperatures [2].

Materials and Methods

Elemental iron and aluminum powders were used to obtain the intermetallic composition Fe_3Al, followed by synthesis of the intermetallic phase and consolidation of the synthesized powder by sintering [3] and hot forging [4] methods(Fig.1). For comparison, intermetallics were also obtained by arc melting.

Results and Discussion

The results of the studies have shown that the highest mechanical characteristics were obtained at the optimum sintering temperature of 1450 °C. In this case, iron aluminide has a structure A2 and demonstrates high strength: σ_{TRS} = 940 MPa, K_{1C} = 23,8 MPa $m^{1/2}$. Higher sintering temperatures, including the melting, showed a lower level of strength due to significant enlargement of the structure (σ_{TRS} = 300 – 450 MPa). The use of hot forging (temperature densification 1100 °C) allowed to increase the strength characteristics to 1200 MPa, K_{1C} = 30 MPa $m^{1/2}$. The high-temperature studies of iron aluminides produced by various powder technologies demonstrated an abnormal temperature dependence of the yield strength with a maximum at 500 °C, which is typical for this class of materials. Sintered and forged powder materials demonstrated the highest high-temperature strength. The yield strength of powdered iron aluminide under compression at elevated temperatures was 500-600 MPa (Fig.2), which is 25 – 40% higher than the yield strength of cast materials of similar composition.

Rapid high-temperature creep tests showed that the deformation rate of the samples when tested at 600 °C varied in the range of 10^{-7} – 10^{-6} s^{-1}, and at 650 °C in the range of 10^{-6} – 10^{-5} s^{-1}. During 3 hours of creep tests (primary stage), the total deformation of the samples at 600 °C reaches approximately 0.1 to 1 %, and at 650 °C it is approximately 10 times higher. The highest creep resistance at both temperatures is demonstrated by the hot-forged and sintered powder samples.

Thus, the presented results show that the powder materials obtained by the developed technologies are superior to cast analogues both in terms of high-temperature strength and parameters characterizing creep resistance, and therefore may be promising for high-temperature applications.

Further improvement of high-temperature strength and creep resistance is associated with alloying iron aluminide with additional elements that can create disordered crystal structures of solid solutions or composites with particles of coherent and incoherent phases. An increase in creep resistance is also achieved by the allocation of dispersed particles of carbides, borides or oxides, and the best method of realizing such structures may be powder metallurgy technologies.

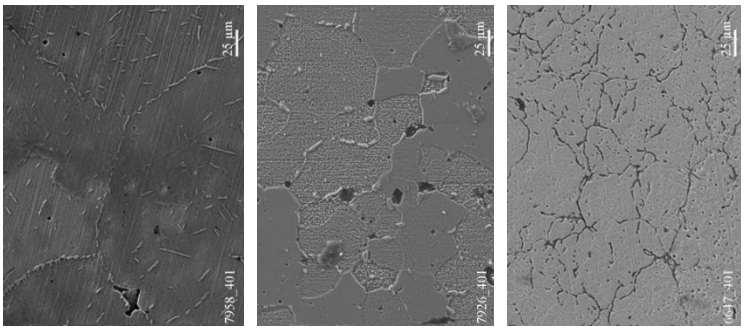

a b c

Fig.1 SEM images of samples after: a) arc melting, b) sintering (1450 °C) and c) hot forging (1100 °C)

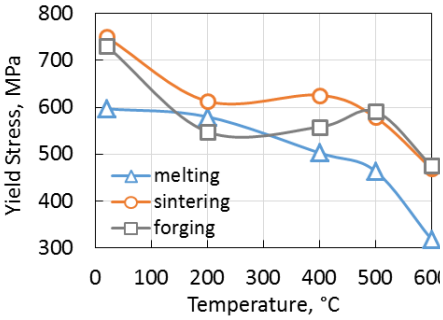

Fig.2 Temperature dependences of the yield strength of the studied materials

References

[1] Degueldre, C. A. (**2017**). The analysis of nuclear materials and their environments (p. 295). Springer.

[2] M. Palm, F. Stein, G. Dehm, Annual Review of Materials Research. **2019**, 49, 297-326

[3] O. I. Tolochyn, O. V. Tolochyna, H. A. Bagliuk, Y. I.Yevych, Y. M. Podrezov, A. A. Mamonova. Powder Metallurgy and Metal Ceramics. **2020**, 59, 150-159.

[4] O. Tolochyna, O. Tolochyn, G. Bagliuk, Y. Podrezov, O. Zgalat-Lozynskyy, I. Okun. JOM. **2023**, 75(3), 825-836.

SCP10.3

Equilibria Among Ordered Phases in Fe-Pd Near the Eutectoid: L1' and Two-Phase Coexistence

Jerrold A. Floro, Adrian Savovici and William A. Soffa

Department of Materials Science and Engineering, University of Virginia, USA, jaf9r@virginia.edu, as5fj@virginia.edu, was2n@virginia.edu

Introduction

Binary metallic systems such as Fe-Pt, Co-Pt and Fe-Pd exhibit disorder/order, eutectoid transformations, A1→$L1_0$+$L1_2$. The tetragonal $L1_0$ phase is typically ferromagnetic, with high uniaxial magnetocrystalline anisotropy. The cubic, $L1_2$ phase is either ferro- or paramagnetic, with low anisotropy. In Co-Pt, eutectoid decomposition leads to the self-assembly of a *nanochessboard* structure, which is a pseudo-periodic, 2+1D structure where the ordered phases can be on the nanoscale. We have previously investigated both the phase transformation, and magnetic exchange coupling, in Co-Pt nanochessboards. Our current work focuses on the eutectoid region in Fe-Pd near 60 at% Pd, where a very narrow $L1_0$+$L1_2$ region is thought to exist. Essentially nothing is known about the microstructure in this region, and in fact, we have found an interesting new phase can form, which we label as L1'. The L1' phase, which we currently believe is an equilibrium phase, was first predicted in 1938 by William Shockley [1], but has not been definitively identified since.

Materials and Methods

Bulk, polycrystalline Fe-Pd alloys were arc melted. The nominal compositions were from 62 ± 0.5 at% Pd, determined by inductively-coupled plasma – optical emission spectroscopy (ICP-OES). Homogenization was achieved by repeated cycles of rolling, then annealing at 1000°C for 24 hours. Furnace annealing was always performed in evacuated quartz ampoules that were backfilled with argon. Samples were subsequently aged under different thermal protocols, including continuous cooling and isothermal annealing. X-ray diffraction (XRD) was performed using a Panalytical Empyrean system in □□□□ powder geometry, employing Cu-K□$_1$ radiation. Transmission electron microscopy (TEM) was performed using a FEI Titan at 300 kV, in bright- and dark-field modes (BF, DF).

Results and Discussion

For alloy composition just inside the single-phase $L1_0$ region, aging quenched-in A1 at 650°C produces the expected $L1_0$ phase; however, aging at 525°C produces a different phase, which we identify as L1'. L1' is a tetragonal (P4/mmm) phase that can form when composition is intermediate to $L1_0$ and $L1_2$; it places excess Fe atoms at a specific Wycoff site and can be viewed as a hybrid of $L1_0$ and $L1_2$. It's identification is non-trivial. XRD demonstrates a clear tetragonal distortion, albeit where the tetragonality is reduced vis-à-vis $L1_0$. Additional superlattice reflections appear, such as (100) and (101), that are not allowed in $L1_0$. While these *are* allowed reflections of $L1_2$, DF-TEM imaging of the microstructure makes a strong case for single-phase L1', see Figure 1. In particular, the microstructure entirely consists of so-called polytwins, which are conjugate pairs having different c-axis orientations, separated by {110} boundaries having invariant plane strain. The polytwin structure is a well-known characteristic of the formation of the ordered tetragonal phase, A1→$L1_0$, and it does not result for A1→$L1_2$. Dark-field image contrast is consistent with the predicted L1' structure factor, as is the selected area electron diffraction pattern. No two-phase coexistence is evident at this composition in TEM.

At slightly more Pd-rich compositions that are within the two-phase field, we do observe two-phase coexistence, either $L1_0$+$L1_2$ (as predicted by the phase diagram), or L1'+$L1_2$, depending on the temperature, determined both by XRD and TEM. In both cases, a dominant polytwin microstructure forms, but now the $L1_2$ phase coexists in the form of nanometer-scale lamellae that wet the polytwin boundaries and anti-phase boundaries (APB). These lamellar wetting layers are readily evident in DF-TEM imaging using a g=110 reflection (see Figure 2), and high-resolution imaging demonstrates their cubic nature. This phase morphology is nominally consistent with prior predictions from phase field modeling,[2] however the microstructural *evolution* is non-trivial. In particular, the $L1_2$ phase forms first during continuous cooling through the eutectoid isotherm. Then, with isothermal aging below the isotherm, polytwinned $L1_0$ forms in an order-to-order transformation, with apparently simultaneous formation of the $L1_2$ twin/APB wetting layers. Nucleation of a 'bundle' of $L1_0$(or L1')+$L1_2$ occurs in localized, anisotropic fashion, propagating rapidly along a single direction, followed by much slower lateral growth to consume the $L1_2$ matrix. The mechanism defining the rapid, uniaxial growth process is not currently understood.

The formation of L1', either as a single-phase, or co-existing with $L1_2$, occurs when we age metastable A1 at temperatures of 525°C, whereas aging at 650°C produces $L1_0$ or $L1_0$+$L1_2$, depending on composition. This suggests that a phase boundary exists between these temperatures, where $L1_0$→L1' upon cooling, likely via a higher-order transformation. To explore this, we have first transformed an A1 sample entirely to $L1_0$ by extended heating at 650°C, then aged this at 525°C for extended times. To date, we have NOT observed the transformation to occur. This is concerning, but may result from a very low driving force, and slow kinetics.

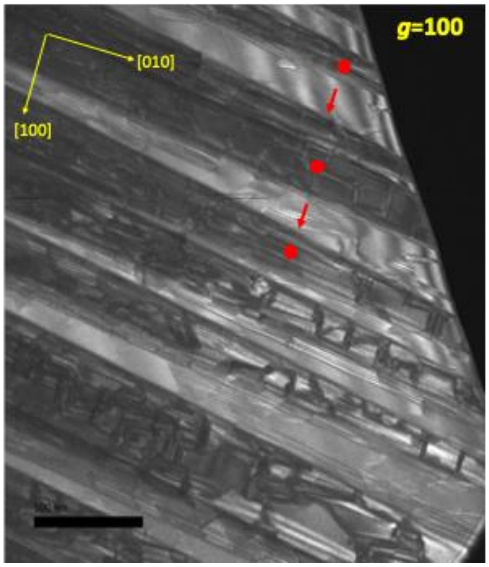

Fig. 1: DF-TEM along a [001] zone axis,showing single-phase, L1' polytwin structure with twin boundaries inclined at 45° relative to the [001] zone axis. Coarse bands are the twin "conjugate" pairs that have different c-axis orientations (shown by red arrows and circles), while fine contrast modulation arises from both Moire' effects, and APBs. Scale bar is 500 nm.

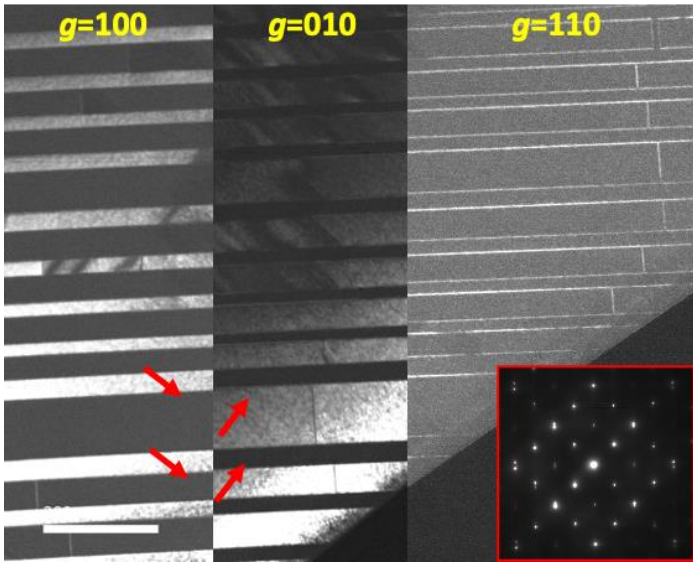

Fig. 2: DF-TEM of a more Pd-rich sample than Fig. 1, where two-phase coexistence occurs after aging at 650°C. Imaging with g=100/010 highlights the conjugate $L1_0$ orientations (c-axes indicated by red arrows), while imaging with g=110 highlights the $L1_2$ phase decorating the twin boundaries and APBs. The selected area diffraction pattern of this region is shown inset. Scale bar is 200 nm.

Conclusions

We have explored phase equilibria in Fe-Pd alloys with compositions about 61 at% Pd, which is in the vicinity of the eutectoid, A1→ordered-tetragonal + ordered-cubic. For slightly Pd-poor compositions that are in the single-phase tetragonal region, aging metastable A1 at 650°C produces $L1_0$ while aging at 525°C produces the L1' phase. First predicted in 1938, there has not been an unambiguous determination of L1' in bulk as an equilibrium phase. We combined XRD, DF-TEM and structure factor calculations in order to provide reasonable certainty of its existence. For more Pd-rich compositions, 650°C aging produces $L1_0$+$L1_2$ and 525°C aging produces L1'+$L1_2$, both readily evident in XRD. In both situations, the tetragonal phase occurs in a polytwin configuration, with the $L1_2$ phase wetting the {110} twin boundaries and antiphase boundaries. The evolution of these configurations is complex and highly anisotropic.

Support from the U.S. National Science Foundation through grant DMR-1709914 is gratefully acknowledged.

References

[1] W. Shockley, J. Chem. Phys. **1938**, 6, 130-144.
[2] Y. Ni and A. G. Khachaturyan, Acta Mater. **2008**, 56, 4498-4509.

SCP11.1R

Hydrogen in Intermetallic Compounds

Jean-Marc Joubert

ICMPE, CNRS, 2-8 rue Henri Dunant, 94320 Thiais, France, jean-marc.joubert@cnrs.fr

Intermetallic compounds have been considered for a long time as possible hydrogen storage materials. The large amount of possible elemental combination, the number of accessible crystal structures and the possible changes of the properties by substitution make them really attractive. This presentation will be an introduction to this specific topic.

The structural properties including the determination of hydrogen position and site occupancies in the crystal structure using neutron diffraction by Rietveld analysis will be reported. The thermodynamic properties and how they can be adapted to a specific application will be described. The way these properties may be modelled using the Calphad method will also be addressed.

Examples will be given in the different families (AB_5 based on the $CaCu_5$ structure (Fig. 1), AB_2 Laves phases, AB with CsCl structure…).

Finally, various applications, including hydrogen storage materials and electrodes for the so-called nickel-metal hydride batteries will be presented.

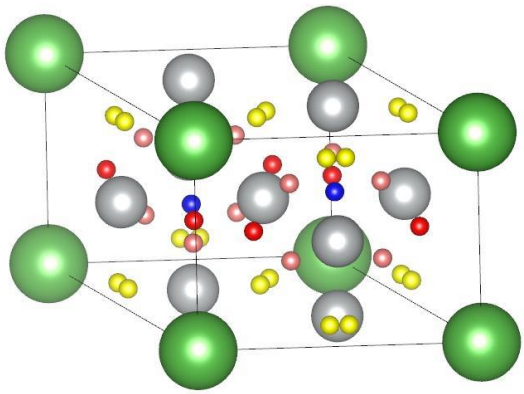

Fig. 1: $CaCu_5$ crystal structure with possible interstitial tetrahedral sites occupied by hydrogen.

SCP11.2

Tuning the composition in R_6TX_2 intermetallics (R = Gd, Tb, Dy; T = Fe, Mn, Co, Ni; X=Sb, Te) to optimize magnetic refrigeration near Room Temperature

I.R. Aseguinolaza[1], A. Herrero[1], A. Oleaga[1], A.J. Garcia-Adeva[1], E. Apiñaniz[1], A.V. Garshev[2], V. O. Yapaskurt[3] and A.V. Morozkin[2]

[1]Departamento de Física Aplicada, Escuela de Ingeniería de Bilbao, Universidad del País Vasco UPV/EHU, Plaza Torres Quevedo 1, 48013 Bilbao, Spain

[2]Department of Chemistry, Moscow State University, Lenisnkie Gory, House 1, Building 3, Moscow, GSP-2, 119991, Russia

[3]Department of Petrology, Geological Faculty, Moscow State University, Leninskie Gory, Moscow, 119991, Russia

Introduction

The intermetallic family Zr_6CoAl_2-type R_6TX_2 (space group *P-62m, N 189, hP9*) has interesting magnetic and magnetocaloric properties in different temperature ranges, depending on the particular composition. The combination of different rare earths, transition metals and *p*-block elements allows to tune these properties to a desired temperature and to improve them. We show in this work how this can be done close to room temperature based on the accumulated experience with this family [1, 2]. The thermal properties (thermal diffusivity, thermal effusivity, specific heat) have also been measured as they are extremely relevant in order to evaluate the practical applicability of these magnetocaloric materials in real refrigerator systems.

Materials and Methods

Nine selected compounds of the R_6TX_2 (R= Gd, Tb, Dy; T= Mn, Fe, Co, Ni; X=Sb, Te) intermetallic family have been studied in detail: $Gd_3Tb_3FeSbTe$, $Tb_2Dy_4FeSb_2$, $Tb_2Dy_4Fe_{0.75}Mn_{0.25}Sb_2$, $Gd_2Dy_4Fe_{0.75}Mn_{0.25}Sb_2$, $Gd_2Tb_4Fe_{0.75}Mn_{0.25}SbTe$, $Tb_6Fe_{0.75}Mn_{0.25}SbTe$, $Tb_6Co_{0.75}Mn_{0.25}SbTe$, $Tb_6Ni_{0.75}Mn_{0.25}SbTe$ and $Tb_6Ni_{0.5}Mn_{0.5}SbTe$. They have all been prepared by arc-melting [3]. Phase analysis of the alloys was carried out using X-ray diffraction and energy dispersive X-ray spectroscopy microprobe elemental analysis (EDS). Magnetic measurements have been performed using a VSM (Vibrating Sample Magnetometer) module in PPMS (Physical Properties Measurement System) by Quantum Design. The thermal properties of the materials have been measured using a high-resolution ac photopyroelectric calorimeter (PPE), in its back detection configuration for thermal diffusivity measurements, and in its front detection configuration for thermal effusivity measurements.

Results and Discussion

The compounds were selected based on previous studies on this family [1-2] in order to optimize their magnetocaloric performance and increase their working temperature up to room temperature, or close to it. In every alloy present in this study there are two magnetic phase transitions: a paramagnetic to ferromagnetic (PM-FM) transition in the range 182-282 K and a spin reorientation transition in the range 26-76 K. The increase of the rare earth atomic radius enlarges the atomic cell volume and *a* cell parameter, resulting in an increase of the Curie temperature. Regarding the effect of the substitution of the transition metal element, the strongest effect on T_C is observed with Mn, which greatly increases the PM-FM transition temperature. This element has the largest atomic radius among the transition metal elements studied in this work, and causes a big enlargement of the *c* cell parameter and cell volume, with a small shortening of the *a* cell parameter in comparison to Fe, Ni or Co. A stronger hybridization of Mn with the other elements of the compounds is proposed to be the reason for the change on T_C. Three clear trends for the increase of Curie temperature with the enlargement of the *c* cell parameter have been observed, depending on the rare earth element, transition metal and *p*-block element.

As a consequence of the two magnetic transitions in each alloy, two peaks related to a direct magnetocaloric effect (DMCE) appear in the magnetic entropy change, generating a wide table-like plateau region in between both peaks, which is required to improve the efficiency of refrigerators following an Ericsson cycle. Besides, this makes these materials suitable to work as magnetic refrigerators in both room temperature region and gas liquefaction region. The highest magnetic entropy peak value for $\mu_0\Delta H$ = 5 T is found for $Tb_2Dy_4FeSb_2$, with 7.72 J/kg K around 182 K (see Fig. 1). For the same applied field the other compounds show moderate values around room temperature (2.88-4.53 J/Kg K). However, the superposition of the two peaks results in huge refrigerant capacity values, up to $RC_{FWHM}(5\ T)$=1103.04 J/kg in the case of $Tb_2Dy_4FeSb_2$. The comparison of the magnetocaloric properties with the ones previously obtained on R_6TX_2 intermetallic family compound reveals that there is a clear improvement in those properties.

The thermal diffusivity, thermal effusivity and specific heat have been measured at room temperature, and the temperature dependence of the former has been obtained around the relevant magnetic phase transitions

region, with values in the range 1.3-2.3 mm^2/s, which are good for magnetic refrigerators under high working frequencies (see Fig. 2).

The study is completed with a rigorous critical behavior analysis of the second order PM-FM transition. This analysis shows that besides $Tb_2Dy_4FeSb_2$, which unequivocally belongs to a Mean Field universality class, the remaining compounds do not match any theoretical model. The critical exponent γ points to long range order interactions, in general, while values are in the range (0.59-0.90), indicating a deviation from theoretical models as a reflection of the magnetic complexity in these compounds. These deviations are common in this R_6TX_2 intermetallic family, and point to the necessity of developing new theoretical models addressing more complex magnetic interactions that may explain the experimentally observed deviations. The critical exponents have been used to confirm the scaling relations of magnetocaloric properties, and the scaling of the refrigerant capacity (*RC*) values in materials presenting two magnetic phase transitions is addressed, concluding that for a correct scaling of *RC* the magnetic entropy change peak must be considered symmetric. Finally, the collapse of the magnetic entropy change curves into a single universal curve has also been observed, confirming the second order nature of the PM-FM transition. The combination of the scaling laws, critical exponents and universality curves allows the extrapolation of magnetic entropy curves to magnetic fields, which are not experimentally accessible.

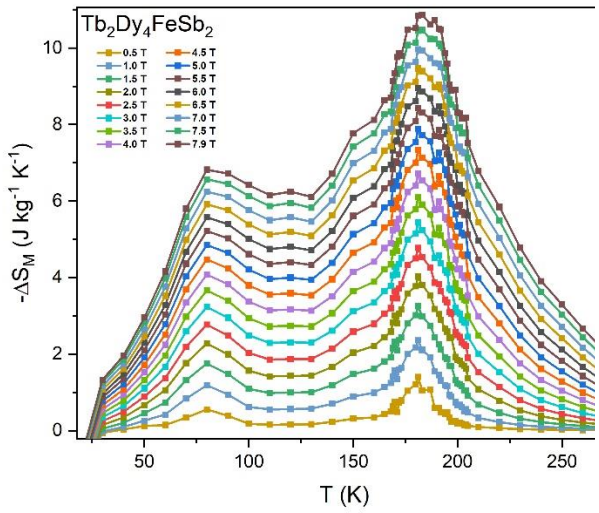

Fig. 1: Magnetic entropy change for $\mu_0\Delta H$ from 0.5 to 7.9 T

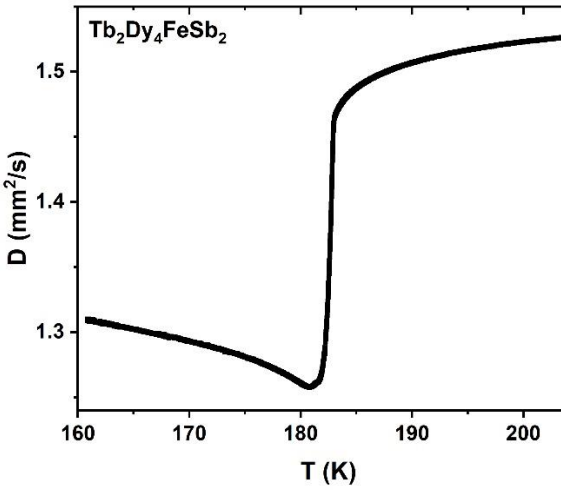

Fig. 2: Thermal diffusivity as a function of temperature around T_C

References

[1] A. Herrero, A.Oleaga, I. R. Aseguinolaza, A.J. Garcia-Adeva, E. Apiñaniz, A.V. Garshev, V.O. Yapaskurt, A.V. Morozkin, Journal of Alloys and Compounds. **2021**, *890*, 161849.

[2] A.Oleaga, A. Herrero, A Salazar, A.V. Garshev, V.O. Yapaskurt, A.V. Morozkin, Journal of Alloys and Compounds. **2020**, *843*, 155937.

[3] A. Herrero, I.R. Aseguinolaza, A. Oleaga, A.J. Garcia-Adeva, E. Apiñaniz, A.V. Garshev, V. O. Yapaskurt, A.V. Morozkin, Dalton Transactions **2023**, Accepted. DOI 10.1039/D3DT00223C.

SCP11.3

Effect of Ni interlayer thickness on the solid-state growth of intermetallic phases in Cu(Ni)-Sn-Ni system

Abhilaash Ajith Kumar and Werner Hügel

Automotive Electronics/Engineering Assembly Interconnection Technology (AE/EAI), Robert-Bosch-Str. 2, 71701 Schwieberdingen, Germany, Abhilaash.Ajithkumar@de.bosch.com

Introduction

Need for automotive electrification in recent years have increased the reliability temperature requirements of electronic solder joints. Ni is being increasingly used as a terminal/under layer to restrict intermetallic (IMC) growth during soldering and high temperature service (T > 398K). In contrast, there is also a need to reduce/minimize Ni thickness currently used in the industry due to environmental concerns. The composition and growth kinetics of the IMC layer ($(Ni,Cu)_3Sn_4$ or $(Cu,Ni)_6Sn_5$) depends on the mutual solubility of Cu and Ni in the IMC phases at the reaction interfaces [1]. This influences the overall IMC thickness and its morphology which affects the reliability of solder joints. This study focusses on the complex microstructural development and diffusion kinetics of the IMC phases in Cu(Ni-*x*)-Sn-Ni system with three different Ni interlayer thickness (*x*) of 0.2, 0.6 and 1.6 µm.

Materials and Methods

Pure Cu pins were electroplated with Ni interlayer of either 0.2, 0.6 or 1.6 µm which were derived from typical Ni layer specification sheets of electronic components. The pins were then subsequently electroplated with 20 µm matte-Sn (columnar grains of width 3-5 µm) and 5 µm Ni as shown in figure 1. The error in the thickness of the electroplated layers were controlled within industrial tolerance limits. The electroplated pins were sectioned into 5 mm length samples and were placed in a temperature-controlled convection oven under ambient conditions and aged at 398K, 423K, 453K and 473K for times ranging from 8hrs to 14 days. The temperature calibration was done using a K-type thermocouple (±2°C). Once the isothermal aging is complete, the samples were immediately quenched in cold water to stop the diffusion process. Optical microscopy was used to capture microstructure and measure IMC thickness on both Cu-Side and Ni-side greater than 2 µm. For thinner IMC phases, scanning electron microscopy (SEM) in the backscattered electron mode (BSE) was done after coating the polished surface with 5 nm Au via PVD process. Energy dispersive spectroscopy (EDS) allowed composition measurement of the phases.

Results and Discussion

Figure 2 shows the cross-sectional images of Cu(Ni-*x*)-Sn-Ni samples with Ni interlayer thicknesses (*x)* of 0.2 µm, 0.6 µm and 1.6 µm aged at 473K for 14 days. The evolution of morphology and composition of the IMC phases varied with samples of different Ni interlayer thickness. Both Ni interlayer thickness of 0.2 µm and 1.6 µm showed uniform layer growth of the IMC phases whereas Ni interlayer thickness of 0.6 µm showed anisotropic facetted growth. In some cases, the facets which grew from opposite sides coalesced to produce continuous IMC plates mainly along Sn grain boundaries.

$(Ni,Cu)_3Sn_4$ grew as continuous layer in the initial stage on Ni|Sn interfaces on both Cu-side and Ni-side for all the three cases. As the Ni interlayer is consumed by growth of $(Ni,Cu)_3Sn_4$ phase with time , Cu concentration within Sn phase increases due to its higher solubility in Sn than Ni [2,3]. When Cu concentration in Sn exceeded a critical threshold, there is thermodynamic driving force for conversion of $(Ni,Cu)_3Sn_4$ into $(Cu,Ni)_6Sn_5$ [4] . The Ni concentration within transformed $(Cu,Ni)_6Sn_5$ phase resulted in facetted growth for Ni-rich (> 10at.% upto 20 at.%) $(Cu,Ni)_6Sn_5$ phase as seen in samples with 0.6 µm and 1.6 µm Ni interlayer thickness. EDS line scan revealed that, in Ni-gradient exists within the $(Cu,Ni)_6Sn_5$ phase during the initial stages and it equilibrates to 15 at.% Ni for longer times. Uniform layer growth was observed for Ni-poor(< 10at.%) $(Cu,Ni)_6Sn_5$ phase in 0.2 µm Ni interlayer samples. $(Cu,Ni)_3Sn$ with negligible solubility of Ni is also observed close to the Cu interface for Ni-poor cases.

Higher growth rate of $(Cu,Ni)_6Sn_5$ than $(Ni,Cu)_3Sn_4$ can be explained by the higher solubility of Ni in $(Cu,Ni)_6Sn_5$ phase (upto 20 at.%) than solubility of Cu in $(Ni,Cu)_3Sn_4$ phase (upto 8 at.%) [4]. The faster growth of $(Cu,Ni)_6Sn_5$ engulfs the initially formed $(Ni,Cu)_3Sn_4$ consuming the smaller grains resulting in dispersed precipitates of $(Ni,Cu)_3Sn_4$ (initial large grains) within $(Cu,Ni)_6Sn_5$ phase as seen in 0.2 µm microstructure.

Grain boundary diffusion is the main diffusion mechanism controlling the growth of the IMC phases within the studied temperature range. Addition of small amount of Ni to (Cu, $Ni)_6Sn_5$ phase acts as a grain refiner resulting in smaller IMC grains. The higher IMC thickness on the Cu-side in 0.2 µm samples is due to the finer grain size of Ni-poor $(Cu,Ni)_6Sn_5$ aiding in the grain boundary diffusion of Sn to the Cu interface [5]. The presence of initial

formed $(Ni,Cu)_3Sn_4$ precipitates closer to the Sn boundary also corroborates for Sn dominant diffusion. For 0.6 µm samples, the Ni-rich $(Cu,Ni)_6Sn_5$ phase grows as single crystal with a fixed orientation relationship with Sn [6]. Although growth rate is faster along certain directions where the Sn grains are favorably oriented, there is overall less grain boundary area resulting in lower average IMC area in comparison to 0.2 µm samples.

The free standing single crystalline facets poses a significant reliability risk due to its brittle nature of fracture. But if the facets from both Cu-side and Ni-side coalesce to form continuous IMC plate as seen in figure 2, it can strengthen the solder joint. The Ni interlayer with 1.6 µm thickness exhibited the slowest and uniform growth of $(Ni,Cu)_3Sn_4$ with very low Cu content thereby acting as an effective diffusion barrier for Cu-substrates. The activation energies and the diffusion constants of the individual IMC phases calculated in this study enable to model the system in future with techniques such as phase field simulation.

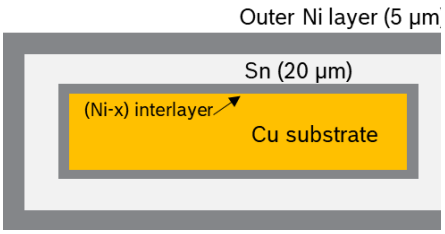

Fig. 1: Schematic of the cross section of a Cu(Ni-x)-Sn-Ni electroplated sample where x can be 0.2, 0.6 or 1.6 µm.

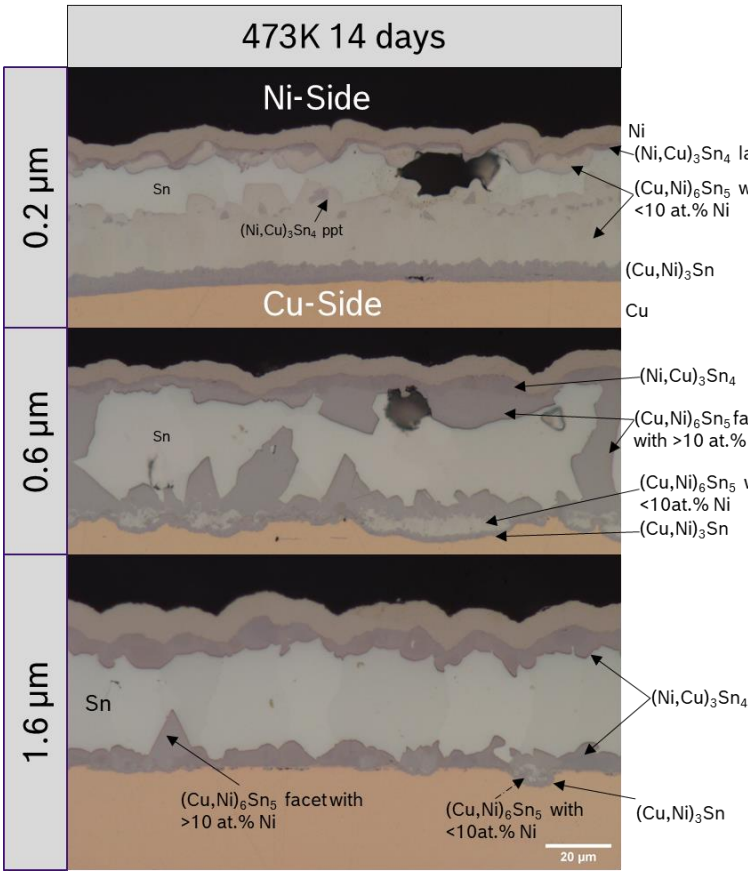

Fig. 2: Microstructure images of Cu(Ni-x)-Sn-Ni with x = 0.2, 0.6 or 1.6 µm after aging at 473K for 14 days showing the different IMC phases formed on Cu-side and Ni-side.

References

[1] T. Laurila, V. Vuorinen, J.K. Kivilahti, Materials Science and Engineering: R: Reports. **2005,** 1-60.

[2] T. Massalski, Binary Alloy Phase Diagrams, ASM, **1996**.

[3] N. Saunders and A. P. Miodownik, Bulletin of Alloy Phase Diagrams. 11 (3), **1990**, 278.

[4] H. Yu, V. Vuorinen, J.K. Kivilahti, Journal of electronic materials. **2007**, 136-46.

[5] V. A Baheti, S. Islam, P. Kumar, R. Ravi, R. Narayanan, D. Hongqun, V. Vuorinen, T. Laurila, A. Paul, Philosophical Magazine, **2016**, 96(1), 15-30.

[6] A. Wierzbicka-Miernik, J. Wojewoda-Budka, K. Miernik, L. Litynska-Dobrzynska, N. Schell, Journal of Alloys and Compounds, **2017**, 693:1102-8.

SCP11.4

The identification and the role of Mg_2Sn in Al alloy-Sn-based Miscibility Gap Alloys for Thermal Energy Storage purposes

Matteo Molteni[1], Paola Bassani[2], Isaia Bettega[1] and Elisabetta Gariboldi[1]

[1]Department of Mechanical Engineering, Politecnico di Milano, Milano (MI) 20156, Italy,
matteo1.molteni@polimi.it, isaia.bettega@mail.polimi.it, elisabetta.gariboldi@polimi.it
[2]CNR-ICMATE, via Previati 1/E, 23900 Lecco (LC), Italy, paola.bassani@cnr.it

Introduction

In the view of the incoming energy crisis, the research on Phase Change Materials (PCMs) for Thermal Energy Storage (TES) purposes have been increasingly gained more and more attention in the last decades. Indeed, PCMs offer the possibility to absorb energy at constant temperature as latent heat of transformation, when they experience a phase transition. The energy collected is then released with the inverse process. The possibility of absorbing heat is also attractive for Temperature Management (TEM) purposes. Solid-liquid phase change is the most studied one. The high phase transition temperature and the high latent heat of fusion per unit volume, combined with the high thermal conductivity, make metals a very promising solution for the development of efficient TES/TEM systems. However, the problems related to the corrosiveness and the reactivity of molten metals severely limit their spread.

Such an issue can be smartly tackled with the adoption of Miscibility Gap Alloys (MGAs) [1]. MGAs are composed by elements which do not interact at both the solid and liquid state. In the case of binary alloys, the resulting system at room temperature consist of two phases whose composition roughly corresponds to the one of the pure elements. Aluminum and Tin, already exploited in the TES field for service temperatures close to the melting temperature of pure Sn, i.e., 232°C, represent a significant example.

The PCM activation temperatures can be tuned with the addition of other elements which do not modify the miscibility gap nature of the system. In the case of Al-Sn binary alloy, Si demonstrates to be a good solution [2]. Besides, few information is available for additions of other elements (e.g. Mg), generally found in commercial aluminum alloys, which possibly modify the response of the system.

Hence, in this study, the authors propose to investigate the microstructural features and intermetallics arisen in PCMs, obtained from the combination of a commercial casting Al-based alloy, i.e., A356, with pure Sn. The selected production process was water granulation, that the possibility to obtain products with the desired microstructure with very limited temporal efforts [2]. The impact of secondary phases and intermetallics on the thermal performances of the resulting PCM is evaluated and compared to the one of the binary Al-Sn alloy.

Materials and Methods

The water granulated PCMs were obtained adding Sn (99.85%wt, BS EN 610: 1996) to commercially pure Al ingots or A356 alloy casting scraps in order to obtain a mass ratio of 40:60. A more detailed explanation about the production process is provided in [2]. The composition of the multicomponent system, hereafter simply referred as A356-Sn, was simulated with the thermodynamic equilibrium calculator of the commercially available software Thermocalc in aid of phase identification. Microstructural analyses were performed with both optical microscopy (Leitz Aristomet Light Optical Microscope) and electron microscopy (SU-70 Hitachi). EDS analyses were performed with UltraDry silicon drift X-ray detector (Thermo Fisher Scientific, USA). Besides, Philips Xpert Pro diffractometer (Cu Kα source) was used for crystallographic investigations.

The thermal stability of the PCM was evaluated with heat treatments, performed with Terside Carbolite Furnace in Ar atmosphere, at 200°C with different dwell times (0.5, 1, 3 and 5h), as well as with Differential Scanning Calorimetry (DSC25, TA instruments) tests from room temperature to 300°C.

Results and Discussion

The preliminary analyses carried out on A356-Sn with Thermocalc software highlight the appearance of the MG2SI_C1 phase at temperatures close to the pure Sn solidification (Figure 1), i.e., the PCM working temperature range. The definition is referred to either to Mg_2Si or Mg_2Sn, sharing the same crystallographic structure. However, the lower Gibbs free energy for the formation of the latter intermetallic compound suggests MG2SI_C1 to be identified with Mg_2Sn [3].

In addition, the EDS analyses, performed on the micrographs, highlight the tendency of Mg to be dispersed within the Sn-rich phases rather than Si-rich regions.

However, both optical microscopy and XRD tests do not allowed the identification of Mg_2Sn, possibly due to its very small size. On the other hand, SEM investigation revealed the presence of lamellar compounds dispersed in the Sn-rich phases (Figure 2), consistent with Mg_2Sn-Sn appearance [4]. This latter compound seems to be beneficial in terms of adhesion between the Al-rich phase and the Sn phase, which easily detach in the case of the binary Al-Sn alloy.

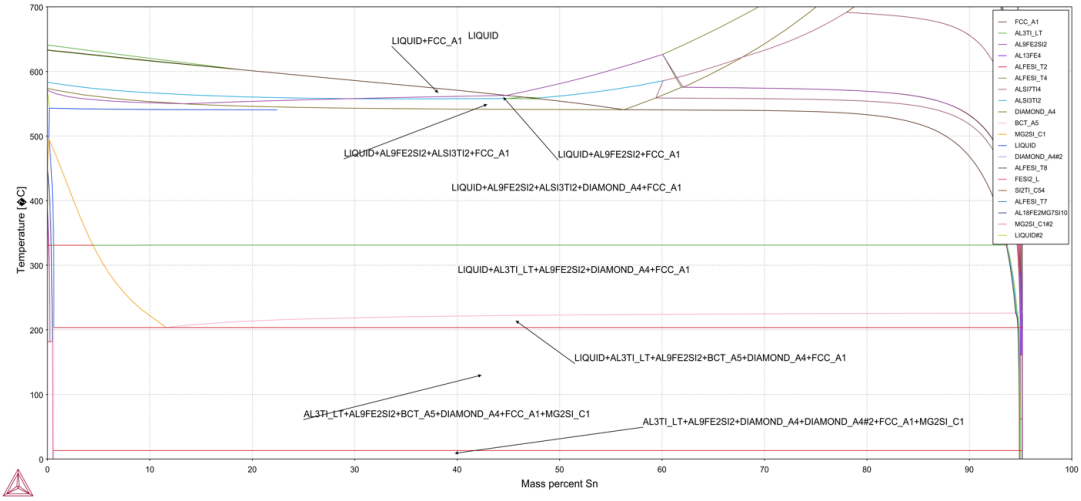

Fig. 1: A356-Sn phase diagram, computed with Thermocalc

The heat treatments performed on A356-Sn and Al-Sn lead to exudation of the low-melting phase only in the first case, in accordance to Thermocalc data. SEM analyses performed on the leaked material, that underwent a re-solidification process, revealed the presence of an eutectic lamellar microstructure (Figure 2), similar to the one detected in the as-produced microstructure. The compositional analyses performed on the lamellae are consistent with the previous hypothesis.

Mg_2Sn melting in A356-Sn, close to 200°C, is detected also by the DSC analyses, in addition to the pure Sn transition, differently from the curve of Al-Sn, which exhibits only this latter phase change. Moreover, Mg_2Sn demonstrates to be stable also under repeated thermal cycles. Hence the presence of this phase does not negatively affect potential use of the alloy as PCM for TES purpose. Besides, it is useful in widening the heat absorption temperature range: the energy is stored over a wider temperature span than in the binary system.

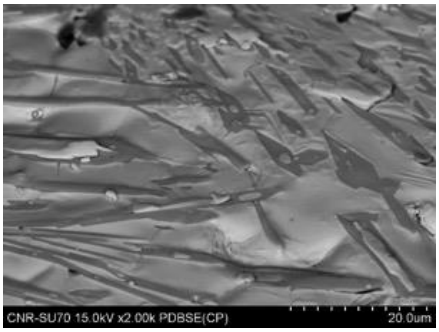

Fig. 2: SEM micrograph of the lamellar structure found in the leaked material from A356-Sn after heat treatment.

This work underpins that the introduction of intermetallics in multicomponent PCM systems is not generally a negative feature, and it can be useful in order to tune activation temperatures and obtaining more flexible devices in term of applications.

References

[1] H. Sugo, E. Kisi, D. Cuskelly, Appl. Therm. Eng. **2013** 51 1345–1350.

[2] P. Bassani, M. Molteni, E. Gariboldi, Materials & Design **2023** 229 111879.

[3] D. Zhou, J. Liu, S. Xu, P. Peng, Comput. Mater. Sci. **2012** 51 409–414.

[4] H.Y. Chen, N. Savvides, Journal of electronic materials **2010** 39 1792–1797.

SCP11.5

Novel processing routes for Ni-Mn-Sn Heusler alloys: Electron beam and laser powder bed fusion

Silja-Katharina Rittinghaus, Hamed Shokri and Bilal Gökce

Materials Science and Additive Manufacturing, School of Mechanical Engineering and Safety Engineering, University of Wuppertal, Gaußstr. 20, 40234 Wuppertal, Germany

Introduction

Additive manufacturing (AM) is a versatile way to consolidate near-net-shape geometries from powder materials while enabling unique microstructures through special cooling conditions. Magnetocaloric alloys are particularly interesting because of their huge potential for magnetic refrigerators and actuator applications. The magnetocaloric effect requires good control of phase transition and magnetism by considering chemistry, microstructure, and ambient conditions to improve functional properties.

A promising group are Ni-Mn-X Heusler alloys with X = In, Sn (or Ga, Al). Especially ferromagnetic alloys of the type $Ni_{50}Mn_{50-y}X_y$ are of particular interest with regard to solid-state refrigeration, exploiting the high potential of the magnetocaloric effect (MCE) [1]. Alloyed with Ga, In, Sn or Sb, the ferromagnetic alloys undergo a coupled spin-lattice martensitic transformation (MT) and generate thermal energy in response to the application of external stimuli, e.g., magnetic fields or pressure [2,3]. Amongst others, $Ni_{50}Mn_{50-y}Sn_y$ has come into focus because of large magnetic entropy changes, and desirable Curie temperatures (T_C ~ 340 K [4]) close to room temperature combined with comparatively good mechanical properties. At the same time, the elements of this alloy type are widely available.

With regard to manufacturing, casting, melt spinning, powder metallurgy, directional solidification and, most recent, additive manufacturing are researched, yielding a wide range of differing properties provided in an extensive overview by [5]. Typical X2YZ Heusler alloys crystallize in a fully ordered structure of $L2_1$-type while increased Y content promotes a $L2_1$-B2-type disordered structure [6]. This makes AM by powder bed fusion (PBF) a feasible considered approach [7], the latest successful demonstration of which by choosing laser radiation as an energy source (PBF-LB) is reported by W. Sun et al. in [5] and K. Sun et al. in [8]. Solids with dimensions of several ten millimeters with a composition of $Ni_{45}Mn_{44}Sn_{11}$ (at.-%) have been built; still, intergranular cracking due to anisotropic volume change during phase transformation remained an issue limiting the structural integrity.

The AM method of Electron Beam Powder Bed Fusion (PBF-EB) not only creates optimal conditions for investigating this particular alloy under oxygen-free atmospheres. PBF-EB is characterized by a much higher energy absorbance and penetration depth compared to PBF-LB (µm- vs. nm-range). Typically, very high preheating temperatures over 1000°C can be applied [9]. Thus, residual stresses are comparatively low [10], favoring this method for manufacturing brittle and crack-sensitive materials [11]. Up to now, research on magnetic materials processed with PBF-EB has been scarce [12]. In [13], the fabrication of fully dense samples out of ball-milled pre-alloyed Al-53Mn (wt.%) powder with PBF-EB could be achieved. In combination with proper annealing, the coercivity was found to equal the one measured in conventionally produced samples. By this, the suitability of PBF-EB to fabricate magnets has been proven. The authors of [14] studied PBF-EB of soft magnetic Fe-6.5Si (wt.%) material. It was shown that by using different processing parameters, magnetic and electrical properties could be adjusted. Despite these individual studies, to the best knowledge of the authors, no processing of magnetic materials with PBF-EB has been reported yet.

Materials and Methods

PBF-EB and PBF-LB of a magnetocaloric Ni-Mn-Sn alloy was experimentally studied. Spherical powder material was produced and analyzed by VTT, Finland with a composition determined by XRF of approx. 47.15Ni-39.2Mn-13.0Sn (at.-%). PBF-EB was performed using a freemeltONE machine by freemelt SE, Sweden. An individually developed spot-melt pattern was selected to consolidate the samples with varied spot distance resulting in applied volume energy densities (E_V) of approx. 20 J/mm³ at a processing temperature of ~700°C. For PBF-LB experiments, an AconityMINI (Aconity GmbH, Germany) was used with melting parameters yielding E_V ~30 J/mm³ and approx. 500°C preheating temperature was applied. As selected geometries, cubes with an edge length of 7 mm (PBF-EB) and 5 mm (PBF-LB) were built. Annealing heat treatment for microstructure homogenization was conducted at 900°C for 20 hrs followed by water quenching. The consolidated material was investigated by LM, SEM, EDS, XRD and PPMS.

Results and Discussion

PBF-EB built samples showed no cracking with a relative density of 99.5% and while no crack-free samples could be achieved in PBF-LB experiments, a maximum relative density of 99.6% was measured. Observed defects are mostly spherical pores of up to 20 (LB) and 40 µm (EB) respectively. Characteristic, perpendicular crack progression in PBF-LB samples indicates that thermal stresses induced by high temperature gradients and cycling reheating exceed the yield point of the material, resulting in presumably sub-solidus cracking along grain boundaries of the brittle material.

EDX measurements revealed post-processing compositions of approx. 43.7Ni-31.7Mn-24Sn (EB) and 43.8Ni-31.4Mn-24.1Sn (LB), indicating a Mn-loss of approx. 1.5 (EB) to 1.7 (LB) ±0.4 percentage points in weight.

Epitaxial grain growth exceeding the respective layer height is visible in both material types and caused by directional solidification, however, is more pronounced in the PBF-LB sample owing to the differences in applied scanning strategies. As expected from estimated differences in cooling rates of at least an order of magnitude, due to larger melt pool sizes and processing temperature in PBF-EB, the grain structure in the PBF-LB samples is comparatively finer. After annealing, both samples show a homogeneously recrystallized grain structure with an average grain size of 70-100 µm. While in the PBF-EB sample the grain structure can be described as equiaxed the original growth direction is still recognizable in the PBF-LB specimen while the grain width remains visibly smaller. The XRD pattern of the PBF-EB sample indicate a two-phase region of presumably $L2_1$ ffc austenite and 4O martensite, while the PBF-LB/M sample shows an almost fully martensitic microstructure. Annealing diminishes the austenite phase fraction. No reflections of secondary phases ($MnSn_2$, MnNi or oxide) are detected, which can be attributed to high processing temperatures. A magnetic entropy change ΔS_{max} under the external field of 1 T of 0.24 J/kg K is determined for PBF-EB/M material compared to 0.21 J/kg K for the respective PBF-LB/M, both in annealed condition.

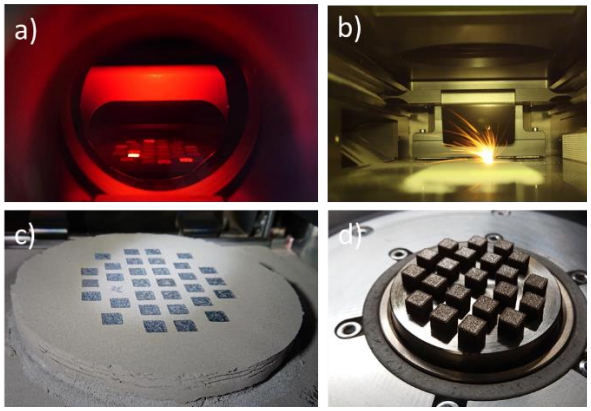

Fig. 1: Processing (a,b) and photographs (c,d) of PBF-EB (a,c) and PBF-LB (b,d) Ni-Mn-Sn samples

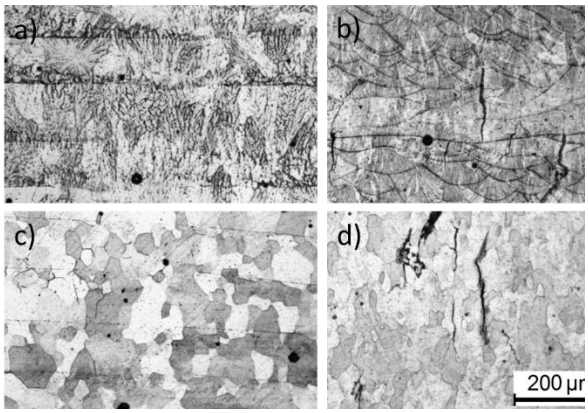

Fig. 2: Microstructure of PBF-EB (a,c) and PBF-LB (b,d) Ni-Mn-Sn samples, as-built (a,b) and heat treated (c,d)

Acknowledgments

We'd like to thank our colleagues from University of Darmstadt, Dr. David Koch and Dr. Enrico Bruder, as well as Dr. Natalia Shkodich and Prof. Farle from University Duisburg-Essen for supporting us with their analytical capabilities and expertise, and Daniel Borchert and Dr. Ingo Erdmann (BUW) for assisting. The production and analysis of the powder material by Juha Lagerbom (VTT) is also highly acknowledged. This research was funded by DFG via CRC/TRR 270, project ID 405553726, GO 2566/10-1-(Project-ID 445127149) and INST 218/90-1 (Project-ID 510085108).

References

[1] Y. Sutou, Y. Imano, N. Koeda, T. Omori, R. Kainuma, K. Ishida, and K. Oikawa, Appl. Phys. Lett. **2004**, 85, 4358 DOI10.1063/1.1808879

[2] L. Manosa, D. Gonzalez-Alonso, A. Planes, E. Bonnot, M. Barrio, J.-L. Tamarit, S. Aksoy, M. Acet, Nat. Mater. **2010**, 9 (6), 478–481, DOI:10.1038/ nmat2731.

[3] H. Hou, S. Qian, I. Takeuchi, Nat. Rev. Mater. **2022**, 7, 633–652, DOI:10.1038/s41578-022-00428-x.

[4] S.M. Podgornykh, S.V. Streltsov, V.A. Kazantsev, E.I. Shreder, Journal of Magnetism and Magnetic Materials **2007**, 311 (2), 530-534, DOI:10.1016/j.jmmm.2006.08.024

[5] W. Sun, X. Lu, Z. Wei, Q. Li, Z. Li, Y. Zhang, J. Liu, Additive Manufacturing **2022**, 59 (A), 103125, DOI:10.1016/j.addma.2022.103125

[6] C. Passamani, V.P. Nascimento, C. Larica, A.Y. Takeuchi, A.L. Alves, J.R. Proveti, M.C. Pereira, J.D. Fabris,Journal of Alloys and Compounds **2011**, 509 (30), 7826-7832, DOI:10.1016/j.jallcom.2011.05.018

[7] V. Laitinen, A. Salminen, K. Ullakko, J. Laser Appl. 31 (2) (2019), DOI:10.2351/1.5096108.

[8] K. Sun, A. E.-M. A. Mohamed, S. Li, M. Jeong, J. Head, M.M. Attallah, Additive Manufacturing **2023**, 69, 103536, DOI:10.1016/j.addma.2023.103536.

[9] C. Körner, M. Ramsperger, C. Meid, D. Bürger, P. Wollgramm, M. Bartsch, G. Eggeler, Metall. Mater. Trans. A **2018**, 49(9), 3781–3792. DOI:10.1007/s11661-018-4762-5

[10] G. Mladenov, E. Koleva, L. Koleva, V. Dzharov, Electrotechnica & Electronica (E+E) **2016**, 51 (5-6), 14-24.

[11] L. Sochalski-Kolbus, E.A. Payzant, P.A. Cornwell, T.R. Watkins, S.S. Babu, R.R. Dehoff, M. Lorenz, O. Ovchinnikova, C. Duty, Metall. Mater. Trans. A **2015**, 46(3), 1419–1432.

[12] Z. Fu, C. Körner, European Journal of Materials **2022**, 2:1, 54-116, DOI:10.1080/26889277.2022.2040342

[13] I.A. Radulov, V.V. Popov Jr., A. Koptyug, F. Maccari, A. Kovalevsky, S. Essel, J. Gassmann, K.P. Skokov, M. Bamberger, Additive Manufacturing **2019**, 30, 100787, DOI:10.1016/j.addma.2019.100787

[14] J. Yang, Z. Fu, J. Ye, D. Kübrich, C. Körner, Scripta Mat. **2022**, 210, 114460, DOI:10.1016/j.scriptamat.2021.114460

SCP11.6

Additive manufacturing of Cu–Al–Ni Shape Memory Alloys with grain refiners

Mikel Pérez-Cerrato[1], José Fernando Gómez-Cortés[1], Ernesto Urionabarrenetxea[2,3], Isabel Ruiz-Larrea[1], Iban González[4], María Luisa Nó[1], Nerea Burgos[2,3] and Jose San Juan[1]

[1]Dpt. of Physics, Faculty of Science and Technology, University of the Basque Country (UPV/EHU), Bilbao, Spain, mikel.perez@ehu.eus, josefernando.gomez@ehu.eus, isabel.ruiz@ehu.eus, maria.no@ehu.eus, jose.sanjuan@ehu.eus

[2]CEIT-Basque Research & Technology Alliance (BRTA), Manuel Lardizabal 15, Donostia, Spain, eugomez@ceit.es, nburgos@ceit.es

[3]Universidad de Navarra, Tecnum, Manuel Lardizabal 13, Donostia, Spain

[4]LEITAT, c/de la Innovació 2, Terrasa, Spain, igonzalez@leitat.org

Introduction

Shape memory alloys (SMAs) are functional materials that are being applied in practically all industries, from aerospace to biomedical sectors, and at present the scientific and technologic communities are looking to gain the advantages offered by the new processing technologies of additive manufacturing (AM). However, the use of AM to produce functional materials, like SMAs, constitutes a real challenge due to the particularly well controlled microstructure required to exhibit the functional property of shape memory. Although Ti–Ni is the most worked SMA, other kinds of SMAs are attracting attention, specifically Cu–based SMAs [1,2]. However, they are challenging for AM processing due to the inherent difficulties to process copper and copper–rich alloys, associated with their high thermal conductivity and the high reflectance of the red and infrared lasers.

In the present work, the design of the complete AM processing route, from powder atomization to laser powder bed fusion (LPBF) for AM and hot isostatic pressing (HIP), is approached for a Cu–Al–Ni SMA (CAN-BZ) with the addition of B and Zr as grain refiners.

Materials and Methods

We produced atomized powders of a 82.2Cu–13.3Al–4.5Ni (%wt.) SMA to feed the AM process through gas atomization. The composition of the alloy was characterized by ICP–OES while the particle size distribution was measured by laser diffraction. The LPBF samples were produced in a Renishaw AM400 machine equipped with a reduced build volume module. We used a variety of different parameters in order to minimize the porosity and optimize the AM process. Samples undergo a HIP post-processing. The microstructure of the LPBF samples was characterized through SEM and EDX, to observe the different phases and compositions. The transformation temperatures, enthalpies and hysteresis were measured via DSC. Finally, we prepared samples to study the shape memory (SME) and superelastic (SE) properties at different temperatures on both tensile and compressive tests.

Results and Discussion

We performed two gas atomizations (of 3kg each) of the previously mentioned Cu–Al–Ni alloy. The composition, particle size distribution and transformation temperatures of the powders were studied and showed an excellent reproducibility of the atomization process. The powders from both atomizations were mixed and sieved to particle sizes between 20 and 45 microns. This was the material used to produce the LPBF samples.

The LPBF samples were made using different sets of parameters. We varied the laser power, hatch distance, scanning speed and exposition time, in order to obtain the best results of minimizing the porosity of the samples. We observe that the laser power is one of the most crucial parameters to take into account. As Cu has a high reflectivity for red lasers, low values of the power do not fully melt the alloy powders, producing a high amount of pores that reached sizes up to 0.5 mm wide. However, adjusting the LPBF parameters correctly, we can obtain samples with high consolidation. A final HIP post-process is used to try to eliminate the remaining porosity. According to the requirements established in previous works [1], the samples are then thermally treated at 900°C and quenched at 0°C to recover the austenitic metaestable phase.

The microstructure of the LPBF samples was characterized in the optical microscope and the SEM. We observe a number of bright inclusions that correspond to the grain refiners. The EDX measurements show that are particles composed mainly of Zr, that appear mainly over grain boundaries but also in the middle of some grains. As the sample transforms at temperatures above room temperature (≈ 65°C), the material is fully transformed into martensite, and the martensite plates are clearly visible in the SEM images (see Fig.1). Even on samples that did not undergo the HIP post-process, a thermal solubilization treatment is necessary to eliminate the precipitation of the stable phases of the Cu–Al–Ni system. This is shown in the DSC calorimetries because, even a small number of precipitates, change the amount of Al in the matrix, which greatly modifies the transformation temperatures of the alloy.

The samples for the tensile tests were electro-cut into dog-bone shaped samples from the LPBF-built prisms. The superelastic tests were performed at different temperatures between 90°C and 150°C, and for maximum strain values. We obtain a full recovery of the deformation up to 2.75% (see Fig.2), and the Clausius-Clapeyron coefficient was determined by measuring the critical stress at different temperatures. On the other hand, we cycled a sample 150 times at 1.5% maximum strain. The results show that the material stabilizes after the first 10 cycles, showing very similar hysteresis after that. Finally, we performed shape memory effect experiments by bending one of the tensile samples at room temperature (martensite phase). After heating the probe with hot air we recorded the full recovery of the deformation as the material transforms back to austenite.
All these results validate the present methodology and the technique of LPBF for the additive manufacturing of Cu–Al–Ni SMAs. However, the design of the alloys, and the optimization of the processing and post-processing parameters are matters that still require further research in order to obtain the best properties out of these kind of materials.

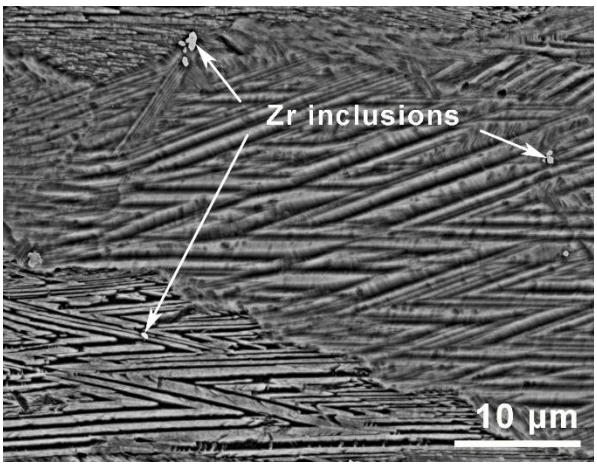

Fig. 1: SEM image of a CAN-BZ LPBF sample. Some inclusions of the Zr grain refiner can be observed, but the material is fully transformed into martensite and with small grain sizes.

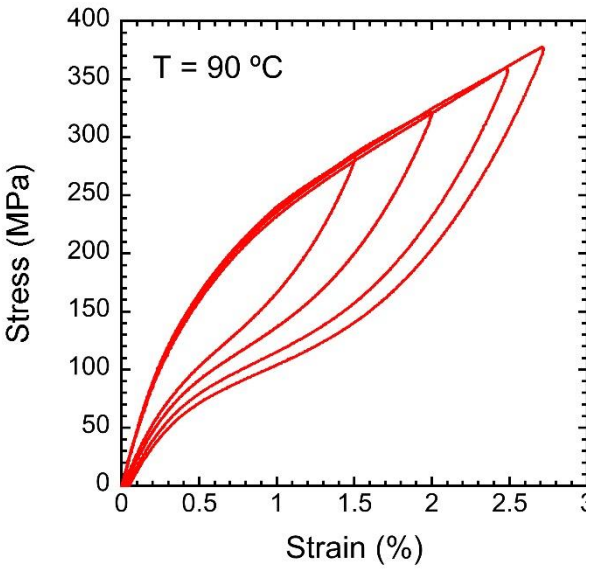

Fig. 2: Tensile superelastic tests at different maximum strain values of a CAN-BZ LPBF sample at a temperature of 90°C. The graphs show a full strain recovery up to 2.75%.

References

[1] M. Pérez-Cerrato, I. Fraile, J.F. Gómez-Cortés, E. Urionabarrenetxea, I. Ruiz-Larrea, I. González, M.L. Nó, N. Burgos, J. San Juan, Materials. **2022**, *15*, 6284.

[2] N. Babacan, S. Pilz, S. Pauly, J. Hufenbach, T. Gustmann, Materials Science & Engineering A. **2023**, 862, 144412.

SCP12.1R

{1$\bar{1}$01} <$\bar{1}$102> twins and {1$\bar{1}$01}-{2$\bar{2}$01}/{2$\bar{2}$01}-{1$\bar{1}$01} double twins in the $D0_{19}$ ordered hexagonal α_2-Ti_3Al phase

Lin Song[1], Fritz Appel[2], Florian Pyczak[2] and Tiebang Zhang[1]

[1]State Key Laboratory of Solidification Processing, Northwestern Polytechnical University, Xi'an, Shaanxi 710072, China, songlin@nwpu.edu.cn, tiebangzhang@nwpu.edu.cn
[2]Institute of Materials Research, Helmholtz-Zentrum Hereon, Max Planck-Str. 1, Geesthacht, 21502, Germany, fritz.appel@hereon.de, florian.pyczak@hereon.de

Introduction

The plastic deformation of α_2-Ti_3Al is known to be very anisotropic. The shear components could be generated by glide of <*c*+*a*> type dislocations on pyramidal planes, but this is strongly hindered by high glide resistance and therefore only occurs in exceptional cases [1]. In contrast to disordered HCP metals, the α_2-Ti_3Al phase is reluctant to twin deformation, although its *c/a* ratio is similar to that of the disordered α-Ti, when ordering of the α_2 phase is disregarded. This is mainly due to the large order shuffles, which are required to restore the $D0_{19}$ structure in the twin [2]. However, twin structures were observed in Al-rich single phase α_2 alloys as well as in the α_2 phase of multiphase titanium aluminide alloys [3, 4]. More recently, a unique type of successive internal {20$\bar{2}$1}<$\bar{1}$014> twins was reported, which was believed to accommodate the local <*c*+*a*> shear [5]. the existence of {1$\bar{1}$01}<$\bar{1}$102> twin, which are common in disordered HCP metals, have not yet been reported for the α_2 phase. In this study, the observation of these twins is reported, and two types of double twins ({1$\bar{1}$01}-{2$\bar{2}$01} and {2$\bar{2}$01}-{1$\bar{1}$01}) are observed. The variant selection mechanism of the secondary twin is also discussed.

Materials and Methods

Cylinders with the dimension of Ø8 mm×12 mm were cut from of the as-cast Ti-45Al-8.5Nb-0.2W-0.2B-0.02Y alloy (prepared by plasma-arc melting) and hot compressed at 800°C and strain rate 0.001 s^{-1} to a strain of 0.3 in a Gleeble 3500 equipment. The stress strain curve is typically characterized by a rise to a plateau followed by a period of steady state flow stress of about 850 MPa. After deformation, slices for transmission electron microscopy (TEM) observation were cut parallel to the loading direction, and TEM foils were prepared by a twin-jet polishing method. TEM and high-resolution TEM (HRTEM) observations were conducted on a FEI TITAN 80-300 microscope operated at 300 kV. To observe the deformation twins in the α_2 phase, all the TEM images are obtained with the beam parallel to the $[11\bar{2}0]_{\alpha 2}$ direction. The lattice parameters of the α_2 phase are a=0.563 nm, c=0.458 nm, with c/a=0.81.

Results and Discussion

The multi-beam micrograph below shows a relatively wide α_2 lamella with three polygon-like areas that were imaged brighter than the rest of the lamella (indicated by yellow arrowheads). Therefore, these α_2 domains were reoriented during compression. The diffraction pattern of the area includes both the parent α_2 lamella and part of the reoriented domain. The α_2 phase is easily recognized in the two areas by its superlattice diffraction spots. There appears to be a twin relationship between the parent α_2 lamella and the reoriented domain, as illustrated in the diffraction pattern. The approximate twinning plane was estimated as (1$\bar{1}$01). The {1$\bar{1}$01} twin interface are asymmetrical interface facets that place {0$\bar{1}$10} prismatic (P) and (0001) basal (B) planes face-to-face. The twinned domains therefore do not have the lenticular shape commonly observed in mechanical twins but have a more equiaxed shape. Two types of double twinning were observed involving {1$\bar{1}$01} and {2$\bar{2}$01} twins. Secondary twinning occurred within primary {2$\bar{2}$01} twins and vice versa. The rotation of the grains in the twinned region leads to a relatively good fit of the double twinned α_2 domain (DTW) with the adjacent γ_T domain, resulting in the well-known Blackburn orientation relationship at their common interface, which indicate that variants are selected under the condition that the smallest possible mismatch with the surrounding structure is achieved. However, only the [$\bar{1}$102] shear variant is suitable for the secondary twin to ensure the consistent plane or shear and the overall shear continuity at this local position, i.e., the shear transfer across the lamellar interface.

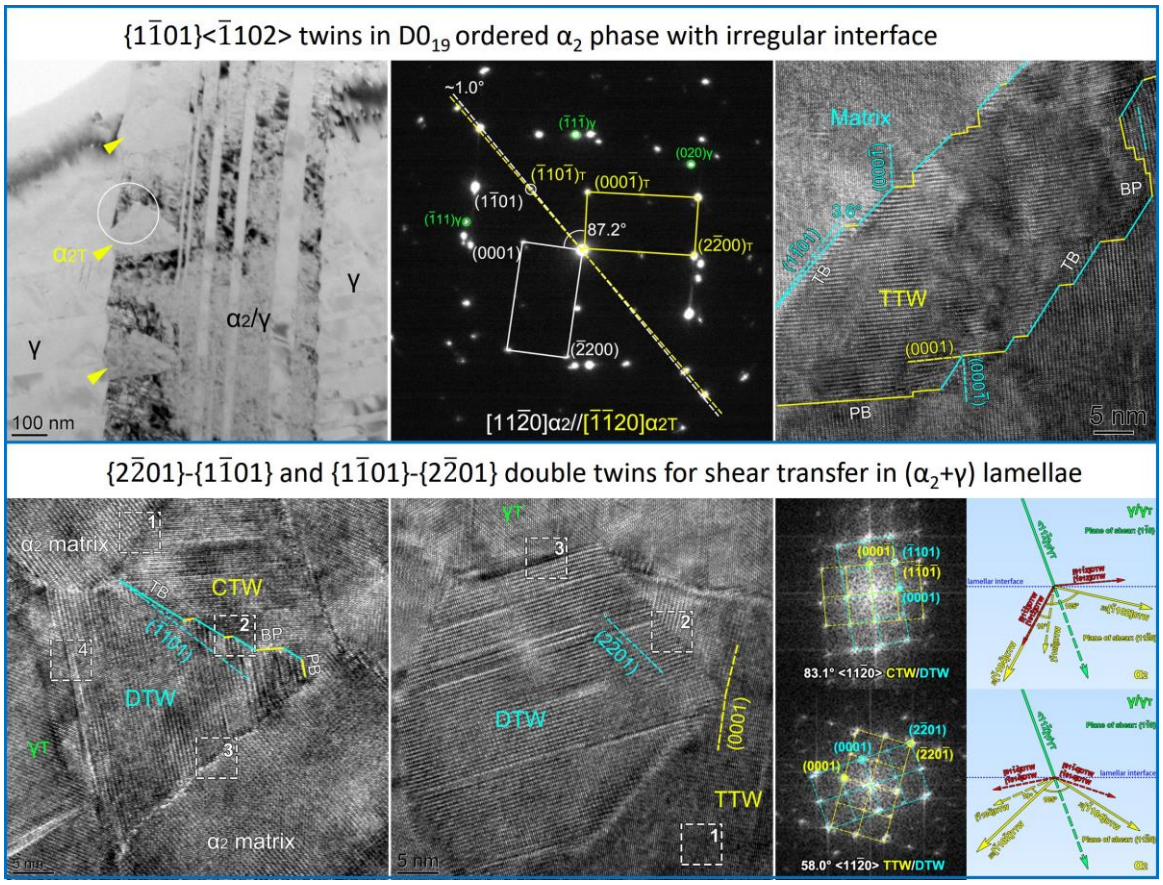

Fig 1: The morphology and diffraction patterns of the {1$\bar{1}$01}<$\bar{1}$102> twin and {1$\bar{1}$01}-{2$\bar{2}$01}/{2$\bar{2}$01}-{1$\bar{1}$01} double twins. The twin interface is composed of PB/BP segments and non-ideal twin plane segments. The shear accommodation across the lamellar interface is schematically shown.

References

[1] H. Inui, Y. Toda, Y. Shirai, M. Yamaguchi. Philos. Mag. A 69 (1994) 1161-1177.
[2] J.W. Christian, D.E. Laughlin. Acta Metall. 36 (1988) 1617-1642.
[3] H.A. Lipsitt, D. Shechtman, R.E. Schafrik. Metall. Trans. A 11A (1980) 1369-1375.
[4] P. Wang, D. Veeraraghavan, V.K. Vasudevan. Scripta Mater. 34 (1996) 1601-1607..
[5] L. Song, F. Appel, F. Pyczak, Z.B. He, J.P. Lin, T.B. Zhang. Acta Mater. 222 (2022) 117391.

SCP12.2

An application of the handedness sensitive microstructure analysis: EBSD and HR-STEM investigations of the transition region between the enantiomorphs in non-centrosymmetric CoSi

Ulrich Burkhardt, Wilder Carrillo-Cabrera, Paul Simon and Yuri Grin

Max Planck Institut für Chemische Physik fester Stoffe, Nöthnitzer Straße 40, 01187 Dresden, Germany, ulrich.Burkhardt@cpfs.mpg.de; Wilder.Carrillo-Cabrera@cpfs.mpg.de, Paul.Simon@cpfs.mpg.de, Juri.Grin@cpfs.mpg.de

Introduction

Intermetallic phases with B20 structure (FeSi type) have been the subject of many investigations for some time, since some representatives of the structure type can exhibit unusual electronic (charge density waves, superconductivity) and/or magnetic order states (skyrmions and other helical orders) [1]. The structure type is very unusual in many respects, since both elements have the same coordination number 7, the crystal structure is chiral, and both enantiomorphs are described by the symmetry of the same space group ($P2_13$; #198). Of particular importance for the unusual physical and chemical properties seems to be the chirality i.e. the absence of mirror planes and inversion centers in the crystal structure. Perturbations of the real structure such as twinning where mirror planes or inversion centers occur are therefore of particular interest. In the present work, twinned crystallites (single crystal XRD) of CoSi phase (FeSi type) have been studied by HR-STEM. The aim is to develop a model for the transition region between the enantiomorphs which describes the change of handedness. Of key importance here is the spatially resolved determination of handedness in a polycrystalline material using EBSD.

Materials and Methods

Polycrystalline crystallites were prepared by chemical gas transport using iodine as a transport agent, studied metallographically, and characterized by EBSD measurements (Bruker CrystAlign EBSD system). The handedness is assigned by the EBSD pattern evaluation using the full pattern matching approach as described in [2]. The enantiomorph distribution map prepared in this way allows to localize the transition regions between the enantiomorphs in the microstructure. FIB sections (Quanta 200 3D ion/electron dual beam; FEI Company) perpendicular to the boundary line between domains of different chirality provided TEM lamellae with [001], [10-1] and [101] orientation. The arrangement of atoms was studied by HR-STEM (300 kV JEM-ARM300F, Jeol TEM).

Results and Discussion

In former projects it was shown that the EBSD method can be used to determine the handedness of chiral phases reliably with sub-micrometer spatial resolution in polycrystalline materials [2]. The actual EBSD analyses revealed that the CoSi crystallites are built up by several grains of both enantiomorphs. Moreover, several grains with uniform crystallographic orientation according to conventional EBSD analysis are formed by well-defined domains with different handedness. The HR-STEM images of these transition regions confirm the change of the handedness. They are well described by the projection of both enantiomorphs. Nevertheless, the EBSD based handedness assignment is important for the interpretation of the HR-TEM images. Atomic arrangements, that are not known from the undisturbed CoSi structure are observed only in a very narrow transition region. The model describing the transition in the handedness is essentially based on a common atomic segment which is stacked in different ways in the two enantiomorphic structure variants.

Acknowledgment

The authors thanks Marcus Schmidt (MPI-CPfS) for sample preparation by CVT, Markus König (MPI-CPfS) for FIB preparation, Horst Borrmann (MPI-CPfS) for single crystal XRD, and Aimo Winkelmann (AGH, Krakow, Poland) for EBSD pattern evaluation.

References

[1] D.S. Sanchez; I. Belopolski; T.A. Cochran; X. Xu, J.-X. Yin; G. Chang; W.I Xie; K. Manna; V. Süß; Ch.-Yi Huang; N. Alidoust; D. Multer; S. S. Zhang; N. Shumiya; X. Wang; G.-Q. Wang; T.-R. Chang, C. Felser, S.-Y. Xu; S. Jia; H. Lin, and M. Z. Hasan Nature **2019** 567, 500–505.

[2] U. Burkhardt, H. Borrmann, P. Moll, M. Schmidt, Yu. Grin, A. Winkelmann, A., Scientific Report **2020** 10:4065

SCP12.3

Analysis of interatomic interactions in the vicinity of lattice defects in Mg_2Ge and Ni_3Si intermetallics

Martin Zelený[1], Ondřej Fikar[1] and Martin Friák[2]

[1]Institute of Material Sciences and Engineering, Faculty of Mechanical Engineering, Brno University of Technology, Technická 2896/2, Brno, CZ-61669, Czech Republic, zeleny@fme.vutbr.cz, ondrej.fikar@vutbr.cz
[2]Institute of Physics of Material, Czech Academy of Sciences, Žižkova 22, Brno, CZ-61600, Czech Republic, friak@ipm.cz

Introduction

Defects in crystal lattices are critically important for many properties of metallic materials and their thermodynamic stability. Due to the fact that solely pairwise interactions are not able to described the energetics of systems with transition metals containing defects, inclusion of more complicated interactions is usually needed [1]. In order to obtain characteristics of these interactions, an analysis of changes in interatomic bonding induced by defects is often employed to reveal the exact nature of defect-related phenomena. Moreover, the interatomic interactions in the vicinity of a defect in intermetallic compounds differ from those in ordinary metals because of the constraints imposed on the defects by the superlattice crystal structure [2], which make the analysis even more complex.

The way of judging the strength of an interatomic bond from the point of view of lattice dynamics is based on a projection of the force constant obtained from phonon calculation on the unit vector along each bonding direction. It provides information about "bond stiffness" for a particular pair of atoms [3]. To get a deeper insight into mutual chemical interaction between individual atoms we employed the analysis of crystal orbital Hamilton population (COHP) [4], which helps us to identify weaker chemical bonds in the vicinity of defects. Here a negative value of COHP represents bonding interaction in particular bands, whereas a positive COHP corresponds to antibonding interactions. Bands which do not participate in bonding between particular atoms do not appear in COHP curves. Thus, an integral of COHP up to Fermi level (ICOHP) represents the "chemical strength" of interaction between two atoms, where more negative value of ICOHP means a stronger interaction [5].

In the present work, we analyze the first- and second-nearest-neighbor interactions in (i) the vicinity of Sn substitutional impurity in Mg_2Ge intermetallic with antifluorite structure and (ii) Σ5(210) grain boundaries (GBs) in Ni_3Si intermetallic with Cu_3Au structure. In addition, we also analyze the effect of Al impurity segregated in Ni_3Si GB.

Materials and Methods

The information about interatomic interactions in studied systems has been obtained by ab initio calculations performed with help of Vienna Ab initio Simulation Package (VASP) [6,7] in which the electron-ion interaction was described by potentials based on projector augmented-waves method [8]. Regarding the exchange and correlation energy, we employed the generalized gradient approximation as parametrized by Perdew, Burke, and Ernzerhof [9]. Lattice-dynamics calculations were performed with the Phonopy [10] package via the supercell finite-displacement method [11]. The COHP analysis is based on projection of plane waves to a local basis [12] implemented in the program LOBSTER 2.1 [13,14]. The obtained information about strength of interatomic interactions is visualized using the VESTA package [15].

Results and Discussion

In case on Sn impurity in Mg_2Ge we expect that a Sn atom will substitute atoms in Ge sublattice, because Mg_2Ge and Mg_2Sn exhibit the same structure. The bond stiffness of bonds between the impurity atom and its first nearest neighbors, i.e. Sn-Mg bonds, is significantly higher than bond stiffness of Mg-Ge bonds in bulk Mg_2Ge. The bond stiffness increases from 1.65 eV/Å to 2.17 eV/Å. This increase corresponds very well to the reported higher heat capacity of Mg_2Sn compare to Mg_2Ge [16]. The other first-nearest-neighbor bonds, i.e. Ge-Mg bonds as well as Mg-Mg bonds in the structure seem to be not affected by the presence on the impurity.

Regarding the second system, two different chemical compositions of Σ5(210) in Ni_3Si are considered in this work. The GB plane could contain either solely Ni (denoted as $\Sigma5(210)^{Ni,Ni}$) or both Ni and Si atoms ($\Sigma5(210)^{Si,Ni}$). The GB variant containing both Ni and Si atoms at the interface is shown to be unstable with respect to a shear deformation. The COHP and bond stiffness analysis reveal that this instability originates in a weak interaction far from the GB interface between the Ni atoms in the 3rd plane and the atoms in the 4th, 5th, 6th plane (see blue arrows in Fig. 1). The bond stiffness decreases from 3.35 eV/Å to 0.68 eV/Å and 1.12 eV/Å in case of Ni-Ni bonds and from 1.40 eV/Å to 0.11eV/Å in case of Ni-Si bond. However, this bond weakening is a consequence of a very strong interaction between the Si atoms in the GB plane and Ni atoms in the 3rd plane of the GB interface (see

red arrows in Fig. 1) [17]. The bond stiffness increases from 1.40 eV/Å to 2.43 eV/Å. The described bond weakening was not observed in $\Sigma5(210)^{Ni,Ni}$ GB and when Si atom at the GB $\Sigma5(210)^{Si,Ni}$ is replaced by Al.

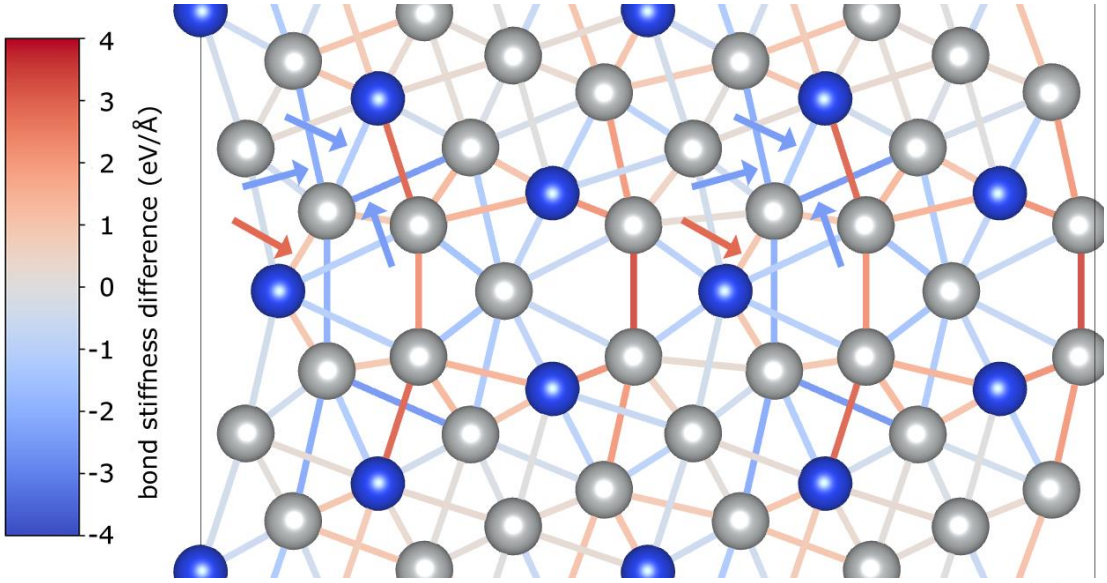

Fig. 1: The bond stiffness difference with respect to bulk values in the vicinity of GB plane in $\Sigma5(210)^{Si,Ni}$ of Ni_3Si. The blue atoms correspond to Si and gray atoms to Ni.

Acknowledgement

The authors acknowledge the Czech Science Foundation for the financial support within the Project No. 22-22187S. The theoretical calculations were performed at the IT4I facilities, which are supported through the project e-INFRA CZ [ID:90140].

References

[1] M.H. Müser, S.V. Sukhomlinov, L. Pastewka, Adv. Phys. X. **2023**, *8*, 2093129.
[2] Y.Q. Sun, MRS Bull. **1995**, *20*, 29–36.
[3] V.L. Deringer, R.P. Stoffel, M. Wuttig, R. Dronskowski, Chem. Sci. **2015**, *6*, 5255–5262.
[4] R. Dronskowski, P.E. Bloechl, J. Phys. Chem. **1993**, *97*, 8617–8624.
[5] T. Hughbanks, R. Hoffmann, J. Am. Chem. Soc. **1983**, *105*, 3528–3537.
[6] G. Kresse, J. Hafner, Phys. Rev. B. **1993**, *47*, 558–561.
[7] G. Kresse, J. Furthmüller, Phys. Rev. B. **1996**, *54*, 11169–11186.
[8] G. Kresse, D. Joubert, Phys. Rev. B. **1999**, *59*, 1758–1775.
[9] J.P. Perdew, K. Burke, M. Ernzerhof, Phys. Rev. Lett. **1996**, *77*, 3865–3868.
[10] A. Togo, I. Tanaka, Scr. Mater. **2015**, *108*, 1–5.
[11] K. Parlinski, Z.Q. Li, Y. Kawazoe, Phys. Rev. Lett. **1997**, *78*, 4063–4066.
[12] V.L. Deringer, A.L. Tchougréeff, R. Dronskowski, J. Phys. Chem. A, **2011**, *115*, 5461–5466.
[13] S. Maintz, V.L. Deringer, A.L. Tchougréeff, R. Dronskowski, J. Comput. Chem. **2013**, *34*, 2557–2567.
[14] S. Maintz, V.L. Deringer, A.L. Tchougréeff, R. Dronskowski, J. Comput. Chem. **2016**, *37*, 1030–1035.
[15] K. Momma, F. Izumi, J. Appl. Crystallogr. **2011**, *44*, 1272–1276.
[16] S. Ganeshan et al., Journal of Alloys and Compd. **2010**, *498*, 191-198.
[17] M. Friák, M. Zelený, M. Všianská, D. Holec, M. Šob, Materials. **2018**, *11*, 2263.

SCP12.4

Anti-Phase Domain Formation According to Ordering of Carbon in $E2_1$ Co_3AlC_{1-x} Based Alloys and Effects of APD Size on Deformation Behavior

Yoshisato Kimura and Yaw Wang Chai

Tokyo Institute of Technology, School of Materials and Chemical Technology, Department of Materials Science and Engineering, Mail-box J3-19, 4259 Nagatsuta-cho, Midori-ku, Yokohama, Kanagawa 226-8502, Japan, kimura.y.ac@m.titech.ac.jp, chai.y.aa@m.titech.ac.jp

Introduction

The intermetallic compounds $E2_1$ M_3AlC_{1-x} exist as a stable phase widely in the alloy systems where M is Co, Ni, Fe, Mn, Ti, and so forth. The $E2_1$ ordered structure can be regarded as the ternary $L1_2$ ordered structure being stabilized by an interstitial carbon atom at the cell center. Note that $L1_2$ Co_3Al does not exist as a stable phase in the binary system. Since the $E2_1$ ordered structure quite resembles that of the $L1_2$ Ni_3Al, which is well-known strengthener of Ni-base superalloys, $E2_1$ M_3AlC_{1-x} could be a potential candidate of heat resistant alloy or strengthener. In the chemical formula of Co_3AlC_{1-x}, *x* stands for the deficiency of a carbon atom as a vacancy at the carbon-site of the $E2_1$ cell center. Authors' research group reported that the extra ordering of C atoms occurs along with the phase transition from $E2_1$ Co_3AlC_{1-x} to $E2_1$' $Co_3AlC_{0.5}$ at T_c around 1325 K. Here, the $E2_1$' ordered structure is consisting of four $E2_1$ and four $L1_2$ unit cells as shown in Fig. 1(a). The anti-phase boundary (APB) is formed according to the ordering of carbon atoms, being related to two variants regarding the carbon atom sites. The size of anti-phase domain (APD) varies depending on heat treatment conditions particularly on the cooling rate at the ordering temperature, as shown in Fig. 1 (b) coarse APD by slow cooling and (c) fine APD by rapid cooling. It was reported by our research group that $E2_1$' $Co_3AlC_{0.5}$ shows excellent ductility and relatively high strength at ambient temperatures in poly- and single-crystal alloys, which can be attributed to the alternate stacking of carbon-containing $E2_1$-(111) planes and carbon-free $L1_2$-(111) planes in the $E2_1$' ordered structure [1,2]. It is interesting that the interaction between slip dislocations and APBs, hence the APD size, affects strength and ductility. Hereafter ordered structures of $E2_1$ and $E2_1$' are simply denoted as $E2_1$. The operative slip systems of $E2_1$ Co_3AlC_{1-x} are the octahedral slips, which are the same as $L1_2$ Ni_3Al. On the other hand, the possibility of the cube slip at higher temperatures has not confirmed so far. The objective of the present work is firstly to understand the relative phase stability between $E2_1$ and $E2_1$' by the evaluation of the size of APD being formed due to the ordering of carbon. Moreover, we focused the effects of APB and APD size on deformation behavior of $E2_1$ Co_3AlC_{1-x} based alloys in this research.

Materials and Methods

Single crystal and/or single phase polycrystal alloys of the $E2_1$ Co_3AlC_{1-x} were fabricated by the unidirectional solidification using the optical floating zone melting method (OFZ) under the flowing argon gas atmosphere with positive pressure. Prior to the OFZ, high-carbon mother ingots were prepared using the induction melting in an alumina crucible, and subsequently the alloy ingots were prepared using the arc-melting. The additions of quaternary elements such as Ni, Fe, Mn, and Cr were conducted to examine the relative phase stability between $E2_1$ and $E2_1$'. Changes in the ordering temperature were considered by the evaluation of APD size formed under the same cooling rate condition. Compression tests were performed from room temperature to 1273 K at the initial strain rate 1.4×10^{-4} s^{-1} using 3 x 3 x 6 mm^3 specimens. The crystallographic orientation was analyzed using the back reflection Laue method to select the loading axis for compression tests. Microstructure was observed and analyzed using scanning and transmission electron microscopy for OFZ as-grown samples before and after deformation in compression, and APD size were measured using the image analysis for various heat-treated samples.

Results and Discussion

The APD size varies depending on the cooling rate passing through the ordering temperature T_c, transition from carbon-disordered $E2_1$ to carbon-ordered $E2_1$', as mentioned in the introduction and shown in Fig. 1 (b) and (c). In general, the APD size is governed by the balance between nucleation rate and growth rate. High cooling rate enhances the nucleation rate through gaining large super cooling ΔT, while it decreases the growth rate which is controlled by diffusion. Effects of the quaternary addition of X on the averaged APD size are shown in Fig. 2, where X is 3d transition metal elements, Ni, Fe, Mn, ad Cr. It should be noted that $E2_1$ M_3AlC_{1-x} exists as a stable phase where M is Ni, Fe, and Mn, but for Cr. Provided that the ordering temperature is lowered by the addition of element X, ΔT becomes larger under the same cooling rate condition, and thereby, averaged APD size tends to become finer because of enhanced nucleation rate and supressed diffusion-controlled growth rate. It is indicated in Fig. 2 that all the X elements reduce the ordering temperature, and the effect of reducing the

ordering temperature is stronger in Fe and Mn than in Cr and Ni. In terms of phase stability, comparing with Cr and Ni, Fe and Mn must have stronger effect to stabilize carbon-disordered $E2_1$ phase relatively to carbon-ordered $E2_1$' phase. It corresponds to the fact that the ordering of carbon atoms takes place in Co_3AlC_{1-x} phase as well as in $(Co,Ni)_3AlC_{1-x}$ continuous solid solution phase, while it never occurs in Fe_3AlC_{1-x} nor Mn_3AlC_{1-x}. Based on the recent results, we assume not only quaternary element substitution but also off-stoichiometric composition, Co-rich or Al-rich, may affect the relative phase stability between $E2_1$ and $E2_1$'.

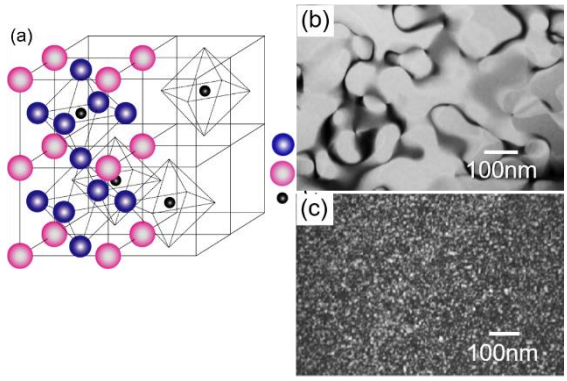

Fig. 1: (a) Unit cell of $E2_1$' $Co_3AlC_{0.5}$ ordered structure consisting of four $E2_1$ and four $L1_2$ unit cells. TEM 1/2(111) dark field image of (b) coarse APD formed in OFZ as-grown sample, and (c) fine APD formed by water quenching from 1373 K.

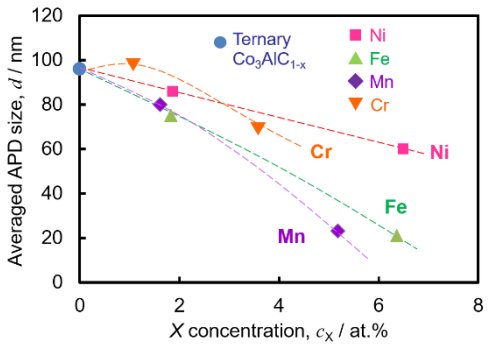

Fig. 2: Averaged APD size of $E2_1$ Co_3AlC_{1-x} based alloys as a function of quaternary element X concentration, where X is Ni, Fe, Mn, and Cr. All the samples were air-cooled from 1373 K after holding for an hour in the Ar gas atmosphere.

The $E2_1$ Co_3AlC_{1-x} OFZ as grown single crystal, having the coarse APD (Fig. 1(b)), shows high critical resolved shear stress of about 400 MPa for the octahedral slip with the loading axis normal to (123) plane in compression, and exhibit excellent ductility of virtually unlimited plastic strain. It was revealed by TEM observation that dislocations with a relatively high density are tangled and stacked at the APBs, which indicates that the APB works effectively as the high resistance against the dislocations glide. On the other hand, $E2_1$ Co_3AlC_{1-x} single crystal being water-quenched from 1373 K, having the fine APD (Fig. 1(c)) as a result, fractures in the elastic region at high stress level and shows almost no plastic deformability. It should be dominant cause that a high density of APBs increases the strength through the interaction with dislocations. Additionally, the degree of order could be quite low in the fine APD, which results in the situation that octahedral dislocation slip is not fully allowed since carbon-free $L1_2$-(111) planes are not formed sufficiently. The relationship between the critical pop-in load P_c and corresponding excursion depth h was reported by our research group for $E2_1$ Co_3AlC_{1-x} using nanoindentation [3]. It is surprising that coarse APD specimens show remarkably high P_c values around 1000 N and quite large h values around 40 nm. Once the dislocations are successfully generated at sufficiently high density, they could easily glide for a certain distance. Contrary to this, fine APD specimens show high P_c values around 800 N but small h values around nm. The fine APD results in the restriction of the dislocation glide, while high density of APBs can be the effective dislocation generation source, which may enable multiplication of mobile dislocations at extremely high stress level.

Acknowledgement

This work was partially supported by the JSPS Grant-in-Aid for Scientific Research, Challenging Research (Exploratory) No.17K18977.

References

[1] Y. Kimura, K. Sakai, Y. Mishima, Phase Equilibria and Diffusion. **2006**, *27*, 14-21.
[2] Y. Kimura, K. Sakai, F.G. Wei, Y. Mishima, Intermetallics. **2006**, *14*, 1262-1269.
[3] Y. Kimura, S. Murasue, Y.W. Chai, M. Watanabe, and T. Ohmura, Proceedings Intermetallics 2021, Eds. M. Heilmaier, M. Krüger, S. Mayer, M. Palm, F. Stein, **2021**, 111–112.

SCP13.1

Interaction of High-Entropy Alloys with Hydrogen, Nitrogen and Carbon under High-Pressure High-Temperature

Kirill Yusenko[1], Konstantin Glazyrin[2], Kristina Spektor[2], Weiwei Dong[2] and Maxim Bykov[3]

[1]Bundesanstalt für Materialforschung und – prüfung (BAM), D-12489 Berlin, Germany
[2]Photon Sciences, Deutsches Elektronen-Synchrotron, Notkestr. 85, 22607 Hamburg, Germany
[3]Institute of Inorganic Chemistry, University of Cologne, Cologne, Germany

Introduction

High-entropy alloys (HEAs) show outstanding constructional and functional properties. HEAs behaviour has been studied in many details including experiments under ambient and extreme conditions [1-3]. HEA's have simple crystal structures combining long range periodicity and high degree compositional disorder on the atomic level. Structural and mechanical stability of high-entropy alloys under extreme conditions emphasizes their potential for general and special applications. Originally developed as materials for structural applications, high-entropy materials were intensively studied as functional and energy-related materials within the fields of catalysis and energy storage.

Binary and ternary metal hydrides were proposed as promising candidates for hydrogen storage applications in fuel cells. At the same time, refractory high entropy alloy *bcc*–TiVZrNbHf can absorb much higher amounts of H_2 than its individual components and reach an H:M ratio of 2.5:1 [4]. Such high H_2 content has never been observed in hydrides based only on transition metals and can be explained by the lattice strain in the alloy that makes it favourable to absorb H_2 in both tetrahedral and octahedral interstitial sites. This observation published in 2016 stimulated finding of several Ti and Mg based HEAs with high H_2 uptake, and it illustrates that HEAs can potentially be used for H_2 storage. Only a few ternaries and HEA's have been characterized under compression with H_2. Their phase transformations are considered to be much more complex in comparison with pure metals and binaries.

In the current study, we investigate an interaction under high-pressure high-temperature of single phase *fcc*-, *hcp*- and *bcc*-structured high-entropy alloys with hydrogen, carbon and nitrogen to obtain high-entropy hydrides, carbides and nitrides. Structural changes in high-entropy alloys upon compression and heating in the presence of these light elements are in the focus of our investigation. An easy route to high-entropy hydrides, carbides and nitrides will open new synthetic horizons in compositionally complex materials. Our study suggests that high-entropy alloys form high-entropy hydrides mainly with a composition close to M:H 1:1 ratio. Hydrides can be obtained under compression with hydrogen as a pressure compression medium or using hydrogen fluid as reactive agent.

Materials and Methods

Here we report investigations of platinum group metals (PGM) alloys *fcc*–$Ir_{0.231(2)}Os_{0.090(1)}Pt_{0.273(1)}Rh_{0.302(2)}Ru_{0.104(2)}$, *hcp*–$Ir_{0.19(1)}Os_{0.22(1)}Re_{0.21(1)}Rh_{0.20(1)}Ru_{0.19(1)}$, and 3d-element based *fcc*–$Al_{0.3}CoCrFeNi$. High-pressure experiments using diamond anvil cells were performed up to 50 GPa at the ESRF (ID15B beamline) or PETRA III (P02.2 beamline) synchrotron facilities. All compressibility curves (He, Ne pressure media) were collected at room temperature with ruby or gold powder as internal pressure calibrants. Similar experiments were performed in hydrogen or nitrogen as pressure transmitting media and reactive agents. Further heating has been performed using laser heating systems installed at the synchrotron facilities. High-temperature high-pressure reaction with carbon and hydrogen fluid with relatively large samples at 10 GPa has been studied in the Hall-type 6 ram large volume multi anvil press Aster-15 (MAVO press LPQ6-1500-100) installed at the P61B energy-dispersive beamline at the PETRA III synchrotron facility.

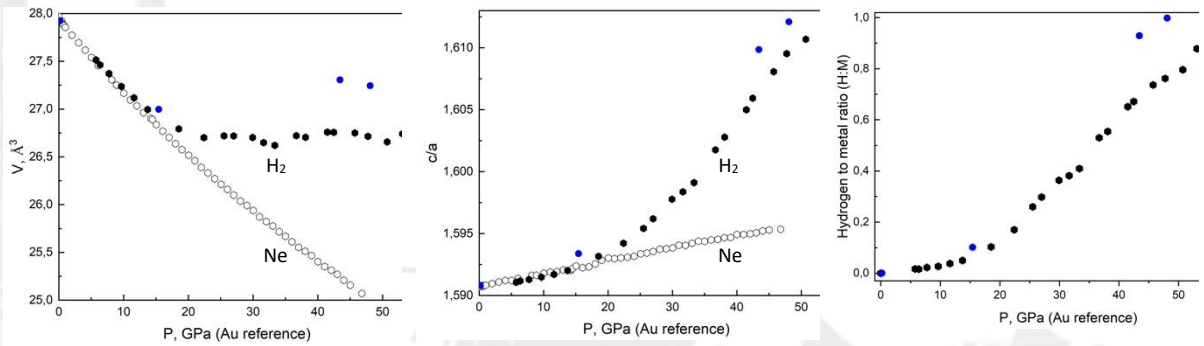

Fig. 1. Room temperature compression of *hcp*–$Ir_{0.19}Os_{0.22}Re_{0.21}Rh_{0.20}Ru_{0.19}$ in hydrogen-loaded DACs. Left: Volume *vs. P*; Middle: *c/a vs. P;* Right: hydrogen composition *vs. P*. Open hexagons correspond compression in Ne as pressure transmitting media and reference equation of state line; black hexagons correspond to compression in H_2; blue circles correspond to decompression in H_2.

Results and Discussion

Previously compressibility and phase transformations in a set of ultra-incompressible binary (*fcc* and *hcp* Ir–Os, Ir–Re, Pt–Os, Rh–Ir, Ru–Ir), ternary (Ir–Ru–Os), and HEAs (*hcp*–$Ir_{0.19}Os_{0.22}Re_{0.21}Rh_{0.20}Ru_{0.19}$ and *fcc*–$Ir_{0.26}Os_{0.05}Pt_{0.31}Rh_{0.23}Ru_{0.15}$) were studied in DACs. To obtain refractory multicomponent alloys, we developed a single-source precursors strategy [1-3]. Our approach allows us to prepare powdered homogeneous alloys with discrete pre-specified composition free from effects of preferential orientation and mechanical stress. Our study of the compression of *hcp*–$Ir_{0.19}Os_{0.22}Re_{0.21}Rh_{0.20}Ru_{0.19}$ in H_2-loaded DACs at ambient temperature suggests the hydrogen uptake above 12-15 GPa (Fig. 1). Alloys investigated do not form any intermetallic compounds and stable against H_2 at low pressures and adsorb large amount of H_2 only above 20 GPa without large expansion which makes them surprisingly perspective as H_2-corrosion resistant materials at low pressures. At higher pressures, the hydrogen-loaded phase at 53 GPa corresponds to an H:M ratio of 0.88:1. Uptake under compression seems to be efficient and characterized by a broad hysteresis upon decompression. We also noted that nearly complete H_2 desorption (according to unit cell volume) in *hcp*–$Ir_{0.19}Os_{0.22}Re_{0.21}Rh_{0.20}Ru_{0.19}$ occurs without heating which makes the system much more efficient as H_2 storage material (if not for high pressure). The hysteresis on decompression could related with slower kinetics of desorption. Our study using pulsed laser heating suggest decomposition of *hcp*-PGM HEA in the presence of H_2 at the area heated by laser. The observations include phase separation (*hcp+fcc* mixture) and formation of primitive cubic structure, similar to [5].

Aluminium substituted *fcc*–$Al_{0.3}$CoCrFeNi HEA also shows complex behaviour upon hydrogen absorption (Fig. 2). Upon heating at 10 GPa, above 400 °C the system decomposes into two phases: H-rich HEA as major phase with M:H 1:0.8 composition, retaining the *fcc* structure, and new minor H-deficient HEA with additional diffraction lines at *d* = 1.3 and 1.2 Å. Second minor phase has approximate composition close to M:H 1:0.2. On cooling below 400 °C the additional diffraction lines disappear but *fcc*-structured H-deficient HEA remains upon decompression.

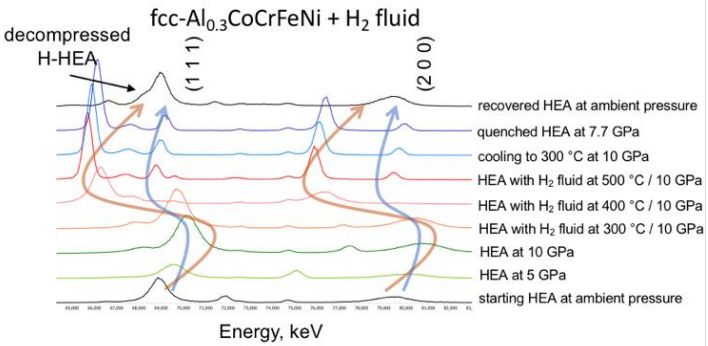

Fig. 2. Energy resolved in situ X-ray diffraction data for *fcc*-$Al_{0.3}$CrFeCoNi alloy upon compression, heating, cooling and decompression in H_2-fluid preformed in LVP with NH_3BH_3 as H_2 fluid source.

Reaction of high-entropy alloys with nitrogen and carbon is far from being trivial. Individual PGM and 3d metals form quite structurally different carbides and nitrides which cannot be assigned to one single structural type. After heating with nitrogen, PGM- as well as 3d-based high-entropy alloys form a mixture of several nitrides and carbides. Our study suggests that interstitial high-entropy hydrides can be formed under compression above critical pressures or at elevated temperatures. It is highly peculiar that despite structural disorder at lower pressures HEA exhibit enhanced resistance to hydrogen. Structurally, hydrogen interstitially occupies octahedral sites in fcc and hcp closed packings with a formation of 1:1 hydrides at pressures below 50-60 GPa. PGM-based high-entropy hydrides can be obtained at pressures above 10-15 GPa. Low pressure and room temperature stability of high-entropy alloys under hydrogen makes possible to use HEAs as hydrogen-resistive materials at moderate pressures and temperatures.

References

[1] Yusenko et al., Journal of Alloys Compounds, 2017, 700, 198;
[2] Yusenko et al., Scripta Materialia, 2017, 138, 22 ;
[3] Yusenko et al., Acta Materialia, 2017, 139, 236;
[4] Sahlberg et al., Scientific Reports, 2016, 6, 36770;
[5] Scheler et al., Phys. Rev. Lett., 2013, 111, 215503.

SCP13.2

Laves Phase in Refractory Complex Concentrated Alloys

Nikita Stepanov

Belgorod State University, Belgorod, Russia, stepanov@bsu.edu.ru

Introduction

Refractory high entropy alloys (RHEAs) and associated refractory complex concentrated alloys (RCCAs) are widely considered as promising high-temperature materials with potential to break the temperature limits of Ni-based superalloys [1]. Although single body-centered cubic (bcc) phase RHEAs can demonstrate unusually high strength at elevated temperatures [2], the common wisdom suggests that the required balance between the high-temperature strength, oxidation resistance, and damage tolerance can be achieved by generating multiphase structures in RCCAs [3]. In this case, strengthening usually comes from hard intermetallic phase. One of the most frequent intermetallic phases in RCCAs is the Laves phase, which is often found in Cr-doped alloys. Here we report our findings on the structure and properties of the Laves phase reinforced low-density RCCAs of the Al-Cr-Nb-Ti-V-Zr system.

Materials and Methods

The examined alloys were produced from a mixture of high-purity elements by vacuum arc melting. The structure of the alloys was examined mostly using standard methods, including X-ray diffraction (XRD), scanning (SEM) and transmission electron microscopy (TEM). The mechanical properties were accessed mostly using compression tests at room and elevated temperatures.

Results and Discussion

First, we focus on the prediction of the Laves phase formation in Al-Cr-Nb-Ti-V-Zr RCCAs using different methods. For that purpose, database on the experimental phase composition of various RCCAs containing Laves phase was collected. Empirical criteria (phase formation rules) including atomic size difference and electronegativity difference for the Laves phase formation were proposed. The parameters governing the C14→C15 Laves phase polytype transformation were accessed. Good validity of the CALPHAD (ThermoCalc software with TCHEA database) prediction for the Laves phase formation was established. This finding suggests opportunity for the efficient computational search for the Laves phase reinforced alloys with the desired structures and properties.
Then, we show the applicability of the CALPHAD approach for the development of eutectic Al-Cr-Nb-Ti-Zr alloys. By systematic CALPHAD calculation, we find unique eutectic point in multi-dimensional composition space. Then, we prepare a set of experimental alloys with presumably eutectic, hypo- and hyper-eutectic structure. The experimental investigations have found excellent credibility of the CALPHAD calculation. The unique orientation relationship between the B2 and the C14 Laves phases in the eutectic $Al_{28}Cr_{20}Nb_{15}Ti_{27}Zr_{10}$ (in at. %) was found. Good crystallographic match between the B2 and the Laves phases was supposed as the main reason behind the surprising stability of the eutectic structure during high-temperature deformation of the alloy, and thus the high strength of the eutectic alloy at elevated temperatures. However, most of the studied alloys suffered from brittleness at room temperature. In addition, oxidation resistance of the eutectic, hypo- and hyper-eutectic alloys was examined. Promising environmental resistance of the hypoeutectic $Al_{23}Cr_{20}Nb_{15}Ti_{32}Zr_{10}$ alloy at 800-1000°C was revealed. The oxidation mechanisms of the alloy were studied in detail.
Finally, we estimate the effect of bcc matrix chemical composition on structure and mechanical properties of the Laves phase strengthened alloys. For that purpose, pure Nb and equiatomic NbTi and NbTiZr (all with single bcc phase structure) were doped with different amounts of Nb. In all examined systems (Nb-Cr, NbTi-Cr, and NbTiZr-Cr) addition of Cr has resulted in formation of the Laves phase particles, but its amount showed strong dependence not only on the Cr percentage in the alloy, but also on the “base” alloy composition. The experimental results agree reasonably with the CALPHAD predictions. Addition of Cr significantly strengthens the alloys both at room and elevated temperatures. However, complex relationship between the strength of the alloys, amount of the Laves phase, and the chemical composition of the bcc matrix was revealed. Also, the surprisingly high ductility of some alloys containing high amount of the brittle Laves phase was revealed.

Conclusions

The results obtained in this study can be useful for the future development of the Laves-phase reinforced RCCAs with advanced set of properties.

Acknowledgements
This study was supported by the Russian Science Foundation (RSF) under the grant № 19-79-30066 (https://rscf.ru/en/project/23-79-33001/).

References
[1] O.N. Senkov, D.B. Miracle, K.J. Chaput, J.-P. Couzinie, Journal of Materials Research**. 2018**, *33(19)*, 3092-3128.
[2] F. Maresca, W.A. Curtin, Acta Materialia. **2020**, *182*, 235-249.
[3] D.B. Miracle, J.D. Miller, O.N. Senkov, C. Woodward, M.D. Uchic, J. Tiley, Entropy. **2014**, *16(1)*, 384–421.

SCP13.3

Effect of B2 ordering on the tensile mechanical properties of Al-containing refractory medium-entropy alloys

Nikita Yurchenko, Evgeniya Panina, Vseslav Novikov, Gennady Salishchev, Sergey Zherebtsov and Nikita Stepanov

Belgorod National Research University, Russia, yurchenko_nikita@bsu.edu.ru, panina_e@bsu.edu.ru, novikov_v@bsu.edu.ru, salishchev_g@bsu.edu.ru, zherebtsov@bsu.edu.ru, stepanov@bsu.edu.ru

Introduction

Refractory high/medium-entropy alloys (RH/MEAs) are a new class of materials with advanced high-temperature properties [1]. These alloys are frequently doped with Al, that leads to the density reduction, improvement of oxidation resistance and strength [2,3]. However, many Al-containing RH/MEAs have inferior ductility at ambient and intermediate temperatures even under compression compared to Al-free counterparts [4]. The main reason for that is often considered being the Al-induced B2 ordering, yet systematic studies revealing the direct relationships between the B2 ordering and mechanical properties are absent. Moreover, most of the data available in literature are presented for compression loading [1], while tensile testing is more preferred for the evaluation of the potential for practical applications of RH/MEAs. In this work, we tried to systematically study the effect of B2 ordering on the tensile mechanical properties in a wide temperature interval.

Materials and Methods

The alloys with nominal compositions of $Al_x(NbTiZr)_{100-x}$ (x = 0; 2.5; 5; 7.5 at.%) and $Al_yNb_{40}Ti_{40}V_{20-y}$ (y = 0; 15; 20 at.%) were prepared by vacuum arc melting. As-cast ingots were processed according to the procedures described elsewhere [5–7]. Mechanical properties were evaluated under tensile tests at 25–900 °C. Microstructure of the alloys were characterised using X-ray diffraction (XRD), electron backscatter diffraction (EBSD), energy dispersive spectroscopy (EDS), and transmission electron microscopy (TEM). The more detailed information on materials and methods is given in [5–7].

Results and Discussion

Experimental investigation of the $Al_x(NbTiZr)_{100-x}$ alloys revealed that the Al additions first provoked the bcc-to-B2 transition (between the $Al_{2.5}(NbTiZr)_{97.5}$ and $Al_5(NbTiZr)_{95}$ alloys), i.e. resulted in the formation of the B2 nanodomains with a very small size, and then increased the degree of B2 ordering (between the $Al_5(NbTiZr)_{95}$and $Al_{7.5}(NbTiZr)_{92.5}$ alloys) due to growing of these B2 nanodomains (Fig. 1). The $Al_{7.5}(NbTiZr)_{92.5}$ alloy was stronger than the NbTiZr counterpart at T ≤ 600 °C by 20–30 %, while having the same strength at 800 °C (Fig. 1). Higher yield strength values at T ≤ 600 °C were explained by the operation of B2 nanodomain-induced order strengthening using quantitative analysis. In turn, loss of superiority at 800 °C appeared due to the activation of the dislocation climb. B2 nanodomains in the $Al_{7.5}(NbTiZr)_{92.5}$ alloy had relative mechanical and thermal stability and confined the dislocation motion within mutually intersected dislocation bands at T < 600 °C. At T ≥ 600 °C, the activation of dynamic recrystallisation and more homogeneous distribution of dislocations were observed.

Experimental investigation of the $Al_yNb_{40}Ti_{40}V_{20-y}$ showed that the $Nb_{40}Ti_{40}V_{20}$ alloy had a single-phase bcc structure, while $Al_{15}Nb_{40}Ti_{40}V_5$ and $Al_{20}Nb_{40}Ti_{40}$ alloys were classified as weakly and highly B2-ordered ones, respectively (Fig. 2). At 22 °C, Al had a minor effect on the tensile strength, increasing the yield strength from 650 to 795 MPa (Fig. 2). Wherein, the weakly B2-ordered $Al_{15}Nb_{40}Ti_{40}V_5$ alloy achieved a higher uniform elongation compared to the bcc $Nb_{40}Ti_{40}V_{20}$ alloy, but the highly B2-ordered $Al_{20}Nb_{40}Ti_{40}$ counterpart was brittle. At 500 °C, all three alloys underwent a gradual softening, which was less pronounced in the highly B2-ordered $Al_{20}Nb_{40}Ti_{40}$ alloy. Both B2-ordered alloys remained stronger than the bcc $Nb_{40}Ti_{40}V_{20}$ alloy. At 700 °C, the bcc $Nb_{40}Ti_{40}V_{20}$ and weakly B2-ordered $Al_{15}Nb_{40}Ti_{40}V_5$ alloys softened drastically, while, in the highly B2-ordered $Al_{20}Nb_{40}Ti_{40}$ alloy, the strength reduction was minor. At 900 °C, the B2-ordered alloys showed lower strength than the bcc $Nb_{40}Ti_{40}V_{20}$ alloy (Fig. 2). Loss of strength in all the alloys was induced by the activation of diffusion-controlled dislocation climb/glide. In turn, the advantage from the B2 ordering was suggested to diminish due to disordering or decreasing degree of B2 ordering. In all three alloys, dynamic recrystallisation was active.

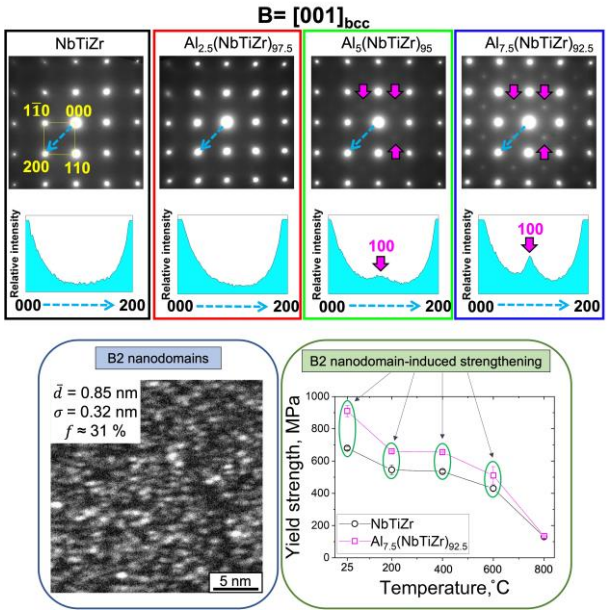

Fig. 1: Charaterisation of microstructure and mechanical properties of the $Al_x(NbTiZr)_{100-x}$ alloys.

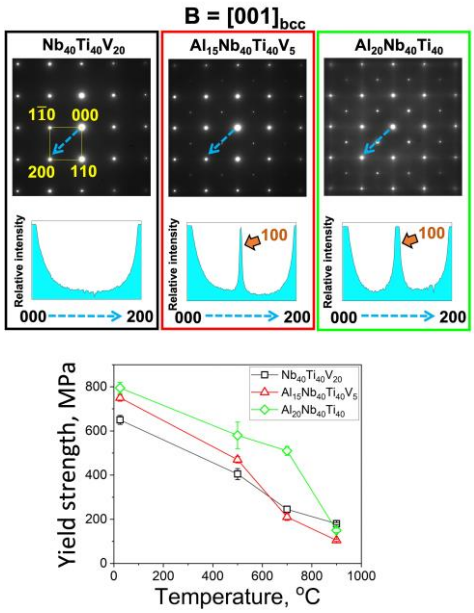

Fig. 2: Charaterisation of microstructure and mechanical properties of the $Al_yNb_{40}Ti_{40}V_{20-y}$ alloys.

Conclusions

Herein, we investigated the effect of B2 ordering on the mechanical properties of $Al_x(NbTiZr)_{100-x}$ (x = 0; 2.5; 5; 7.5 at.%) and $Al_yNb_{40}Ti_{40}V_{20-y}$ (y = 0; 15; 20 at.%). We showed that tailoring of B2 ordering degree through controlled Al additions could conquer the strength-ductility synergy.

Acknowledgements

This work was supported by the Russian Science Foundation Grant no. 21-79-10043 (https://rscf.ru/en/project/21-79-10043/). The work was carried out using the equipment of the Joint Research Center of Belgorod State National Research University "Technology and Materials".

References

[1] O. Senkov, D. Miracle, K. Chaput, J. Couzinie, Journal of Materials Research. **2018**, *33*, 3092–3128.
[2] O. Senkov, S. Senkova, C. Woodward, Acta Materialia. **2014**, *68*, 214–228.
[3] B. Gorr, S. Schellert, F. Müller, H. Christ, A. Kauffmann, M. Heilmaier, Advanced Engineering Materials. **2021**, *23*, 2001047–2001047.
[4] W. Wang, Z. Zhang, J. Niu, H. Wu, S. Zhai, Y. Wang, Materials Today Communications. **2018**, *16*, 242–249.
[5] N. Yurchenko, E. Panina, A. Tojibaev, S. Zherebtsov, N. Stepanov, Materials Research Letters. **2022**, *10*, 813–823.
[6] N. Yurchenko, E. Panina, A. Tojibaev, V. Novikov, G. Salishchev, S. Zherebtsov, N. Stepanov, Journal of Alloys and Compounds. **2023**, *937*, 168465–168465.
[7] N. Yurchenko, E. Panina, A. Tojibaev, R. Eleti, D. Volosevich, O. Klimova-Korsmik, G. Salishchev, S. Zherebtsov, N. Stepanov, Materialia. **2023**, *28*, 101766.

P-01

Ab initio modeling of stability and properties of O-phase in different TiAl-M systems (M=W, Mo, Ta, V, Nb)

Zeinab Heidari Pebdani[1, 2] and Florian Pyczak[1, 2]

[1]Helmholtz-Zentrum Hereon, Max-Planck-Straße 1, 21502 Geesthacht, Germany,
[2]Brandenburgische Technische Universität Cottbus-Senftenberg, Konrad-Wachsmann-Allee 17, Cottbus 03046, Germany, zeinab.heidaripebdani@hereon.de; florian.pyczak@hereon.de

Introduction

Current γ-TiAl alloys in or foreseen for industrial use contain increasing amounts of additional alloying elements to improve the properties for service and/or processing. In addition to the phases γ-TiAl and α_2-Ti_3Al, other phases could occur if the content of additional alloying elements is high enough. Recently it was shown experimentally that for sufficiently high additions of a ternary element M, being W, Mo, Ta, or V, the orthorhombic O-phase (Fig. 1-a) could be found in such alloys [1]. First-principles calculations also indicate that elements such as Ta or V can stabilize the O-phase [2]. The O-phase is especially well known and investigated in the Ti-Al-Nb system where it has the stoichiometric prototype Ti_2AlNb. Experimental investigations of the O-phase in those different Ti-Al-M systems are extremely challenging, as for example, synchrotron-generated X-rays with their high brilliance have to be used for unambiguous identification of the O-phase. Thus, first-principles calculations using density functional theory (DFT) are a good means to acquire a faster insight into the stabilities and properties of O-phases in different Ti-Al-M systems. DFT calculations proved to be a valuable tool to understand the properties of γ-TiAl alloys [3]. By DFT such properties as the energy of formation, lattice constant, or elastic properties can be calculated. In the present work, this was applied for a series of Ti_2AlM O-phases with M being Nb, Mo, V, W, and Ta.

Methods

All our density functional theory (DFT) calculations were performed using the Vienna Ab Initio Simulation Package VASP, projector augmented wave (PAW) pseudopotentials and the Perdew-Burke-Ernzerhof (PBE) generalized gradient approximation (GGA) exchange-correlation functional with Perdew and Wang parameterization (PW54). Based on convergence tests with fully relaxed structures to achieve a precision of less than 0.2 meV/atom all calculations were done with a cut-off energy of 600 eV and a Monkhorst-Pack k-point grid of 9 × 9 × 9 or higher. until the difference in atomic forces were below 1 meV/ Å. Total energies were evaluated for different lattice parameters of the O-phase of each system while keeping the cell volume constant. The ground state energy and volume were derived from a fit to a Birch-Murnaghan equation of state. The single-crystal elastic constants of the obtained ground state structures are determined from the Hessian matrix calculated using the finite differences executed inherently in the VASP package. From the single crystal elastic constants, the shear (G) and bulk (B) modulus are calculated via the Voigt-Reuss-Hill (VRH) approximation. In addition, Young's modulus (E), Poisson's ratio (ν), Pugh's ratio, Cauchy pressure, and Debye temperature (Θ_D) are derived.

Results and Discussion

Density functional theory (DFT) with generalized gradient approximation (GGA-PBE) was used to investigate the effect of ternary alloying elements M (M=Mo, W, Ta, Nb, V) on the stabilities, electronic structure, and elastic properties of the O-phases of Ti_2AlM type. The calculated lattice parameters are in good agreement with the experimental and other theoretical results found in the literatures [1-8]. As a measure for the stability of the different types of O-phase their energy of formation, which is the difference between the energy of the O-phase structure and the weighted sum of the constituting elements in their respective stable ground state (i.e. hcp-Ti, fcc-Al, bcc-Mo, W, Ta, Nb, V), was calculated (Fig. 1-b). The O-phase of the Ti_2AlMo type exhibits the lowest energy of formation while Ti_2AlV is the least stable according to formation energies. The electronic density of states as shown for Ti_2AlMo in Fig. 1-c can be used to determine the reasons for the stability of the different Ti_2AlM type O-phases based on their bonding behavior. Both, the *p-d* covalent bond strength in Ti_2AlM O-phase, which was determined from the overlap of the Ti *p*-orbital with the M *d*-orbital, and the *d-d* bond strength, which was determined from the overlap of the Ti *d*-orbital with the M *d*-orbital, changes in the following order: Ti_2AlW <Ti_2AlV<Ti_2AlNb<Ti_2AlTa<Ti_2AlMo. Thus, the overlap of *p-d* and *d-d* bonds shows the same order as the formation energies except for a swap between Ti_2AlW and Ti_2AlV. Accordingly, strong bonding between the *p*- and *d*-orbitals of the ternary element M and the *d*-orbital of Ti stabilizes the O-phase. All the investigated O-phase systems fulfill the elastic stability criterion [4-5]. According to Pugh's ratio, all the Ti_2AlM O-phases are ductile. However, Ti_2AlV is at the ductile-brittle boundary. The trend in Cauchy pressures and Poisson's ratio (*v)* of all the O-phase systems is the same as for Pugh's ratio with the order Ti_2AlMo>Ti_2AlW>Ti_2AlTa>Ti_2AlNb>Ti_2AlV. The calculations

suggest that among all O-phase types investigated Ti_2AlMo has the best combination of mechanical properties with the highest bulk modulus and Young's modulus. In addition, Ti_2AlMo exhibits the lowest formation energy as compared to other systems. The Debye temperature of Ti_2AlM intermetallic follows a similar trend from the elastic constants and VRH shear and bulk modulus. The comparison of these constants indicates that the current results are in decent compromise with those reported in the literature for the O-phase Ti_2AlNb [7, 8], and better consistency with the experimental data than those reported in the literature [9, 10].

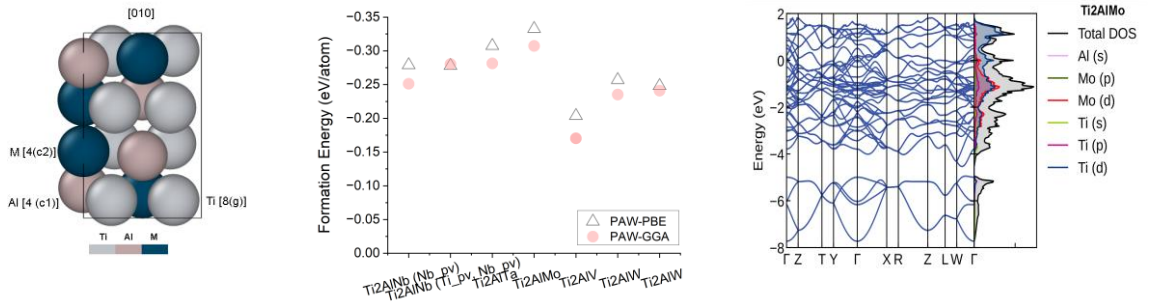

a) b) c)

Fig.1. a) Crystal cell used to simulate O-phase Ti_2AlM structure. b) Formation energies of O-phases of Ti_2AlM type (M=Mo, Ta, V, W, Nb) in (eV/atom) using PAW-GGA and PAW-PBE pseudopotentials. b) Electronic band structures and density of states (DOS) of Ti_2AlMo O-phase.

Conclusion

In summary, we predict the stability of different O-phases of the Ti_2AlM type by DFT. All investigated Ti_2AlM O-phase with M being VB group metals V, Nb and Ta and VIB group metals Mo and W exhibit negative formation energies and are elastically stable. Of the different O-phase types investigated Ti_2AlMo is the most stable and Ti_2AlV the least stable when comparing energies of formation.

References

[1] M. W. Rackel, et al. Screening for O phase in advanced γ-TiAl alloys. Intermetallics. **2021**, 131, 107086.

[2] Q. M. Hu, et al. Geometric and electronic structure of Ti_2AlX (X=V, Nb, or Ta). Phys Rev B. **2003**, 68, 054102.

[3] D. Holec, et al. Electrons Meet Alloy Development: A γ-TiAl-Based Alloy Showcase. Adv. Eng. Mater. **2022**, 24, 2100977.

[4] C. Chen, et al. Elastic properties of orthorombic $YBa_2Cu_3O_7$ under pressure. Crystals. **2019**, 9, 497.

[5] G.V.Sin'ko and N.A. Smirnov. Ab initio calculations of elastic constants and thermodynamic properties of bbc, fcc, and hcp Al crystals under pressure. J.Phys. Condense. Matter. **2002**, 14, 6989.

[6] C. Dai, et al. Composition and temperature dependence of α_2 phase decomposition in high Nb-containing lamellar γ-TiAl alloys: Experiments and first-principles calculations. Acta Mater. **2021**, 221, 117419.

[7] K. Hu, et al. Elastic and thermodynamic properties of the Ti_2AlNb orthorombic phase from first-principles calculations. Phys Status Solidi B. **2017**, 254, 1600634.

[8] Z. Y. Wei, et al. Pressure-induced structure, electronic, thermodynamic and mechanical properties of Ti_2AlNb orthorhombic phase by first-principles calculations. Mater. Res. Express. **2019**, 6, 096510.

[9] A. Pathak and A. K. Singh. A first principles study of Ti_2AlNb intermetallic Solid. State Commun. **2015**, 204, 9.

[10] F. Chu, et al. Elastic properties of the O-phase in Ti-Al-Nb alloys. Intermetallics. **1997**, 5, 147.

P-02

Oxidation of Zr-containing TiAl alloys – impact of the fluorine-effect

H.-E. Zschau[1], A. Donchev[2], M. Allen[3], P. Spoerk-Erdely[4], M. Musi[4], H. Clemens[4] and M. Galetz[2]

[1]Werkstoffprüfung und –forschung, Roitzscher Weg 32 c, D-04808 Wurzen, Germany, dr.zschau@hotmail.com
[2]DECHEMA-Forschungsinstitut, Theodor-Heuss-Allee 25, D-60486 Frankfurt am Main, Germany, alexander.donchev@dechema.de, mathias.galetz@dechema.de
[3]GfE Metalle und Materialien GmbH, Höfener Str. 45, D-90431 Nuremberg, Germany, melissa.allen@gfe.com
[4]Department of Materials Science, Montanuniversität Leoben, Franz-Josef-Str. 18, A-8700 Leoben, Austria, petra.spoerk.erdely@unileaben.ac.at, micael.musi@unileoben.ac.at, helmut.cemens@unileoben.ac.at

Introduction

Intermetallic alloys based on the γ-TiAl phase possess high specific strength at elevated temperatures. Hence, components made of such alloys are used as turbine blades in the last stages of the low-pressure turbine of several advanced jet engines. Their use at elevated temperatures requires a sufficient oxidation resistance so that the components withstand the service conditions for the envisaged lifetime. Most technical TiAl alloys consist of at least the two phases γ-TiAl and α_2-Ti_3Al. These alloys can be summarized by the following composition, Ti-(42-48)Al-(0-10)(Cr, Mn, Nb, Ta)-(0-3)(Hf, Mo, W, Zr)-(0-1)(B, C, Si)-(0-0.5) rare-earth metals in at.-% [1]. Novel developments have led to the addition of several at.-% of Zr. Zr is known to improve the oxidation resistance of alumina formers, i.e. FeCrAl alloys [2]. The addition of Zr leads to improved mechanical properties of TiAl, but the impact of Zr on the oxidation behavior of TiAl is not yet properly investigated. In this study several alloys with Zr additions up to 8 at.-% were investigated and compared to a binary material with the same Al content. Their oxidation behavior at 900°C in air will be presented and the effects of fluorine surface treatments will be discussed in view of the so-called fluorine effect.

Oxidation of Zr containing TiAl alloys

TiAl alloys form a non-protective mixed scale during exposure to air at elevated temperatures [3]. The addition of Zr could influence the oxidation resistance of γ-TiAl based alloys analogous to Fe- or Ni-based materials [2]. The binary Ti-46.5Al alloy was compared with the following Zr-containing alloys Ti-46.5Al-XZr (X = 2, 4, 8 at.-%). Isothermal exposure tests at 900°C were performed under laboratory air atmosphere for 120 h. After exposure, all materials reveal major spallation of the oxide scales (Figs. 1a-d), which indicates similar oxidation behavior. Fluorination via a liquid phase treatment, which is utilized for the protection of technical alloys like TiAl 4822 (Ti-48Al-2Nb-2Cr, in at.-%) led to reduced spallation but could not totally prevent this phenomenon (Figs. 2a-d).

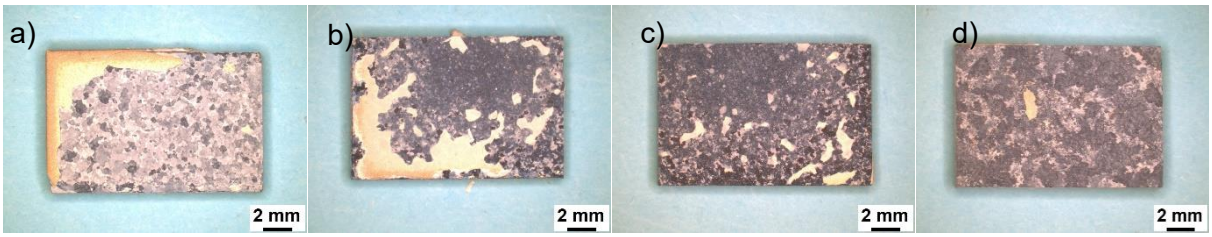

Figure 1: Macroscopic images of the untreated alloys after isothermal exposure at 900°C in air for 120 h taken with a light optical microscope: a) Ti-46.5Al, b) Ti-46.5Al-2Zr, c) Ti-46.5Al-4Zr, and d) Ti-46.5Al-8Zr.

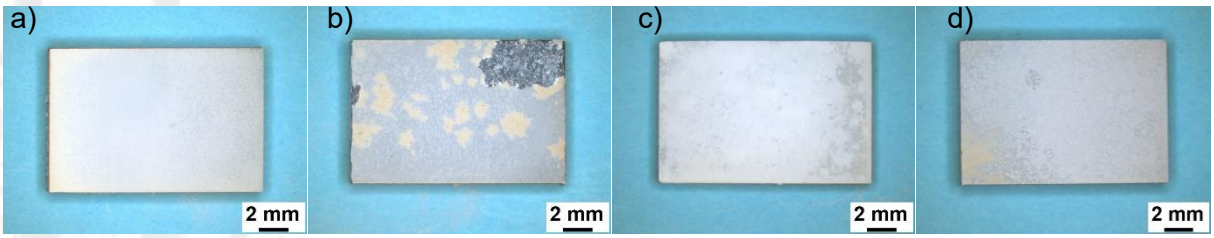

Figure 2: Macroscopic images of the F-treated alloys after isothermal exposure at 900°C in air for 120 h taken with a light optical microscope: a) Ti-46.5Al, b) Ti-46.5Al-2Zr, c) Ti-46.5Al-4Zr, and d) Ti-46.5Al-8Zr.

Change of the oxidation behavior via the fluorine effect

The addition of defined small amounts of fluorine into the surface zone of γTiAl alloys changes the oxidation behavior from mixed scale formation with limited protective effects [4] towards alumina formation which protects γ-TiAl based components up to 1050°C under thermocyclic conditions up to several thousand hours in complex environments [5]. This so-called fluorine effect is based on the intermediate formation of gaseous aluminum fluorides whose partial pressures exceed the ones of titanium fluorides by several orders of magnitude if a defined amount of fluorine is applied [6]. However, due to the higher thermodynamic stability of ZrO_2 compared to Al_2O_3, internal oxidation cannot be prevented.

Fluorination

Fluorine can be applied by several methods. Beam line ion implantation (BLI²) can be used to deposit certain amounts of fluorine at a certain depth by varying the energy and the time [7]. This method is limited to basic studies, but not suitable for complex technical components. Such samples can be treated via liquid or gas phase treatments [8]. The fluorine effect developed after equally spraying a fluorine containing polymeric compound or dipping in diluted HF at room temperature and subsequent exposure at elevated temperature [9]. In order to optimize the fluorination, BLI² will be employed and the results of the implanted samples after exposure will be presented.

References

[1] H. Clemens, S. Mayer, Adv. Eng. Mat. 15 (2013) 191
[2] J. Engkvist, S. Canovic, K. Hellström, A. Järdnäs, J.E. Svensson, L.G. Johansson, M. Olsson, M. Halvarsson, Oxid. Met. 73 (2010) 233
[3] M. Yoshihara, K. Miura, Adv. Mat. 93 (1994) 225
[4] R. Pflumm, S. Friedle, M. Schütze, Intermetallics 56 (2015) 1
[5] A. Donchev, M. Schütze, A. Kolitsch, R. Yankov, Mat. Sci. Forum 706-709 (2012) 1061
[6] A. Donchev, B. Gleeson, M. Schütze, Intermetallics 11 (2003) 387
[7] J.P. Biersack, J.F. Ziegler; TRIM III 1997
[8] A. Donchev, M. Schütze, Mat. Sci. Forum 461-464 (2004) 447
[9] H.-E. Zschau, M. Schütze, Mat. Sci. Forum 696 (2011) 366

P-03

Fabrication of bismuth telluride-based thermoelectric legs by Binder Jetting

Matteo d'Angelo, Francesco Bertolini, Carmen Galassi, and Nora Lecis

Department of Mechanical Engineering, Politecnico di Milano, Milano 20156, Italy,
matteo.dangelo@polimi.it, francesco.bertolini@polimi.it, carmen.galassi@polimi.it, nora.lecis@polimi.it

Introduction

Nowadays energy and pollution crisis raised interest towards alternative ways to harvest energy, like thermoelectric conversion of waste heat into electrical energy (i.e., thermoelectric generators, TEGs). The most challenging is the direct conversion of energy by employing lightweight and quiet devices, without moving parts, therefore at zero green-house gases emission. Intermetallic materials are often used in these applications (e.g., half-Heuslers alloys). Bismuth telluride and its alloys (p-type $Bi_xSb_{2-x}Te_3$ and n type $Bi_2Se_{3-x}Te_x$) are the most used and studied materials [1]. Binder jetting (BJ) is a layer-by-layer additive manufacturing process that involves the deposition of a liquid binder on a powder bed using a specific pattern. Some advantages are the fast and inexpensive method of 3D printing, and the freedom in complex shapes. The disadvantages are rough surface finish and poor mechanical properties compared to conventional manufacturing methodologies; however, research is addressing these issues [2].

Currently, the utilization of this technology for the preparation of thermoelectric legs has never been explored.

In conclusion, the aim of this preliminary work is to study the issues related to the shaping of bismuth telluride alloys by binder jetting including the strategies to densify the cold consolidated body that shows a quite low green body density.

This is performed by microstructural and structural analysis of the intermetallic materials when cold consolidated and sintered in different conditions.

Materials and Methods

The powder was prepared by hand-grinding and then by planetary milling n-type and p-type bismuth telluride ingots (planetary mill Retsch PM400). The ingots were purchased by TianJin METEK METAL Technology Co. Ltd). The powder mean size after milling was in the micrometric range, as required for binder jetting ($d_{90} \simeq 5$ µm). Oxidation takes place very easily in bismuth telluride, especially in presence of air and moisture. For this reason, the powders were milled in an argon-filled zirconia jar and were handled always in an argon-filled glovebox (250 cc zirconia jar and zirconia beads of 5 mm). Cold consolidation was performed by Innovent+ binder jetting 3D printer (ExOne). The as-printed samples were cured at 180 °C for 6 hours. Following to curing, the samples were sintered in argon atmosphere (Tube Furnace Carbolite TZF 12/75/700). The microstructure of the samples was characterized by field emission-scanning electron microscope analysis and by energy dispersive analysis (Zeiss Sigma 500 SEM and EDS). The samples were embedded in a conductive resin and polished with 320 grit up to 4000 grit paper (the samples were analyzed longitudinally and transversally to the printing direction).

The crystallographic characterization was carried out by XRD analysis (Rigaku SmartLab X-ray diffractometer). The density of the samples was measured by geometrical measurement, and hydrostatics balance (Mettler Toledo scale).

One cured sample (i.e., green) for each geometry is shown in Figure 1.

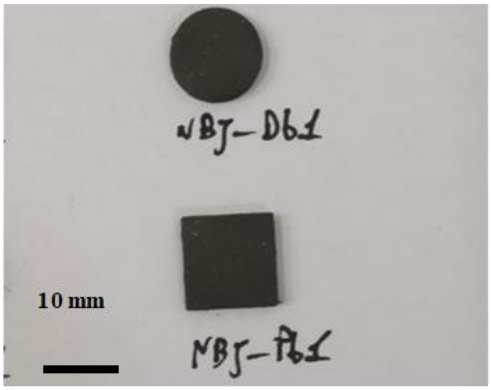

Fig. 1: Printed N type bismuth telluride green samples by binder jetting, after curing.
Disk geometry on top, square geometry on bottom.

Results and Discussion

This preliminary study demonstrated that is possible to fabricate bismuth telluride-based thermoelectric legs by binder jetting with good geometrical control and high green density (relative green density around 45 %), if compared to other green bodies prepared with the same technique. After sintering the final density (was around 60 %) and the pore size distribution was quite large. The low performance of the printed material is probably due to oxidation, since Innovent+ 3D printer does not operate in controlled atmosphere, and an aqueous binder is used (AquaFuse). XRD analysis did not evidence the presence of oxides in the pre-sintered and sintered samples. However, the low sintering extent attained in this preliminary study is probably related to the presence of oxides around the particles, which hinders necking and so densification of the samples. The absence of the Bi_2O_3, TeO_2, Sb_2O_3 and SeO_2 reflections in the XRD spectra is probably related to the low fraction of oxides (i.e., amount lower than the detection limit) [3]. The presence of oxides in between the particles was studied using EDS analysis. The SEM image of a p-type sample fabricated by binder jetting is shown in Figure 2: the black material between the particles is richer in oxygen (red circle), and the position of the oxides between the particles would explain the low sintering extent. Further, the black isles (green circle) are zirconia contamination due to milling, and the holes (yellow circle) are un-sintered areas of the material (poor distribution of the porosities and defects). Regardless of the low performance of the material, the best sintering parameters for the materials were determined. In the case, it was determined that sintering should be performed in two steps: a first, and short step close to melting temperature (575 °C for around 2 h), and a longer step at lower temperature (560 °C for 20 h).

After this preliminary study it was concluded that the samples should be sintered at reducing atmosphere: the possibility to reduce the different oxides might favor the densification mechanism (95% Ar + 5% H_2 atmosphere) [4].

To conclude, this preliminary study demonstrated the feasibility of fabricating thermoelectric legs based on bismuth telluride by binder jetting. However, the oxidation problem remains to be further investigated.

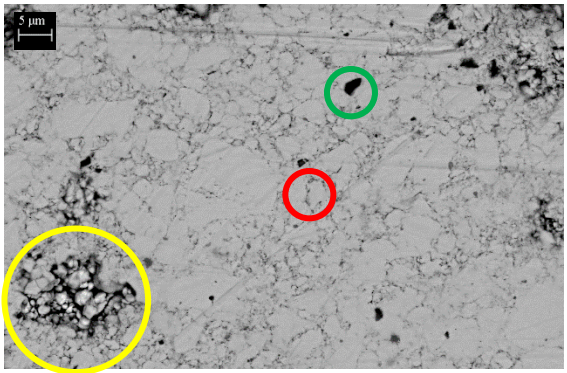

Fig. 2: SEM image of printed P type bismuth telluride samples by binder jetting and sintered in argon for 24 h at 550 °C. Image taken using SEM Zeiss Sigma 500.

Acknowledgments

The project is partially funded by STMicroelectronics.

References

[1] M. Gupta, *Review on Heat Recovery Unit with Thermoelectric Generators*, Power **4**, 2021 (2014).

[2] M. Ziaee and N. B. Crane, *Binder Jetting: A Review of Process, Materials, and Methods*, Addit. Manuf. **28**, 781 (2019).

[3] C. Kenel, M. M. F. Al Malki, and D. C. Dunand, *Microstructure Evolution during Reduction and Sintering of 3D-Extrusion-Printed Bi_2O_3+TeO_2 Inks to Form Bi_2Te_3*, Acta Mater. **221**, 117422 (2021).

[4] T. Matsuda, D. Yamagiwa, H. Furusawa, K. Sato, H. Yashiro, K. Nagao, J. Kim, T. Sano, Y. Kashiba, and A. Hirose, *Reduction Behavior of Surface Oxide on Submicron Copper Particles for Pressureless Sintering Under Reducing Atmosphere*, J. Electron. Mater. **51**, 1 (2022).

P-04

Competing Magnetic Structures in YMn_2

Pavel Papež[1,2], Martin Friák[1] and Ilja Turek[1]

[1]Institute of Physics of Materials, Czech Academy of Sciences, Žižkova 22, Brno, 616 00, Czech Republic,
[2]Institute of Materials Science and Engineering, Faculty of Mechanical Engineering,
Brno University of Technology, Technická 2896/2, Brno, 616 69, Czech Republic,
papez@ipm.cz, friak@ipm.cz, turek@ipm.cz

Introduction

The intermetallic compound YMn_2 was a subject of many studies regarding its magnetic configuration and anomalous thermal expansion [1–6] but the effects are yet to be completely described. The compound crystallizes in antiferromagnetic C15 Laves phase and undergoes a first order phase transition at Néel temperature of 100 K [5]. Regarding the most stable antiferromagnetic configuration, there are unfortunately conflicting reports in different studies, both experimental and theoretical. To shed some light on the most stable magnetic configuration we have employed density functional theory calculations and applied them to a few possible magnetic configurations.

Methods

We have performed *ab initio* calculations using the Vienna Ab initio Simulation Package (VASP) [7]. We have employed projector augmented wave pseudopotentials (PAW) [8,9]. The exchange and correlation energy was treated within both localized density approximation (LDA) and generalized gradient approximation (GGA). Three different parametrizations of the GGA pseudopotentials were used, Perdew-Wang 91 (PW91), Perdew-Burke-Ernzerhof (PBE) [10] and PBEsol [11]. The plane wave cut-off energy was set to 500 eV. The k-point mesh was set to 11x11x11. Calculations were performed using a conventional unit cell of C15 Laves phase YMn_2 consisting of 24 atoms with 16 Mn and 8 Y atoms. The four magnetic configurations were ferromagnetic (FM) and three different collinear antiferromagnetic configurations (AFM1, AFM2 and AFM3), see Fig. 1 where magnetic moments are drawn as red arrows. To analyze the effect of spin-polarization we have calculated the non-spin-polarized state (NM) as well. The AFM1 configuration was set up with antiferromagnetic alignment of neighboring Mn atoms in the same plane while the AFM2 configuration was reported as a potential configuration observed in experiments by Nakamura et al. in [12] and similarly, the AFM3 was later reported by Shiga in [1].

Results and Discussion

The resulting E-V curves are presented in Fig. 2. The AFM1 configuration yields the lowest energy in all calculations but the energies for different magnetic states often overlap. The overlap is present, in particular, in the case of the LDA results, for which the AFM1 states exhibit the lowest energies at higher volumes. Regarding the GGA results, the energies of the FM states are very similar to those of the NM states for lower volumes till 439 $Å^3$ for GGA PW91 and 456.5 $Å^3$ for PBE, at which the FM trends break off into a different curve. This break-off can also be seen as a sudden increase of the value of magnetic moments of Mn atoms. For PW91 the magnetic moment increased from 1.376 μ_B for 439 $Å^3$ to 2.138 μ_B for 456.5 $Å^3$. PBE potentials had the same behavior but already at 421.9 $Å^3$. This can be explained by the interatomic distance between two Mn atoms: according to Shiga [1] a critical distance after which magnetic moment becomes unstable is 2.73 Å and for the volume equal to 456.5 $Å^3$ the Mn-Mn distance is then equal to 2.72 Å. This would explain the breakaway from the non-spin-polarized parabola into a FM state. The AFM2 configuration follows the curve of the NM states for the whole range of volumes and after relaxation shows zero magnetic moment for all Mn atoms.

Generally, there were 4 groups containing 4 Mn atoms with the same size of magnetic moments. For the AFM1 configuration Mn atoms in these groups also had the same orientation, while for the AFM3 they kept the same value but some atoms had opposite orientation. This follows the magnetic structure reported by Ballou by means of neutron diffraction [13].

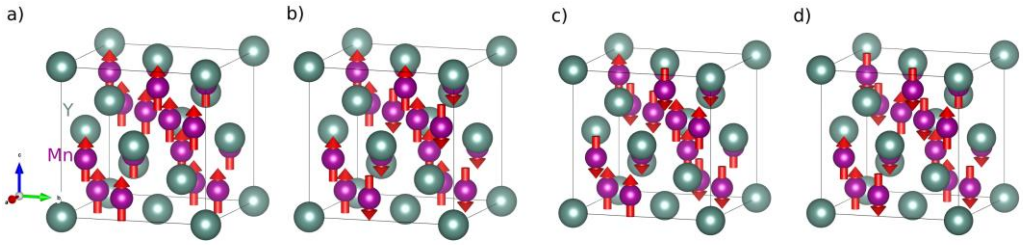

Fig. 1 The unit cell used for *ab initio* calculations with a) FM, b) AFM1, c) AFM2 and d) AFM3 magnetic configurations.

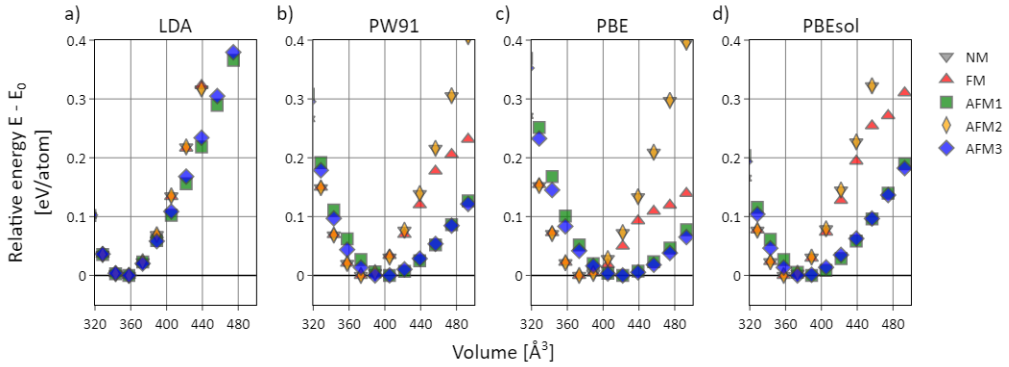

Fig. 2 The energy vs. volume curves for different potentials, a) LDA, b) GGA PW91, c) GGA PBE, d) GGA PBEsol. The GGA PBE pseudopotential with the AFM1 configuration gives the closest results to experimental values. The lattice parameter reported in experiments is equal to 7.7 Å [5,14,15] and our calculation results in 7.48 Å which is about 3% difference. The Mn magnetic moments for AFM1 which were equal to 2.67 μ_B, -2.55 μ_B, 2.59 μ_B, -2.54 μ_B are also in a very good agreement with experimentally measured values as well as other theoretical results (2.7 μ_B), see Refs. [1,16].

Funding

The authors acknowledge the Czech Science Foundation for the financial support within the Project No. 23-04746S.

References

[1] M. Shiga, Physica B+C. **1988**, *149*, 293–305. https://doi.org/10.1016/0378-4363(88)90256-2.
[2] M. Shiga, J. Magn. Magn. Mater. **1994**, *129*, 17–25. https://doi.org/10.1016/0304-8853(94)90425-1.
[3] H. Nakamura, M. Shiga, J. Alloys Compd. **2001**, *326*, 157–165. https://doi.org/10.1016/S0925-8388(01)01250-6.
[4] M. Shiga, H. Wada, Y. Nakamura, J. Magn. Magn. Mater. **1983**, *31–34*, 119–120. https://doi.org/10.1016/0304-8853(83)90179-8.
[5] G. Oomi, T. Terada, M. Shiga, Y. Nakamura, J. Magn. Magn. Mater. **1987**, *70*, 137–138. https://doi.org/10.1016/0304-8853(87)90381-7.
[6] H. Nakamura, N. Metoki, S. Suzuki, F. Takayanagi, M. Shiga, J. Phys.: Condens. Matter **2001**, *13*, 475-500. https://doi.org/10.1088/0953-8984/13/3/309.
[7] G. Kresse, J. Furthmüller, Phys. Rev. B. **1996**, *54*, 11169. https://doi.org/10.1103/PhysRevB.54.11169.
[8] P.E. Blochl, Phys. Rev. B. **1994**, *50*, 17953. https://doi.org/10.1103/PhysRevB.50.17953.
[9] G. Kresse, D. Joubert, Phys. Rev. B. **1999**, *59*, 1758. https://doi.org/10.1103/PhysRevB.59.1758.
[10] J.P. Perdew, K. Burke, M. Ernzerhof, Phys. Rev. Lett. **1996**, *77*, 3865. https://doi.org/10.1103/PhysRevLett.77.3865.
[11] J.P. Perdew, A. Ruzsinszky, G.I. Csonka, O.A. Vydrov, G.E. Scuseria, L.A. Constantin, X. Zhou, K. Burke, Phys. Rev. Lett. **2008**, *100*, 136406. https://doi.org/10.1103/PhysRevLett.100.136406.
[12] Y. Nakamura, M. Shiga, S. Kawano, Physica B+C. **1983**, *120*, 212-215. https://doi.org/10.1016/0378-4363(83)90376-5
[13] R. Ballou, Can. J. Phys. **2011**, *79,* 1475-1485. https://doi.org/10.1139/cjp-79-11/12-1475.
[14] H. Yamada, Physica B+C. **1988**, *149*, 390–402. https://doi.org/10.1016/0378-4363(88)90270-7.
[15] R.S. Liu, I. Baginskiy, H.T. Kuo, S.M. Filipek, R. Wierzbicki, R. Sato, A. V. Tsvyashchenko, L. Fomicheva, H.H. Wu, C.B. Tsai, C.C. Yang, R. Asmatulu, J.C. Ho, Y.Y. Chen, Int. J. Hydrogen Energy. **2011**, *36*, 2285–2290. https://doi.org/10.1016/J.IJHYDENE.2010.11.037.
[16] S. Iwasaki, T. Fukazawa, M. Ogura, H. Akai, J. Phys. Soc. Jpn. **2011**, *81*, 32.

P-05

Novel series of R_2Pt_2Sn intermetallics (R = Sc, Y, La-Sm, Gd-Lu) with Mo_2FeB_2-type structure

V.V. Romaka, B. Büchner and S. Seiro

Leibniz Institute for Solid State and Materials Research (IFW) Dresden, Helmholtzstr. 20, 01069 Dresden, Germany, v.romaka@ifw-dresden.de

Introduction

A fertile ground for topological phases is offered by frustrated magnets, where geometry and interactions conspire to give rise to unconventional ground states. Among various geometric lattices prone to magnetic frustration by preventing magnetic interactions to be simultaneously satisfied, a particularly interesting arrangement is the so-called Shastry-Sutherland lattice (SSL). Metallic SSL systems based on rare-earth elements have the potential for more complex magnetic phase diagrams and open up the possibility of studying the interplay with conduction electrons. Relatively new representatives of the metallic SSL systems are rare-earth (R) based R_2T_2X compounds (T – transition metal, X – p-block element) which crystallize in the anisotropic Mo_2FeB_2 (space group *P*4/*mbm*) structure type. Its structural peculiarity is the formation of a mosaic of triangles and squares from the R atoms, which represents the 2D Shastry-Sutherland lattice with magnetic ions of the R metals. Thus, the formation of complex noncollinear magnetic structures in R_2T_2X compounds, associated with the rare-earth atom sublattices, is expected. A piece of very brief information on the formation, crystal structure, and magnetic properties of Ce_2Pt_2Sn is presented in [1]. The compound is reported to crystallize in the U_3Si_2 structure type (a basic structure of the Mo_2FeB_2-type superstructure) but only lattice parameters are reported and further details of the crystal structure remain open. It is a Curie-Weiss paramagnet above 40 K with two anomalies at ~6.5 and ~2.5 K on the magnetization curve. The authors assume that the anomaly at ~6.5 K may correspond to the ferromagnetic CePt impurity. In the present work, we report the formation, stability, crystal structure, DFT study, and magnetic properties of the new R_2Pt_2Sn series of intermetallics.

Materials and Methods

Pure elements in form of rare-earth metal pieces (99.9%), Pt bars (99.999%), and Sn pieces (99.999%) were used for the preparation of alloys by conventional arc-melting technique followed by annealing in a vacuum at 800 (2 weeks), and 1000°C (1 week) and water quenching. The melting and solidification behavior of some alloys has been analyzed up to a maximum temperature of 1400°C by employing a DTA technique (Setaram 92-24) in flowing He (99.999%). The X-ray powder diffraction profiles of as-cast and annealed alloys were collected using STOE STADI in transmission geometry (Mo$K\alpha_1$ radiation) equipped with a germanium monochromator and a DECTRIS MYTHEN 1K detector. The microstructure and chemical composition of alloys was analyzed by SEM on a ZEISS - EVO MA 15 equipped with an energy-dispersive X-ray (EDX) detector operated at 30 kV.

The DFT calculations were carried out with the Vienna Ab initio Simulation Package VASP v.5.4.4 (PAW-type potentials) and Elk v8.5.10 – all-electron full-potential linearized augmented-plane wave (FP-LAPW) code. The Perdew-Burke-Enzerhoff exchange-correlation functional in the generalized gradient approximation (GGA) with an 11×11×11 Monkhorst-Pack k-point set was used. In VASP, the plane wave cut-off was set to 400 eV in all calculations. For Sn, the 3d states were treated as valence states, while for magnetic rare-earths, the semi-core 4f-electrons were treated as core states. In Elk, the proper values of the muffin-tin radii were selected automatically at the initial stage of the calculations, and the $R_{min}(MT)\times\{|G+k|\}$ was set to 8, where $R_{min}(MT)$ is the minimum muffin-tin radius used in the system. Full geometry relaxation (atomic positions as well as lattice parameters) was achieved to calculate the enthalpy of formation. The Bader charge density analysis was performed using the Bader v1.04 code.

Magnetization measurements down to 1.8 K on a crystal were carried out in a Vibrating Sample Superconducting Quantum Interference Device Magnetometer (SQUID-VSM) from Quantum Design. All field-dependent measurements were done after a zero-field cooling procedure (ZFC). To reduce the remanent magnetic field to less than 2 Oe, before each measurement a 5T magnetic field was applied at 300K and then removed in an oscillation mode.

Results and Discussion

Alloys of $R_{40}Pt_{40}Sn_{20}$ composition were synthesized with all rare-earth metals and both, as-cast and annealed at 800°C and 1000°C alloys appeared to be air-stable. The weight losses during synthesis were ~1 wt.% and according to SEM/EDX analysis of the as-cast alloys, their overall composition fitted the initial stoichiometry. A more detailed analysis of microstructures revealed the presence of a ternary phase with a composition that corresponds to the R_2Pt_2Sn compound. In general, the Sn content in all alloys was systematically below 20 at.% and ranged between 19 and 16 at.%. All as-cast alloys additionally contained grains of the primary RPtSn ternary

phase and traces of the RPt binary. In some parts of the alloys, signs of R_2Pt_2Sn decay into RPt and RPtSn were observed, which could be easily spotted using both electron and optical microscopies – the binary RPt phase appeared to be harder in comparison to the ductile R_2Pt_2Sn and RPtSn and after polishing caused a rough surface of the R_2Pt_2Sn phase. The speed of decay depends on the temperature gradient during casting and a type of rare-earth metal. In the case of alloy with Lu, only some amount of the unaffected Lu_2Pt_2Sn was observed, while with Yb – only trace amounts were detected. After annealing, the alloys contained mainly the ternary RPtSn and the RPt binary phases (Fig. 1). It is worth noting that no Eu_2Pt_2Sn was observed in the as-cast and annealed alloys. Powder XRD of the as-cast alloys revealed that all R_2Pt_2Sn phases crystallize in the Mo_2FeB_2-type structure. The unit cell volume increases almost linearly with the ionic radii of the rare-earth metals. However, the question of whether the R_2Pt_2Sn compounds are high-temperature or metastable phases is still open.
The most intriguing appeared to be the Sm_2Pt_2Sn phase, which is characterized by the two-branches homogeneity region similar to those reported for Ce_2Pd_2In in [2]. The composition of the first branch ranges from $Sm_{41}Pt_{40}Sn_{19}$ to $Sm_{46}Pt_{38}Sn_{16}$, while the second from $Sm_{41}Pt_{40}Sn_{19}$ to $Sm_{40}Pt_{44}Sn_{16}$. The unit cell volume is in the range of 0.2246- 0.2268 nm^3, depending on the composition. Optimization of the synthesis procedure allowed us to obtain almost single-phase samples of Sm_2Pt_2Sn.

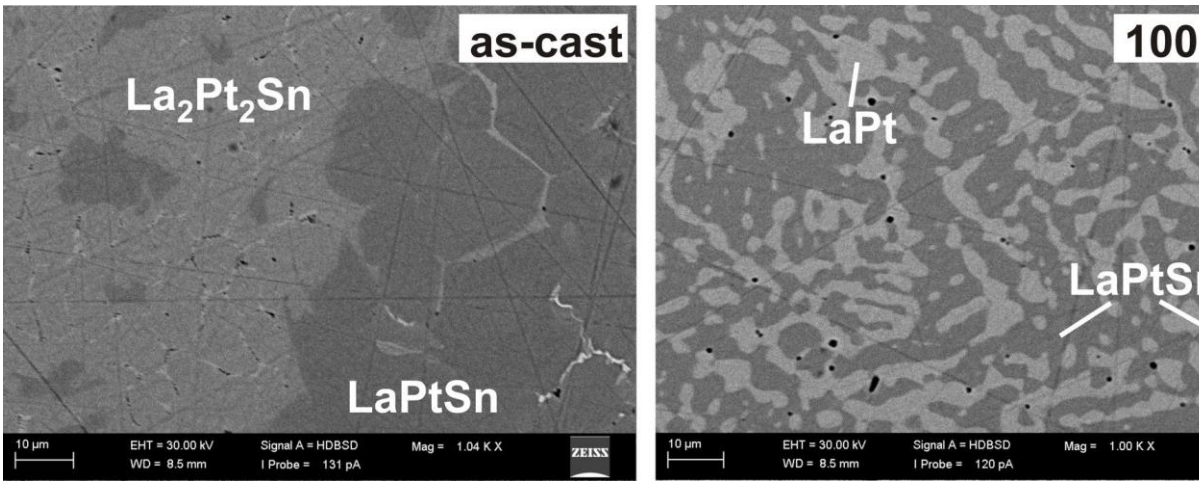

Fig. 1: SEM images (BSD) of the as-cast and annealed $La_{40}Pt_{40}Sn_{20}$ alloys showing decomposition of the La_2Pt_2Sn phase

DFT modeling of the R_2Pt_2Sn compounds was performed w/ and w/o spin-orbit coupling (soc) using both PAW and FP-LAPW methods. The unit cell volume obtained after geometry optimization is in good agreement with experimental data and shows comparable dependence on the rare-earth ionic radii. However, the calculated enthalpies of formation are affected by spin-orbit coupling (eg. La_2Pt_2Sn: −1122 (w/o soc, PAW), −1089 (w/ soc, PAW), −1104 (w/o soc, FP-LAPW), −1010 (w/ soc, FP-LAPW) meV/atom). To check the stability of the R_2Pt_2Sn compounds, the enthalpies of formation were additionally calculated for the corresponding RPtSn and RPt compounds in their known modifications. The results showed that the enthalpy of R_2Pt_2Sn is mostly slightly above (depending on the method and soc) the tie-line that connects RPtSn and RPt, which is consistent with experimental observations. However, off-stoichiometry could be the factor that additionally stabilizes these phases at higher temperatures. To shed more light on the bonding of R_2Pt_2Sn the calculations of the charge density, its difference, and electron localization function (*elf*) were performed. A strong deficit of the charge density on the rare-earth atoms and an excess of the charge density on Pt and Sn are observed.
Preliminary magnetic measurements of some R_2Pt_2Sn compounds revealed a Curie-Weiss behavior with antiferromagnetic ordering at low temperatures. The off-stoichiometry and homogeneity regions of the discovered R_2Pt_2Sn phases allow us to use their chemical flexibility as a knob to navigate the magnetic phase diagram in search of “topological” textures.

The authors thank U. Nitzsche for technical assistance in running the DFT calculations on the ITF/IFW compute cluster. This work is funded by the Deutsche Forschungsgemeinschaft (DFG project RO 6386/2-1).

References

[1] B. Chevalier, F. Fourgeot, D. Laffargue, J. Etourneau, F. Bouree, T. Roisnel, Physica B. **1997**, *230-232*, 195-197.
[2] M. Giovannini, H. Michor, E. Bauer, G. Hilscher, Physical Review B - Condensed Matter and Materials Physics. **2000**, *61*, 4044–4053.

P-06

Formation and Structural Disorder of Half-Heusler Phase in Dy-Ni-Sb Ternary System

V.V. Romaka[1], L. Romaka[2], Yu. Stadnyk[2] and A. Horyn[2]

[1]Leibniz Institute for Solid State and Materials Research (IFW) Dresden, Helmholtzstr. 20, 01069 Dresden, Germany, v.romaka@ifw-dresden.de

[2]Department of Inorganic Chemistry, Ivan Franko National University of Lviv, Kyryla and Mefodiya Str. 6, 79005 Lviv, Ukraine

Introduction

The RNiSb half-Heusler compounds (R – Sc, Y, Gd-Lu) which crystallize in the cubic MgAgAs-type structure (space group *F*-43*m*), exhibit semiconducting behavior (narrow gap semiconductors) and can be used as the basis for promising thermoelectric or magnetic materials. However, their thermoelectric performance is strongly affected by microstructure, heat treatment, the presence of a homogeneity region, and structural disorder effects. During the investigation of the {Y,Gd,Lu}-Ni-Sb ternary systems [1,2] the disorder in the crystal structure of the half-Heusler YNiSb, GdNiSb, and LuNiSb phases with deficiency of Ni atoms was established. It was shown that structural defects in the RNiSb phases directly affected their semiconducting behavior. For the R-Ni-Sb system, the isothermal sections of the corresponding phase diagrams were constructed only for Y, Gd, Er, Tm, and Lu [1-3], while for other heavy rare-earths, only individual compounds were studied.

In our work, we report the isothermal section of the Dy-Ni-Sb system at 873 K and structural data of the ternary compounds accompanied by the detailed study of the structural disorder of DyNiSb, its electrical transport properties, and electronic band structure.

Materials and Methods

Polycrystalline alloys were synthesized by a conventional arc-melting technique using Dy (99.9%), Ni (99.99%), and Sb (99.999%). The evaporative losses of Sb during arc-melting were compensated by additional excess of Sb (3-5 wt.% depending on the composition). The overall weight losses of the alloys after arc-melting were generally less than 1 wt.%. The alloys were annealed in a vacuum at 873 K (700 hours) and quenched in cold water. All samples were characterized by the standard powder XRD and SEM/EDX methods. Measurements of the electrical resistivity were performed in the temperature range of 80-400 K employing the two-probe method on millimeter-scale, well-shaped pieces cut by spark erosion from the polycrystalline samples. The temperature dependence of the thermoelectric power was measured using a standard differential method (pure copper as a reference material) in the temperature interval 80-400 K.

The DFT calculations were carried out with the Vienna Ab initio Simulation Package VASP v.5.4.4 (PAW-type potentials w/ and w/o spin-orbit coupling) and AkaiKKR (KKR-CPA method). The Perdew-Burke-Enzerhoff exchange-correlation functional in the generalized gradient approximation (GGA) was used. Manual geometry optimization was performed using the Universal Equation of State. Crystal structures of supercells were generated using the combinatorial approach.

Results and Discussion

The Dy–Ni–Sb ternary system was studied at 873 K in the whole concentration range. Four ternary compounds are formed: $Dy_5Ni_2Sb_{0.85}$ (Mo_5SiB_2-type), $DyNi_{1-x}Sb$ (MgAgAs-type), $Dy_3Ni_6Sb_5$ ($Y_3Ni_{5.8}Sb_5$-type), $DyNi_{1-x}Sb_2$ ($HfCuSi_2$-type). In the ternary part, a formation of the solid solution $Dy_5Ni_xSb_{3-x}$ (Mn_5Si_3-type) up to ~10 at. % of Ni was observed. Solubility of Ni in the DySb binary (NaCl-type) extends up to ~10 at.% by filling the vacant 8*c* site of the structure with smaller Ni atoms giving the formula of the solid solution $DyNi_xSb$. The most prominent is the homogeneity region of the off-stoichiometric half-Heusler $DyNi_{1-x}Sb$ phase. It extends from 32 down to 20 at.% of Ni towards the $DyNi_xSb$ solid solution. The crystal structure of $DyNi_{1-x}Sb$ and $DyNi_xSb$ are very similar and so are their diffraction patterns. Nevertheless, the doubling of the diffraction peaks from both phases in the two-phase region was observed at high 2θ angles.

DFT modeling of $DyNi_{1-x}Sb$ (*F*-43*m*) and $DyNi_xSb$ (*Fm*-3*m*) by both PAW and KKR-CPA methods showed a slight positive enthalpy of mixing (<20 meV/atom for PAW), which means that the configurational entropy of mixing plays the main role in stabilization of the homogeneity regions from both structures. The modeled lattice parameter *a* of $DyNi_{1-x}Sb$ increases with Ni content and shows a positive deviation from the linear dependence. The formation of vacancies in the 4c site (Ni atoms) of the DyNiSb structure affects the electronic band structure (Fig. 1), by generating additional states in the valence band significantly shrinking the effective band gap. On the other hand, the band structure of $DyNi_xSb$ predicts a metallic type of conductivity and the absence of the band gap near the Fermi level.

Temperature dependences of electrical resistivity lnρ(1/T) and thermopower coefficient α(1/T) for DyNiSb are typical for doped and compensated semiconductors with high- and low-temperature activation regions (Fig. 2). From the high- and low-temperature activation parts of the α(1/T) dependence of DyNiSb the values of activation energy $\varepsilon_{1\alpha}$ = 31.3 meV and $\varepsilon_{3\alpha}$ = 1.9 meV were calculated, which are proportional to the amplitude of large-scale fluctuations of continuous energy bands and small-scale fluctuations of highly doped and highly compensated semiconductors. The thermopower coefficient of the studied sample is characterized by positive values indicating the dominance of p-type conductivity.

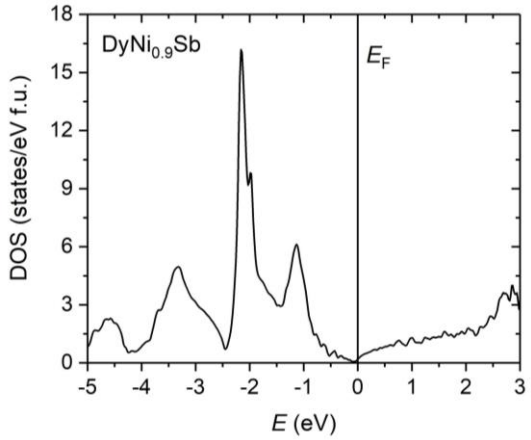

Fig. 1: The density of electronic states (DOS) of $DyNi_{0.9}Sb$ (KKR-CPA method).

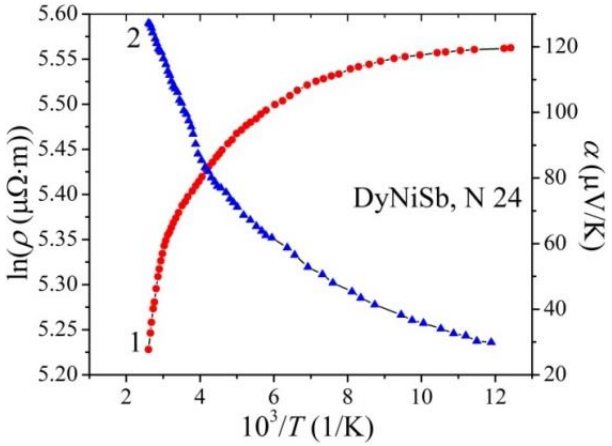

Fig. 2: Temperature dependences of electrical resistivity *r* (1) and thermopower coefficient *a* (2) for DyNiSb.

The authors thank U. Nitzsche for technical assistance in running the DFT calculations on the ITF/IFW compute cluster. This work was supported by the Ministry of Education and Science of Ukraine under Grant No. 0121U109766, by the BMBF UKRATOP project (01DK18002), and partly by the Simons Foundation (Award Number: 1037973).

References

[1] V.V. Romaka, L. Romaka, A. Horyn, P. Rogl, Yu. Stadnyk, N. Melnychenko, M. Orlovskyy, V. Krayovskyy, Journal of Solid State Chemistry. **2016**, *239*, 145–152.
[2] V.V. Romaka, L. Romaka, A. Horyn, Yu. Stadnyk, Journal of Alloys and Compounds. **2021**, *855*, 157434.
[3] L. Zeng, L. Tan, Journal of Alloys and Compounds. **2002**, *346*, 197-199.

P-07

Investigation of refractory high-entropy alloys $(NbMo)_x(CoM)_{100-x}$ (M = Ti, Zr, Hf) with bcc-B2 structure

E. Panina, N. Yurchenko, G. Salishchev, S. Zherebtsov and N. Stepanov

Belgorod National Research University, Belgorod 308015, Russia, panina_e@bsu.edu.ru, yurchenko_nikita@bsu.edu.ru, salishchev_g@bsu.edu.ru, zherebtsov@bsu.edu.ru, stepanov@bsu.edu.ru

Introduction

Conventional paradigm says that intermetallics should be embedded as coherent reinforcements in a disordered and soft matrix to provide balanced mechanical properties. When intermetallic compounds stand as a matrix, the alloys are expected to be strong but brittle. Meantime, some intermetallics such as Co-X (X = Ti, Zr, Hf) B2 phases were found to be ductile at room temperature, albeit with low strength[1–3]. Due to their high melting point, these alloys can be useful for high-temperature applications. In this study, we demonstrated that the bcc phase could significantly strengthen these B2 compounds. The resulting dual-phase structure provided the optimal combination of strength and ductility. The relationships between the chemical composition, microstructure, and mechanical properties of the alloys were discussed.

Materials and Methods

The alloys of the $(NbMo)_x(CoM)_{100-x}$ (M = Ti, Zr, Hf) system were produced by vacuum arc melting. Structure of the alloys was examined using X-ray, scanning (SEM), transmission (TEM) and scanning transmission (STEM) microscopy, and energy-dispersive spectroscopy (EDS). Mechanical properties were evaluated using compression tests at 22-1000°C. More detailed information on the microstructural and mechanical properties characterization are given in [4–6].

Results and Discussion

The $(NbMo)_x(CoHf)_{100-x}$ alloys had mostly a dual-phase structure comprising the disordered (Nb, Mo)-rich bcc and the ordered (Hf, Co)-rich B2 phases. In addition, small portions of the Nb-rich bcc particles were detected in the alloys (Fig. 1 a-c).

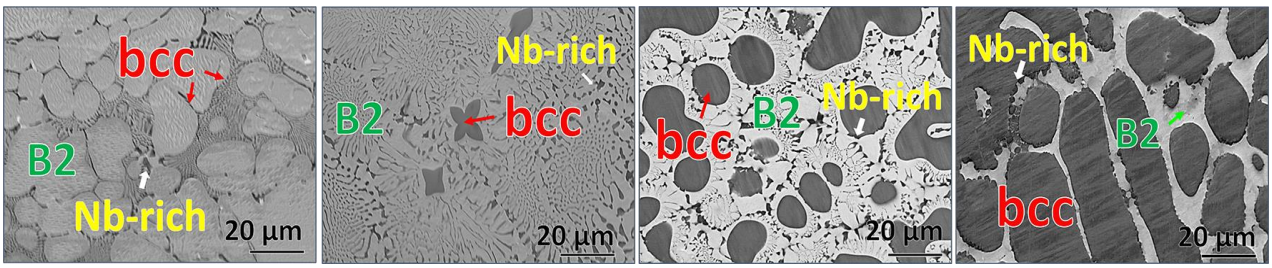

Fig. 1: Microstructure of the $(NbMo)_x(CoHf)_{100-x}$ system alloys: (a) $NbMo_{10}CoHf_{90}$; (b) $NbMo_{25}CoHf_{75}$; (c) $NbMo_{60}CoHf_{40}$; (d) $NbMo_{75}CoHf_{25}$.

Despite significant variations in the volume fraction of the B2 and bcc phases, morphology and scale of the microstructure (fig. 1), the $(NbMo)_{25}(CoHf)_{75}$, $(NbMo)_{60}(CoHf)_{40}$, and $(NbMo)_{75}(CoHf)_{25}$ alloys exhibit very similar yield strength – 1155-1280 MPa at 22 °C and 370-460 MPa at 1000 °C (Fig. 2). This finding can be associated with rather a close hardness of the B2 and bcc phases in the alloys (Fig. 3). The hardness enlargement of both B2 and bcc phases could originate from several factors, including solid solution-like strengthening, long-range stress fields from the interphase boundaries and variations in the stoichiometry of the B2 phase.

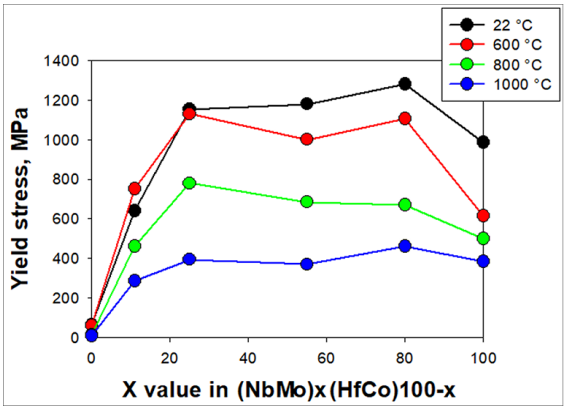

Fig. 2: Mechanical properties of the $(NbMo)_x(CoHf)_{100-x}$ alloys.

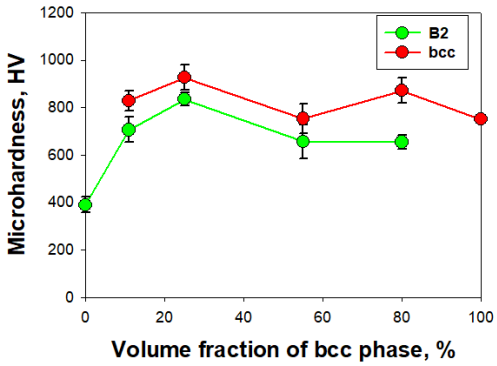

Fig. 3: Microhardness of the B2 and bcc phases in the $(NbMo)_x(CoHf)_{100-x}$ alloys.

Additionally, we have replaced Hf with lighter elements such as Zr and Ti. The substitution of Hf with Ti did not lead to a significant change in the mechanical properties (Fig. 4), but decreased the density. The $(NbMo)_{60}(CoTi)_{40}$ alloy showed a higher specific yield strength than the $(NbMo)_{60}(CoZr)_{40}$ and $(NbMo)_{60}(CoHf)_{40}$ alloys, as well as some Ni- and Co-based superalloys (Fig. 5).

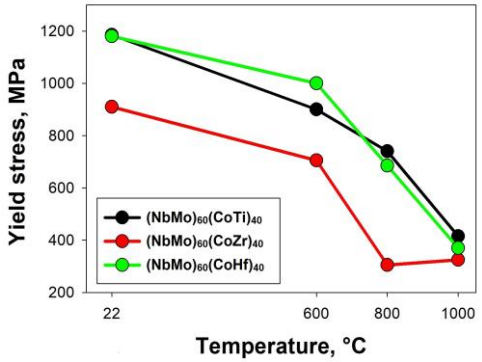

Fig. 4: Temperature dependence of yield stress of the $(NbMo)_{60}(HfCo)_{40}$, $(NbMo)_{60}(ZrCo)_{40}$, and $(NbMo)_{60}(TiCo)_{40}$ alloys.

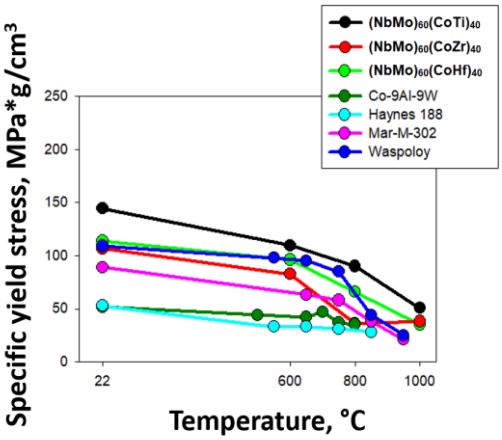

Fig. 5: Temperature dependence of specific yield stress of the $(NbMo)_{60}(HfCo)_{40}$, $(NbMo)_{60}(ZrCo)_{40}$, and $(NbMo)_{60}(TiCo)_{40}$ alloys in comparison with some other Ni- and Co-based superalloys.

Conclusions

Using the $(NbMo)_x(CoM)_{100-x}$ (M = Ti, Zr, Hf) alloy system, we showed the possibility of forming a structure with a soft B2 matrix and hard bcc phase resulting in balanced mechanical properties.

Acknowledgments

This work was supported by the Russian Science Foundation Grant no. 19-79-30066.

References

[1] M.Y. T. Takasugi, O. Izumi, J. Mater. Sci. **1991**, 26, 2941–2948.
[2] T. Yamaguchi, Y. Kaneno, T. Takasugi, Scr. Mater. **2005**, 52, 39–44.
[3] T. Agnew, S R; Ungar, Mater. Sci. Eng. **2019**, 580, 012001.
[4] N. Yurchenko, E. Panina, Ł. Rogal, L. Shekhawat, S. Zherebtsov, N. Stepanov, Mater. Res. Lett. **2022**, 10, 78–87.
[5] N. Yurchenko, E. Panina, D. Shaysultanov, S. Zherebtsov, N. Stepanov, Materialia. **2021**, 20, 101225.
[6] E. Panina, N. Yurchenko, A. Tojibaev, M. Mishunin, S. Zherebtsov, N. Stepanov, J. Alloys Compd. **2022**, 927, 167013.

P-08

A Mechanical Spectroscopy study of the Relaxation processes in Fe-Mn-Cr-Co-Ni Cantor High Entropy Alloys

Lucia del-Río[1], José M. San Juan[1], Guillaume Laplanche[2] and Maria L. Nó[1]

[1]Dpt. Of Physics, Faculty of Science and Technology, University of the Basque Country (UPV/EHU), Bilbao, Spain,
lucia.delrio@ehu.eus ; jose.sanjuan@ehu.eus ; maria.no@ehu.eus
[2]Institut für Werkstoffe, Ruhr-Universität Bochum, D-44801 Bochum, Germany,
guillaume.laplanche@rub.de

Introduction

Contrary to the conventional idea of alloys for millennia, the new High Entropy Alloys (HEA), among others the Cantor family [1], offer a very high strength (>1GPa) together with a very high ductility (>60%) even at very low temperatures (77K), currently being the existing materials with the highest fracture toughness [2][3]. Thus, they open up many potential applications, from cryogenic devices for superconductors to aerospace applications.
In addition, HEA exhibit in general a sluggish diffusion, making them more stable at high temperature, which is a relevant factor in its creep behavior. However, the compositional complexity of the HEA makes the study of the microscopic mechanisms that govern them a challenge.

In the present work, a first study of the relaxation processes In Cantor alloys Fe-Mn-Cr-Co-Ni is approached in a broad temperature range. The aim of our work is to identify the relaxation peaks associated with the mobility of structural defects, such as dislocations and point defects.

Materials and Methods

Alloys with a nominal composition of 20Fe-20Mn-20Cr-20Co-20Ni at% were prepared by casting, followed by a homogenization treatment at 1200ºC for 48 hours and a hot swaging process. From the annealed ingots, samples for microstructure characterization and mechanical spectroscopy studies were cut. Microstructure in initial stated and after recrystallization was examined by scanning electron microscopy (SEM) and its corresponding EDX analysis. At different frequencies, internal friction measurements, in addition to its dynamic modulus, were carried out in a temperature range between 600K and 1400K in order to identify the relaxation processes or diffusional mechanisms. These measurements were made in a low frequency sub-resonant torsion pendulum.

Results and Discussion

After the recrystallization process at 1200ºC for 1 hour, the obtained microstructure is presented in Figure 1. As it is observed from the image in Figure 1(a), the grain size varies throughout the sample from approximately 100µm to 400µm. It can also be noted that regardless of their size, the grains tend to form twins. Regarding the composition, the alloys are shown to be homogeneous, keeping the nominal cantor proportions. However, there is a continuous presence of inclusions, which are proven to be chromium and manganese oxides, as shown in Figure 1(b).

Figure 2. shows the Internal Friction spectra, along with the dynamic modulus, measured for different frequencies, from 2Hz to 0.01Hz, as a function of temperature for a Fe-Mn-Cr-Ni-Co HEA, Cantor alloy. The Internal friction spectra exhibits a broad peak between 800 and 1250K, which is associated to the presence of some low temperature relaxation peaks that clearly shift with frequency. In addition, a high temperature peak appears around 1300K, with a very small shift in temperature, together with an exponential high temperature background.
In parallel to the internal friction peaks, the dynamic modulus variation also evolves in temperature. There is a significant decrease at approximately 1300K, which is the same temperature as the high temperature IF peak.
However, to analyze these spectra, some calculation must be made, that is, remove the high temperature background, and plot the data as a function of 1/T. Then the IF spectra as a function of 1/T is analysed.

As the high temperature peak does not change in frequency, it is concluded that it is related to some diffusion phase transition. According to literature it may be associated with the sigma σ phase [4]. On the other hand, after the analysis and deconvolution of the broad IF spectra, the obtained results can be associated, in a first approach, with the mobility of structural defects. Nonetheless, further investigation is needed in order to discern and interpret the obtained data and its associated phenomenon.

Acknowledgements

This work was supported by the, PhD Grant PRE_2022_1_0109 of Lucía Del-Rio and the Project ELKARTEK MINERVA, from the Basque Government, and by the Excellence Research Group GIU-21/024 from the University of the Basque Country.

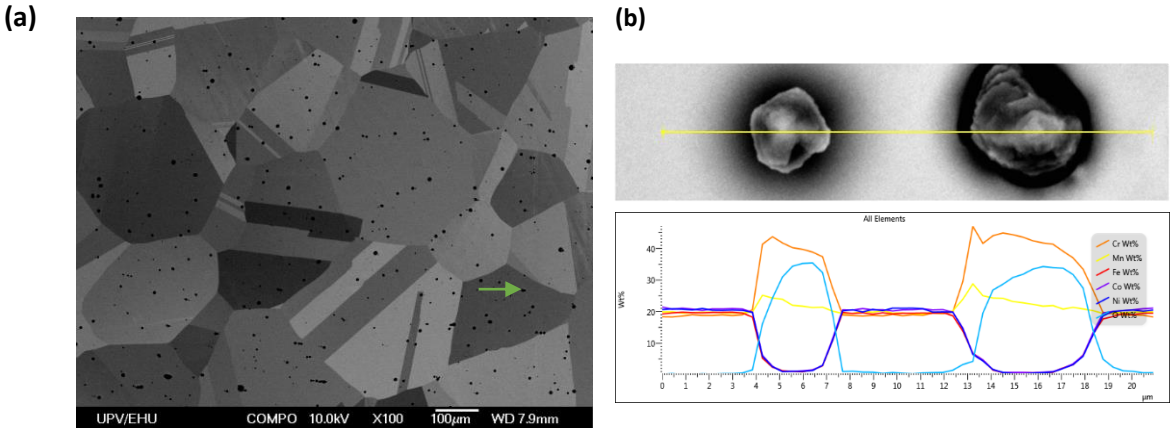

Fig. 1: (a) Scanning Electron Microscopy Image of a Cantor HEA sample after a recrystallization treatment at 1200ºC for 1 hour. (b) EDX line analysis of two black spots that shows the existence of Cr and Mn oxides.

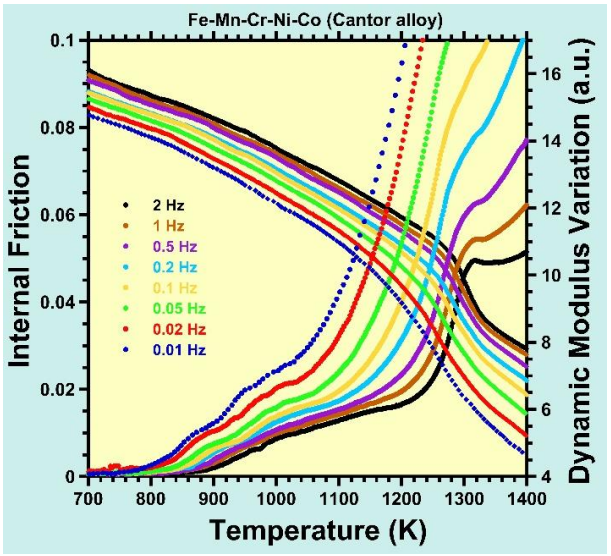

Fig. 2: Internal Friction spectra measured at different frequencies (2Hz-0.01Hz) as a function of temperature for an Fe-Mn-Co-Cr-Ni Cantor HEA.

References

[1] B. Cantor et al., Material Science Engineering A 375-377, **2004**, 213-218.
[2] B. Gludovatz et al., Science 345, Issue 620, **2014**, 1153-1158.
[3] E.P. George, D. Raabe, R.O. Richie, Nature Reviews | Materials 4, **2019**, 515-534.
[4] C. Wagner et al., Acta Materialia 227, **2022**, 117693.

P-09

The New Calphad Optimizer in FactSage

Cassie Frueh, Florian Tang, Philipp Keuter, Bruno Reis and Moritz to Baben

Kaiserstrasse 103, 52134 Herzogenrath, Germany, cf@gtt-technologies.de

Introduction

The CAlculation of PHAse Diagrams or CALPHAD modeling is a technique used for the prediction of equilibrium phase stabilities and thermodynamic properties of multi-component systems including intermetallics. CALPHAD assessments are normally completed on the pure elements, binary and ternary systems and then extrapolated to higher order systems. The assessments consist of three steps: (1) the collection of experimental data, (2) the setup of thermochemical models, (3) the optimization of the models with the experimental data. The last step is accomplished using an optimization software. FactSage (www.gtt-technologies.de) is one of the largest fully integrated thermodynamic software and database packages in chemical thermodynamics. The software package itself includes different modules and while FactSage was introduced in 2001, recently a new Calphad Optimizer has been introduced, greatly improving the CALPHAD optimization process of building individual databases.

Results and Discussion

The new Calphad Optimizer in FactSage, shown in Figure 1, provides an intuitive interface to guide beginners and established Calphadians through their optimizations. The interface has four sections: Experimental Data, Parameters, Optimization, and Results. In the first section Experimental Data the relevant experimental data, such as liquidus temperatures, eutectics, and activity constituents, is entered for the optimization with tailored recipes. In the second section (Parameters) the model parameters to be optimized at one time can be controlled. The Optimization section allows the selection from two different optimizers and adjustments of the optimization settings. Alternatively it can show a default user information for beginners. The last section of Results allows for real-time plotting of the experimental information against the optimization and phase mapping for extensive feedback during the optimization.

The new Calphad optimizer greatly improves the optimization process as well as allowing for more or less control on all optimization steps while making use of a user-friendly, well defined interface.

Fig. 1: The user interface of the new Calphad optimizer in FactSage

P-10

Tailoring α_2/γ and γ/γ interfaces in TiAl alloys via segregation: A multi-method study

David Holec[1], Dominik Gehringer[1], Liam Huber[2] and Jörg Neugebauer[2]

[1] Department of Materials Science, Montanuniversität Leoben, Franz-Josef-Straße 18, 8700 Leoben, Austria, david.holec@unileoben.ac.at

[2] Max-Planck-Institut für Eisenforschung GmbH, Max-Planck-Straße 1, 40237 Düsseldorf, Germany

Introduction

In this present contribution, we employ a coupled multi-method quantum-mechanics/molecular mechanics (QM/MM) approach well suited for studying compositionally complex extended defects. We focus on the interfacial phenomena of γ/α_2 and γ/γ phase boundaries in intermetallic TiAl alloys.

Methods

For the first time, we apply QM/MM to an interface constituted by two distinct phases. We shortly introduce the methodology and point out its advantages compared to conventional modeling approaches. We show that our newly implemented algorithm can accurately reproduce site-preference energies of solutes reported by previous density functional theory studies. We employ the site-preference energy to establish a formalism to describe segregation mechanisms in multi-sublattice and multi-phase systems. Using our formalism, we have studied a wide variety of 3*d*, 4*d*, and 5*d* transition metals to decorate the crystal defects. Furthermore, we have performed static cleavage calculations to quantify the impact of solute segregation in the interface on its mechanical properties.

Results and Discussion

We use the model to predict the preferred positions of solutes at the interface(s) and different segregation/partition mechanisms. Our theoretical predictions are consistent with Atom Probe Tomography measurements reporting phase preference and phase boundary segregation for many of the studied solutes.

Moreover, knowing the behavior of solutes at the interfaces, we have investigated their impact on mechanical properties (Fig. 1). We have calculated critical strength, debonding energy, unidirectional Young's modulus, and an estimation of the fracture toughness of nano-lamellar γ/α_2 and γ/γ packets. The thus obtained values will be presented in the context of experimental data from the literature.

Finally, we present a strategy for combining the information from our predictions to illustrate how theoretical methods can enrich the understanding of important phenomena and enlighten the alloy development process.

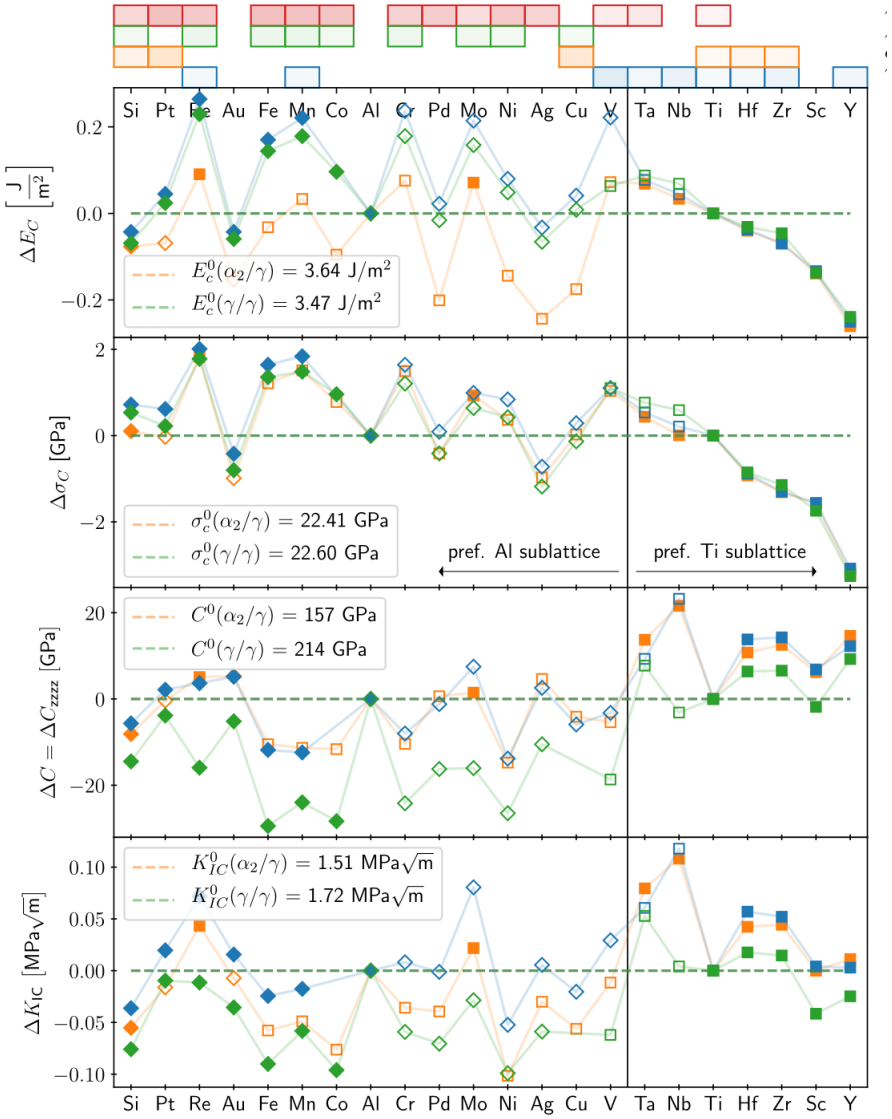

Fig. 1: Predicted impact of segregated solutes at the γ/α$_2$ on interfacial properties: critical interface stress σ_C, interfacial cleavage energy E_C, directional Young's modulus (normal to the interface-plane) C_{zzzz} and estimated fracture-toughness of (α_2/γ, γ/γ) lammellar packet K_{IC}. The boxes above each solute denote whether there is a tendency for the solute to segregate: $\gamma_{bulk} \rightarrow$ γ/γ (green), $\alpha_{2,bulk} \rightarrow \alpha_2/\gamma$ (orange) and $\gamma_{bulk} \rightarrow \alpha_2/\gamma$ (blue); phase preference γ → α$_2$ is indicated by the red boxes. Squares and diamond symbols indicate Ti and Al sublattice preference, respectively. Full and open symbols distinguish between strong and compositionally dependent site-preference. The orange curve denotes that the solute was placed on the α$_2$-side of the α$_2$/γ phase-boundary, while the blue curve corresponds to the γ side of the interface. The green curve shows the values for solutes at the γ/γ twin boundary.

References:

D. Gehringer, L. Huber, J. Neugebauer, D. Holec, Physical Review Materials **2023**, 7, 063604.

P-11

The New Thermo-Calc Additive Manufacturing Module

Andre Schneider, Amer Malik, Quang Minh Do, Andreas Markström and Johan Jeppsson

Thermo-Calc Software AB, Stockholm, Sweden, andre@thermocalc.com

Thermo-Calc has spent the last few years developing new models to predict thermophysical material properties to incorporate with CALPHAD-based materials descriptions. This is currently used to extract CALPHAD-based materials data for use in dedicated FEM codes and is now laying the foundation for our development of a completely integrated tool to simulate Additive Manufacturing (AM) processes. The AM Calculator is released in Thermo-Calc version 2023b, and it gives a unique possibility to address the problem of solidification during AM, where we obtain a unified treatment of both process parameters and chemistry-dependent thermophysical properties when solving the multi-physics problem of a moving heat source that melts and solidifies metal powder. The updated Scheil calculator allows for pre-generating a solidification profile, now also including evaporation properties, that can be saved into your own materials library, or used directly as input to the AM Calculator. Examples of the AM module applied to different material classes such as nickel-based alloys strengthened with intermetallic phases are shown. One of the examples is shown in Figures 1 and 2. Figure 1 shows the steady state simulation of alloy 718 using Scheil with freeze in model. This simulation uses the temperature-dependent thermophysical properties heat per mole, viscosity, thermal conductivity, and surface tension for this alloy shown in Figure 2.

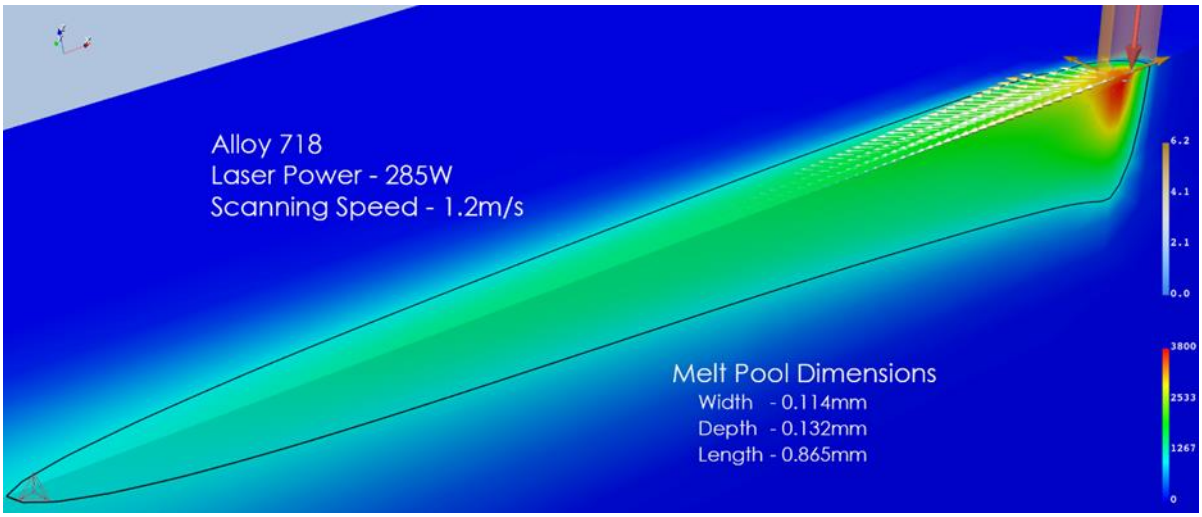

Fig. 1: Steady state simulation of alloy 718 using the below calculated thermophysical properties calculated using Scheil with freeze in model for a specific 718 chemistry.

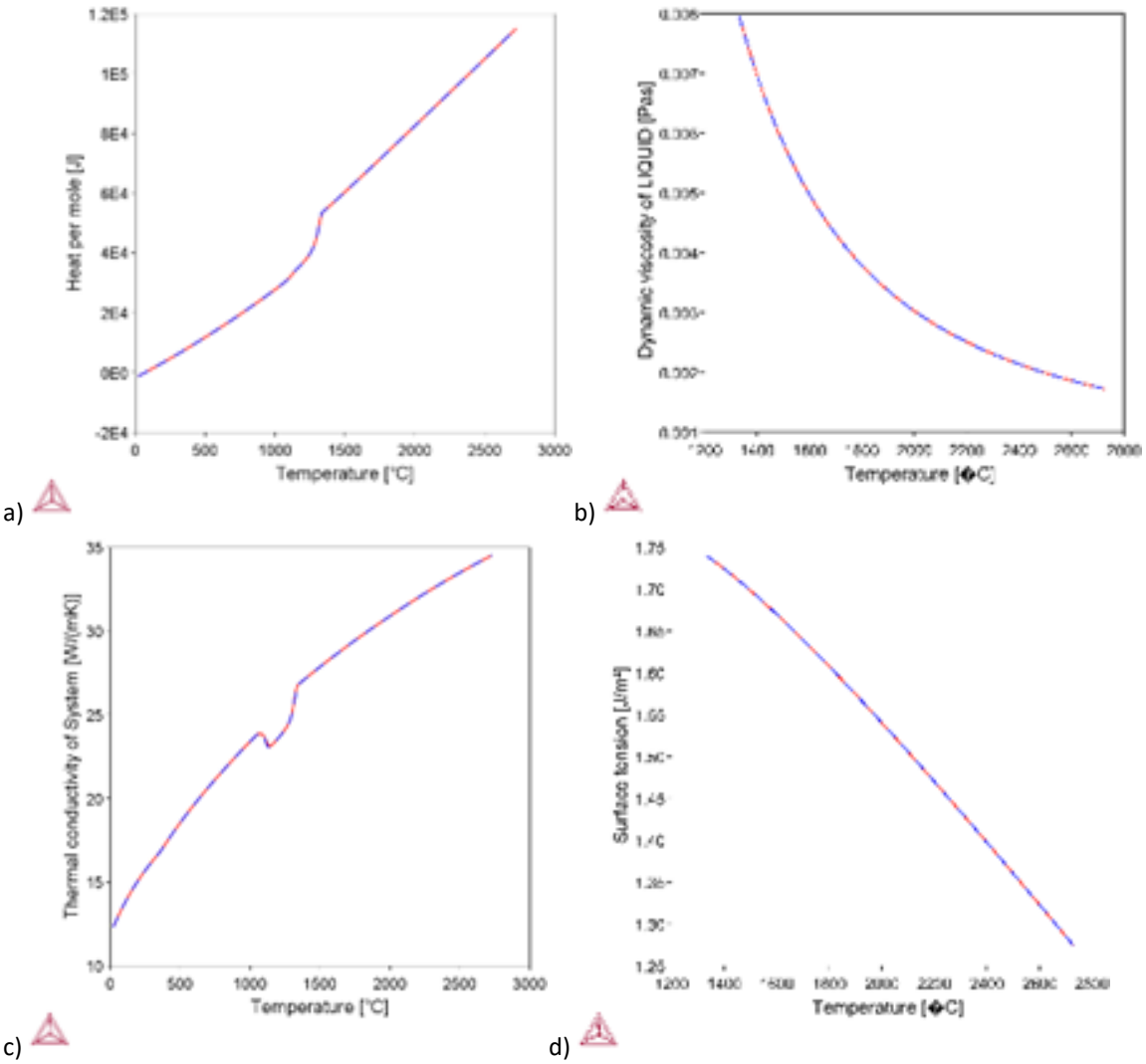

a) b) c) d)

Fig. 2: a-d. (a) Heat per Mole vs Temperature, (b) Viscosity vs Temperature, (c) Thermal Conductivity vs Temperature, and (d) Surface Tension of Liquid vs Temperature.